MODELING OF THERMO-MECHANICAL AND IRRADIATION BEHAVIOR OF METALLIC AND OXIDE FUELS FOR SODIUM FAST REACTORS

ARCHIVES
MASSACHUSETTS INSTITUTE OF TECHNOLOGY
MAR 1 2 2010
LIBRARIES

by
Aydın Karahan
M.S. Nuclear Science and Engineering
Massachusetts Institute of Technology, 2007
B.S. Nuclear Engineering
M.S. Nuclear Engineering
Hacettepe University, 2005

Submitted to the Department of Nuclear Science and Engineering
in partial fulfillment of the requirements for the degree of

DOCTOR OF PHILOSOPHY IN NUCLEAR SCIENCE AND ENGINEERING

at the

MASSACHUSETTS INSTITUTE OF TECHNOLOGY

30 June 2009

© Massachusetts Institute of Technology 2009. All rights reserved.

Author.....
Department of Nuclear Science and Engineering
June, 2009

Certified by.....
Jacopo Buongiorno
Associate Professor of Nuclear Science and Engineering
Thesis Supervisor

Certified by.....
Mujid S. Kazimi
Professor of Nuclear Engineering
Thesis Reader

Accepted by.....
Jacquelyn C. Yanch
Professor of Nuclear Science and Engineering
Chairman, Committee for Graduate Studies

"Peace at Home, Peace in the World"

Mustafa Kemal Atatürk

MODELING OF THERMO-MECHANICAL AND IRRADIATION BEHAVIOR OF METALLIC AND OXIDE FUELS FOR SODIUM FAST REACTORS

by
Aydın Karahan

Submitted to the Department of Nuclear Science and Engineering
on June 30, 2009 in partial fulfillment of the
requirements for the degree of
DOCTOR OF PHILOSOPHY IN NUCLEAR SCIENCE AND ENGINEERING

ABSTRACT

A robust and reliable code to model the irradiation behavior of metal and oxide fuels in sodium cooled fast reactors is developed. Modeling capability was enhanced by adopting a non-empirical mechanistic approach to the extent possible, so that to increase the ability to extrapolate the existing database with a reasonable accuracy.

Computational models to analyze in-reactor behavior of U-Zr and U-Pu-Zr metallic alloy fuel pins and UO_2-PuO_2 mixed oxide fuel pins have been developed and implemented into a new code, the Fuel Engineering and Structural analysis Tool (FEAST). FEAST has several modules working in coupled form with an explicit numerical algorithm. These modules describe (1) Fission Gas Release and Swelling, (2) Fuel Chemistry and Restructuring, (3) Temperature Distribution, (4) Fuel Clad Chemical Interaction, (5) Fuel and Clad Mechanical Analysis and (6) Transient Creep-Fracture Model for the clad. Given the fuel pin geometry, composition and irradiation history, FEAST can analyze fuel and cladding thermo-mechanical behavior at both steady state and design-basis accident scenarios.

FEAST was written in FORTRAN-90 program language. The FEAST-METAL code mechanical analysis module implements the old Argonne National Laboratory (ANL)'s LIFE code algorithm. Fission gas release and swelling are modeled with the Korean GRSIS algorithm, which is based on detailed tracking of the fission gas bubbles within the metal fuel. Migration of the fuel constituents is modeled by means of the thermo-transport theory. Fuel Clad Chemical Interaction (FCCI) models were developed for steady-state and transient situations, based on precipitation kinetics. A transient creep fracture model for the clad, based on the constrained diffusional cavity growth model, was adopted. FEAST-METAL has been benchmarked against available EBR-II

database for (steady state) and furnace tests (transients). The results show that the code is able to predict important phenomena such as cladding strain, fission gas release, clad wastage, clad failure time and axial fuel slug deformation, satisfactorily.

A similar code for oxide fuels, FEAST-OXIDE, was also developed. It adopts the OGRES model to describe fission gas release and swelling. However, the original OGRES model has been extended to include the effects of Joint Oxide Gain (JOG) formation on fission gas release and swelling. The fuel chemistry model includes diffusion models for radial actinide migration, cesium axial and radial migration, formation of the JOG, and variation of the oxygen to metal ratio. Fuel restructuring is also modeled, and includes the effects of porosity migration, irradiation-induced fuel densification and grain growth. The FEAST-OXIDE predictions has been compared to the available FFTF, EBR-II and JOYO databases, and the agreement between the code and data was found to be satisfactory.

Both metal and oxide versions of FEAST are rather superior compared to many other fuel codes in the literature. Comparing metal and oxide versions, FEAST-OXIDE has a more sophisticated fission gas release and swelling model, which is based on vacancy flow. In addition, modeling of the chemistry module of the oxide fuel requires a much more detailed analysis to estimate its impact on the thermo-mechanical behavior with a reasonable accuracy. Finally, the melting of the oxide fuel and its effect on the thermo-mechanical performance have been modeled in case of transient scenarios.

Thesis Supervisor: Jacopo Buongiorno
Title: Associate Professor of Nuclear Science and Engineering

Thesis Reader: Mujid S. Kazimi
Title: TEPCO Professor of Nuclear Engineering

ACKNOWLEDGEMENTS

This work was supported by United States Nuclear Regulatory Commission.

I would like to express my deepest gratitude to my advisor, Professor Jacopo Buongiorno. His trust, guidance, encouragement and numerous discussions were very critical to the ultimate success of this work.

It is author's great pleasure to thank Professor Mujid S. Kazimi. He allowed me to work in very diverse fields during my stay at MIT. His trust and many fruitful discussions were greatly helpful.

I am indebted to Professor Üner Çolak, Professor Osman Kemal Kadiroğlu, Professor Yalçın Sanalan, Professor Cemal Niyazi Sökmen, Professor Mehmet Tombakoğlu and Professor Okan Zabunoğlu in Nuclear Engineering Department, Hacettepe University, Turkey. This work would not have been possible without their contribution to my engineering skills.

I am very grateful to my mother, Zekiye Karahan, my brother, Haydar Karahan, my grandmother, Şükran Cebeci, my grandfather, Mustafa Cebeci, and my aunt, Gülen Karahan for their encouragement, support and love.

I believe the ability of mathematical thinking is a key element to success in engineering. My father, Ali Karahan, had an outstanding comm and of mathematics. I consider myself very lucky to have inherited a piece of math ability from him. This work, therefore, is dedicated to Ali Karahan.

TABLE OF CONTENTS

ABSTRACT 3
ACKNOWLEDGEMENTS 5
TABLE OF CONTENTS 6
LIST OF FIGURES 12
LIST OF TABLES 17
LIST OF ACRONYMS 19
NOMENCLATURE 21
1. INTRODUCTION 39
1.1. Motivation 39
1.2. Background 39
1.3. Objectives 41
2. MODELS FOR METALLIC FUEL 43
2.1. Introduction 43
2.1.1. Description of a Typical Metal Fuel Pin 44
2.1.2. Project Objectives and Review of Current Metal Fuel Codes 44
2.1.3. Thermo-mechanical Behavior of the Metal Fuel 48
2.1.4. FEAST-METAL Code Structure 48
2.2. Fission Gas Release and Swelling Module 52
2.2.1. Introduction 52
2.2.2. Fission Gas Release and Swelling Behavior of Metal Fuel 53
2.2.3. Modeling of the Fission Gas Behavior 54
2.2.4. Governing Equations for GRSIS Model 57
2.2.5. Bubble-1 Nucleation Rate 59
2.2.6. Gas Diffusion 59
2.2.7. Coalescence by Bubble Diffusion 60
2.2.8. Coalescence by Bubble Growth 61
2.2.9. Open Bubble Surface Area and Volume Correction 63
2.2.10. Swelling 63
2.2.11. Fission Gas Release 64
2.2.12. Critical review of simplifying assumptions made by the GRSIS model 64

2.3. Modeling of Constituent Redistribution in U-Zr and U-Pu-Zr fuel 67
2.3.1. Introduction 67
2.3.2. Major Assumptions 67
2.3.3. Fundamental Data 68
2.3.4. Model Development 72
2.3.5. Boundary Conditions 73
2.3.6. Model Verification 74
2.4. Temperature Distribution Model 79
2.4.1. Introduction 79
2.4.2. Coolant Temperature Distribution 79
2.4.3. Fuel Pin Radial Temperature Calculation 82
2.4.4. Energy Balance Method 83
2.4.5. Material Properties 85
2.4.6. Sensitivity Study and Benchmarking 88
2.5. Fuel Clad Chemical Interaction Module 89
2.5.1. Introduction 89
2.5.2. Precipitation Kinetics Model 91
2.5.3. Sodium Corrosion 97
2.6. Mechanical Analysis 98
2.6.1. Introduction 98
2.6.2. General Assumptions 98
2.6.3. Governing Equations 99
2.6.4. Solution Method 100
2.6.5. Boundary Conditions 103
2.6.6. Calculation of the Interfacial Pressure 104
2.6.7. Axial Force Balance 105
2.6.8. Creep and Plasticity 106
2.6.9. Swelling 108
2.6.10. Anisotropic Fuel Slug Deformation 110
2.6.11. Verification of the Mechanical Analysis Module against the Analytical Solution for the Radial Distribution of Thermal Stresses 112

2.7. Transient Creep Fracture Modeling 114
2.7.1. Cumulative Damage Fraction Model 115
2.7.2. Constrained Diffusional Cavity Growth Model 115
3. VERIFICATION OF FEAST-METAL 121
3.1. Steady State 121
3.1.1. X430 Benchmark 121
3.1.2. X425 Benchmark 129
3.1.3. X447 Benchmark 133
3.1.4. Comparison with the ALFUS Code for the Current Metal Fuel Irradiation in the PHENIX Reactor 135
3.2. Transients 141
4. METALLIC FUEL DESIGN AND PARAMETRIC STUDIES 144
4.1. Metal Fuel Parametric Study 144
4.1.1. Steady State 144
4.1.2. Transients 146
4.2. A Breed and Burn Reactor Design, an Application of FEAST-METAL 151
4.2.1. Driver Fuel 152
4.2.2. Seed Fuel 159
4.3. Annular Metal Fuel Modeling 167
4.3.1. Temperature Distribution 168
4.3.2. Mechanical Analysis 170
4.3.3. Fuel Clad Chemical Interaction 172
4.3.4. Steady State Analysis 172
4.3.5. Transient Analysis 175
5. MODELS FOR MIXED OXIDE FUEL 179
5.1. Introduction 179
5.1.1. Description of the Mixed Oxide Fuel Pin 180
5.1.2. Thermo-mechanical Behavior of the Oxide Fuel 181
5.1.3. Project Objectives and Review of Current Oxide Fuel Codes 182
5.1.4. FEAST-OXIDE Code Structure 185
5.2. Fission Gas Release and Swelling 189

5.2.1. Introduction 189
5.2.2. Intragranular Gas Model (OGRES-I) 189
5.2.3. Grain Boundary Gas Behavior (OGRES-II) 199
5.2.4. Gas Bubble Swelling 207
5.2.5. Swelling due to solid fission product swelling 207
5.2.6. Benchmarks 207
5.3. Fuel Chemistry and Restructuring 210
5.3.1. Introduction 210
5.3.2. Modeling the Burnup Dependency of the Oxygen to Metal Ratio 211
5.3.3. Radial Redistribution of the Oxygen to Metal Ratio 216
5.3.4. Radial Migration of the Actinides 220
5.3.5. Cesium Migration 221
5.3.6. As-fabricated Porosity Migration 227
5.3.7. Irradiation-induced Fuel Densification 230
5.3.8. Grain Growth 231
5.3.9. Fuel Cracking and Relocation 232
5.4. Temperature Distribution 232
5.4.1. Introduction 232
5.4.2. Heat Generation Rate 233
5.4.3. Numerical Algorithm to Simulate the Melting 233
5.4.4. Melting Temperature 234
5.4.5. Fuel Thermal Conductivity 236
5.4.7. Specific Heat of Fuel 240
5.4.8. Verification of the Thermal Analysis Model 241
5.5. Fuel Clad Chemical Interaction 244
5.5.1. Introduction 244
5.5.2. Model Description 245
5.5.3. Other FCCI Models 246
5.5.4. Model Verification 247
5.5.5. Parametric Study 248
5.6. Mechanical Analysis 251

5.6.1. Introduction 251
5.6.2. Fuel Material Properties 251
5.6.3. Fuel Cracking and Healing 255
5.6.4. Hot Pressing 256
6. VERIFICATION OF FEAST-OXIDE 257
6.1. Steady State 257
6.1.1. FFTF Benchmarks 257
6.1.2. EBR-II Benchmarks 267
6.1.3. JOYO Benchmarks 274
6.2. Transients 276
7. SUMMARY, CONCLUSIONS AND FUTURE WORK 282
7.1. Summary 282
7.2. Conclusions 289
7.3. Future Work 290
Appendix-A: Material Properties 302
A.1. HT9 Cladding Mechanical Properties 302
A.1.1. Young's Modulus, Shear Modulus and Poisson's Ratio 302
A.1.2. Thermal Expansion 302
A.1.3. Irradiation Creep 302
A.1.4. Thermal Creep 303
A.2. D9 Cladding Mechanical Properties 304
A.2.1. Thermal Expansion [42] 304
A.2.2. Irradiation Creep [122] 304
A.2.3. Swelling [123] 304
A.2.4. Thermal Creep [122] 305
A.3. 20 % Cold Worked 316 Stainless Steel Mechanical Properties 305
A.3.1. Irradiation and Thermal Creep [122] 305
A.4 Fuel Mechanical Properties 306
A.4.1. Thermal Expansion Coefficient 306
A.4.2. Modulus of Elasticity [23] 306
A.4.3. Yield Strength 307

Appendix-B: Oxygen Potential 308
Appendix-C: FEAST Input Description 309
C.1. FEAST-METAL Input Description 309
C.2. Metal Fuel Bencmhark Inputs 311
C.3. FEAST-OXIDE Input Description 327
C.4. Oxide Fuel Benhmark Inputs 329

LIST OF FIGURES

Figure-1: Description of the metallic fuel 44
Figure-2: Flow sheet of FEAST-METAL 51
Figure-3: Fission gas release of ANL fuel irradiation tests [26] 53
Figure-4: Fission gas and bubble movement model 55
Figure-5: Empirical correlation for fission gas release (Experimental data is taken from Ref. [26]) 56
Figure-6: Pseudo binary phase diagram for U-Pu-Zr Fuel for fixed Pu content [34] 69
Figure-7: T-179 fuel data and temperature profile at a location 230 mm above the bottom of the fuel 74
Figure-8: Radial zirconium distribution within the T179 fuel pin at an axial location 230 mm from the bottom of the fuel 75
Figure-9: Fuel temperature distribution 76
Figure-10: Case-1 fuel constituent redistribution results 76
Figure-11: Case-2 fuel constituent redistribution results 77
Figure-12: Case-3 fuel constituent redistribution results 77
Figure-13: DP-11 fuel rod irradiation history [37] 78
Figure-14: Zirconium atom fraction 79
Figure-15: Radial discretization of the fuel pin 83
Figure-16: Sensitivity of the fuel temperature distribution to important irradiation effects 88
Figure-17: Node sensitivity to temperature distribution calculation 89
Figure-18: Phases present at fuel clad interface (U-10 Zr/HT9) [46] 91
Figure-19: $(U,Pu)_6$ Fe minimum liquefaction (eutectic formation) temperature [47] 91
Figure-20: Precipitation kinetics theory [50] 92
Figure-21: Growth of the reaction zones [46] and [48] 93
Figure-22: Axial clad wastage profile of X447 fuel pins at End of Life and FEAST calibration 95
Figure-23: Subdivision of the fuel element into radial and axial nodes [2] 102
Figure-24: Cladding strain dependency on number of radial nodes at 12 at % 103
Figure-25: Anisotropy factor 111
Figure-26: Radial stress distribution in radial direction 113
Figure-27: Hoop stress radial distribution 113
Figure-28: Axial stress radial distribution 114
Figure-29: Creep fracture map of a typical ferritic-martensitic stainless steel [55] 114
Figure-30: Cavitating polycrystalline [59] 116
Figure-31: HT9 creep rupture behavior at constant stress and temperature (Low Temperature) 119
Figure-32: HT9 creep rupture at constant stress and temperature (High Temperature) 120
Figure-33: Irradiation history of T-654 122
Figure-34: Axial power profile 122
Figure-35: Fission gas release behavior of T-654 fuel rod. 123
Figure-36: (a) Swelling at 50 %, (b) Swelling at 93 % of the fuel slug length for T-654 fuel rod 124
Figure-37: Contact and plenum pressure for T-654 fuel rod 124
Figure-38: (a): Peak cladding strain for T-654 fuel rod (b): Axial distribution of the cladding strain at EOL 125
Figure-39: U-10Zr/HT9 cladding strain behavior (fuel smear density is ~75 %) [20] 126

Figure-40: U-19Pu-10Zr/HT9 clad strain data (72 % smear density) [21] 127
Figure-41: U-19Pu-10Zr/HT9 clad strain data (72 % smear density) [19] 127
Figure-42: U-19Pu-10Zr/HT9 clad strain data (85 % smear density) [19] 128
Figure-43: Approximate irradiation history of X425 assembly 129
Figure-44: Fission gas release behavior of the X425 fuel rod 130
Figure-45: (a) Swelling at 36 %, (b) Swelling at 93 % of the fuel slug length for X425 peak fuel rod 131
Figure-46: Contact and plenum pressure for X425 assembly 131
Figure-47: Peak cladding strain for X425 assembly 132
Figure-48: Axial variation of cladding strain (peak burnup is 15.8 at %) 132
Figure-49: DP04 fuel rod irradiation history 133
Figure-50: Fission gas release behavior of DP-04 fuel rod 134
Figure-51: Peak cladding strain for DP04 fuel rod 135
Figure-52: (a): Total peak neutron flux (b): Peak linear power [64] 136
Figure-53: Axial power profile [64] 136
Figure-54: Creep modulus [67] 137
Figure-55: Swelling behavior of CW 15-15Ti at 460 ^{o}C and 500 ^{o}C [67] 138
Figure-56: Swelling behavior of CW 15-15Ti at 540 ^{o}C [67] 139
Figure-57: (a) ALFUS prediction (b): FEAST prediction 140
Figure-58: (a) ALFUS prediction (b): FEAST prediction 140
Figure-59: (a) ALFUS prediction (b): FEAST prediction 141
Figure-60: Cladding strain at 7.23 at % 141
Figure-61: The effect of plenum to fuel ratio on clad strain 144
Figure-62: The effect of fuel smear density on clad strain 145
Figure-63: Variation of fission gas release with coolant outlet temperature 146
Figure-64: Power history in simulated UTOP scenarios 147
Figure-65: Peak clad temprature history in simulated UTOP scenarios 147
Figure-66: Fuel clad mechanical interaction and plenum pressure in simulated UTOP transients 148
Figure-67: Power history in the simulated ULOHS/ULOF scenarios 149
Figure-68: Peak clad temprature history in simulated ULOHS/ULOF scenarios 150
Figure-69: Fuel clad mechanical intereaction in simulated UTOP transients 150
Figure-70: Driver fuel centerline and inner clad temperature distribution at BOL 153
Figure-71: Driver fuel centerline and inner clad temperature distribution at EOL 153
Figure-72: Zirconium radial distribution at EOL (the axial location is 63 % from the bottom of the fuel) 154
Figure-73: Driver fuel fission gas release 154
Figure-74: Driver fuel axial elongation 155
Figure-75: Driver fuel contact pressure variation at peak clad strain location and plenum pressure 156
Figure-76: Driver fuel swelling 156
Figure-77: Driver fuel clad strain axial variation with burnup 157
Figure-78: Driver fuel inner clad wastage at EOL 158
Figure-79: Driver fuel cladding dose increase with burnup 158
Figure-80: Seed fuel centerline and inner clad temperature distribution at BOL 159
Figure-81: Seed fuel centerline and inner clad temperature distribution at EOL 160

Figure-82: Zirconium radial redistribution at EOL (the axial position is 63 % from the fuel bottom) 160
Figure-83: Seed fuel fission gas release 161
Figure-84: Seed fuel axial elongation 161
Figure-85: Seed fuel contact pressure variation at peak clad strain location and plenum pressure 162
Figure-86: Seed fuel swelling 163
Figure-87: Seed fuel peak clad strain variation with burnup 164
Figure-88: Seed fuel inner clad wastage at EOL 165
Figure-89: Seed fuel cladding dose variation with burnup 165
Figure-90: A typical annular fuel pin geometry 168
Figure-91: Fuel temperature distribution 169
Figure-92: Fuel temperature distribution 171
Figure-93: Radial stress 171
Figure-94: Hoop stress 172
Figure-95: Z-component of stress 172
Figure-96: FCMI for Case-A 174
Figure-97: FCMI for Case-B 174
Figure-98: FCMI for Case-C 175
Figure-99: Variation of the power and flow 176
Figure-100: Variation of the coolant temperature 176
Figure-101: FCMI stress early after transient initiates 177
Figure-102: Cross-sectional view of a mixed oxide fuel pin [16] 180
Figure-103: Flow sheet of FEAST-OXIDE 188
Figure-104: Grain size as a function of the fuel temperature (as-fabricated grain size is 8 μm) 196
Figure-105: Edge and face bubbles before interlinkage [83] 199
Figure-106: Face and Edge bubbles, after interlinkage [83] 200
Figure-107: Fission gas release from fuel irradiated at 1250 K (grain size is 10 μm) 208
Figure-108: Fission gas release from the fuel irradiated at 1500 K (grain size is 10 μm) 209
Figure-109: Fission gas release from the fuel irradiated at 1750 K (grain size is 23μm) 209
Figure-110: Fission gas release from the fuel irradiated at 2000 K (grain size is 32 μm) 210
Figure-111: A unit volume of mixed oxide fuel irradiated as a constant mass system [2] 212
Figure-112: Variation of the plutonium valence with burnup 216
Figure-113: Oxygen to metal ratio as a function of radius for a typical sodium fast reactor condition (OXIRED predictions) [85] 219
Figure-114: Oxygen to metal ratio as a function of radius for a typical sodium fast reactor condition (FEAST predictions) 219
Figure-115: MOX fuel with 27 wt % PuO_2 [80] 221
Figure-116: Evolution of fission gas retention [15] (When the effect of JOG formation is considered, fission gas retention decreases around 7 at % and saturates. On the other hand, the calculation ignoring the effect of JOG formation predicts a continuous increase in fission gas retention. 222
Figure-117: Evolution of the JOG size [15] 223
Figure-118: Aspect of JOG formation in pellet cladding gap [88] 223
Figure-119: Comparison of the JOG thickness predictions between FEAST and PHENIX experimental data 226

Figure-120: Limiting as-fabricated porosity fraction (initial porosity is 10 %) 229
Figure-121: Comparsion of the porosity distribution predicted by Ref. [93] and FEAST 230
Figure-122: Comparison of the fuel temperature distribution predicted by Ref. [93] and FEAST 230
Figure-123: Melting temperature of the oxide fuel in burnup dependent form for two different measurements [99] 234
Figure-124: Melting temperature of the mixed oxide fuel in burnup dependent form [100] 236
Figure-125: Temperature distribution at 66 kW/m 242
Figure-126: Temperature distribution at 70 kW/m 242
Figure-127: Temperature distribution at 90 kW/m 243
Figure-128: Linear heat rate history 243
Figure-129: Temperature distribution at 40 seconds 244
Figure-130: Fuel clad chemical interaction model [108] 245
Figure-131: FCCI model verification 248
Figure-132: Burnup= 25 MWd/kg ..... Burnup = 100 MWd/kg 249
Figure-133: Burnup=25 MWd/kg 249
Figure-134: Burnup = 100 MWd/kg 250
Figure-135: Burnup = 100 MWd/kg 250
Figure-136: FFTF axial power profile 258
Figure-137: (a): Linear heat rate (b): Peak coolant temperature 259
Figure-138: Comparison of the ACO-1 clad strain data with FEAST-OXIDE 260
Figure-139: Variation of the contact pressure with local burnup at 97 % height from the bottom of the fuel 260
Figure-140: (a): Linear heat rate (b): Peak coolant temperature 261
Figure-141: The variation of the contact pressure with peak power location (middle region) 262
Figure-142: The variation of the contact pressure with local burnup at 97 % height from the bottom of the fuel 262
Figure-143: Normalized fuel solid fission product swelling 263
Figure-144: Comparison of the ACO-3 clad strain predictions between FEAST-OXIDE and LIFE-4 at End of Life 263
Figure-145: Comparison of the ACO-3 fuel pin central void diameter predictions between FEAST-OXIDE and LIFE-4 at End of Life 264
Figure-146: (a): Linear heat rate (b): Peak coolant temperature 265
Figure-147: The variation of the contact pressure with peak power location (middle region) 266
Figure-148: Comparison of the clad strain predictions between LIFE-4, SIEX and FEAST-OXIDE 266
Figure-149: SS-316 rupture time behavior as a function of temperature and stress [116] 268
Figure-150: Sample-1 contact pressure variation with burnup at peak power location 269
Figure-151: Sample-1 clad Strain at peak power location 269
Figure-152: Sample-1 cumulative damage fraction 270
Figure-153: Sample-2 contact pressure variation with burnup at peak power location 271
Figure-154: Sample-2 clad strain at peak power location 271
Figure-155: Sample-2 cumulative damage fraction 272
Figure-156: Sample-3 contact pressure variation with burnup at peak power location 273
Figure-157: Sample-3 clad strain at peak power location 273

Figure-158: Sample-3 cumulative damage fraction 274
Figure-159: Fission gas release behavior of MK-I type fuel 275
Figure-160: Fission gas release behavior of MK-II type fuel 276
Figure-161: Transient overpower history 278
Figure-162: Peak fuel temperature for the WT180 fuel pin at 910 seconds (end of the transient) 278
Figure-163: The variation of the contact pressure at the top node (WT180 fuel pin) 279
Figure-164: The increase in transient cladding strain (WT180 fuel pin) 280

LIST OF TABLES

Table-1: Steady-state metallic fuel codes 45
Table-2: Description of the burnup history (72 % smear density U-19Pu-10Zr Fuel) 48
Table-3: Comparison of metal and oxide fuel diffusion coefficients (m^2/s) 60
Table-4: Reference data for FEAST and GRSIS 66
Table-5: Comparison of gas diffusion coefficients (m^2/s): 67
Table-6: Solubility Lines 69
Table-7: Effective heat of transport (kJ/mol) 70
Table-8: Diffusion coefficients for U-Zr alloy phases 71
Table-9: Diffusion coefficients for U-Pu-Zr alloy phases (Pu is > 8 wt %) 72
Table-10: 4S design fuel data [34] 75
Table-11: X447 fuel specifications 78
Table-12: Fuel specifications 88
Table-13: Fuel specifications 89
Table-14: Transient clad wastage predictions 97
Table-15: Slug axial elongation 111
Table-16: Approximate metal fuel properties 112
Table-17: Parameters [57] 118
Table-18: Critical crack radius (microns) (HT9) 120
Table-19: X430 fuel data 121
Table-20: X430 assembly peak cladding strain at low burnup 126
Table-21: X430 assembly peak cladding strain at high burnup 128
Table-22: X425 fuel data 129
Table-23: X425 Peak cladding strain (%) 133
Table-24: X447 fuel data 133
Table-25: Fuel specifications 135
Table-26: Key pin parameters 142
Table-27: Furnace test results and comparison 143
Table-28: UTOP analysis results at 1000 seconds 148
Table-29: ULOHS/ULOF analyses results at 1000 seconds 151
Table-30: The selected breed and burn reactor design fuel pin specifications 152
Table-31: Fuel specifications 169
Table-32: Fuel geometry and properties 170
Table-33: Fuel specifications 173
Table-34: Results at EOL 173
Table-35: Transient results after 1000 seconds 177
Table-36: Description of the burnup history of the typical FFTF fuel with no swelling clad. 181
Table-37: Probable chemical and physical states of fission products in near stoichiometric mixed oxide fuel [2] 211
Table-38: Constants for the Equation-5.4.14 241
Table-39: Fuel properties 241
Table-40: Constants for the fuel thermal expansion 254
Table-41: Fuel specifications for ACO-1 fuel pins 258
Table-42: Fuel specifications for ACO-3 fuel pins [13] 261

Table-43: Fuel specifications for CDE fuel pins [111], [112] [113] 264
Table-44: EBR-II high smear density fuel specifications 267
Table-45: JOYO MK-1 and MK-II fuel specifications 274
Table-46: Fuel specifications for TOP-1D test elements 277
Table-47: Initial and final conditions during the overpower transient 277
Table-48: Comparison of the results with FEAST-OXIDE 281
Table-49: Enthalpy [2] 308
Table-50: Entropy [2] 308
Table-51: FEAST-METAL input description 309
Table-52: FEAST-OXIDE input description 327

LIST OF ACRONYMS

AISI	American Iron and Steel Institute
ANL	Argonne National Laboratory
BOL	Beginning of Life
CDCG	Constrained Diffusional Cavity Growth
CDE	Core Demonstration Experiment
CDF	Cumulative Damage Fraction
CEA	Commissariat à l'Énergie Atomique
CPU	Central Processing Unit
CRIEPI	Central Research Institute of Electric Power Industry
DPA	Displacement Per Atom
EBR-II	Experimental Breeder Reactor-II
EOL	End of Life
FCCI	Fuel Clad Chemical Interaction
FCMI	Fuel Clad Mechanical Interaction
FEAST	Fuel Engineering and Structural analysis Tool
FEAST-METAL	The metal fuel version of FEAST code
FEAST-OXIDE	The oxide fuel version of FEAST code
FFTF	Fast Flux Test Facility
GNEP	Global Nuclear Energy Partnership
GRSIS	Gas Release and Swelling in ISotropic fuel matrix
HEDL	Hanford Engineering Development Laboratory
JOG	Joint Oxide Gain
KAERI	Korea Atomic Energy Research Institute
LWR	Light Water Reactor
MA	Minor Actinides
MIT	Massachusetts Institute of Technology
MOX	Mixed Oxide Fuel
NEFIG	Non-Equilibrium FIssion Gas
ODS	Oxide Dispersion Strengthened
OGRES	Operational Gas RElease and Swelling

RE	Rare Earth Elements
TRAFIC	TRAnsient Fuel Interpretive Code
TRU	Transuranic Nuclei
ULOF	Unprotected Loss of Flow
ULOHS	Unprotected Loss of Heat Sink
UK	United Kingdom
US	United States
UTOP	Unprotected Transient Overpower

NOMENCLATURE

Section-2.2

a_o^2 : Area occupied by a gas atom at the bubble surface (m^2).

A_i : Surface area of bubble-i (m^2)

ab_{ij} : Transfer rate of bubble-i into bubble-j by bubble diffusion (atom/s/m^3),

B: Van der Waals Parameter (85×10^{-30} m^3/atom)

Bu: Average fuel rod burnup (at %)

C_g : Gas atom concentration in the fuel matrix (atoms/m^3)

C_{gb1} : Concentration of gas atoms present as bubble-1 in the matrix (atoms/m^3)

C_{gb2} : Concentration of gas atoms present as bubble-2 in the matrix (atoms/m^3)

C_{gb3} : Concentration of gas atoms present as bubble-3 in the matrix (atoms/m^3)

D_{bi} : Diffusion coefficient of bubble-i (m^2/s)

D_g : Diffusion coefficient of gas atom (m^2/s)

D_{go} : Diffusion Constant (m^2/s)

D_s : Surface diffusion coefficient (m^2/s)

E_{gbi} : Empirical bias factor for gas diffusion to the bubble-i

E_{bb} : Empirical bias factor for bubble diffusion to other bubbles

f: Fission gas release fraction

F: Fission density (fission/s/m^3)

$f_{i,i+1}$: Transition probability of bubble-i into bubble-(i+1) by collision with bubble

f_{th} : Fraction of closed bubbles that interconnect to the open bubbles when the threshold swelling is exceeded

f_s : Fractional surface area of a closed bubble after interconnecting to the open bubbles

f_v: Fractional volume of a closed bubble after interconnected to the open bubbles

FGR: Fission gas release

gab_{ij} : Transfer rate of bubble-i into bubble-j by radial growth of bubble-i (atom/s/m³)

J_{gi} : Gas diffusion rate to bubble-i (atoms/s/m³)

$J_{b_1,nuc}$: Bubble-1 nucleation rate (atoms/s/m³)

k : Boltzman Constant (J/K)

$k_{b_1 nucl}$: Bubble-i nucleation constant (bub-1/s atom)

k_{gi} : Gas diffusion constant to bubble-i (m³/s)

k_{ij} : Collision or integration constant of bubble-i into bubble-j (m³/s).

l_j : the average distance between bubbles (m)

N_{bi} : the bubble-i concentration (bub-i/m³)

P_{ij} : The probability per unit time of a closed bubble-i colliding with a closed bubble-j due to radial growth of bubble-i (1/s)

Q_g : The activation energy for a mole of jumps = 52000 cal/g-mol

R: Gas Constant (1.987 cal/g-mol/K)

R_i : Radius of Bubble-i (m)

r_{bi} : Radius of bubble-i (m)

S_c : Swelling of the closed bubbles

S_g : Total swelling of the open and closed bubbles

S_{th} : Threshold gas swelling

S_t : Total fuel swelling

V_i : Volume of bubble-i (m³)

V_{bi} : Volume of the Bubble-i (m³/bubble-i)

Y: Fission yield of gas atoms

ρ_{gi} : Density of gas atom in a bubble-i (atoms/bub-i)

γ: Surface Tension = 0.8 N/m

σ_h : Hydrostatic stress (Pa)

Δr_{bi} : Change rate of radius of bubble-i (m/s)

Section-2.3

C_{Zr} : Zirconium concentration (mol/m³)

D_{Zr}^{eff} : Effective interdiffusion coefficient of zirconium in γ phase (m²/s)

G_{Zr}^{E} : Free energy of Zirconium (J/mol)

J_{Zr} : Interdiffusion flux (mol/m²/s)

J_{+}^{i} : Positive zirconium current emerging from node-i towards outer part of the fuel. Its sign is positive (mol/m²/s)

J_{-}^{i} : Negative zirconium current emerging from node-i towards inner part of the fuel. Its sign is negative (mol/m²/s)

Q_{Zr} : Heat of transport of zirconium in γ phase (J/mol)

R: Gas constant (J/mol/K)

r^i : Outer boundary of node-i (m)

rc^i : Weight center of the radial node-i (m)

s: Zirconium production rate by fission. The Zirconium yield is 0.2 for the fission of plutonium

T : Temperature (K)

x_U : Uranium mole fraction

x_{Zr} : Zirconium mole fraction

x_{Pu} : Plutonium mole fraction

V_1 : Volume fraction of a phase-1

$\Delta \overline{H}_s$: Enthalpy of solution (J/mol)

α : Alpha phase in metal fuel

β : Beta phase in metal fuel

δ : Delta phase in metal fuel

γ : Gamma phase in metal fuel

Section-2.4

A_f: Coolant flow area (m^2)

A_i: Cross-sectional area of the radial node-i (m^2)

axn: Total number of axial nodes

c_p: Coolant specific heat (J/kg/K)

c_{pc}: Specific heat of HT9 (J/kg/K)

c_p^j: Specific heat of the coolant evaluated at T_m^j at axial node-j (J/kg/K)

c_{p1}: Specific heat of metal fuel α+δ phase (J/kg/K)

c_{p2}: Specific heat of metal fuel γ phase (J/kg/K)

c_{p3}: Specific heat of metal β+γ phase (J/kg/K)

D_e: Equivalent diameter (m)

D_h: Heated diameter (m)

$\dot{E}_{acc}$: Energy Accumulated in a radial node (W)

$\dot{E}_{in}$: Heat flow into node-i from node-(i-1) and (i+1) (W)

$\dot{E}_g$: Energy generated within node-i (W)

h: Coolant heat transfer coefficient ($W/m^2/K$)

h_{in}: Coolant inlet enthalpy (J/kg)

h_{out}: Coolant outlet enthalpy (J/kg)

k: Thermal conductivity (W/m/K)

k_0: As-fabricated thermal conductivity (W/m/K)

$k_{i-1,i}$: Thermal conductivity between node-(i-1) and node-i evaluated at the average temperature (W/m/K)

k_{Na}: Sodium conductivity (W/m/K)

k_f: Fuel thermal conductivity (W/m/K)

k_c : HT9 thermal conductivity (W/m/K)

L_j: Axial length of the node-j (m)

$\dot{m}_{eff}$: Effective subchannel mass flow rate (kg/s)

$\dot{m}$: Coolant mass flow rate (kg/s)

M_A: Average atomic mass of the fuel mixture (kg)

Nu: Nusselt Number

Pe: Peclet Number

$\frac{P}{D}$: Pitch to diameter ratio

P_c: Porosity correction factor with sodium infiltration

P_{Na}: Fraction of the fuel which is filled with sodium

P: Fuel porosity fraction

q_i''' : Heat generation rate (W/m^3)

q_j': Heat deposited into the coolant channel j (W/m)

Q^j: Power produced in the fuel section associated with node-j (W)

Q_{tot}: The total power produced in the fuel rod (W)

R_{co}^j: Clad outer radius at axial node-j (m)

T: Clad temperature (^{0}C)

T_1: α+δ to β+γ phase transition temperature (^{0}C)

T_2: β+γ to γ phase transition temperature (^{0}C)

T_i: Temperature of node-i (K)

T_{i-1}: Temperature of node-(i-1) (K)

T_c^{j-1}: Node-j coolant inlet temperature (K)

T_c^j: Node-j coolant exit temperature (K)

T_{co}^j: Clad outer temperature at axial node-j (K)

T_m^j: Mean coolant temperature at axial node-j (K)

V: Coolant velocity (m/s)

W_{Zr}: Zirconium weight percent in the fuel

W_{Pu}: Plutonium weight percent in the fuel

ρ: Coolant density (kg/m^3)

Section-2.5

C_O : Concentration of B atoms in α phase

C_{0L} : Concentration of the lanthanide atoms in the fuel.

C_{0Fe} : Iron concentration within the clad = 0.78 (atom fraction)

C_α : Solubility limit of B atoms in α phase

$C_{\alpha L}$: Solubility limit of the lanhanides in the fuel (zero)

$C_{\alpha Fe}$: Solubility limit of iron within the clad = 0.0 (atom fraction)

C_β : Solubility limit of B atoms in β phase

$C_{\beta L}$: Solubility limit of the lanthanides in the clad (0.1)

$C_{\beta Fe}$: Solubility limit for iron within $(U,Pu)_6Fe$ layer = 0.14 (atom fraction)

D: Diffusion coefficient of B atoms in α phase (m^2/s)

D_L : Diffusion coefficient of lanthanides (m^2/s)

D_{0L} : Diffusion constant for lanthanides (m^2/s) = 1350 m^2/s

D_{Fe} : Diffusion coefficient of iron (m^2/s)

D_{0Fe} : Diffusion constant for iron (m^2/s) = 4.2×10^6 m^2/s

$\dot{F}$: Fission rate ($fission/m^3/s$)

n_{tot} : Total fuel atom density ($atom/m^3$)

Q_{Fe} : Activation energy for iron diffusion = 400000 J/mol

Q_L : Activation energy for lanthanide diffusion = 300000 J/mol

R: Gas Constant (J/mol/K)

$\dot{R}$: The rate of clad wastage formation at cladding outer layer (m/s)

t: Time (sec)

T: Clad inner temperature (K)

X: β layer thickness (m)

X_w: Clad wastage layer thickness (m)

Y_L: Fission yield of lanthanides

Section-2.6

dr_{crack}: The difference in cracked and uncracked fuel slug radius (m)

E: Young's modulus (Pa)

f^{crack}: Anisotropy factor for the axial fuel slug deformation

M_f: Number of fuel radial nodes

M_c: Number of clad radial nodes

n: # of moles of gas

P_p: Plenum Pressure (Pa)

$\frac{q}{D_o}$: Average linear power divided by the diameter of the slug (W/cm²)

r_o: As-fabricated fuel slug radius (m)

r^{eff}: Effective fuel slug radius (m)

r_{slug}: Fuel slug radius (m)

R: Gas Constant (J/mol/K)

T_{av}: Average Temperature (K)

$T_{void}(j)$: Radially averaged temperature of the open porosity in axial node-j (K)

u: Radial displacement (m)

V_{pl}: Plenum Volume (m³)

$V_{void}(j)$: Radially averaged open porosity in axial node-j. It does not include sodium infiltrated porosity (m³)

σ_r: Principle stress in radial direction (Pa)

σ_θ: Principle stress in azimuthal direction (Pa)

σ_z: Principle stress in axial direction (Pa)

ε_r : Priciple strain in radial direction

ε_θ : Principle strain in azimuthal direction

ε_z : Priciple strain in axial direction

ε^s : Swelling

ε_r^c : Creep strain in radial direction

ε_θ^c : Creep strain in azimuthal direction

ε_z^c : Creep strain in axial direction

αT : Linear strain due to thermal expansion

ν : Poisson's ratio

α_c : Open porosity compressibility factor

$\dot{\varepsilon}_{eq}$: Equivalent strain rate (1/s)

$\Delta\varepsilon^{opn-}$: Strain due to open porosity compression

ε_s^{clad} : Clad Swelling strain

Section-2.7

a: Cavity radius (μm)

$CDF(t_n)$: Cumulative damage fraction at time, t_n

d: grain boundary diameter (m)

D_b : Grain boundary diffusion coefficient (m^2/s)

n: Dislocation creep exponent

$t_r(\sigma_i, T_i)$: Failure time calculated with the stress and temperature at time step (i) (sec)

Δt : Magnitude of a time step (sec)

σ_l^∞ : Applied hoop stress (Pa)

σ_{eq} : Equivalent stress (Pa)

σ_0 : Sintering stress (Pa)

λ : Uniform spacing (m)

∂ : Grain boundary thickness (m)

Ω : Atomic Volume (m^3)

γ_b : Grain boundary free energy (J/m^2)

γ_s : Free surface energy (J/m^2)

$\dot{\varepsilon}_{eq}$: Equivalent creep strain rate (1/s)

Section-3

C : Constant (840,000)

q''' : Volumetric heat generation rate (W/m^3)

ϕ : Neutron flux ($n/cm^2/s$)

Section-5.2

a: Grain size (m)

A_f: The area of a grain face available for face bubbles (m^2)

a_r: Grain radius (m)

b: Probability per unit time that a particular bubble will be completely destroyed by a fission fragment (1/s)

c_b: Bubble density ($bubble/m^3$)

c_b: Face bubble concentration ($1/m^2$)

c_e: The local vacancy volume concentrations adjacent to edge bubbles ($atom/m^3$)

c_f: The local vacancy volume concentrations adjacent to face bubbles ($atom/m^3$)

c_g: Gas atom density within the fuel matrix ($atom/m^3$)

c_{gb}: Gas atom density within the gas bubbles ($atom/m^3$)

c_t: Total gas atom density ($atom/m^3$)

c_v: the mean vacancy volume concentration over the grain face ($atom/m^3$)

d: Hard sphere radius (nm)

D_b: Bubble diffusion coefficient (m^2/s)

D_b: The vacancy migration coefficient in the boundary (m^2/s)

D_g: Gas atom diffusion coefficient (m^2/s)

D_s: Surface diffusion coefficient (m^2/s)

D_u : Cation self-diffusion coefficient (m^2/s)

e: Radius of the grain face not occupied by the grain edge porosity (m)

E: The fraction of edge porosity connected to a free surface

F: The fraction of bubbles which survive their journey to the grain boundaries

$\dot{F}$: Fission rate ($fission/m^3/s$)

$\dot{G}$: Gas atom deposition rate to the grain boundary by bubble migration ($atom/m^3/s$)

h: The distance a bubble moves before being destroyed (m)

h_r: Radius of the grain face (m)

k : Boltzmann constant = 1.3806×10^{-23} J/K

K: Gas bubble nucleation rate constant (1/s)

K_e: Geometric curvature of the grain edge bubbles

K_g: Gas atom generation rate due to fission ($atom/m^3/s$)

k_b^2: Sink strength of bubbles for the migrating gas atoms ($atom/m^2$)

k_f^2: The sink strengths of face bubbles

k_e^2 : The sink strengths of edge bubbles

l_f: Length of the fission spike (6 μm)

n_b: # of gas atoms per bubble

n_b: The concentration of gas atoms released in total to the grain boundary ($atom/m^3$)

n_e: The concentration of gas atoms on the grain edges ($atom/m^3$)

n_{el}: A measure of the final gas concentration per unit current volume after complete interlinkage

n_f : The concentration of gas in face bubbles ($atom/m^3$)

n_{f1} : A measure of the final concentration of gas atoms on faces after complete interlinkage

n_r: The concentration of gas released from the fuel ($atom/m^3$)

p_{gas}: Gas pressure in the bubble (Pa)

p: the probability per unit time that a particular bubble is destroyed

P: Bubble Pressure (Pa)

p^{ex}: The effective bubble excess pressure (Pa)

p_b: The pressure to which gas is vented (Pa)

p_f: The internal gas pressures of face porosity (Pa)

p_e: The internal gas pressures of edge porosity (Pa)

Q_s: Heat of transport = 0.42 MJ/mol

r_b: Bubble radius (m)

r_e: Edge bubble radius of curvature (m)

r_f: Face bubble radius of curvature (m)

R: Rating (W/kg)

R: Gas constant (8.314 J/mol/K)

R_c: The effective capture radius of the bubbles for gas (40 nm)

R_f: Radius of the fission spike (6 nm)

s: Half distance between the bubbles (m)

S_{Cs}: Swelling due to cesium

S_e: Swelling due to the grain edge bubbles

S_f: Swelling due to the grain face bubbles

S_g: Total gas swelling

S_{int}: Intra-granular gas swelling

S_t: Total grain boundary swelling

T: Temperature (K)

V: Bubble volume (m^3)

v_b: The bubble velocity (m/s)

Y: Fission yield of gas atoms generated by fission (0.25 for U and Pu in fast reactors)

σ: External stress (Pa)

γ: Surface tension (1 J/m^2)

δ_s: Effective surface thickness = 0.34 nm

∇T: Temperature gradient (K/m)

Ω: Atomic volume (4.09E-29 m^3)

λ: Thickness of the diffusivity layer = $\Omega^{1/3}$ (m)

ν: The number of atomic volumes associated with each gas atom in solution (2)

θ: 50^0

β_s: is the rate of production of vacancies on the grain face (atom/m³/s)

β_f: The rate of vacancy emission from face bubbles (atom/m³/s)

β_e: The rate of vacancy emission from edge bubbles or tunnels (atom/m³/s)

δ_b: The grain boundary width (m)

μ_f: Vacancy chemical potential for the face bubble

μ_e: Vacancy chemical potential for the edge bubble

β_s: The rate of production of vacancies on the grain boundary (atom/m³/s)

Section-5.3

a_{Mo}^f: The thermodynamic activity of molybdenum in the fuel matrix

a_{Mo}^m: The thermodynamic activity of molybdenum in the metallic inclusions

Bu: Burnup (at %)

c_i: Atomic fraction of interstitial atoms

c_v: Atomic fraction of oxygen vacancies

c_v^0: Content of vacancy

C: Pu atom fraction

D: Fuel grain size (m)

D_o: Diffusion coefficient of oxygen (m²/s)

D_{Pu}: U-Pu interdifusion coefficient (m²/s)

D_{FP}: The diffusion coefficient for monoatomic molecule fission product gas (m²/s)

D_{ci}: Clad inner diameter (mm)

D_m: Maximum allowed fuel grain size (m)

DR: Diameter relocation (μm)

f_{mo}: The fraction of the total molybdenum present

G: Diameter gap size (μm)

J : Radial cesium current (m^2/s)

J_+^i : Positive oxygen current emerging from node-i towards the outer part of the fuel. Its sign is positive (m^2/s)

J_-^i : Negative oxygen current emerging from node-i towards the inner part of the fuel. Its sign is negative (m^2/s)

J_+^i : Positive cesium current emerging from node-i towards the outer part of the fuel. Its sign is positive (m^2/s)

J_-^i : Negative cesium current emerging from node-i towards the inner part of the fuel. Its sign is negative (m^2/s)

J_v: Jump frequency

k: Cesium mobility (1/s)

K' : Generation rate of a defect

N_i includes all of group-i that has been formed in the unit volume of fuel

N_U^o: Initial amount of atoms of uranium

N_{Pu}^o: Initial amount of atoms of plutonium

N_O^o : The number of oxygen atoms in the fresh fuel

N(h): The concentration of cesium on the hotter side ($atoms/m^3$)

N(c): The concentration of cesium on the cooler side ($atoms/m^3$)

N_p : Pore concentration

$\frac{O}{M}$: As-fabricated fuel oxygen to metal atom ratio

p_{O_2} : Oxygen pressure (atm)

P_i^t: Porosity fraction at radial node-i and at time t.

q_o : Initial cation fraction of plutonium

Q: Molar effective heat of transport of oxygen (J/mol)

Q_{Pu} : Heat of transport of plutonium atoms (35000 cal/mol)

Q_{Cs} : Cesium heat of transport (60000 cal/mol)

Q_v: The heat of transport of the oxygen vacancies (J/mol)

Q_i: The heat of transport of the oxygen interstitial atoms (J/mol)

r_i: Outer boundary of node-i (m)

rc^i: Center of node i (m)

r_i: Node-i radial location (m)

r_i: Outer boundary of node-i (m)

rr_i: Inner boundary of node-i (m)

rr_{i+1}: Outer boundary of node-i+1 (m)

R: Gas constant = 1.987 cal/mol/K

S: Jump distance of fission product gas atoms

T: Fuel temperature (K)

V_U: Probable charge of the Uranium atoms

V_{Pu}: Probable charge of the Plutonium atoms

V_p^i: Pore velocity at node i

V_p: Pore velocity (m/s)

x: Deviation from stoichiometry

X_{Cs}: Cesium atom fraction

x_{Pu}: Atomic fraction of Plutonium at a radial position r

x_{Pu0}: Pin average atomic fraction of plutonium

y_f^{Mo}: The cation fraction of Mo in the fuel matrix

y_m^{Mo}: The atom fraction of Mo in the metal phase

Y_i: The sum of the elemental yields of all fission products in group i

Y_{Ba-Sr}: Elemental yield of Ba-Sr group

Y_{Zr-Nb}: Elemental yield of Zr-Nb group

Y_{Y-Re}: Elemental yield of Y-Re group

Y_{Mo}: Elemental yield of Molybdenum

Z: Number of sites surrounding a defect

β: Burnup fraction

ΔG_{Mo}^o: The free energy of formation of MoO_2 (J/mol)

ΔG_{O_2}: Free energy of formation of oxygen in the fuel (J/mol)

α_s: Sink intensity

ϕ: Total axial flux of cesium (atoms)

ΔH_v : The partial molar heat of vaporization of cesium (J/mol)

ρ: Fuel density fraction

ρ_o: Initial fuel density fraction

Section-5.4

c_p^f: Fuel specific heat capacity (J/kg/K)

D_{JOG}: JOG thickness (m)

D_{gap}: Gas filled gap thickness (m)

h_{JOG} : JOG heat transfer coefficient (W/m²/s)

H_{G+J} : Heat transfer due to conduction through gas and JOG (W/m²/s)

K_{JOG} : Thermal conductivity of JOG (W/m/K)

k_{He}: Helium thermal conductivity (W/m/K)

k_{Xe}: Xenon thermal conductivity (W/m/K)

k: Mixed oxide fuel thermal conductivity (W/m/K)

k_g: Mixed gas thermal conductivity (W/m/K)

O/M: Oxygen to metal atom ratio

P: Fuel Porosity

P_o: As-fabricated porosity

q''': Volumetric heat generation at a radial position r (W/m³)

q_o''' : Radially average (nominal) volumetric heat generation rate (W/m³) obtained from the specified linear heat generation rate at the axial location fo interest

q'_{G+J} : Heat transfer rate though the JOG and gas in the gap region (W/m)

q'_{rad} : Linear heat rate transferred from the fuel to the clad via radiation (W/m)

r: Fuel radial location (m)

Ro: Fuel and clad roughness (4 μm)

R: Universal gas constant = 8.314 (J/mol/K)

r_{gap}: Average gap radius (m)

r_o: Fuel pellet outer radius (m)

T: Temperature (K)

T_{fo}: Fuel outer surface temperature (K)

T_{ci}: Clad inner surface temperature (K)

T_{gap} : Gap Temperature (K)

T_m: Melting temperature (K)

x: The fraction of the helium gas

X_1: Plutonium fraction $\frac{Pu}{Pu+U}$

X_2: Americium fraction $\frac{Am}{Pu+U+Am}$

X_3: Burnup (GWd/t)

X_4: O/M atom ratio

Y: Oxygen to metal atom ratio

α: Porosity factor

β: Burnup (at %)

ε_f : Fuel surface emissivity

ε_c : Clad surface emissivity

θ: The Einstein temperature (K)

Section-5.5

B: Burnup (MWd/t)

B_o: Burnup at which O/M=1.994 (Oxidation of the Molybedum starts)

BU: Local Burnup (at %)

D: Clad wastage (μm)

O/M: As-fabricated fuel oxygen to metal atom ratio

T: Clad Inner Temperature (K)

R: Gas Constant (1.987 cal/mol/K)

Section-5.6

d: Grain size (μm)

D: Fuel density (fraction of the theoretical density)

E: Young's Modulus (Pa)

E_D: Energy of formation of a defect

ES: Young's Modulus of the stoichiometric UO_2 fuel

E' : Young's Modulus for the cracked fuel

f: PuO_2 content of the fuel (weight fraction)

k: Boltzmann Constant (1.38×10^{-23}) (J/K)

n: Stress exponent for the dislocation creep = 4.4

N: Number of cracks

P: As-fabricated porosity fraction

R: Universal gas constant (J/mol/K)

T: Fuel Temperature (K)

$\dot{\epsilon}$: Fuel Creep Rate (h^{-1})

σ: Stress (MPa)

$\dot{\varepsilon}_f$: Fuel irradiation creep rate (h^{-1})

σ : Stress (MPa)

ϕ: Fission/m³/s

x: The magnitude of the deviation from stoichiometry in in $MO_{2\mp x}$ fuel

X_m: Fraction of the molten fuel

x_{Pu} : PuO_2 weight fraction

ν_U: Poisson's Ratio of UO_2

ν_{Pu}: Poisson's Ratio of PuO_2

$\frac{\Delta L}{L_o}$: Linear strain caused by thermal expansion

$\frac{\Delta L}{L_o}(T_m)$: Linear strain of the solid fuel at the melting point

σ: Fracture stress (MPa)

σ : Yield strength (MPa)

ν' : Poisson's ratio for the cracked fuel

α_1: Diffusional creep coefficient (1/MPa)

α_2: Dislocation creep coefficient ($1/MPa^{4.4}$)

σ: External stress (MPa)

1. INTRODUCTION

1.1. Motivation

The development of recent US Department of Energy Programs such as the Generation IV initiative, the Advanced Fuel Cycle Initiative and the Global Nuclear Energy Partnership have renewed and invigorated US interest in sodium-cooled fast reactors for long term actinide management and energy production [1]. Analyses of these complex systems require the coupling of diverse fields, such as thermal-hydraulics, neutronics, structural mechanics and fuel behavior. Understanding the behavior of the fast reactor fuel remains a critical step in the fast reactor optimization. Computer modeling of complex physical systems provides a valuable tool for the design and optimization of all kinds of industrial processes and engineering, and modeling of the behavior of the fast reactor fuel is no exception.

Four types of fuels have been considered for fast reactor applications. They are oxide, metal, carbide and nitride fuels. Each fuel type has advantages and disadvantages with respect to the others. With the success of the metal and oxide fuels demonstration through 1980s, and early 1990s, a considerable infrastructure and knowledge base have been accumulated to support these two fuel types, while the interest in the carbide and nitride fuels has waned in United States [1]. As a consequence, only the metal and oxide fuel modeling were considered in this thesis.

1.2. Background

A reactor fuel pin is conceptually a simple object; its basic parts are cylindrical pellets (or slugs) of fissile material encased in a metal tube. However, the apparent simplicity of the fuel pin is deceptive [2]. During operation, fast reactor fuel evolves drastically due to fission gas release and swelling, creep of the fuel and clad, irradiation effects, thermal diffusion of the fuel constituents and fuel restructuring. Hence, a rigorous approach to model like a fast reactor fuel pin should include thermal, mechanical and chemical and fission gas behavior models in coupled form, together with a complete material property data set.

The oxide fuel modeling efforts dates back to the early 1960s [3]. Lack of high-performance computational power and poor understanding of the fuel behavior forced scientists to develop

purely empirical models to describe the relevant phenomena. The first oxide fuel code was PATRICE [3], written in Mercury auto-code, for thermal reactors. It embodies most of the characteristics of the later codes. Fuel temperature calculation and a gas release model are included in the code. PATRICE was able to calculate the deformation of the cladding due to plenum pressure as well as fuel clad mechanical interaction. The main limitations were the assumption of a rigid pellet, made in the calculation of the fuel-clad mechanical interaction, and the inability to model varying conditions along the fuel rod. The fast reactor oxide fuel codes developed in the early 1970s were superior to PATRICE. LIFE [4] developed in the US and COMETHE [5] developed in Belgium and FRUMP [6] developed in the UK had much more reliable mechanical analysis and temperature calculation models. However, the fission gas release and swelling, and the fuel chemistry models were quite weak. FRUMP is the first fast reactor code which has mechanistic physically-based models for fission gas release and swelling and fuel restructuring [3]. However, accurate models representing the actual physics for the fission gas release and swelling were not available in the early 1970s.

During the 1970s, there were numerous attempts to describe the fission gas release and swelling behavior of the oxide fuel at fast reactor conditions for steady state as well as transient scenarios. Harwell Institute and Berkeley Nuclear Laboratory in the United Kingdom were perhaps the most successful places. In the early 1980s, UK Laboratories came up with very advanced and physics based fission gas release and swelling models [7-10]. An oxide fuel performance code called TRAFIC was developed using these advanced models [11]. In the USA, the Argonne National Laboratory was the leading organization in the development of fast reactor fuel modeling. Although they were following the new models developed in the UK, their approach to modeling fission gas release and swelling behavior was somewhat simpler [12]. ANL developed the LIFE-IV [13] oxide fuel code in the 1980s. However, the importance of the fuel chemistry effects on the thermal and mechanical behavior of the fuel, particularly the effect of Joint Oxide Gain formation, was underestimated in both the TRAFIC and LIFE-IV codes.

The GERMINAL code [14-15] developed by CEA in France was a fully empirical treatment. However, its basis has a much stronger dependency on the fuel chemistry and thus, the code was superior to any other previous codes in that respect. Note that the recent findings of the Japan

Nuclear Fuel Cycle Engineering Laboratory about the effect of JOG formation on the fuel thermal, mechanical and gas release behavior are in agreement with the empirical description adopted in the GERMINAL code [16-17].

Developing a fuel modeling code is a time consuming process. Examining the experimental data and understanding the actual physics, building physics based models and incorporating them into a new code with a satisfactory numerical algorithm are the critical steps to develop a fuel code. LIFE-METAL [18] was developed at ANL in a relatively short time to estimate the steady state and transient metal fuel behavior. It is more empirical than the LIFE-IV oxide fuel code; hence, its reliability when applied beyond the narrow database for which it was developed is a concern.

Metal fuel modeling efforts continued during the 1990s and up to now in the US, Japan and South Korea. The ALFUS [19] code, developed in Japan, allows for more mechanistic models to describe the metal fuel compared to LIFE-METAL. Perhaps its major limitation is its fission gas release and swelling model which is an extrapolation from the oxide-fuel models. MACSIS [20], developed in South Korea, is a less sophisticated code compared to ALFUS. It is developed to estimate the behavior of U-Zr fuel and only at steady state.

In summary, there have been numerous attempts to model the fast reactor fuel behavior in the last 40 years. The US currently does not have a fully reliable tool to simulate the behavior of metal or oxide fuels in fast reactors. The experimental database, necessary to validate the codes, is also very limited.

1.3. Objectives

This thesis aims at (i) developing a physics-based metal and oxide-fuel code for Sodium Fast Reactor applications by using and improving the most advanced models, and (ii) validating the code using the experimental database in the literature. The resulting code will be called Fuel Engineering And Structural analysis Tool (FEAST). FEAST-METAL will be the metal fuel version and FEAST-OXIDE will be the oxide fuel version of the code. The expectation is that FEAST will accurately reflect the physical behavior of the fuel and, hence, it will be capable of

extrapolation beyond the existing experimental database for steady state as well as transient scenarios.

2. MODELS FOR METALLIC FUEL

2.1. Introduction

Metal fuel typically consists of a binary alloy of uranium and zirconium or a ternary alloy of uranium, plutonium and zirconium. Addition of about 10% by weight zirconium to a uranium-plutonium alloy raises the solidus temperature of the fuel[1] and prevents fuel-cladding interdiffusion at temperatures typical of steady operating conditions [21]. The fuel/clad gap is filled with liquid sodium, which acts as a thermal bond. The attractive characteristics of metal fuel include:

- High thermal conductivity, which combined with a highly conducting gap, maintains fuel temperatures low and reduces stored energy, an important feature during transients, such as the unprotected loss of primary flow and loss of heat sink.
- High heavy metal density and low moderating power, which provide for a harder spectrum and excellent neutron economy.
- Low Fuel Clad Mechanical Interaction (FCMI) at the upper part of the fuel pin, which enables achievement of high burnup.
- Good compatibility with the coolant.
- Ease of manufacturing and reprocessing by pyrochemical methods.

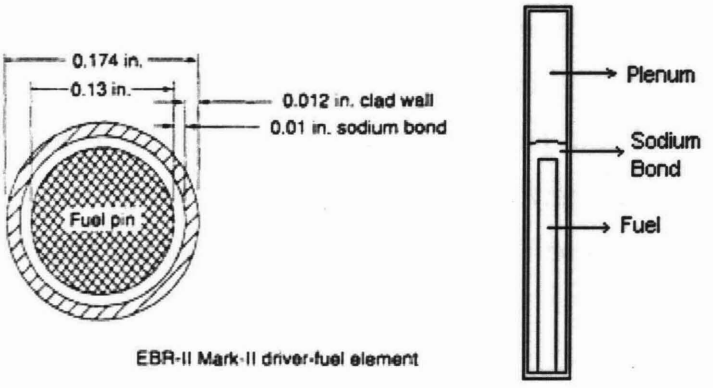
However, various phenomena limit the in-core performance of metal fuel assemblies, including clad thermal, irradiation creep and void swelling, fuel restructuring and Fuel/Clad Chemical Interaction (FCCI). It is obvious that any credible attempt at assessing the performance of metal fuel must include a model that is able to predict the temperature, stress and strain time-dependent distributions within the clad and fuel for given operating and abnormal conditions. This model should include the effects of fuel restructuring, FCCI, thermal expansion, thermal creep, irradiation creep, fuel swelling and fission gas release. Checking of these models against the experimental data as well as code vs. code is perhaps the most crucial step. However, the metal fuel irradiation database is limited and mostly based on irradiations in the EBR-II during the

[1] Some researchers however feel that the relatively low melting point of metal fuel is a serious drawback compared to oxide fuel [22].

integral fast reactor program, which was protected as Applied Technology, and thus not easily accessible outside the national laboratory system.

2.1.1. Description of a Typical Metal Fuel Pin

A typical metal fuel pin is shown in Figure-1. A solid cylindrical metal fuel slug is submerged into liquid sodium and is encapsulated within the cladding. The reference cladding material for the past twenty years has been HT9, a low-swelling ferritic-martensitic stainless steel. Note that a certain free volume is provided in the upper part of the fuel pin to relieve the pressure due to fission gas release from the fuel.



Fuel	U-Pu-Zr
Gap	Liquid Sodium
Clad	HT9
Coolant	Liquid Sodium

Figure-1: Description of the metallic fuel

2.1.2. Project Objectives and Review of Current Metal Fuel Codes

The objective of this work is to develop a robust and reliable code, which we will call Fuel Engineering And Structural analysis Tool (FEAST-METAL), to model the irradiation behavior of metal fuels in sodium-cooled fast reactors. Given the fuel pin geometry, composition and irradiation history, FEAST-METAL can analyze the fuel slug and cladding thermo-mechanical behavior at both steady state and transient conditions. The ultimate goal is to use FEAST-METAL in the licensing process of metal-fuelled fast reactors for the GNEP and Generation-IV programs.

A literature review has been completed to identify and assess the major metallic fuel codes in use or being developed to date. A comparison of the features of the various codes is given in Table-

1. Note that in all cases the overall code structure consists of several modules describing the important phenomena.

The LIFE code was originally developed for oxide fuel and was later modified to analyze mixed-carbide and mixed nitride fuel. LIFE-METAL [18] is the metal-fuel version of the carbide/nitride version of LIFE. It implements a detailed thermo-mechanical analysis of the fuel-cladding system in the radial direction. Axial variations in operating conditions are accounted for by assigning the specific power and fast flux at up to nine axial nodes. The axial nodes are thermally coupled through the calculated coolant temperatures, however, axial heat conduction is neglected and there are no provisions for mechanical coupling between axial nodes. LIFE-METAL calculates the fission gas release fraction and fuel swelling strains by empirical correlations of burnup, temperature and porosity. The fuel constituent redistribution is also based on an empirical model. The code cannot model anisotropic fuel deformation, which is however observed in the experiments.

Table-1: Steady-state metallic fuel codes

Modules	LIFE-METAL [18]	SESAME [23]	ALFUS [19]	MACSIS [20]	FEAST-METAL
Developer	ANL (US)	CRIEPI (JAPAN)	CRIEPI (JAPAN)	KAERI (Korea)	MIT (US)
General Capabilities	Steady-state and Transient Behavior	Steady-state Behavior	Steady-state Behavior	Steady-state Behavior	Steady-state and Transient Behavior
Fission Gas Release and Fuel Swelling	Empirical Correlation	Empirical Correlation	Mechanistic Model, based on UO_2 Fuel	Mechanistic Model, Based on UO_2 Fuel	Mechanistic Model, Based on Metallic Fuel
Constituent Redistribution	Empirical Correlation	Chemical Equilibrium Model	Thermo-transport theory	Thermo-transport theory	Thermo-transport theory
Temperature Distribution	1D Model	1D Model	1D Model	1D Model	1D Model
Mechanical Analysis	1D Model	1D Model	2D Model	1D Model	1D Model
FCCI	Empirical Correlation	Not Included	Empirical Correlation	Not Included	Diffusion Model based on Precipitation Kinetics
Creep Fracture	Cumulative Damage Fraction Model	N/A	N/A	N/A	(1) Cumulative Damage Fraction Model (2) Constrained Diffusional Cavity Growth Model

The SESAME [23] code was developed to predict only the steady-state performance of both U-Fissium and U-Pu-Zr alloy metallic fuels. A single fuel element is divided into several axial nodes, each containing several equiaxial radial meshes, in which the important performance variables such as stress, strain, temperature and material properties are assumed to be spatially uniform. Temperature and mechanical analysis modules adopt a 1D finite element method. The fission gas release and swelling module adopts the same empirical model developed for LIFE-METAL. The fuel constituent redistribution model is based on the chemical equilibrium assumption. Anisotropic fuel slug deformation is accounted for by an empirical approach.

The ALFUS code [19] has been developed for stress-strain analysis of U-Pu-Zr ternary metallic fuel pins for steady-state conditions. The mechanical analysis model is based on axisymmetric 2D r-z finite element method, which is similar to FEMAXI-III, the light water reactor fuel performance code [24]. The fuel constituent redistribution model is based on thermal-transport theory, but is not coupled to the mechanical analysis module, so an implicit assumption is made that the mechanical properties are insensitive to local fuel composition. The code uses a mechanistic model, originally developed for UO_2 fuel, for calculation of the fission gas release and fuel swelling [25]. Empirical models are included for compressibility of the interconnected gas pores and anisotropic deformation of the fuel slug.

The MACSIS code [20] analyzes the irradiation behavior of U-10Zr fuel for steady state conditions. It calculates the temperature distribution, dimensional changes, axial growth, fission gas release and radial redistribution of the fuel alloying elements. Axial heat conduction and mechanical coupling of axial nodes are not considered. The fuel constituent redistribution model is based on thermo-transport theory. The fission gas release and swelling module is based on Booth's diffusion theory which was originally developed for ceramic fuels.

It was decided to develop a new metal fuel code, FEAST-METAL, for the following reasons:

- The older codes (LIFE-METAL [18] and SESAME [23]) are highly empirical and cannot be extrapolated beyond the narrow database for which they were developed
- There is a need for a robust code for analysis of fuel behavior during transients

- Regulators will need an independent tool to verify the performance of metal fuel for the next-generation of fast reactors
- The newer codes being developed in Asia (ALFUS [19] and MACSIS [20]) may not become available to researchers/vendors/regulators in the US

The FEAST code is developed for analysis of the steady-state and transient irradiation behavior of U-Zr and U-Pu-Zr metal fuels. It is being developed to be highly flexible, so that constitutive models for other alloys of interest (e.g., TRU-Zr alloys) can be easily added to the code. FEAST's mechanical model is similar to the respective LIFE code algorithm. Variation of material properties (fuel creep, thermal expansion, Young's modulus) with local fuel composition is taken into account. The fuel and cladding regions can be divided into up to 8 radial nodes each; however, six radial nodes in the fuel region and at least two radial nodes within the cladding region are recommended. Axial nodes are also user specified. A maximum of twenty nodes can be assigned in the axial direction. Axial heat conduction is neglected. The fission gas release and swelling module implements the GRSIS algorithm [26] which was originally developed for metal fuel. The fuel constituent redistribution model is based on thermo-transport theory. Empirical models developed for the compressibility of open pores and anisotropic deformation of the fuel slug in ALFUS [19] are implemented into the FEAST-METAL code. Furthermore, an FCCI model based on precipitation kinetics was developed in this study to model cladding wastage. Another important model developed in this study is the creep-fracture of the clad during transients. It is modeled by using the diffusional constrained cavity growth model.

This section of the thesis provides a detailed description of the FEAST-METAL code structure (Section-2.1) and constitutive models (Section-2.2 through Section-2.7). Validation of the code using the available irradiation data is shown in Section-3, for steady state and transients. A parametric study for the steady-state conditions and transients is given in Section 4.1. Then, analyses of the so-called breed-and-burn reactor fuel pins will be given in Section 4.2, as an example of FEAST-METAL application. Finally, an extension of the modeling capabilities of FEAST-METAL to internally and externally annular fuel pins is presented in Section 4.3.

2.1.3. Thermo-mechanical Behavior of the Metal Fuel

Table-2 reports the sequence of key physical phenomena during the irradiation of a typical metal fuel pin, as deduced from the operating experience in the EBR-II reactor at ANL-West in Idaho.

Table-2: Description of the burnup history (72 % smear density U-19Pu-10Zr Fuel)

Burnup (at %)	Relevant phenomena
0.0	Irradiation begins
0.5-1.0	(1) Due to swelling, grain boundary tearing and cracking, the fuel reaches the clad and becomes axially restrained at the 'hot' axial location. (2) Resulting axial friction force is enough to stop the axial growth of the fuel by compressing the existing open gas pores. Furthermore, swelling rate reduces due to axial frictional force. (3) The radial contact pressure between fuel and clad is low due to extrusion of the inner zone fuel into the cracks. (4) Fission gas release into the plenum begins.
1.0-2.0	(1) Cracks are closed and fuel becomes both axially and radially restrained at the hot axial location. (2) Radial contact pressure between fuel and clad rises to a level somewhat higher than plenum pressure. Open gas pores start to be compressed to accommodate for solid/liquid fission product swelling. (3) Fission gas release fraction rises rapidly to 50 %.
2.0-13.0	Contact pressure holds at a level somewhat higher than the plenum pressure as the open pores are further compressed to accommodate accumulation of solid products.
13-20	Fuel does not have enough open pores to accommodate solid fission product accumulation. The resulting fuel-clad contact pressure rises significantly. When open pores are less than 5 %, the contact pressure rises rapidly and breach may result.

2.1.4. FEAST-METAL Code Structure

The FEAST-METAL code is composed of several modules in coupled form to simulate metal fuel thermo-mechanical behavior, as described in Table-1. The code is written in FORTRAN-90 language.

The code implements an explicit numerical algorithm. The flow sheet of the calculations is given in Figure-2. Note that the very high rate of creep strain of the fuel slug requires short time steps, of the order of 10-20 seconds, therefore a typical irradiation simulation requires use of about 10^6

time steps, resulting in an execution time of the order of minutes, when run on a single CPU personal computer.

The input file for the code allows specification of the operating conditions and initial fuel pin and coolant flow path geometry.

The code performs the following steps for each axial node at each time step:

1- Radial power distribution within the fuel slug is calculated based on the actinide concentration within each radial node.
2- Contact pressure between the fuel and clad is calculated as a function of displacement of fuel and cladding.
3- The code calculates the fuel constituent redistribution, which is a relatively slow process, every 10000 seconds to reduce the computational time. Given the phase diagram and thermo-chemical activity of each phase, the code calculates the zirconium current and solves the diffusion equation by an explicit algorithm. Note that, both explicit and semi-implicit algorithms exist for this module. The semi-implicit algorithm could only be computationally efficient if one million second or higher time steps area selected. However, the rapid variation of the temperature distribution does not allow such large time steps; thus, an explicit algorithm is recommended for this module.
4- Temperature distribution in the fuel pin is calculated as a function of radial power, zirconium, porosity distribution and sodium infiltration. Furthermore, the coolant axial temperature distribution is calculated with the Single Mass Velocity Model [27]. Consistently with the fuel constituent redistribution module, the calculation is performed every 10000 seconds. The Gauss-Seidel matrix solver algorithm is used [28].
5- Having calculated the radial temperature distribution, the fuel stress/strain analysis is performed. Using the creep strains and axial strains calculated at the previous step, the average radial displacement can be calculated for each radial ring by using the Gauss-Jordan matrix solver algorithm [29]. After that, the axial force balance is used to calculate either the axial strain if the gap between the fuel and the clad is open; or, the fuel/clad friction force, if the gap between the fuel and the clad is closed. Finally, the

creep and plasticity strains and open pore compressibility strain are calculated which will be used in the next time step.

6- Given the stress, temperature and fission rate of each radial ring, the fission gas release and swelling behavior of the fuel is calculated. Swelling due to diffusion of gas atoms into gas bubbles, coalescence of gas bubbles due to growth and bubble diffusion and open porosity formation have been accounted for. Moreover, an empirical relation is adopted for solid fission product swelling. No matrix solver is necessary in this module.

7- Cladding wastage is calculated using the precipitation kinetics model.

8- Given the contact pressure between fuel and cladding and coolant pressure outside the cladding, the radial displacement for each radial ring in the cladding are solved using the Gauss-Jordan matrix solver. After that, the axial force balance is used to calculate the axial strain. Finally, cladding creep strains are updated again and used in the next time step.

9- Creep fracture margin of the clad is calculated by Cumulative Damage Fraction (CDF) and the constrained diffusional cavity growth models only for transients.

10- The plenum pressure calculation is performed by assuming that the perfect gas law applies. The sum of the open porosity within the fuel slug and the plenum region at the top of the fuel slug constitutes the volume occupied by gas.

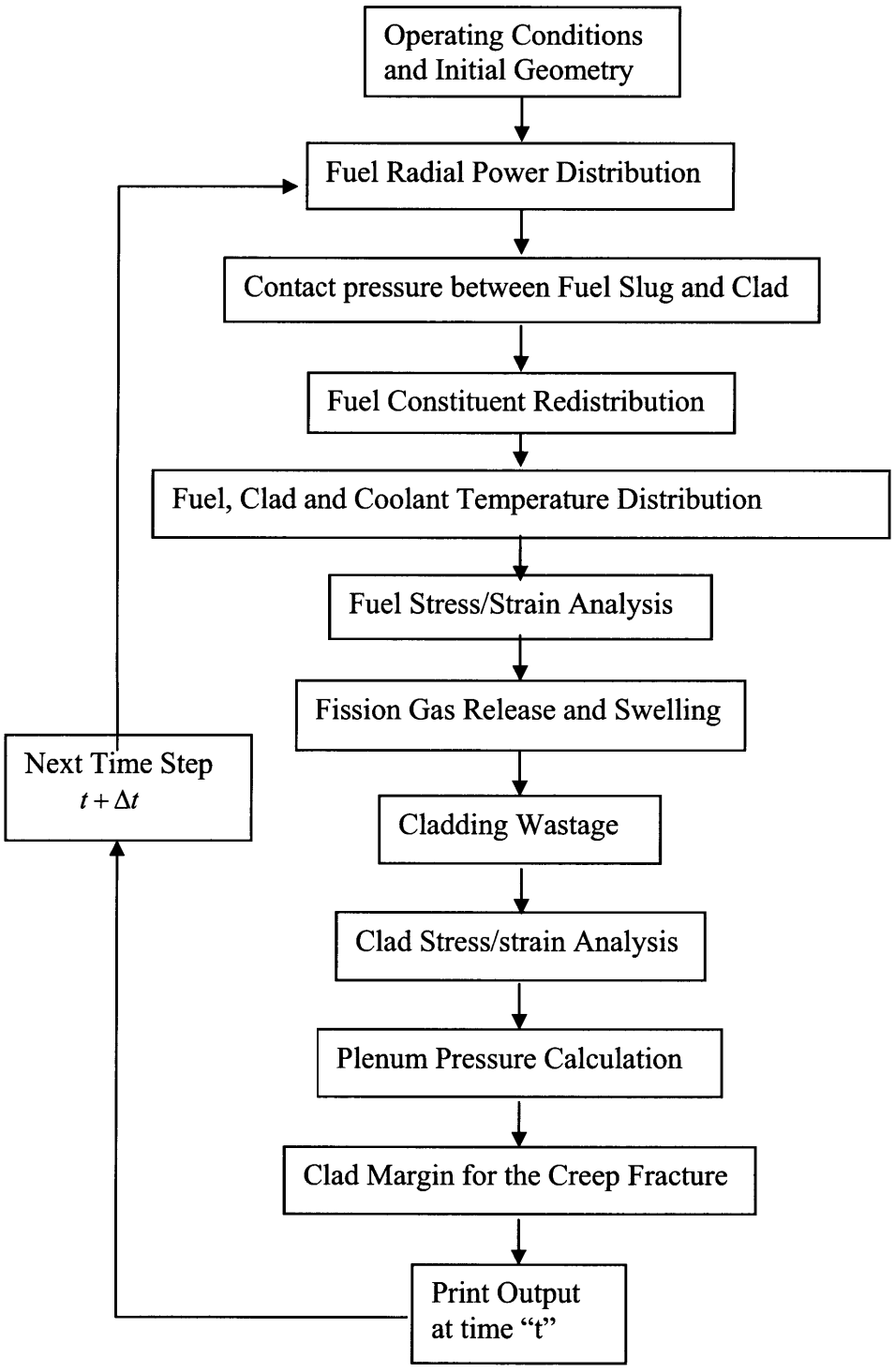


Figure-2: Flow sheet of FEAST-METAL

2.2. Fission Gas Release and Swelling Module

2.2.1. Introduction

The main contributors to fission gas release in metal fuel are xenon and krypton because of their virtually complete insolubility in the fuel matrix. Therefore, if kinetically favorable, xenon and krypton will be rejected from the fuel matrix. These gases are either directly released into the plenum, or accumulate in small bubbles within the fuel. Because the density of the gas in such bubbles is considerably lower than that of the solid fuel, gas atoms residing in bubbles occupy more volume than either the fissile atoms they replaced or fission-product atoms that segregate as solid phases. The precipitation of fission gases thus leads to swelling of the fuel to a larger degree than the volume expansion that would occur if the xenon and krypton had remained dissolved on an atomic scale in the fuel matrix. Swelling adversely affects fuel performance because it promotes fuel-cladding mechanical interaction, which may shorten the cladding lifetime.

Fission gases are considered to be released from the fuel when they reach any space that is connected to the free volume within the fuel pin. Gas connection zones include the fuel/cladding gap and the porosity within the fuel which communicates directly with the gap (open porosity). The following is assumed regarding the gas in the closed bubbles and that in the free volumes (plenum above the fuel slug and open porosity within the fuel slug) [2]:

1- Once the gas is released into the free volumes, its probability of reentering the closed bubbles is zero.
2- The gas pressure in open porosity is equal to that in the plenum. Because of the insolubility of xenon and krypton in solids, there is no direct influence of plenum pressure on the rate of gas escape from the fuel.
3- While the fission gas within the closed bubbles tends to cause swelling, the fission gas in the free volume promotes shrinkage by pressurizing the solid and thereby encouraging collapse of the internal porosity.

2.2.2. Fission Gas Release and Swelling Behavior of Metal Fuel

Figure-3 shows the fractional fission gas release as a function of burnup for the ANL U-Pu-10Zr irradiation database [26]. Fission gases at the fuel rod of peak power start to be released through open channels formed by interconnection of the bubbles at a burnup of about 0.5 %. Then, the fractional fission gas release increases to about 70 % when the burnup reaches 4-5 at % burnup and levels off at about 80 % at 10 at % burnup.

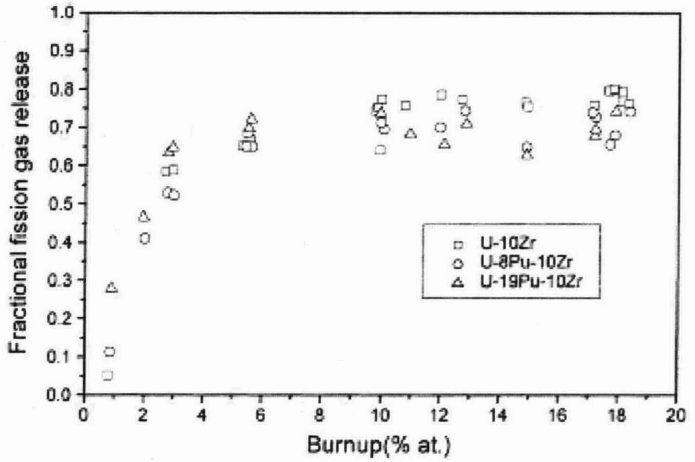


Figure-3: Fission gas release of ANL fuel irradiation tests [26]

Many models have been developed for fission gas release and swelling behavior of the U-Pu-10Zr metallic fuel for liquid metal fast reactors. The model in the LIFE-METAL [18] code is empirical, and calculates the fission gas release by a simple correlation using burnup, porosity and temperature. It does not explicitly consider fission gas bubbles. The ALFUS [19] model considers the bubble formation and growth based upon a model originally developed for UO_2 fuel. Therefore, it is assumed that fission gases are generated inside the fuel grains and then diffuse to the grain boundaries to nucleate a new bubble or be absorbed by an existing bubble at the grain boundaries. However, in metal fuel the fission gas bubbles could nucleate at the phase boundaries inside grains as well as at the grain boundaries. The phase boundaries are distributed quite randomly inside the grains in U-Pu-10Zr metallic fuel. Therefore, the effect of grain size on fission gas behavior in metallic fuel may not be as important as in UO_2 fuel.

2.2.3. Modeling of the Fission Gas Behavior

The FEAST-METAL user can select either a mechanistic fission gas release model or an empirical one.

Mechanistic Model:

The GRSIS model [26] is adopted to model the fission gas behavior of the metallic fuel in the FEAST-METAL code. A schematic diagram of the fission gas bubble nucleation and growth in the metallic fuel according to the GRSIS approach is shown in Figure-4. Fission gas atoms are generated by fission, and then form (nucleate) new bubbles or diffuse into existing bubbles. The bubbles are assumed to nucleate uniformly from the gas atoms in the metallic fuel matrix, since they nucleate at both the grain boundaries and the phase boundaries which are randomly distributed inside grain. The closed bubbles can grow by the diffusion of newly created fission gas atoms, and are classified into two groups depending on their sizes. Small bubbles and large bubbles are defined as having 0.5 and 10 micron radius, respectively. The third group of bubbles is the open bubbles (or open pores), which are connected to each other and open to the external free space. They are assumed to be of the same type as the closed bubbles. When a closed bubble-i becomes an open bubble, it is assumed to be transformed into bubble-3i. When the fuel matrix swelling due to the closed bubbles reaches a threshold value, it is assumed that a certain fraction of the bubbles become interconnected and release their gas into the free volume (i.e., they become open bubbles).

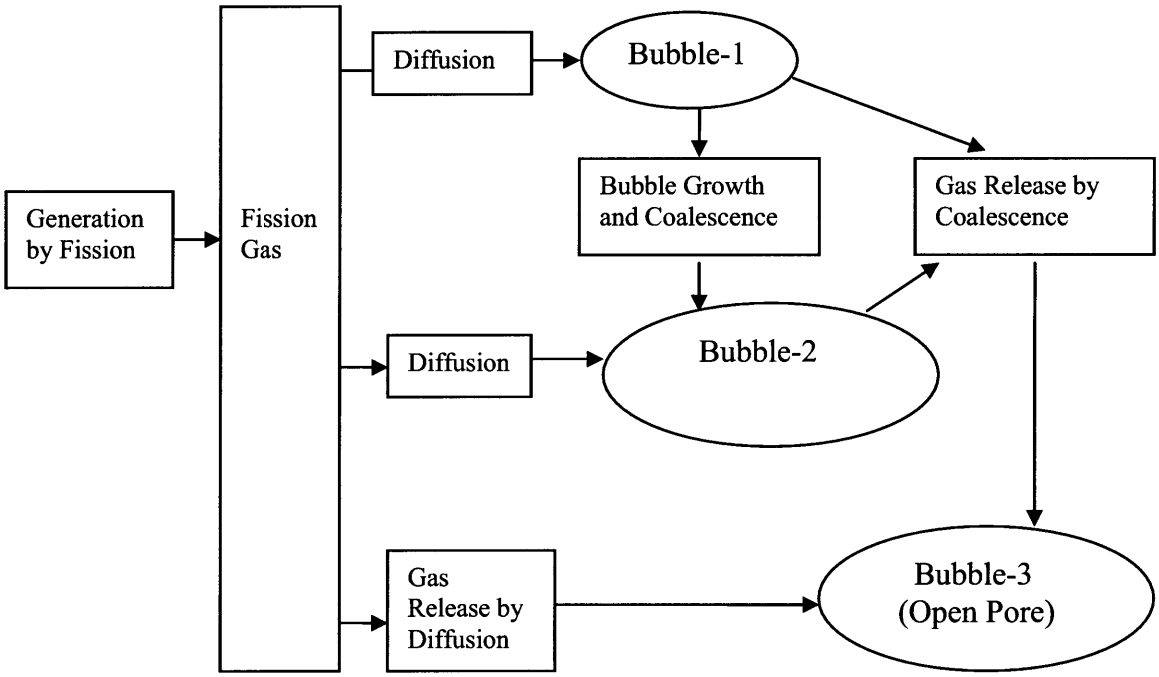


Figure-4: Fission gas and bubble movement model

According to the bubble classification given in Figure-4, the behavior of the fission gas atoms and bubbles can be described as follows.

Bubbles in group 1 are nucleated from the fuel matrix. They can collide with each other by both diffusion and growth, to become bubbles in group 2, with the probability of this process depending on the difference of the bubble sizes between groups 1 and 2. When bubbles in group 1 or 2 collide with bubbles in group 3, they become part of group 3. Bubbles in group 3 (open bubbles) are designated as bubbles-31 and 32, depending on the bubble group from which it came. Open bubbles are assumed not to move (diffuse) since gases in the open bubbles are released into the free volume.

Empirical Model:

The upper part of the fission gas release data band given in Figure-3 represents the typical peak fuel pin fission gas release behavior of EBR-II reactor. The data has been fitted to an exponential function as given in Eq-2.2.1 and shown in Figure-5.

$$f = \begin{cases} 0 & \text{Bu} < 0.8 \\ 0.8 \times \left[1 - \exp\left(-\frac{Bu}{1.8} \right) \right] & \text{Bu} \geq 0.8 \end{cases} \qquad (2.2.1)$$

f: Fission gas release fraction

Bu: Average fuel rod burnup (at %)

This type of a relation is recommended for use only in rough comparative analyses. Because the metal fuel fission gas release behavior shows strong dependency on axial power profile, operating temperature and linear heat rate, such a simplified relation should not be used for studies, in which accuracy is required.

Finally note that the empirical treatment has been developed only for fission gas release, whereas the swelling behavior of the fuel is simulated with the GRSIS model, even when the fission gas release empirical correlation is selected.

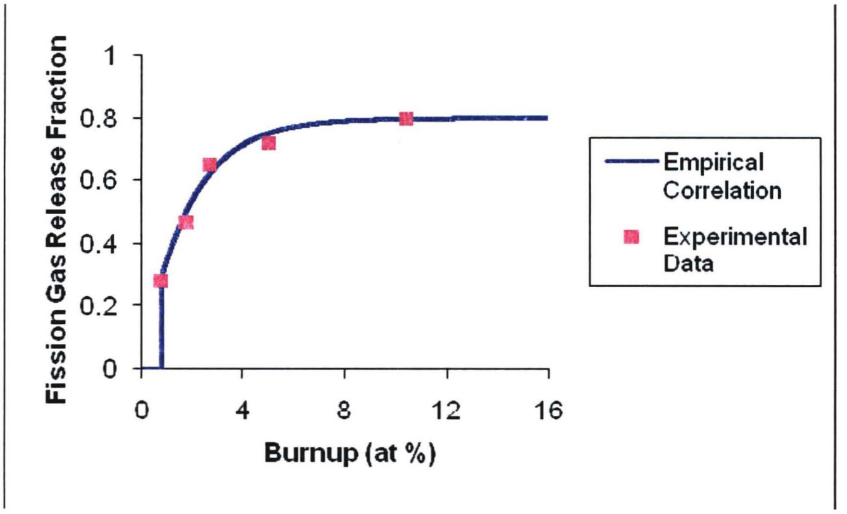


Figure-5: Empirical correlation for fission gas release (Experimental data is taken from Ref. [26])

2.2.4. Governing Equations for GRSIS Model

The governing equations for the gas atoms and bubble groups are:

$$\frac{dC_g}{dt} = YF - (J_{g1} + J_{g2} + J_{g3}) - J_{b_1,nucl}, \tag{2.2.2}$$

$$\frac{dC_{gb1}}{dt} = J_{b_1 nucl} + J_{g1} - (ab_{12} + ab_{13}) - (gab_{12} + gab_{21} + gab_{13}) - f_{12}(ab_{11} + gab_{11}) \tag{2.2.3}$$

- instantaneous release by bubble interconnection at threshold closed bubble swelling

$$\frac{dC_{gb2}}{dt} = J_{g2} + ab_{12} + gab_{12} + gab_{21} + f_{12}(ab_{11} + gab_{11}) - ab_{23} - gab_{23} \tag{2.2.4}$$

- instantaneous release by bubble interconnection at threshold closed bubble swelling.

$$\frac{dC_{gb3}}{dt} = J_{g3} + ab_{13} + ab_{23} + gab_{13} + gab_{23} \tag{2.2.5}$$

+ instantaneous release by bubble interconnection at threshold closed bubble swelling.

C_g : Gas atom concentration in the fuel matrix (atoms/ m³)

C_{gb1} : Concentration of gas atoms present as bubble-1 in the matrix (atoms/ m³)

C_{gb2} : Concentration of gas atoms present as bubble-2 in the matrix (atoms/ m³)

C_{gb3} : Concentration of gas atoms present as bubble-3 in the matrix (atoms/ m³)

Y: Fission yield of gas atoms is assumed to be 0.25 atoms/fission [2]

F: Fission density (fission/s/ m³)

J_{gi} : Gas diffusion rate to bubble-i (atoms/s/ m³),

$J_{b_1,nuc}$: Bubble-1 nucleation rate (atoms/s/m³),

ab_{ij} : Transfer rate of bubble-i into bubble-j by bubble diffusion (atom/s/m³),

gab_{ij} : Transfer rate of bubble-i into bubble-j by radial growth of bubble-i (atom/s/m³),

$f_{i,i+1}$: Transition probability of bubble-i into bubble-(i+1) by collision with bubble

The relation between bubble density, N_{bi}, and the total gas atom density of bubble-i, C_{gbi} is

$$C_{gbi} = \rho_{gi} N_{bi} \tag{2.2.6}$$

ρ_{gi} : Density of gas atom in a bubble-i (atoms/bub-i)

N_{bi} : the bubble-i concentration (bub-i/m³).

$$\rho_{gi} = \left(B + \left[\left(\frac{2\gamma}{kT} \right) \frac{1}{R_i} + \frac{\sigma}{kT} \right]^{-1} \right)^{-1} \times V_{bi} \tag{2.2.7}$$

B: Van der Waals Parameter (85×10^{-30} m³/atom)

γ : Surface Tension = 0.8 N/m from Refs. [25] and [30]

R_i: Radius of Bubble-i

σ: Hydrostatic Stress

k : Boltzman Constant

V_{bi}: Volume of the Bubble-i (m³/bubble-i)

The hydrostatic stress is given as follows:

$$\sigma_h = -\frac{\sigma_r + \sigma_\theta + \sigma_z}{3} \tag{2.2.8}$$

The collision rate of a closed bubble-i with the open pores by diffusion and growth are given by, respectively:

$$ab_{i3} = ab_{i31} + ab_{i32} \tag{2.2.9}$$

$$gab_{i3} = gab_{i31} + gab_{i32} \tag{2.2.10}$$

Then, the balance equations of open pores are as follows:

$$\frac{dC_{gb31}}{dt} = \rho_{g1} \frac{d}{dt} N_{b31} = ab_{131} + ab_{132} + gab_{131} + gab_{132} \tag{2.2.11}$$

$$\frac{dC_{gb32}}{dt} = \rho_{g2} \frac{d}{dt} N_{b32} = ab_{231} + ab_{232} + gab_{231} + gab_{232} \tag{2.2.12}$$

The specific parameters of the gas atoms and bubbles in the above equations can be obtained as follows.

2.2.5. Bubble-1 Nucleation Rate

Bubble-1 nucleation rate, $J_{b_1 nucl}$ is obtained from the bubble nucleation constant and the gas atom concentration in the fuel matrix, such that

$$J_{b_1 nucl} = k_{b_1 nucl} C_g \rho_{g1} \tag{2.2.13}$$

$k_{b_1 nucl}$: Bubble-i nucleation constant (bub-1/s atom)

2.2.6. Gas Diffusion

Diffusion of gas atoms into the bubbles can be calculated from the analytical solution in the case that gas atoms diffuse into a spherical sink. The atomic flux into bubble-i by diffusion, J_{gi}, can be calculated as a function of the gas diffusion constant and the concentrations of gas and bubbles as follows:

$$J_{gi} = k_{gi} C_g N_{bi} \tag{2.2.14}$$

$$k_{gi} = E_{gbi}(4\pi r_{bi}) D_g \tag{2.2.15}$$

k_{gi}: Gas diffusion constant to bubble-i (m^3/s),

E_{gbi} : Empirical bias factor for gas diffusion to the bubble-i,

r_{bi} : Radius of bubble-i (m)

D_g : Diffusion coefficient of gas atom (m^2/s)

$$D_g = D_{go} \exp(-Q_g / RT) \tag{2.2.16}$$

D_{go} : Diffusion Constant (m^2/s)

Q_g : The activation energy for a mole of jumps = 52000 cal/g-mol from Ref. [31]

R : Gas Constant (1.987 cal/g-mol/K)

In Ref. [26] it is noted that there exist large discrepancies in reported gas diffusion coefficients, by up to a factor of 100. In this study, the diffusion factor, D_{go}, is being used as one of the fitting parameters to match the calculated and measured fission gas release and swelling behavior of the metallic fuel. The selected values are given in Table-4.

Comparing the metal fuel diffusion coefficient with the oxide fuel in Table-3, the metal fuel has many orders of magnitude higher diffusion coefficient within the temperature range of interest.

Table-3: Comparison of metal and oxide fuel diffusion coefficients (m^2/s)

Temperature (K)	Metal Fuel (FEAST)	UO_2 Fuel* [32]
1000	9.9E-15	6.0E-21
900	5.4E-16	6.0E-21
800	1.4E-17	6.0E-21
700	1.3E-19	6.0E-21

* At this temperature range oxide fuel diffusivity is fission driven. The diffusion coefficient is calculated assuming the specific heat rate is 200 kW/kg

2.2.7. Coalescence by Bubble Diffusion

The bubble diffusion coefficient can be calculated as a function of surface diffusion coefficient (D_s) and bubble characteristics.

$$D_{bi} = \frac{3a_o^4}{2\pi r_{bi}^4} D_s \tag{2.2.17}$$

D_{bi} : Diffusion coefficient of bubble-i (m^2/s)

a_o^2 : Area occupied by a gas atom at the bubble surface (m^2).

Surface diffusion coefficient, D_s can be obtained by [26]

$$D_s = 1000 D_g \tag{2.2.18}$$

Bubbles can collide by diffusional movement so that the collision constant of bubble-i and bubble-j by bubble diffusion, is k_{ij} (m^3/s)

$$k_{ij} = E_{bb} 4\pi (r_{bi} + r_{bj})(D_{bi} + D_{bj}) \tag{2.2.19}$$

E_{bb} : Empirical bias factor for bubble diffusion to other bubbles

k_{ij} : Collision or integration constant of bubble-i into bubble-j (m^3/s).

Then, the transfer rate of bubble-i into bubble-j by bubble diffusion is

$$ab_{ij} = k_{ij} N_{bi} N_{bj} \rho_{gi} \tag{2.2.20}$$

Jump or transition rate of bubble-i into bubble-i+1 after the collision with bubble-i can be obtained by

$$ab_{ii} = k_{ii} N_{bi}^2 2\rho_{gi} \tag{2.2.21}$$

ab_{ii} : Jump or transition rate of bubble-i into bubble-i+1 (atoms/m³/s).

If two bubbles from the same group coalesce, they will be transformed into the higher size bubble with a certain probability given by

$$f_{i,i+1} = \frac{2\rho_{gi}}{\rho_{gi+1}} \tag{2.2.22}$$

2.2.8. Coalescence by Bubble Growth

When the number density of bubble-i is N_{bi}, the average distance between bubble-i's can be calculated by assuming faced-centered cubic (FCC) lattice. As a result, the average distance between bubbles can be obtained by

$$l_j = 1.122 N_{bj}^{-1/3} \quad \text{(m)} \tag{2.2.23}$$

When there is a bubble-i in the space where bubble-j's are evenly distributed at the number density, N_{bj} with their distance, l_j, the average distance between the centers of bubble-i and bubble-j becomes $0.5 l_j$ which we calculated by means of a simple Monte Carlo simulation of randomly distributed bubbles in 3D space. Note that Ref. [26] recommended using $0.25 l_j$ for the average distance between the centers of bubble-i's, which was based on a (likely incorrect) 2D calculation.

The probability per unit time of a closed bubble-i colliding with a closed bubble-j due to radial growth of bubble-i, P_{ij} is

$$P_{ij} = \frac{\text{radial growth of buble-i}}{\text{distance between the surfaces of bubble-i and j}} = \frac{\Delta r_{bi}}{0.5 l_j - (r_{bi} + r_{bj})} \quad \text{(1/sec)} \tag{2.2.24}$$

Δr_{bi} : Change rate of radius of bubble-i (m/s)

r_{bi} : Radius of bubble-i (m)

r_{bj} : Radius of bubble-j (m)

On the other hand, this expression has been modified for the collision probability per unit time of a closed bubble-i with an open bubble-j as follows:

$$P_{ij} = \frac{\Delta r_{bi}}{d_1 l_j} \tag{2.2.25}$$

Thus, it is assumed that the probability is proportional to the radial growth of bubble-i and inversely proportional to the average distance between two open bubble-j's. d_1 is one of the fitting parameters to match the predicted and measured fission gas release and swelling behavior of the fuel. Its value is given in Table-4.

The radial growth of bubble-i by gas diffusion can be calculated from the following equations. The volume increase (ΔV_{bi}) and radial growth (Δr_{bi}) of bubble-i by gas diffusion are:

$$\Delta V_{bi} = \frac{J_{gbi}}{C_{gbi}} V_{bi} \tag{2.2.26}$$

$$\Delta r_{bi} = \frac{\Delta V_{bi}}{4\pi r_{bi}^2} = \frac{J_{gbi} r_{bi}}{3 C_{gbi}} \tag{2.2.27}$$

Then, the collision (or integration) rate of bubble-i with bubble-j by radial growth of bubble-i, gab_{ij} (atoms/m³/s) can be calculated as

$$gab_{ij} = P_{ij} C_{gbk} \qquad k = \min(i, j) \tag{2.2.28}$$

Thus, a certain fraction of smaller bubbles will become larger bubbles.

In parallel with coalescence by bubble diffusion process, when two bubbles from the same group coalesce by growth, they will be transformed into the higher size bubble with a certain probability given by

$$f_{i,i+1} = \frac{2\rho_{gi}}{\rho_{gi+1}} \tag{2.2.29}$$

2.2.9. Open Bubble Surface Area and Volume Correction

When a bubble-i is incorporated into the open bubble group, it is designated as open bubble-3i. After absorption of bubble-i by an open bubble, the gases in bubble-i are assumed to be released into the free space which has a lower pressure than bubble-i and therefore its surface area and volume may decrease. Therefore, when a bubble-i becomes an open bubble, its volume and surface area may be reduced to certain fractions of the initial values such as f_v and f_s, respectively. In Ref. [26], f_v is assumed to be equal to one and f_s has been used as a fitting function to shape the high burnup behavior of the fission gas release curve. Consistently with Ref. [26], the FEAST code assumes f_v=1. The value of f_s yielding the most accurate fit of the experimental fission gas release curve is given in Table-4.

2.2.10. Swelling

The swelling volume of the closed bubbles, S_c is

$$S_c = V_1 + V_2 \tag{2.2.30}$$

$$V_i = \frac{4}{3}\pi r_{bi}^3 N_{bi} \tag{2.2.31}$$

When swelling due to the closed bubbles reaches the threshold value (S_{th}) for bubble interconnection and opening to the external free space, a certain fraction of the closed bubbles become instantaneously open. Therefore, when $S_c \geq S_{th}$ the volume and surface area of the closed and open bubbles change as follows, respectively:

$$V_i \rightarrow (1 - f_{th})V_i \quad i = 1,2 \tag{2.2.32}$$

$$V_3 = f_{th} f_v (V_1 + V_2) \tag{2.2.33}$$

$$A_i \rightarrow (1 - f_{th})A_i \quad i = 1,2 \tag{2.2.34}$$

$$A_3 = f_{th} f_s (A_1 + A_2) \tag{2.2.35}$$

f_{th}: Fraction of closed bubbles that interconnect to the open bubbles when the threshold swelling is exceeded

f_s: Fractional surface area of a closed bubble after interconnecting to the open bubbles,

f_v: Fractional volume of a closed bubble after interconnected to the open bubbles.

The swelling volume by the open and closed bubbles is

$$S_g = V_1 + V_2 + V_3 \tag{2.2.36}$$

To obtain the total fuel swelling, one needs to account for the swelling due to solid fission products. It is recommended in Ref. [19] that swelling rate due to solid fission products be assumed to be 1.5 % per unit burnup (at %).

Thus, the total swelling becomes as follows

$$S_t = V_1 + V_2 + V_3 + 0.015 \times Bu \tag{2.2.37}$$

Bu: Burnup in atom percent

2.2.11. Fission Gas Release

Then the fission gas release can be calculated as follows:

$$\begin{aligned} FGR &= 0, && S_g < S_{th} \\ &= f_{th}(C_{gb1} + C_{gb2}), && S_g = S_{th} \\ &= C_{gb3}, && S_g > S_{th} \end{aligned} \tag{2.2.38}$$

2.2.12. Critical review of simplifying assumptions made by the GRSIS model

As stated previously, the fission gas release and fuel swelling model in FEAST is based on the GRSIS model. The parameters in GRSIS (i.e., bubble size, bubble nucleation constant, threshold swelling, fraction of bubbles interconnecting at the threshold swelling, volume and surface area correction factors for open bubbles) were used by its developers as fitting parameters, to match

the generic fission gas release behavior of the metal fuel given in Figure-3. The following simplifying assumptions were made in the original development of GRSIS:

1- The fuel is at 550 ^{0}C

Metal fuel usually operates within ~(400-750 ^{0}C) temperature range. However, mechanical properties and phases change significantly within this temperature range; so this assumption may lead to major inaccuracies.

2- Anisotropic fuel slug deformation is neglected.

Metal fuel shows strongly anisotropic fuel slug deformation due to grain boundary tearing (in U-Zr fuel) and radial cracks (in U-Pu-10Zr fuel). Thus, an isotropic swelling behavior may seriously overestimate the time at which the fuel/cladding contact occurs.

3- After the contact pressure reaches the fuel yield stress, further swelling of the fuel is compensated for by the fuel plastic strains.

Fuel plastic behavior depends on the equivalent stress. Due to the very high creep rate of metal fuel, the equivalent stress stays at a level lower than the yield stress, even when the contact pressure exceeds the yield stress of the fuel, so plastic behavior is not encountered. Note that this conclusion is consistent with the prediction of the ALFUS code [19].

4- As the fuel is assumed to freely expand in the axial direction, fuel clad mechanical interaction is neglected even after all open pores are filled with solid fission products at high burnup.

The experimental data [21] do not support this assumption.

5- The threshold swelling is assumed to be 20 %.

According to Ref. [19] 85 % smear density fuel only swells by 17 % and at the end of life, and 60 % of the fission gases are released to the plenum. This behavior can not be explained by GRSIS.

Based on these observations, some of the original GRSIS parameters were changed when the model was implemented in FEAST. Table-4 shows the important parameters for the fission gas release and swelling modules in FEAST and GRSIS.

Table-4: Reference data for FEAST and GRSIS

Variable	FEAST	GRSIS
Radius of Bubble-1 (μm)	0.5 [33]	0.5
Radius of Bubble-2 (μm)	10 [33]	12.5
Surface Tension (N/m)	0.8 [25], [30]	1.0
Gas Diffusion Factor, D_{go} (m^2/s) (fitting factor)*	2.3×10^{-3}	9.5×10^{-8}
Activation Energy of the gas diffusion, Q_g (cal/g-mol)	52000 [31]	32000
Surface Diffusion Factor, D_{so} (m^2/s)**	2.3	9.5×10^{-5}
Activation Energy of the gas diffusion, Q_s (cal/g-mol)**	52000	32000
Area occupied by surface molecule, a_o^2 (m^2)	9×10^{-20} [26]	9×10^{-20}
Bubble-1 Nucleation constant $k_{b_1 nucl}$ (bub-1/s atom)	1×10^{-20} [26]	1×10^{-20}
Bias factor of gas diffusion to closed bubble, E_{gb1}, E_{gb2}	1.0 [26]	1.0
Bias factor of gas diffusion to open bubble, E_{gb3}	1.0 [26]	1.0
Bias factor of bubble diffusion to closed bubble, E_{bb1}, E_{bb2}	1.0 [26]	1.0
Bias factor of bubble diffusion to open bubble, E_{bb3}	1.0 [26]	1.0
Threshold Closed Bubble Swelling (S_{th})	0.1 [19]	0.2
Fraction of interconnected bubbles at threshold swelling, f_{th}	0.01 [19]	0.3
Correction factor for bubble volume after becoming open bubble, f_v	1.0 [26]	1.0
Correction factor for bubble area after becoming open bubble, f_s*	0.2	0.6
Open bubble formation coefficient, d_1 (fitting factor)*	0.235	N/A

* D_{go}, f_s and d_1 are the fitting parameters to match the fission gas release and swelling behavior of the metal fuel.

** Surface diffusion coefficient is assumed to be 1000 times the gas diffusion coefficient [26].

Table-5 shows a comparison of fitted diffusion coefficient and reference diffusion coefficient. The reference gas diffusion coefficient given in the GRSIS description was evaluated at high temperatures (>950 K) in which the single gamma phase is dominant within the fuel. FEAST and GRSIS diffusion coefficients seem to match well within the range of the GRSIS diffusion coefficient. They are in similar order of magnitude; in spite of the large differences in the values of D_{go} and D_{so}. The diffusion coefficient referenced in ALFUS [19] description is the lowest one.

Table-5: Comparison of gas diffusion coefficients (m^2/s):

Temperature (K)	FEAST	GRSIS	ALFUS
1000	9.9E-15	9.6E-15	1.7E-17
900	5.4E-16	1.6E-15	3.9E-18
800	1.4E-17	1.7E-16	6.0E-19
700	1.3E-19	9.7E-18	5.5E-20

2.3. Modeling of Constituent Redistribution in U-Zr and U-Pu-Zr fuel

2.3.1. Introduction

Fuel constituent migration, which has been observed in irradiated metallic fuel, affects the fuel slug material properties such as solidus and liquidus temperatures, thermal conductivity, mechanical properties such as modulus of elasticity, fuel cladding eutectic reaction rate, and radial power density profile, particularly in enriched uranium alloy fuels. Thus, modeling of constituent redistribution is essential when developing a metallic fuel performance code.

Upon constituent redistribution the microstructure of irradiated metal fuel exhibits three distinct concentric zones, a zirconium-enriched central zone, a zirconium-depleted and uranium-enriched intermediate zone, and a zirconium-enriched zone on the outer periphery. The migration of zirconium atoms is driven by the chemical activity gradients that develop within the fuel when the radial temperature distribution creates multiple crystalline phases of the fuel alloy.

2.3.2. Major Assumptions

The model given by Kim in [34] is implemented into the FEAST-METAL code. It is based on thermo-transport theory. The following assumptions are adopted from [34] and [35].

1- Local equilibrium assumption. Phase changes (determined by a change in local concentration and/or temperature) are assumed to occur very rapidly compared with the migration of alloy constituents.
2- Pu does not migrate, thus the U and Zr concentration profiles are opposite.

3- The equilibrium phases of the ternary U-Zr-Pu system are described by using a quasi-binary U-Zr phase diagram (with constant Plutonium content), which is produced from ternary phase diagrams, assuming uniformity of Plutonium in each phase of the multiphase zones.
4- The minimum allowed Zirconium concentration in the Zirconium depleted middle region is 5 at % due to the solubility limit. When the concentration of a radial node drops below 5 at % further diffusion from this node to the adjacent nodes is not allowed. This limit corresponds to depletion of the matrix γ phase in the middle region.
5- The cross-terms, relating the flux of one species to the chemical potential gradient of another species, in the constitutive equations are negligible.
6- The presence of plutonium in the alloy at levels greater than 8 wt% enhances uranium and zirconium migration by an order of magnitude.
7- Only radial migration of zirconium is considered. Axial temperature gradients are relatively small and axial zirconium redistribution has not been observed experimentally.
8- The radial power distribution in the fuel slug is assumed to be directly proportional to the actinide concentration distribution.

The plutonium uniformity assumption is partly justified on the basis of the following observations from Ref. [35]:

1- Plutonium shows relatively large miscibility in various phases of the system in the in-reactor temperature range.
2- Irradiation data of the ternary system show that redistribution of plutonium is minimal.
3- Theoretical calculations show that the equilibrium tie lines in the vicinity of the ternary fuel compositions of interest run approximately parallel to the constant plutonium line in the isothermal sections of the U-Pu-Zr ternary phase diagram for the in-reactor temperature range.

2.3.3. Fundamental Data

The phase diagrams, diffusion coefficients and effective heats of transport of zirconium and uranium in the ternary alloy are the fundamental data required in this model.

Phase Diagrams:

The thermochemical driving force for constituent migration is determined by the various phases present in the fuel at the operating temperatures, an accurate estimate of the phase diagram is essential to the development of the fuel restructuring model. Assuming a fixed Pu concentration of 19 wt %, a simplified pseudo-binary phase diagram was developed for U-Pu-Zr alloys [34], which is based on the available ternary phase diagrams for the temperatures of interest. The U-Zr phase diagram is given in Ref. [36].

Figure-6 shows a generic pseudo-binary phase diagram for U-Pu-Zr alloys. The solubility lines 1 through 6 are linearly interpolated between U-Zr and U-19Pu-Zr fuels, and are given as functions of temperature in Table-6. This approach is adopted to examine the fuel for varying plutonium contents (0-26 wt %). Note that, similar approaches are recommended in Ref. [34] and [35].

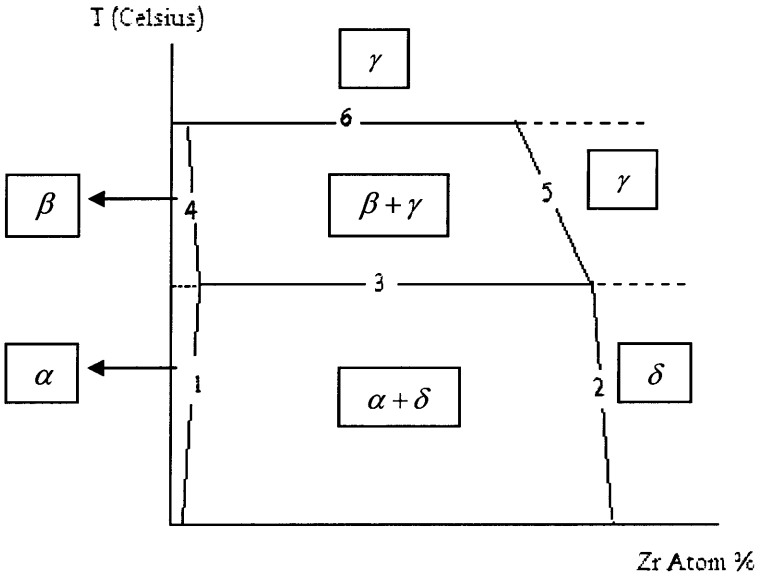


Figure-6: Pseudo binary phase diagram for U-Pu-Zr Fuel for fixed Pu content [34]

Table-6: Solubility Lines

Solubility Line	U-Zr [36]	U-19Pu-Zr [34]
1	$x_{Zr} = 0.01$	$x_{Zr} = 0.001+(T-773.15)/2968.8$
2	$x_{Zr} = \frac{T-813.15}{935.15-813.15} \times (0.588-0.676)+0.676$	$x_{Zr} = 0.539-\frac{T-773.15}{9500.0}$
3	T= 935.15	T= 868.15

4	$x_{Zr} = 0.01$	$x_{Zr} = 0.032 - \frac{T - 868.15}{6111.1}$
5	$x_{Zr} = \frac{T - 935.15}{965.15 - 935.15}(0.444 - 0.588) + 0.588$	$x_{Zr} = 0.529 - \frac{T - 868.15}{440.5}$ $T < 905$ $x_{Zr} = 0.445 - \frac{T - 905.15}{200}$ $T \geq 905$
6	T= 965.15	T= 923.15

x_{Zr} : Zirconium molar fraction

T : Temperature (K)

Enthalpy of Solution:

The enthalpy of solution of Zirconium in α and β phases is negligible [36]. On the other hand, the enthalpy of solution of the γ and δ matrix phases are given in [34] as follows:

$$\Delta\bar{H}_s = G_{Zr}^E - T\frac{\partial G_{Zr}^E}{\partial T} \tag{2.3.1}$$

$$G_{Zr}^E = x_U^2\left(43764.5 - 22T - 44174.7x_{Zr} + 38635.1x_{Zr}^2\right) + x_{Pu}^2\left(6574.7\right) + x_U x_{Pu}\left(15884\right) \tag{2.3.2}$$

$\Delta\bar{H}_s$: Enthalpy of solution (J/mol)

G_{Zr}^E : Free energy of Zirconium (J/mol)

x_U : Uranium mole fraction

x_{Zr} : Zirconium mole fraction

x_{Pu} : Plutonium mole fraction

T : Temperature (K)

Effective Heat of Transport:

The heats of transport for each phase field were obtained by a best fit in Ref. [34] and Ref. [30] to reproduce the measured redistribution profile of U-Pu-Zr and U-Zr fuels, respectively. The results are given in Table-7.

Table-7: Effective heat of transport (kJ/mol)

Phase	U->8Pu-Zr	U-Zr
α	200	0.0
δ	160	0.0

β	450	0.0
γ	−200	-150

Note that the effective heat of transport values are linearly interpolated between their values for the U-Zr and U-8Pu-Zr alloys. For plutonium concentrations above 8 wt %, it is assumed that the effective heat of transport values stay constant.

The negative heat of transport in the γ phase generates the driving force for zirconium to migrate towards the center (hotter) region of the fuel slug, even after zirconium accumulation in the center region creates an opposing concentration gradient. The positive heats of transport for the α, β and δ phases let zirconium migrate toward the fuel surface.

Effective Interdiffusion Coefficients:

The interdiffusion coefficient of Zirconium for U-Pu-Zr is not available. Therefore it was estimated to best fit the experimental data in Ref. [34].

The influence of plutonium addition and irradiation on the zirconium migration kinetics is handled by some enhancement factors. The existence of plutonium in a ternary fuel has been assumed to increase the interdiffusion coefficient [34], and the diffusion coefficients for each phase have been found by matching the experimental data for the T-179 fuel rod [34]. The results are given in Table-8 for the U-Zr alloy [36] and Table-9 for the U-Pu-Zr alloy with Plutonium weight fraction greater than 0.08. The gamma phase diffusion coefficient given in Ref. [36] depends on the zirconium molar fraction. Note that the quadratic dependency of the diffusion coefficient on the zirconium mole fraction is preserved for both U-Zr and U-Pu-Zr fuels.

Table-8: Diffusion coefficients for U-Zr alloy phases

Phases	D_o (m²/s)	Q (kJ/mol)
α	2×10^{-7}	170
δ	2×10^{-7}	150
β	5.7×10^{-5}	180
γ	$10^{(-5.1-8.05x_{Zr}+9.13x_{Zr}^2)}$	$128-107x_{Zr}+174x_{Zr}^2$

Table-9: Diffusion coefficients for U-Pu-Zr alloy phases (Pu is > 8 wt %)

Phases	D_o (m²/s)	Q (kJ/mol)
α	2×10^{-6}	170
δ	2×10^{-6}	150
β	4.0×10^{-4}	180
γ	$10^{(-5.1-8.05x_{Zr}+9.13x_{Zr}^2)}$	$128-107x_{Zr}+174x_{Zr}^2$

The Zr diffusion coefficient for the dual phase $\beta+\gamma$ is calculated by the diffusion coefficient of the β and γ phases from Table-9 multiplied by a factor of 10 depending on whether the β or γ phases exceed 50 %, respectively.

2.3.4. Model Development

The one dimensional continuity equation for zirconium can be expressed in cylindrical coordinates as follows:

$$\frac{\partial C_{Zr}}{\partial t} = -\frac{1}{r}\frac{\partial (rJ_{Zr})}{\partial r} + s \tag{2.3.3}$$

C_{Zr}: Zirconium concentration (atom/m³)

J_{Zr}: Interdiffusion flux (atom/m²/s)

s: Zirconium production rate by fission. The Zirconium yield is 0.2 for the fission of Plutonium.

Within a single γ phase field the zirconium interdiffusion flux is given by

$$J_{Zr} = -D_{Zr}^{eff}\left(\frac{\partial C_{Zr}}{\partial r} + \frac{Q_{Zr}C_{Zr}}{RT^2}\frac{\partial T}{\partial r}\right) \tag{2.3.4}$$

D_{Zr}^{eff}: Effective interdiffusion coefficient of zirconium in γ phase (m²/s)

Q_{Zr}: Heat of transport of zirconium in γ phase (J/mol)

R: Gas constant (8.314 J/mol/K)

T: Local fuel temperature (K)

When the concentration gradient becomes equal to the chemical potential gradient, the diffusion in the γ phase inherently stops.

Within a dual phase field such as $\alpha+\delta$ and $\beta+\gamma$, the driving force for diffusion is affected by the solubility of zirconium in the precipitation phases.

$$J_{Zr} = -V_1 D^{eff}_{Zr,1} C_{Zr,1} \frac{\Delta \bar{H}_{s,1} + Q_{Zr,1}}{RT^2} \frac{\partial T}{\partial r} - V_2 D^{eff}_{Zr,2} C_{Zr,2} \frac{\Delta \bar{H}_{s,2} + Q_{Zr,2}}{RT^2} \frac{\partial T}{\partial r} \quad (2.3.5)$$

V_1: Volume fraction of a phase-1

Note that subscript "1" represents the first phase and subscript "2" represents the second phase.

Discretization of the radial continuity equation results in

$$C^i_{Zr} = C^i_{Zr} + 2\Delta t \frac{J^{i-1}_+ \times rc^{i-1} - J^i_+ \times rc^i + J^i_- \times rc^i - J^{i+1}_- \times rc^{i+1}}{(r^i)^2 - (r^{i-1})^2} + s\Delta t \quad (2.3.6)$$

rc^i: Weight center of the radial node-i (m)

r^i: Outer boundary of node-i (m)

J^i_+: Positive zirconium current emerging from node-i towards outer part of the fuel. Its sign is positive (atom/m²/s)

J^i_-: Negative zirconium current emerging from node-i towards inner part of the fuel. Its sign is negative (atom/m²/s)

s: Zirconium production rate (atom/m³/s)

Δt: Time step (sec)

Eq-2.3.6 is solved for each fuel axial node by an explicit manner.

2.3.5. Boundary Conditions

The boundary conditions are that the negative current at the origin of the fuel slug as well as the positive current at the surface of the fuel slug are zero. That is:

at r=0.0 $J^i_- = 0.0$ (2.3.7)

at r=R $J^i_+ = 0.0$ (Zirconium cannot migrate out of the fuel) (2.3.8)

2.3.6. Model Verification

This section reports comparisons between the model predictions and experimental measured data for pin T179. Predictions of the redistribution profiles in the fuel for the 4S reactor [34] are also compared to Kim's Model predictions. Finally, a benchmark has been accomplished against data for the X447 U-Zr fuel assembly irradiated in EBR-II.

T179 Benchmark:

Figure-7 gives the fuel pin data and the fuel temperature distribution of T-179 estimated based on both experimental data and calculation from fuel microstructure observations [34]. The experimental data for the zirconium radial distribution at 230 mm from the bottom of the fuel slug are given in Figure-8. The calculation for both Kim's model and the FEAST code has been performed for the given temperature profile in Figure-7. The FEAST results in Figure-8, which is performed at constant temperature given in Figure-7, consistently with the Kim Model calculation, match the experimental data reasonably well.

Fuel Alloy Composition (wt %)	U-19Pu-10Zr
Fuel Slug length (mm)	343
Fuel Slug Radius (mm)	2.16
Fuel Slug Density (g/cm^3)	15.8
Fuel Smear Density (%)	72.3
Fuel-cladding gap material	Liquid Na
Sodium level above fuel (mm)	6.35
Cladding thickness (mm)	0.381
Linear heat rate (kW/m)	42
Subassembly coolant temperature ($^\circ C$)	Inlet: 371 Outlet: 486
Irradiation Burnup (at %)	1.9

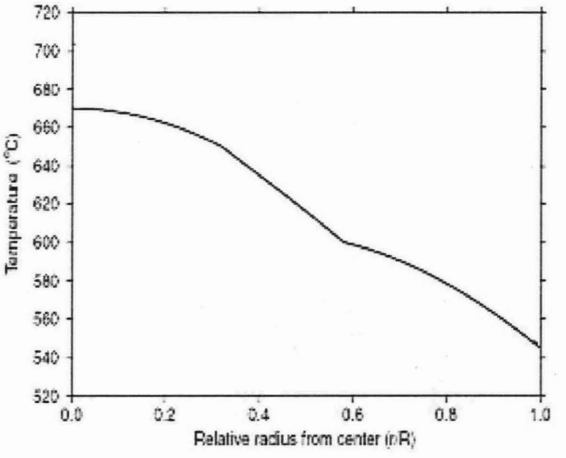


Figure-7: T-179 fuel data and temperature profile at a location 230 mm above the bottom of the fuel

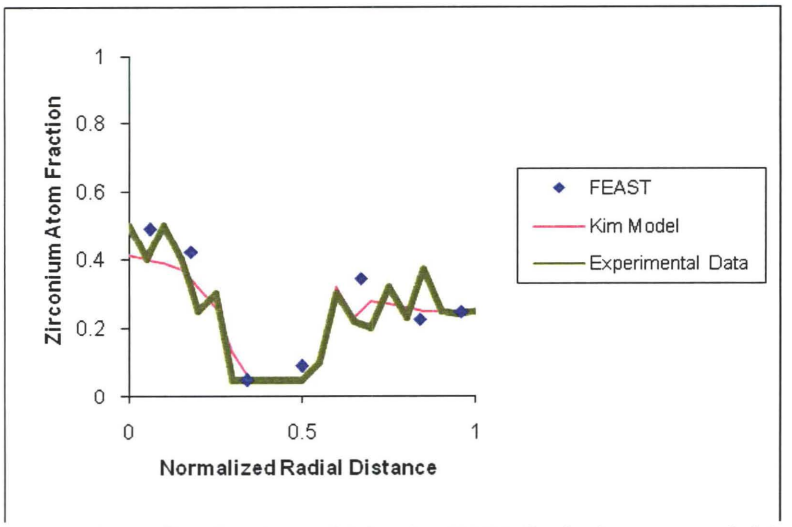


Figure-8: Radial zirconium distribution within the T179 fuel pin at an axial location 230 mm from the bottom of the fuel

4S Benchmark:

Kim's model and its FEAST implementation were applied to predict the 4S reactor fuel constituent redistribution. The calculation was performed for the fuel specifications given in Table-10. Fuel surface, centerline and phase transformation temperatures are given. Three different cases have been analyzed. The temperature distribution is given in Figure-9, and was assumed to be constant with burnup.

Table-10: 4S design fuel data [34]

Parameter	Value
Fuel Type (wt %)	U-20Pu-10Zr
Fuel Length (m)	2.5
Fuel density (g/cm^3)	15.8
Slug Radius (mm)	4.83
Clad Inner Diameter (mm)	10.8
Peak Linear Heat Rate (kW/m)	21.4

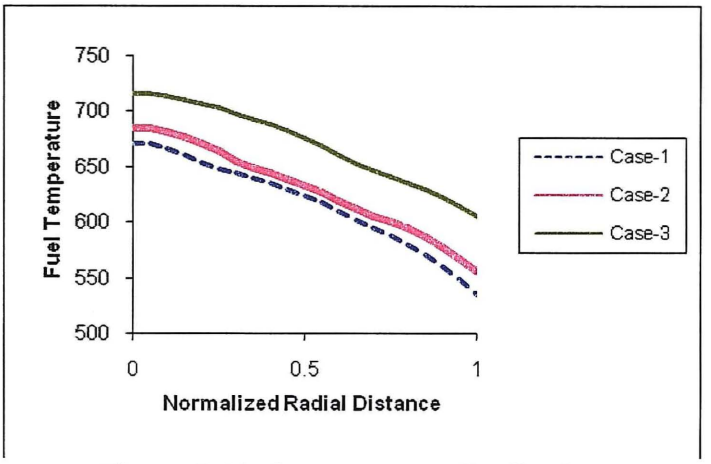


Figure-9: Fuel temperature distribution

Case-1:

In Case-1 the fuel surface temperature is 535 ^{0}C and the burnup is 3.7 at %. Figure-10 shows that the predictions of the Kim model and the FEAST code match reasonably well.

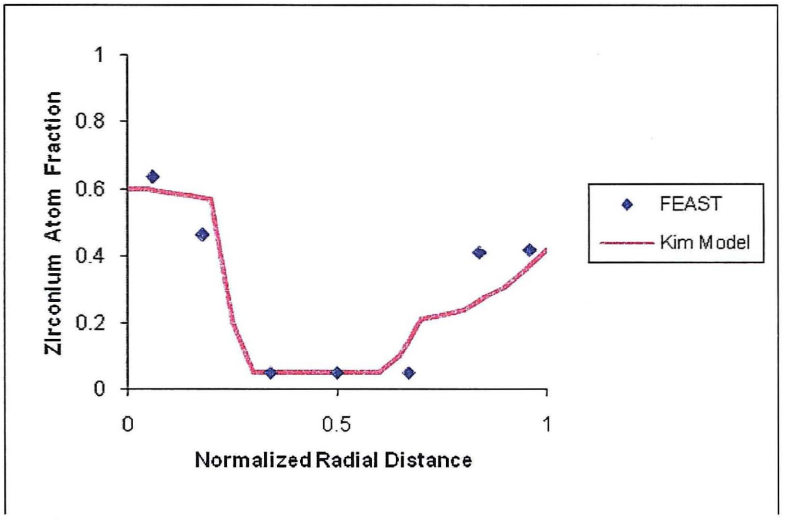


Figure-10: Case-1 fuel constituent redistribution results

Case-2:

In Case-2 the fuel surface temperature is 555 ^{0}C and the burnup is 7.5 at %. Figure-11 shows that in this case the FEAST code predicts a lower Zirconium concentration in the inner region of the fuel and higher in the outer region. However, the agreement is again reasonable.

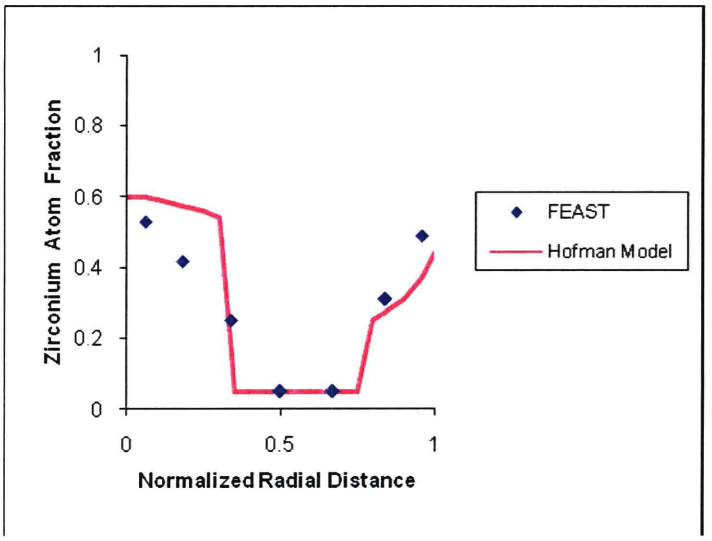


Figure-11: Case-2 fuel constituent redistribution results

Case-3

In case-3 the fuel surface temperature is 605 ^{0}C and the burnup is 3.2 at %. The predictions are reasonably close as shown in Figure-12, but FEAST now predicts a higher Zr concentration near the center.

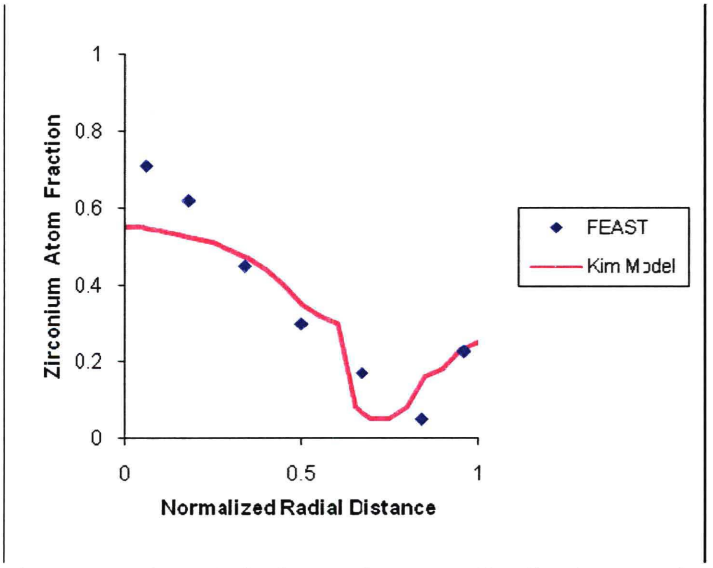


Figure-12: Case-3 fuel constituent redistribution results

X447 Benchmark:

The X447 assembly operated at higher peak cladding temperatures than typical EBR-II conditions. As a result, a significant part of the fuel element was subjected to constituent migration. The input data for X447 are shown in Table-11.

Table-11: X447 fuel specifications

Parameter	Value
Fuel Type (wt %)	U-10Zr
Fuel Length (m)	0.343
Fuel smear density (%)	75
Slug Radius (mm)	2.2
Clad Inner Radius (mm)	2.54
Clad Outer Radius (mm)	2.92
Peak Linear Heat Rate (kW/m)	33.0
Peak Clad Inner Temperature (^{0}C)	660

The irradiation history for the DP-11 fuel pin is shown in Figure-13. The end of cycle experimental data and the FEAST predictions are compared in Figure-14. The predicted distribution matches the trend of the experimental data.

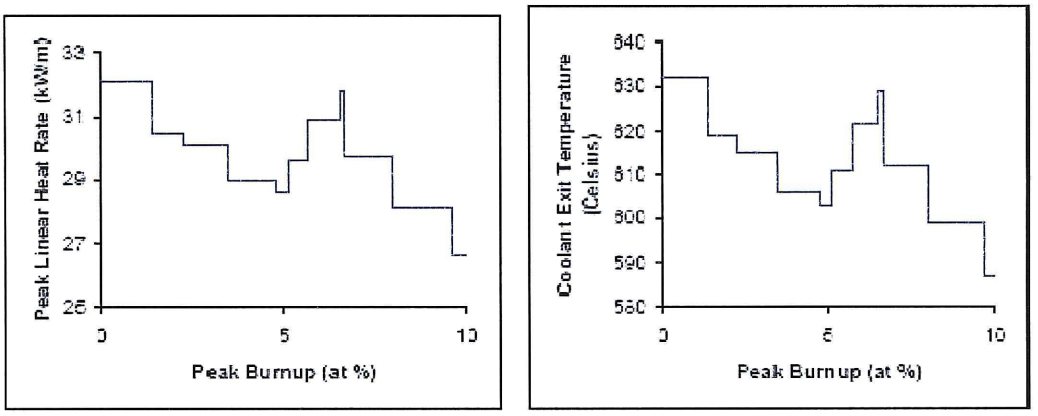


Figure-13: DP-11 fuel rod irradiation history [37]

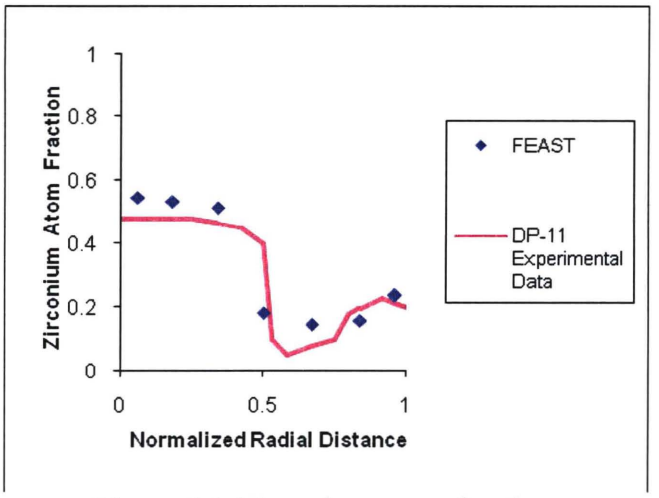


Figure-14: Zirconium atom fraction

2.4. Temperature Distribution Model

2.4.1. Introduction

The temperature distribution module adopts a 1D approach; thus, heat conduction in the axial and azimuthal directions is neglected. The key factors affecting the temperature distribution of metal fuel are known to be porosity, bond sodium infiltration into the porosity and thermal conductivity dependence on fuel constituent redistribution. These parameters are incorporated into the fuel temperature calculation in FEAST-METAL. The position-dependent porosity of the fuel is evaluated by means of the fission gas release and swelling module which was described in Section-2.2. The fuel constituent redistribution module was described in Section-2.3.

2.4.2. Coolant Temperature Distribution

Steady State:

Normally a detailed subchannel analysis would be required to calculate coolant temperature distribution within a fuel assembly. Due mainly to differences in the hydraulic diameter of the subchannels, the sodium coolant may have a non-negligible flow distribution across the fuel assembly in EBR-II. However, in FEAST a simpler single-channel approach is adopted. To estimate the coolant axial temperature distribution associated with the fuel pin of interest, the code uses a user-specified (1) linear heat rate profile, and coolant inlet and exit temperatures to or (2) linear heat rate profile, coolant inlet temperature and coolant mass flow rate. In the option

(1), the effective mass flow rate is calculated in the subchannel from an energy balance. Then the coolant temperature at each axial node can be calculated. On the other hand, if the option (2) is specificed, the energy balance can directly be applied.

The Single Mass Velocity Model [27] is adopted. Thus, the flow is assumed to be incompressible and thermally expandable.

$$\frac{d\dot{m}_{eff}}{dz} = 0 \tag{2.4.1}$$

If the option (1) is selected:

$$\dot{m}_{eff} = \frac{Q_{tot}}{\left(h_{out} - h_{in}\right)} \tag{2.4.2}$$

Then, the form of the energy balance equation is the same for both options:

$$T_c^j = \frac{Q^j}{\dot{m}_{eff} c_p^j} + T_c^{j-1} \quad \text{where j = 0,axn}$$

(2.4.3)

$\dot{m}_{eff}$: Effective subchannel mass flow rate (kg/s)

Q_{tot}: The total power produced in the fuel rod (W)

h_{in}: Coolant inlet enthalpy (J/kg)

h_{out}: Coolant outlet enthalpy (J/kg)

T_c^{j-1}: Node-j coolant inlet temperature (K)

T_c^j: Node-j coolant exit temperature (K)

Q^j: Power produced in the fuel section associated with node-j (W)

c_p^j: Specific heat of the coolant evaluated at T_m^j (J/kg/K)

axn: Total number of axial nodes

The average coolant temperature at node-j is computed as:

$$T_m^j = \frac{T_c^{j-1} + T_c^j}{2} \tag{2.4.4}$$

T_m^j: Mean coolant temperature at axial node-j (K)

Transients:

The same options given for the steady state description are allowed for the transients. If option (1) is specified, the procedure is the same as for the steady state situation. On the other hand, if option (2) is specified, an implicit algorithm is applied to account for the thermal inertia effects by using the following equation:

$$\rho c_p A_f \frac{\partial T_c^j}{\partial t} = q' - \frac{\dot{m} c_p}{L_j}\left(T_c^j - T_c^{j-1}\right) \tag{2.4.5}$$

q': Heat deposited into the coolant channel j (W/m)

A_f: Coolant flow area (m^2)

ρ: Coolant density (kg/m^3)

c_p: Coolant specific heat (J/kg/K)

L_j: Axial length of the node-j (m)

$\dot{m}$: Coolant mass flow rate (kg/s)

Coolant Heat Transfer Coefficient:

The Schad-Modified Correlation has been selected to calculate the coolant heat transfer coefficient [38]. It is known to be one of the most accurate correlations within its range. The Nusselt number is given as a function of pitch to diameter ratio and Peclet number as follows:

$$Nu = \left[-16.15 + 24.96\left(\frac{P}{D}\right) - 8.55\left(\frac{P}{D}\right)^2\right] Pe^{0.3} \tag{2.4.6}$$

$$1.1 \leq \frac{P}{D} \leq 1.5$$

$$150 \leq Pe \leq 1000$$

The resulting coolant heat transfer coefficient becomes:

$$h = \frac{Nu \times k_{Na}}{D_h} \tag{2.4.7}$$

Nu: Nusselt Number

$\frac{P}{D}$: Pitch to diameter ratio

Pe: Peclet Number = Re×Pr = $\frac{\rho V c_p D_e}{k}$

k_{Na}: Sodium conductivity (W/m/K)

D_h: Heated diameter (m)

h: Coolant heat transfer coefficient (W/m²/K)

ρ: Coolant density (kg/m³)

V: Coolant velocity (m/s)

c_p : Specific heat (J/kg/K)

D_e: Equivalent diameter (m)

k: Thermal conductivity (W/m/K)

2.4.3. Fuel Pin Radial Temperature Calculation

The radial temperature profile is calculated for each axial node. First the clad outer temperature is found from Newton's law of cooling:

$$T_{co}^{j} = \frac{Q^{j}}{h^{j} 2\pi R_{co}^{j} L^{j}} + T_{m}^{j} \tag{2.4.8}$$

T_{co}^{j}: Clad outer temperature at axial node-j (K)

R_{co}^{j}: Clad outer radius at axial node-j (m)

L^{j}: The axial length of node-j (m)

2.4.4. Energy Balance Method

Steady State:

Figure-15 shows the generic radial nodes for the fuel, gap and cladding regions. The numerical relation for node-i is formulated by assuming that all the heat goes into node-i [39].

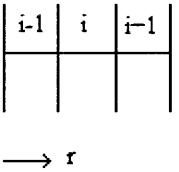


Figure-15: Radial discretization of the fuel pin

$$\dot{E}_{in} + \dot{E}_g = 0 \tag{2.4.9}$$

$\dot{E}_{in}$: Heat flow into node-i from node-(i-1) and (i+1)

$\dot{E}_g$: Energy generated within node-i

$$\frac{T_{i-1} - T_i}{\frac{1}{2\pi k_{i-1,i}} \ln \frac{r_i}{r_{i-1}}} + \frac{T_{i+1} - T_i}{\frac{1}{2\pi k_{i,i+1}} \ln \frac{r_{i+1}}{r_i}} + q_i''' A_i = 0 \tag{2.4.10}$$

T_i: Temperature of node-i (K)

T_{i-1}: Temperature of node-(i-1) (K)

$k_{i-1,i}$: Thermal conductivity between node-(i-1) and node-i evaluated at the average temperature (W/m/K)

q_i''': Heat generation rate. It is assumed to be zero for the gap and clad and coolant regions (W) Thus, all the fission heat is assumed to deposit in the fuel

A_i: Cross-sectional area of the radial node-i (m^2)

The algebraic equation for the ith node (Eq-2.4.10) can be written as follows:

$$\cdots + a_{i,i-1}T_{i-1} + a_{i,i}T_i + a_{i,i+1}T_{i+1} + \cdots = b_i \tag{2.4.11}$$

where 'a' and 'b' are constants.

Putting these algebraic equations for each radial node into 'Ax = b' form, the problem reduces to solving a system of linear algebraic equations, where A is an n×n matrix and b is a vector, characterizing the right hand side of the equations. x is the unknown vector. Gauss-Seidel method [28] was used in FEAST to find the radial temperature distribution of the fuel pin for each axial nodes.

Transients:

The transient part of the fuel pin temperature distribution module has been modeled with the semi-implicit Crank-Nicholson method. This method involves taking the average of the right-hand side of the energy equation (see Eq-2.4.13) between the beginning and the end of the time step. It is a second order method in time and is numerically stable. The Crank–Nicolson method is based on the central difference in space, and the trapezoidal rule in time, giving second-order convergence in time. Equivalently, it is the average of forward Euler and backward Euler in time.

The numerical discretization using Figure-15 is performed as follows:

$$\dot{E}_{acc} = \dot{E}_{in} + \dot{E}_g \tag{2.4.12}$$

$\dot{E}_{acc}$: Energy Accumulated in a radial node

$$\rho c_p A_i \frac{T_i^{t+1} - T_i^t}{\Delta t} = \frac{1}{2}\left(\frac{T_{i-1}^{t+1} - T_i^{t+1}}{\frac{1}{2\pi k_{i-1,i}} \ln \frac{r_i}{r_{i-1}}} + \frac{T_{i-1}^{t} - T_i^{t}}{\frac{1}{2\pi k_{i-1,i}} \ln \frac{r_i}{r_{i-1}}} \right)$$

$$+ \frac{1}{2}\left(\frac{T_{i+1}^{t+1} - T_i^{t+1}}{\frac{1}{2\pi k_{i+1,i}} \ln \frac{r_{i+1}}{r_i}} + \frac{T_{i+1}^{t} - T_i^{t}}{\frac{1}{2\pi k_{i+1,i}} \ln \frac{r_{i+1}}{r_i}} \right) + q_i''' A_i \tag{2.4.13}$$

Equation-2.4.13 can be written in form Equation-2.4.11 and putting all the algebraic eqtions into Ax = b form, FEAST finds the temperature distribution for the time step t+1 by using the Gauss-Jordan method [29] for transients.

2.4.5. Material Properties

Fuel Thermal Conductivity:

The fuel thermal conductivity depends on the fuel temperature, composition, porosity and fraction of the sodium infiltrated into the fuel, and is given in Ref.[18] and [40].

Note that the Zirconium weight percent for each radial node is given by the fuel constituent redistribution module; whereas Plutonium is assumed to be immobile (see discussion in Section 2.3).

Sodium infiltration is described quantitatively in Ref. [40] and semi-quantitatively in Ref. [34]. Based on these descriptions, it is assumed that sodium infiltrates 40 % of the open (interconnected) porosity.

$$k_o = a + bT + cT^2 \qquad \text{(T in Kelvin; } k_o \text{ in W/m/K)}$$

$$a = 17.5\left(\left(\frac{1-2.23W_{Zr}}{1+1.61W_{Zr}}\right)-2.62W_{Pu}\right)$$

$$b = 1.54\times10^{-2}\,\frac{1+0.061W_{Zr}}{1+1.61W_{Zr}}$$

$$c = 9.38\times10^{-6}\left(1-2.7W_{Pu}\right)$$

$$P_c = 1-\frac{3P_{Na}}{1-P}\times\frac{1-\frac{k_{Na}}{k_o}}{1.163+1.837\frac{k_{Na}}{k_o}}$$

$$k_f = P_c \times (1-P)^{1.5} \times k_o \quad (2.4.14)$$

T: Temperature (Kelvin),

k_0: As-fabricated thermal conductivity of the fuel (W/m/K),

W_{Zr}: Zirconium weight percent in the fuel

W_{Pu}: Plutonium weight percent in the fuel

P: Fuel porosity fraction,

P_c: Porositity correction factor with sodium infiltration

P_{Na}: Fraction of the fuel which is filled with sodium

k_{Na}: Sodium thermal conductivity (W/m/K)

k_f: Fuel thermal conductivity (W/m/K)

Thermal Conductivity of liquid sodium:

Thermal conductivity of liquid sodium is given in [41] as follows:

$k_{Na} = 93 - 0.0581T + 1.173 \times 10^{-5}T^2$ (W/m/K) (T in Celsius; k_{Na} in W/m/K) (2.4.15)

Equation-2.4.15 is valid within the temperature region of interest for sodium fast reactors.

Clad Conductivity:

Thermal Conductivity of HT9 is given in [42] as follows:

$$k_c = \begin{cases} 17.622 + 2.42\times10^{-2}T - 1.696\times10^{-5}T^2 & T < 1030 \\ 12.027 + 1.218\times10^{-2}T & T \geq 1030 \end{cases} \quad \text{(T in Kelvin; } k_c \text{ in W/m/K)} \quad (2.4.16)$$

Fuel Specific Heat:

U-Pu-Zr fuel specific heat is given as a function of temperatures and phases present [43].

For the α+δ phase

$$c_{p1} = 26.58 + \frac{0.027}{M_A}T \quad (2.4.17)$$

For the γ phase:

$$c_{p2} = 15.84 + \frac{0.026}{M_A} T \tag{2.4.18}$$

β+γ phase, interpolation has been performed.

$$c_{p1} = 26.58 + \frac{0.027}{M_A} T_1 \tag{2.4.19}$$

$$c_{p2} = 15.84 + \frac{0.026}{M_A} T_2 \tag{2.4.20}$$

$$c_{p3} = \frac{c_{p2} - c_{p1}}{T_2 - T_1}\left(T - T_1\right) + c_{p1} \tag{2.4.21}$$

c_{p1}: Specific Heat of α+δ phase (J/kg/K)

c_{p2}: Specific Heat of γ phase (J/kg/K)

c_{p3}: Specific heat of β+γ phase (J/kg/K)

T: Fuel Temperature (^{0}C)

T_1: α+δ to β+γ phase transition temperature (^{0}C)

T_2: β+γ to γ phase transition temperature (^{0}C)

M_A: Average atomic mass of the fuel mixture (kg)

Specific Heat of HT9:

Specific heat of HT9 clad material is given as a function of temperature as follows [44]:

$$c_{pc} = \frac{1}{6}\left(T - 227\right) + 500 \quad \text{for T} < 527\ ^0\text{C} \tag{2.4.22}$$

$$c_{pc} = \frac{3}{5}\left(T - 527\right) + 550 \quad \text{for T} > 527\ ^0\text{C} \tag{2.4.23}$$

T: Clad temperature (^{0}C)

c_{pc}: Specific heat of HT9 (J/kg/K)

2.4.6. Sensitivity Study and Benchmarking

The sensitivity of the temperature distribution to the important effects is shown in Figure-16 under the assumptions listed in Table-12. Note that the fuel centerline temperature is predicted within less than 10°C of the value reported in Ref. [34].

Table-12: Fuel specifications

Parameter	Value
Fuel	U-20Pu-10Zr
Radius (mm)	4.83
Linear Heat Rate (kW/m)	19.7
Porosity	~0.3
Sodium fraction within the pores	0.08
Fuel Surface Temperature (^{o}C)	535
Estimated Fuel Centerline Temperature with FEAST code (^{o}C)	663
Estimated Fuel Centerline Temperature Reported in Ref. [16] (^{o}C)	671

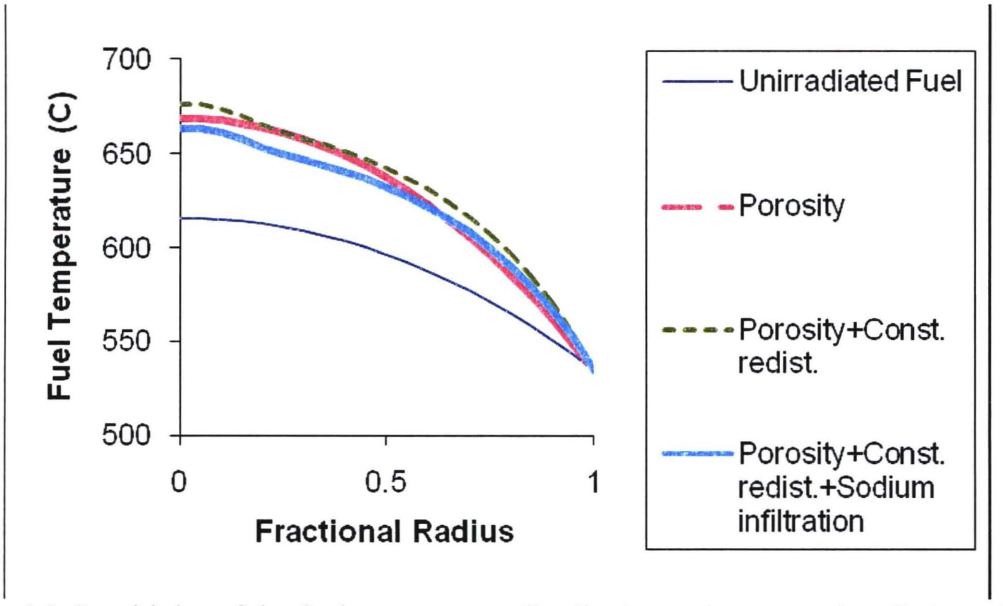


Figure-16: Sensitivity of the fuel temperature distribution to important irradiation effects

To assess the sensitivity of the temperature distribution to the number of radial nodes, a calculation was performed for the as-fabricated fuel given in Table-13, and the results are shown in Figure-17 including the closed form solution of the heat equation. It seems that adequate accuracy would be preserved with as low as five radial nodes.

Table-13: Fuel specifications

Parameter	Value
Fuel	U-19Pu-10Zr
Radius (mm)	2.86
Linear Heat Rate (kW/m)	50.0
Porosity	0.0
Sodium Infiltration	0.0
Fuel Surface Temperature (^{0}C)	600

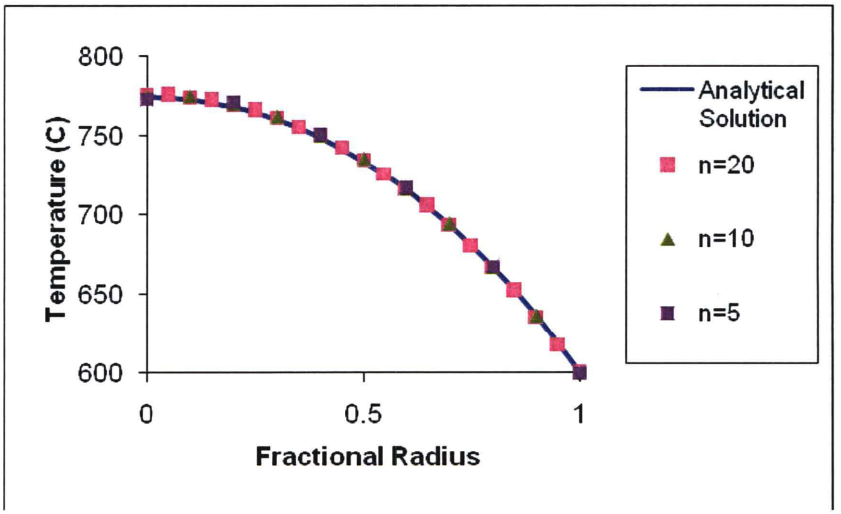


Figure-17: Node sensitivity to temperature distribution calculation

2.5. Fuel Clad Chemical Interaction Module

2.5.1. Introduction

The chemical reaction between the fuel slug and the cladding material is one of the most important issues limiting the in-pile performance of metal fuels. As a result of fuel cladding contact during steady state irradiation, the cladding constituents may diffuse into the fuel and

form a low-melting point alloy (eutectic). As the burnup increases, some fission products (particularly lanthanides) diffuse into the cladding to form low-melting phases with iron.

Furthermore, lanthanide diffusion creates a brittle band, which hardness measurements have shown to be very hard and containing numerous cracks [45].

In addition to the lanthanide layer, the effect of decarburization and grain coarsening of the cladding also contributes to cladding wastage. This layer, which is soft, uncracked and small with respect to the lanthanide layer, is thought to be carbon depleted and was found in areas outside the lanthanide regions [45].

The presence of zirconium in the fuel decreases Fuel/Cladding Chemical Interaction significantly. HT9 clad includes a minor amount of Nitrogen. As a result, a thin ZrN layer forms at the surface of the fuel. This layer hinders diffusion of fuel constituents into the cladding and vice versa. On the other hand, the layer loses its strength above ~600 ^{0}C and it totally disappears above the liquifaction temperature. Reported cladding wastage values at normal operating conditions (500-600 ^{0}C peak cladding temperatures) are less than 5 % for HT9, while operation at 630 ^{0}C to 660 ^{0}C may result in more than 20 % thinning of the clad [45].

During the operation, many phases form on the fuel side due to iron diffusion into the fuel as shown in Figure-18 [46]. Within these phases, $(U,Pu)_6Fe$ layer within the outer surface of the fuel has low melting point [47]. Figure-19 shows the minimum observed melting temperature as a function of the plutonium concentration. The liquefaction temperature has a strong dependency to the plutonium solubility limit [47]. Hence, it decreases with increased plutonium concentration as given in Figure-19. If the liquefaction temperature is exceeded during a transient scenario, melting of the $(U,Pu)_6Fe$ layer may result. Once the melting occurs at the fuel-clad interface, the diffusion of iron atoms into the fuel and the eutectic penetration towards the cladding is promoted significantly. Note that it is not a very rapid process compared to a typical time for the transient simulations of the Sodium Fast Reactors [48]. On the other hand, if the melting temperature of $(U,Pu)Fe_2$ is exceeded (~1000 ^{0}C), instantaneous failure of the clad may occur due to the rapid penetration through the cladding [49]. Note that, it is highly unlikely

for any transient to reach such high clad temperatures without any failure because thermal creep may result in cladding breach before the clad temperature exceeds 1000 ^{0}C.

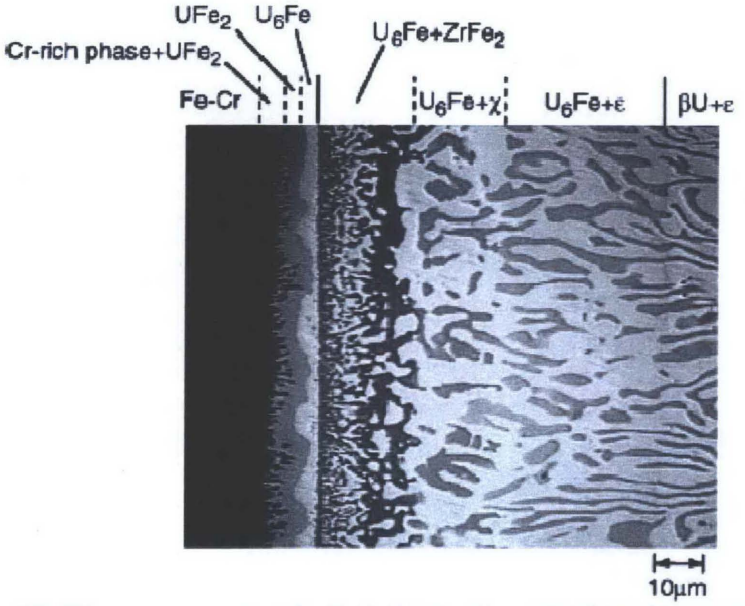


Figure-18: Phases present at fuel clad interface (U-10 Zr/HT9) [46]

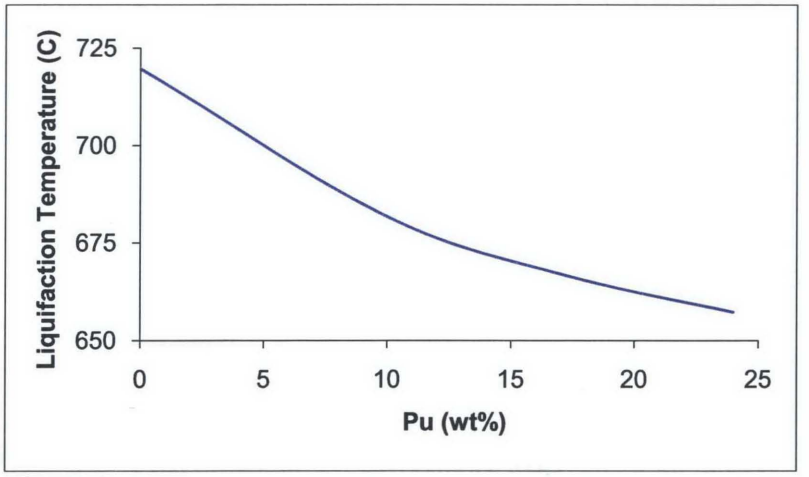


Figure-19: $(U,Pu)_6$ Fe minimum liquefaction (eutectic formation) temperature [47]

2.5.2. Precipitation Kinetics Model

We propose that the precipitation kinetics model given in physical metallurgy [50] could be a good physical based model to describe the fuel clad chemical interaction of the metallic fuels.

The general precipitation kinetics theory is depicted in Figure-20. When the solubility limit of α phase is exceeded, β precipitates form due to the available free energy. The driving force can be related to the concentration gradient of B atoms at the α-β interface, assuming the process is diffusion controlled.

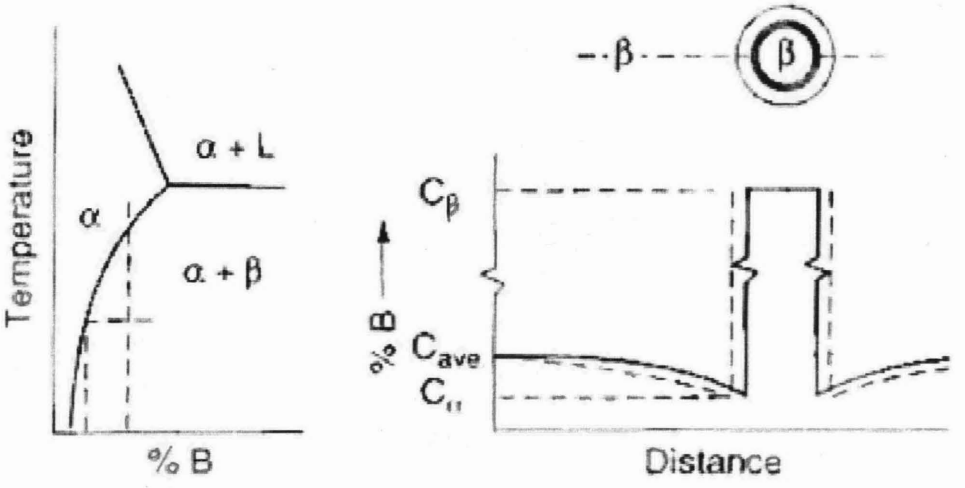


Figure-20: Precipitation kinetics theory [50]

As a result, the growth rate of the β layer is given as follows:

$$\frac{dX}{dt} = \frac{1}{2}\frac{C_o - C_\alpha}{C_\beta - C_\alpha}\sqrt{\frac{D}{t}} \tag{2.5.1}$$

X: β layer thickness (m)

C_o: Concentration of B atoms in α phase

C_α: Solubility limit of B atoms in α phase

C_β: Solubility limit of B atoms in β phase

D: Diffusion coefficient of B atoms in α phase (m^2/s)

t: Time (sec)

Figure-21 shows that the layer growth rate at the metallic fuel and clad interface is proportional to square root of time. It is the major evidence that metal fuel layer growth is a diffusion controlled process. Furthermore, increased burnup may result in an increased concentration of

available diffusing species such as lanthanides; hence, allowing for the concentration dependency of the reactants is also a physical based approach, as supported in Ref. [48].

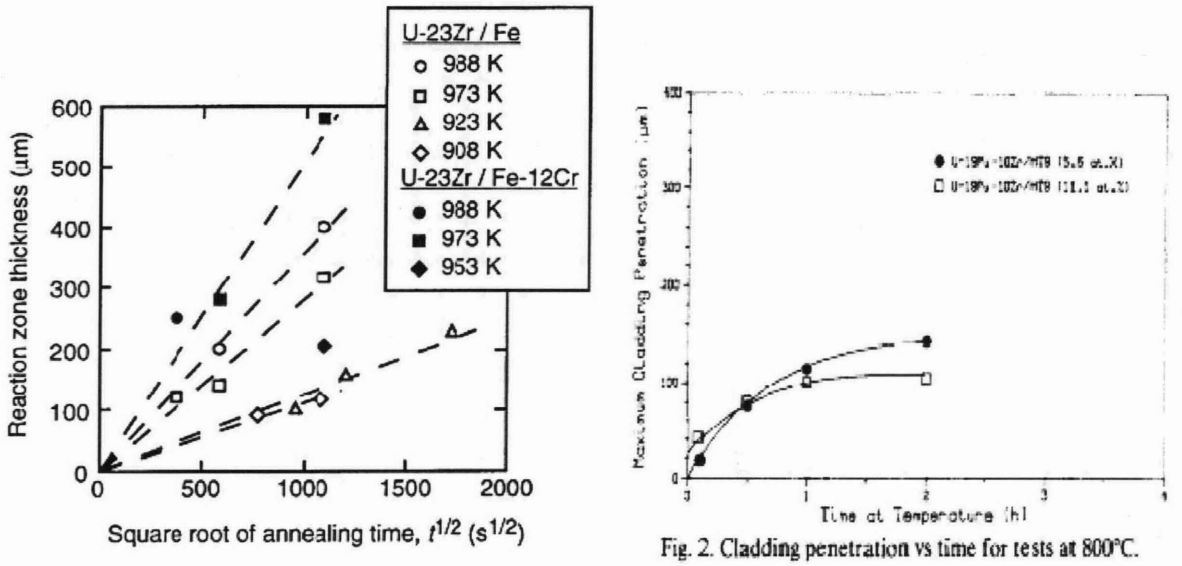


Figure-21: Growth of the reaction zones [46] and [48]

Steady State:

Steady state clad wastage prediction with precipitation kinetics model is given as follows:

$$\frac{dX_w}{dt} = \frac{1}{2}\frac{C_{oL} - C_{\alpha L}}{C_{\beta L} - C_{\alpha L}}\sqrt{\frac{D_L}{t}} \tag{2.5.2}$$

X_w: Clad wastage layer thickness (m)

C_{oL}: Concentration of the lanthanide atoms in the fuel

$C_{\alpha L}$: Solubility limit of the lanhanides in the fuel (zero)

$C_{\beta L}$: Solubility limit of the lanthanides in the clad (0.1)

D_L: Diffusion coefficient of lanthanides at fuel clad interface (m^2/s)

t: Time (sec)

Lanthanide diffusion coefficient is given with following relation.

$$D_L = D_{0L}\exp(-\frac{Q_L}{RT}) \tag{2.5.3}$$

D_{0L} : Diffusion constant for lanthanides (m^2/s) = 1350 m^2/s

Q_L : Activation energy for lanthanide diffusion = 300000 J/mol

R: Gas Constant (8.314 J/mol/K)

T: Clad inner temperature (K)

The concentration of the lanthanides in fuel is calculated as follows:

$$C_{0L}^{t+1} = C_{0L}^{t} + \frac{Y_L \times \dot{F} \Delta t}{n_{tot}} \tag{2.5.4}$$

C_{0L}^{t} : Lanthanide concentration at time t ($atom/m^3$)

n_{tot} : Total fuel atom density ($atom/m^3$)

Y_L : Fission yield of lanthanides

$\dot{F}$: Fission rate ($fission/m^3/s$)

Δt : Time step (sec)

t: Time (sec)

D_{0L} and Q_L are fitted to X447 experimental database as given in Figure-22. Note that, DP70 and and DP75 fuel pins are breached elements, thus, they were not considering in the fitting procedure as suggested in Ref [45].

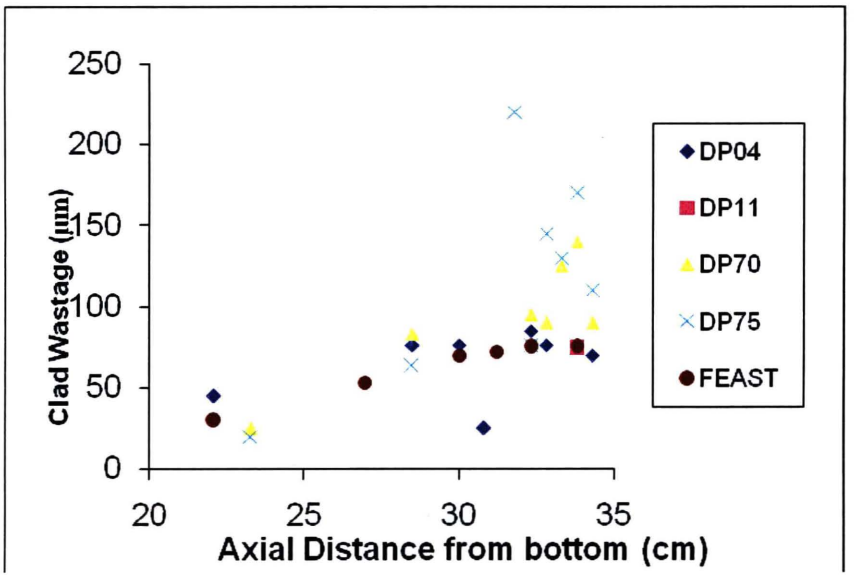


Figure-22: Axial clad wastage profile of X447 fuel pins at End of Life and FEAST calibration

Transients:

The precipitation kinetics model is also applied to the transient scenarios during which liquefaction occurs at the fuel clad interface.

$$\frac{dX_w}{dt} = \frac{1}{2}\frac{C_{0Fe} - C_{\alpha Fe}}{C_{\beta Fe} - C_{\alpha Fe}}\sqrt{\frac{D_{Fe}}{t}} \tag{2.5.5}$$

X_w: Thickness of the transient cladding wastage layer above the liquefaction temperature (m)

C_{0FE} C_o: Iron concentration within the clad = 0.78 (atom fraction)

$C_{\beta Fe}$: Solubility limit for iron within $(U,Pu)_6Fe$ layer = 0.14 (atom fraction)

$C_{\alpha Fe}$: Solubility limit of iron within the clad = 0.0 (atom fraction)

D_{Fe}: Diffusion coefficient of iron (m^2/s)

t: Time (sec)

The diffusion coefficient of iron migrating to the liquified fuel clad interface is given as follows:

$$D_{Fe} = D_{0Fe}\exp\left(-\frac{Q_{Fe}}{RT}\right) \tag{2.5.6}$$

D_{0Fe} : Diffusion constant for iron (m^2/s) = 4.2×10^6 m^2/s

Q_{Fe} : Activation energy for iron diffusion = 400000 J/mol

R: Gas Constant = 8.314 J/mol/K

t: time (sec)

T: Clad inner temperature (K)

The diffusion constant and activation energy are fitting constants. They are fitted to reproduce the experimental database from furnace tests of EBR-II fuel.

In addition, the transient precipitation kinetics model adopts the following assumptions based on the experimental database:

- The penetration rate below 750 ^{0}C seems to be showing weak dependency to temperature, thus, it is assumed the rate is constant between liquefaction temperature and 750 ^{0}C [48]
- When fuel clad gap opens by 50 μm, the reaction stops because, according to the experimental evidence, the liquified layer separates from the cladding [48]

The predictions are also compared with the Ref. [48] empirical clad wastage model. It is an exponential function fitted to the one-hour test results.

$$\frac{dX_w}{dt} = \exp\left(11.646 - \frac{15865}{T}\right) \tag{2.5.7}$$

T: Clad inner temperature (K).

X_w : Clad wastage (μm)

Note that this correlation is a conservative fit to the one-hour test results. Hence, it may not exhibit a good performance for the prediction of the rate of change of the clad wastage. Also, this model is not able to predict the saturation behavior of the wastage in the long term.

Table-14 shows the comparison. The predictions of our diffusion (precipitation kinetics) model are in good agreement with the experiemental data. On the other had, for a long time operation,

the empirical model overestimates the clad wastage very significantly. In addition, for short transients, it is likely that the empirical model could under-predict the wastage layer thickness due to its inability to describe the time dependency of the wastage layer because the time dependency of the clad wastage formation is not linear (see Figure-21).

Table-14: Transient clad wastage predictions

	Temperature (^{0}C)	Burnup (at %)	Time (hours)	Experimental Data (μm)	Diffusion Model (μm)	Empirical Model (μm)
1	675	10.8	12	140	168	277
2	700	9.8	1	58, 76	63	54
3	740	11.3	1.0	58, 87	63	85
4	770	9.6	1.0	80	76	122
5	800	10.8	0.1	42	50	36
6	800	11.3	0.5	79	100	98
7	800	10.0	1.0	100	127	130
8	800	10.5	2.0	104	127	130

2.5.3. Sodium Corrosion

HT-9 Clad has an excellent sodium compatibility up to 650 ^{0}C, a factor of two less than AISI 316 stainless steel [51]. The lower corrosion rate can in part be attributed to the fact that there is less nickel and chromium in the ferritic material. The selective nickel and chromium dissolution from austenitic steels is a significant part of the weight loss from austenitic steels in sodium.

The corrosion data given in Ref. [51] is fitted to an exponential function:

$$\dot{R} = 3.3\times10^{-6}\exp\left(-\frac{16000}{T}\right) \text{ (m/s)} \qquad (2.5.8)$$

R: Rate of wastage layer formation at cladding outer layer (m/s)

T: Clad inner or outer temperature (K)

Corrosion of the clad outer region is calculated during the irradiation. Clad inner corrosion is due to sodium only if the fuel cladding gap is open.

2.6. Mechanical Analysis

2.6.1. Introduction

The first barrier against the release of radioactive fission products into the environment is the cladding of the nuclear fuel rod. The assessment of the cladding stresses and associated deformations is therefore essential in fuel performance calculations. The stress-strain analysis module of FEAST adopts the LIFE algorithm [2] with a 1D finite difference solution.

2.6.2. General Assumptions

1- The fuel and clad are assumed to be axially symmetric.

2- The planes perpendicular to the axial z-direction in each material remain plane during deformation. This is the plane strain assumption.

3- Axial friction between the fuel slug and cladding is considered.

4- The time dependence is inherent in the analysis due to the swelling and creep, which are time-dependent phenomena. However, inertia effects are neglected, so the system is treated as undergoing a succession of (mechanical) equilibrium states.

5- The outer radius of the fuel and inner radius of the cladding are loaded by the plenum pressure if the fuel-cladding gap is open and by the fuel-cladding interfacial pressure if the gap is closed.

6- The outer radius of the cladding is subject to the coolant pressure. The axial variation of the coolant pressure is neglected.

As a result of assumptions 1 and 2, only the normal stresses along the three principal directions in the cylindrical coordinate system are non-zero; these are denoted by the symbols σ_r

, σ_θ and σ_z and are positive if tensile, and negative if compressive, according to the usual sign convention. There are no shear stresses.

2.6.3. Governing Equations

Equilibrium Condition:

The equilibrium conditions are simplified by the elimination of the shear stresses and axial tangential derivatives, which leads to the single equation:

$$\frac{d\sigma_r}{dr}+\frac{\sigma_r-\sigma_\theta}{r}=0 \tag{2.6.1}$$

Kinematics:

Letting ϵ_r, ϵ_θ and ϵ_z be the total strains in the three principal directions, the strain displacement relations become:

$$\varepsilon_r=\frac{du}{dr} \tag{2.6.2}$$

$$\varepsilon_\theta=\frac{u}{r} \tag{2.6.3}$$

$$\epsilon_z = \text{Constant with r (as per assumption 2 above)} \tag{2.6.4}$$

"u" is the radial displacement. The total strain in each direction is the sum of the thermal strains, elastic strains, creep/plastic and swelling strains due to accumulation of fission gas bubbles, open porosity and nongaseous fission products.

Constitutive Relations:

The constitutive relations used in fuel modeling analysis are the generalized Hooke's law:

$$\varepsilon_r=\frac{1}{E}\left[\sigma_r-\nu\left(\sigma_\theta+\sigma_z\right)\right]+\alpha T+\varepsilon^s+\varepsilon_r^c \tag{2.6.5}$$

$$\varepsilon_\theta=\frac{1}{E}\left[\sigma_\theta-\nu\left(\sigma_r+\sigma_z\right)\right]+\alpha T+\varepsilon^s+\varepsilon_\theta^c \tag{2.6.6}$$

$$\varepsilon_z = \frac{1}{E}\left[\sigma_z - \nu\left(\sigma_r + \sigma_\theta\right)\right] + \alpha T + \varepsilon^s + \varepsilon_z^c \tag{2.6.7}$$

Equations 2.6.5 to 2.6.7 apply to both the fuel and the cladding provided the linear thermal-expansion coefficient α, Young's Modulus E, and Poisson's ratio ν are chosen accordingly and appropriate material-specific functions are used for the swelling (ε^s) and creep/plastic (ε^c) strains in each part of the fuel element. The thermal expansion coefficient, Young's modulus and Poisson's ratio of the HT-9 cladding material and U-Pu-10Zr fuel alloy are given in Appendix-A.

2.6.4. Solution Method

The presence of time-dependent permanent (irreversible) strains and the sizeable variation of the mechanical properties of the fuel with position (mainly due to the radial temperature distribution) require a numerical solution of the relevant equations. Moreover, the creep and swelling phenomena introduce time as an explicit variable.

The total strains ε_r and ε_θ are eliminated by combining Eq-2.6.5 to 2.6.7 with Eq-2.6.2 and 2.6.3 and the stresses are expressed in terms of the radial displacement.

$$\sigma_r = \frac{E}{1+\nu}\left[\frac{du}{dr} + \frac{\nu}{1-2\nu}\left(\frac{du}{dr} + \frac{u}{r} + \varepsilon_z - 3\alpha\left(T - T_o\right) - 3\varepsilon^s\right) - \left(\alpha\left(T - T_o\right) + \varepsilon^s + \varepsilon_r^c\right)\right] \tag{2.6.8}$$

$$\sigma_\theta = \frac{E}{1+\nu}\left[\frac{u}{r} + \frac{\nu}{1-2\nu}\left(\frac{du}{dr} + \frac{u}{r} + \varepsilon_z - 3\alpha\left(T - T_o\right) - 3\varepsilon^s\right) - \left(\alpha\left(T - T_o\right) + \varepsilon^s + \varepsilon_\theta^c\right)\right] \tag{2.6.9}$$

$$\sigma_z = \frac{E}{1+\nu}\left[\varepsilon_z + \frac{\nu}{1-2\nu}\left(\frac{du}{dr} + \frac{u}{r} + \varepsilon_z - 3\alpha\left(T - T_o\right) - 3\varepsilon^s\right) - \left(\alpha\left(T - T_o\right) + \varepsilon^s + \varepsilon_z^c\right)\right] \tag{2.6.10}$$

Eq-2.6.8 and 2.6.9 are substituted into the equilibrium condition, Eq-2.6.1, and the following differential equation for the radial displacement is obtained [2]:

$$\frac{d}{dr}\left[\frac{1}{r}\frac{d(ru)}{dr}\right]=\left(\frac{1-2\nu}{1-\nu}\right)\left(\frac{d\varepsilon_r^c}{dr}+\frac{\varepsilon_r^c+\varepsilon_\theta^c}{r}\right)+\left(\frac{1+\nu}{1-\nu}\right)\frac{d}{dr}\left(\alpha\left(T-T_o\right)+\varepsilon^s\right) \tag{2.6.11}$$

The step leading to Eq-2.6.11 requires that the elastic constants E and ν be assumed independent of r (and hence temperature). This approximation is valid only when the radial interval over which the resulting equation applies is small.

Eq-2.6.11 is applied to each ring in the fuel element. Each ring is characterized by subscripts i and j, representing the radial and axial positions in the pin, respectively. Eq-2.6.11 is integrated from the inner boundary of the i-th radial zone (r_{ai}) to radial position "r" within the ring.

$$\begin{aligned}u(r)=&\frac{C_{1i}}{r}+C_{2i}r+\left(\frac{1+\nu}{1-\nu}\right)\frac{1}{r}\int_{r_{ai}}^{r}r'\left(\alpha T+\varepsilon^s\right)dr'\\&+\frac{1}{2}\left(\frac{1-2\nu}{1-\nu}\right)\left[\frac{1}{r}\int_{r_{ai}}^{r}\left(\varepsilon_r^c+\varepsilon_\theta^c\right)r'dr'+r\int_{r_{ai}}^{r}\left(\varepsilon_r^c-\varepsilon_\theta^c\right)\frac{dr'}{r'}\right]\end{aligned} \tag{2.6.12}$$

Where C_{1i} and C_{2i} are constants of integration for the i-th zone which remain to be determined. At this point, it is assumed that the thermal, swelling and permanent strains are constant within each ring which reduces Eq-2.6.12 to

$$\begin{aligned}u(r)=&\frac{C_{1i}}{r}+C_{2i}r+\left(\frac{1+\nu}{1-\nu}\right)\left[\alpha_i\left(T-T_o\right)_i+\left(\varepsilon^s\right)_i\right]\frac{r^2-r_{ai}^2}{2r}\\&+\frac{1}{2}\left(\frac{1-2\nu}{1-\nu}\right)\left\{\left[\left(\varepsilon_r^c\right)_i+\left(\varepsilon_\theta^c\right)_i\right]\frac{r^2-r_{ai}^2}{2r}+\left[\left(\varepsilon_r^c\right)_i-\left(\varepsilon_\theta^c\right)_i\right]r\ln\frac{r}{r_{ai}}\right\}\end{aligned} \tag{2.6.13}$$

Eq-2.6.13 is applied to each ring in the fuel element depicted in Figure-23. Each ring is characterized by the subscripts "i" and "j" representing the radial and axial positions in the pin, respectively. Note that M_f and M_c are the number of radial nodes within the fuel and clad regions, respectively.

Since the radial boundary conditions needed to determine the integration constants apply to the radial stress component as well as to the displacement, Eq-2.6.13 is substituted into Eq-2.6.8 which leads to an equation for $\sigma_r(r)$ as a function of C_{1i}, C_{2i}, the strain components $\left(\alpha(T - T_0)\right)_i$, $(\epsilon^s)_i$, $(\epsilon_r^c)_i$, and $(\epsilon_\theta^c)_i$, the zone boundaries r_{ai} and the axial strain ϵ_z.

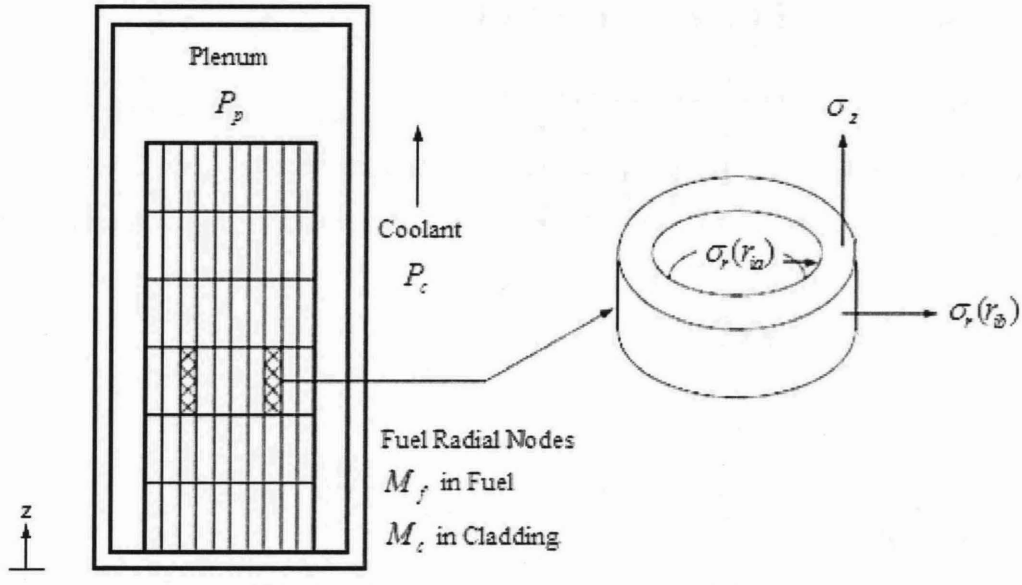


Figure-23: Subdivision of the fuel element into radial and axial nodes [2]

The number of axial zones and radial zones are chosen to find an acceptable-balance between computing time and accuracy. The original LIFE code divided the fuel into three radial zones and represented the entire cladding cross-section into one radial zone. In the FEAST code it is recommended that the fuel be divided into six radial nodes and the cladding in four radial nodes. Note that increasing the radial nodes in the cladding region does not result in any further gain in accuracy as shown in Figure-24. A finer mesh pattern of the fuel region may increase the accuracy somewhat; however, it seriously increases the computational time and may result in a code more susceptible to numerical instabilities, as the solution method used in this algorithm is explicit.

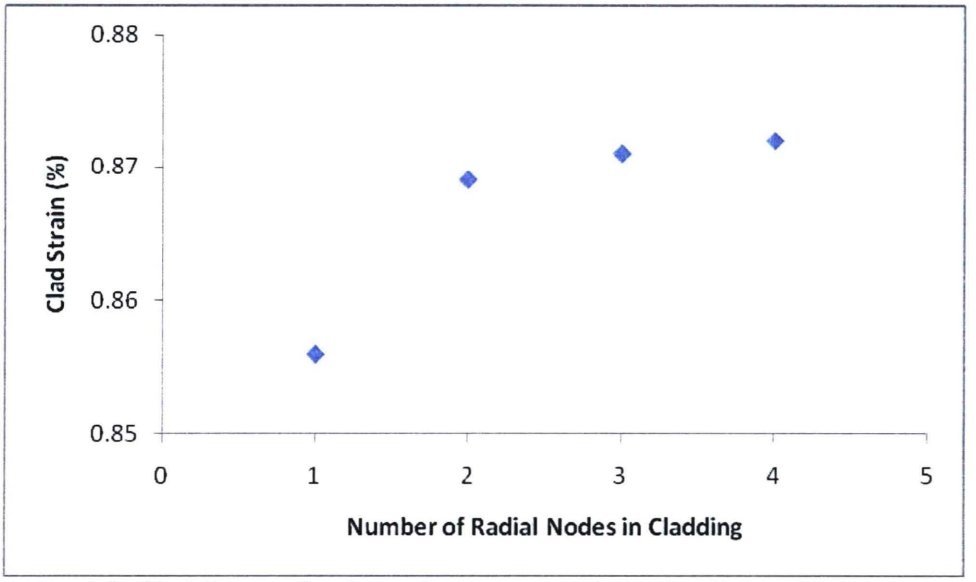


Figure-24: Cladding strain dependency on number of radial nodes at 12 at %

2.6.5. Boundary Conditions

1- $r = 0 \quad \Rightarrow \quad u = 0$ (2.6.14)

2- To ensure continuity of stress and displacement at the radial zone boundaries (ai: inner boundary of node-i; bi: outer boundary of node-i) within the fuel, we have

$\sigma_r(r_{b,i-1}) = \sigma_r(r_{ai})$

$u(r_{b,i-1}) = u(r_{ai}) \qquad 1 < i < M_f$ (2.6.15)

3- The condition at the fuel-cladding interface depends on whether the gap is open or closed. For an open gap;

$\sigma_r(R_f) = -P_p$ (2.6.16)

If the gap is closed the condition becomes,

$\sigma_r(R_f) = -P_{fc}$ (2.6.17)

where P_p and P_{fc} are plenum pressure (Pa) and fuel-cladding interfacial pressure (Pa), respectively.

4- The continuity conditions within the cladding are expressed as

$\sigma_r(r_{i-1,b}) = \sigma_r(r_{ia})$

$$u(r_{i-1,b}) = u(r_{ia}) \qquad 1 < i < M_c \tag{2.6.18}$$

5- At the outer surface of the cladding

$$\sigma_r(R_f + t_c) = -P_c \tag{2.6.19}$$

where P_c is the coolant pressure (Pa) and t_c is the cladding thickness (m).

Solution of the fuel pin radial displacement:

The algebraic equations for each boundary condition ca be written in the following form:

$$a_{1,1}C_{1,1} + a_{1,2}C_{2,1} + a_{1,3}C_{1,2} + a_{1,4}C_{2,2} + a_{1,5}C_{1,3} + a_{1,6}C_{2,3} \cdots = b_1 \tag{2.6.20}$$

$C_{1,i}$ and $C_{2,i}$ are the unknowns in radial displacement equation (Eq-2.6.13) for the radial node-i. The algebraic equations can ben inserted into 'Ax = b' form. 'A' is a 2n×2n matrix and 'b' is a vector, representing the right hand side of Eq-2.6.20. 'x' is the unknown vector. Gauss-Jordan algorithm [29] was adopted to find the 'x' vector. Note that solution of the fuel slug and cladding radial displacement equations are performed, separately. The interfacial pressure and axial frictional force between the fuel and clad provide the coupling.

Unknowns:

Since the boundary conditions were used to determine the integration constants C_{1i} and C_{2i} in each radial zone, the displacement distribution u(r) is now a function of:

1. The strain components $\left(\alpha(T - T_0)\right)_i$, $(\epsilon^s)_i$, $(\epsilon_r^c)_i$, and $(\epsilon_\theta^c)_i$ in each ring,
2. The axial strainϵ_z, which may take on different values in the fuel and in the cladding,
3. The plenum pressure P_p and if the fuel-cladding gap is closed, the interfacial pressureP_{fc}.

At this point the interfacial pressure between fuel and cladding, and the axial strains of fuel and cladding are unknown.

2.6.6. Calculation of the Interfacial Pressure

If the fuel-cladding gap is closed, the incremental change of the fuel outer surface radial displacement within a unit time step should be equal to the change of cladding inner surface

radial displacement in the same time step. Thus, the fuel and clad have to move together. The following relation is applied to find the interfacial pressure:

$$\delta u_{R_f} = \delta u_{R_c} \tag{2.6.21}$$

If the fuel-cladding gap is open, the clad is pressurized solely by the plenum pressure. According to the perfect gas equation, the plenum pressure is given as follows:

$$P_p = \frac{nRT_{av}}{V_{pl} + \sum_{j=1}^{axn} V_{void}(j)} \tag{2.6.22}$$

$$T_{av} = \frac{V_{pl} + \sum_{j=1}^{axn} V_{void}(j)}{\frac{V_{pl}}{T_{pl}} + \sum_{j=1}^{axn} \frac{V_{void}(j)}{T_{void}(j)}} \tag{2.6.23}$$

P_p: Plenum Pressure (Pa)

n: # of moles of gas

R: Gas Constant (8.314 J/mol/K)

T_{av}: Average Temperature (K)

V_{pl}: Plenum Volume (m^3)

$V_{void}(j)$: Radially averaged open porosity in axial node-j. It does not include sodium infiltrated porosity (m^3)

$T_{void}(j)$: Radially averaged temperature of the open porosity in axial node-j (K)

T_{pl}: Plenum temperature (K)

2.6.7. Axial Force Balance

Axial forces acting on the fuel slug between an axial zone "j" and the upper surface of the fuel consist of an average axial stress, the plenum pressure, weight (W) and the sum of the friction

forces acting vertically on the outer surface of the fuel (F). These forces are positive if they restrict axial growth of the fuel and are zero if the fuel cladding gap is open.

Fuel:

$$-2\pi \int_0^{R_f} \sigma_z(r) r dr = \pi R_f^2 P_p + \sum_{k=j}^{N} F_k + \sum_{k=j}^{N} W_{fk} \tag{2.6.24}$$

Clad:

$$-2\pi \int_{R_{ci}}^{R_{ci}+t_c} \sigma_z(r) r dr = \pi \left(R_{ci} + t_c\right)^2 P_p - \pi R_{ci}^2 P_p - \sum_{k=j}^{N} F_k - \sum_{k=j}^{N} W_{fk} \tag{2.6.25}$$

Note that the axial strain of metal fuel remains pretty much constant after the fuel and the clad make contact [19], [21]. Before fuel and clad axially restrained, Eq-2.6.24 and Eq.2.6.25 are used to calculate the fuel and clad axial strain, respectively, by setting the frictional force to zero. After the fuel touches the clad, the fuel and clad locked to each other. The the following condition is applied:

$$\delta\epsilon_f = \delta\epsilon_c \tag{2.6.26}$$

Therefore, the unknowns, the axial fuel and clad strains and the frictional force exerted on the clad, are found by solving Eq-2.6.24 and Eq-2.6.25 and Eq-2.6.26.

During the transient scenarios, metal fuel surface liquifaction may occur due to the eutectic formation (see section-2.5). In this situation, the friction force is set to zero; hence the fuel is allowed to expand axially; while it may be radially constrained by the cladding.

2.6.8. Creep and Plasticity

The permanent strains labeled ε_i^c $(i = r, \theta, or\ z)$ in the equations are the sum of the creep and plastic strains.

$$\epsilon_i^c = \epsilon_i^{creep} + \epsilon_i^{plastic} \tag{2.6.27}$$

Creep and plastic deformations occur at constant volume [2]; so the radial, azimuthal and axial components of $\mathcal{E}_c$ are related by the following equation:

$$\epsilon_r^c + \epsilon_\theta^c + \epsilon_z^c = 0 \tag{2.6.28}$$

Formulation of the permanent strains is based on the von Mises assumption that creep and plastic deformations occur only when the stress state deviates from pure hydrostatic tension or compression. This assumption leads to the stress-strain relations known as the Prandtl-Reuss flow laws or the Soderberg equations:

$$\Delta\varepsilon_r^c = \left(\frac{\varepsilon_{eq}}{\sigma_{eq}}\right)\left[\sigma_r - \frac{1}{2}(\sigma_\theta + \sigma_z)\right] \tag{2.6.29}$$

$$\Delta\varepsilon_\theta^c = \left(\frac{\varepsilon_{eq}}{\sigma_{eq}}\right)\left[\sigma_\theta - \frac{1}{2}(\sigma_r + \sigma_z)\right] \tag{2.6.30}$$

$$\Delta\varepsilon_z^c = \left(\frac{\varepsilon_{eq}}{\sigma_{eq}}\right)\left[\sigma_z - \frac{1}{2}(\sigma_r + \sigma_\theta)\right] \tag{2.6.31}$$

The equivalent stress for the porous fuel is given in Ref. [19] as follows:

$$\sigma_{eq} = \left[\frac{1}{2}((\sigma_r - \sigma_\theta)^2 + (\sigma_\theta - \sigma_z)^2 + (\sigma_z - \sigma_r)^2) + 3\alpha_c(\sigma_r + \sigma_\theta + \sigma_z + 3P_p)^2\right]^{0.5} \tag{2.6.32}$$

$(\sigma_r + \sigma_\theta + \sigma_z + 3P_p)$ is the net effective hydrostatic stress applied to the open pores. Note that the gas plenum pressure is equal to the internal pressure of the open pores. α_c is the open pore compressibility factor given as follows [19]:

$$\alpha_c = \begin{cases} 0.0 & \varepsilon_{sw}^{opn} = 0.0 \\ \frac{1}{6}\left(\frac{\varepsilon_{sw}^{opn}}{0.1}\right)^{1.5} & 0 < \varepsilon_{sw}^{opn} < 0.1 \\ \frac{1}{6} & 0.1 < \varepsilon_{sw}^{opn} \end{cases} \tag{2.6.33}$$

Note that α_c equals zero for the cladding region.

The equivalent creep strain rate for the fuel is given as follows [52]:

$$\dot{\varepsilon}_{eq} = \begin{cases} T < 923.15\ \text{K} & (5\times10^3\sigma_{eq} + 6\times\sigma_{eq}^{4.5})\times\exp(-26170/T) \\ T \geq 923.15\ \text{K} & (0.08\times\sigma_{eq}^3 \times \exp(\text{-}14350/\text{T}) \end{cases} \text{ (1/sec)} \tag{2.6.34}$$

T: Fuel Temperature (K)

σ_{eq}: Equivalent Stress (MPa)

The plastic behavior of the fuel is modeled with the "perfectly plastic" approach. If the fuel exceeds the yield stress (Appendix-A), the strain rate increases so much that the fuel stays at the yield stress level. Note that it is unlikely for the fuel to enter and stay in this region during the steady state operation because fuel creep is very effective in relaxing the stresses.

The thermal and irradiation creep equations which are used for the HT9 cladding material in FEAST are given in Appendix-A.

2.6.9. Swelling

The fuel swelling strain (ϵ^s) is given by

$$\varepsilon^s = \frac{1}{3}\left[\left(\frac{\Delta V}{V}\right)_{\substack{Solid \\ FP}} + \left(\frac{\Delta V}{V}\right)_{\substack{Closed \\ Bubble}} + \left(\frac{\Delta V}{V}\right)_{\substack{Open \\ Porosity}} - \left(\frac{\Delta V}{V}\right)_{\substack{Hot \\ Pressing}}\right] \tag{2.6.35}$$

Fuel swelling is isotropic within the fuel. Hence, each direction shares one-third of the total swelling. One-third of the total swelling of fuel is given by Eq-2.6.35. Swelling due to solid fission product accumulation is taken into account by an empirical relation dependent on burnup (Eq-2.2.37). The gaseous fission product swelling term is related to the size and concentration of the fission-gas bubbles calculated by the fission gas release and swelling model together with open porosity.

The hot-pressing contribution to fuel swelling is negative inasmuch as porosity is removed by this process as a result of fuel clad mechanical interaction. When the initial gap space between the fuel and the cladding is filled with the swollen fuel slug, further gas swelling is restrained by the cladding. The volume of the existing open pores decreases so that further buildup of the fission products is accommodated. Fuel Clad Mechanical Interaction remains at a low level as long as enough open porosity is available. The mechanism is assumed to be creep-dependent as given by Eq-2.6.36.

$$\Delta\varepsilon^{opn-} = 9\alpha_c\left(\sigma_r + \sigma_\theta + \sigma_z + 3P_p\right)\left(\frac{\Delta\varepsilon_{eq}}{\sigma_{eq}}\right) \tag{2.6.36}$$

The compressibility factor given in Equation-2.6.33 rapidly drops when the open pore concentration is below 5 %.

In the cladding the swelling strain is due solely to void formation.

$$\varepsilon_s^{clad} = \frac{1}{3}\left(\frac{\Delta V}{V}\right)_{\substack{Void \\ Swelling}} \tag{2.6.37}$$

However, swelling is not observed for HT9 cladding before a high fast-neutron damage is reached (100 dpa at 400 ^{0}C). For EBR-II conditions the corresponding burnup value is of the order of 20 at %, which is beyond the scope of the analysis given in this thesis.

2.6.10. Anisotropic Fuel Slug Deformation

The empirical approach given in Ref. [19] is adopted to model anisotropic deformation of the metal fuel slug in FEAST-METAL.

After the fuel slug comes into contact with the cladding, further axial growth is restrained. However, slug deformation prior to slug-cladding contact is anisotropic. This is due to the formation of large radial cracks in the brittle ternary fuel. Tearing at the grain or phase boundaries in the peripheral region of the slug also occurs due to anisotropic irradiation growth of α-U crystals. The latter effect is more important in U-Zr fuels, while the former dominates in U-Pu-Zr fuels. To incorporate these effects, the effective fuel slug radius is defined:

$$r^{eff} = r_o + dr_{slug} + dr_{crack} = r_{slug} + dr_{crack} \tag{2.6.38}$$

r_o is the as-fabricated slug radius and dr_{slug} is the radial strain increment due to thermal expansion, elasticity, creep/plasticity, closed bubble, open pore and solid fission product swelling. The increment dr_{crack} is due to the cracks and also the tearing. After the slug comes into contact with the cladding, the swelling of the fuel is accommodated by the closure of the tears and cracks. This process prevents the FCMI stress from growing. During this stage of contact, the area of the contact interface continues to increase without significant FCMI stress, while the slug sticks to the cladding.

According to this description, the fuel/cladding contact condition can be divided into three time intervals:

(I) $r^{eff} < r_i$: no restraint by the cladding (no contact)
(II) $r^{slug} < r^i = r^{eff}$: axial restraint by the cladding, no radial restraint.
(III) $r^i = r^{slug}$: both axial and radial restraint by cladding

Where r_i is the inner radius of the cladding.

$$dr^{crack} = f^{crack} \times r_o^{gap} \tag{2.6.39}$$

where r_o^{gap} is the initial gap width between the fuel and cladding. The anisotropy factor, f^{crack}, is given in Figure-25, which is calculated based on references [33], [53] and [54] as a function of Plutonium content and $\frac{q}{D_o}$ (average linear power divided by the diameter of the slug). Note that the value of f^{crack} 'saturates' above 19 wt % Plutonium and 790 W/cm² $\frac{q}{D_o}$ value.

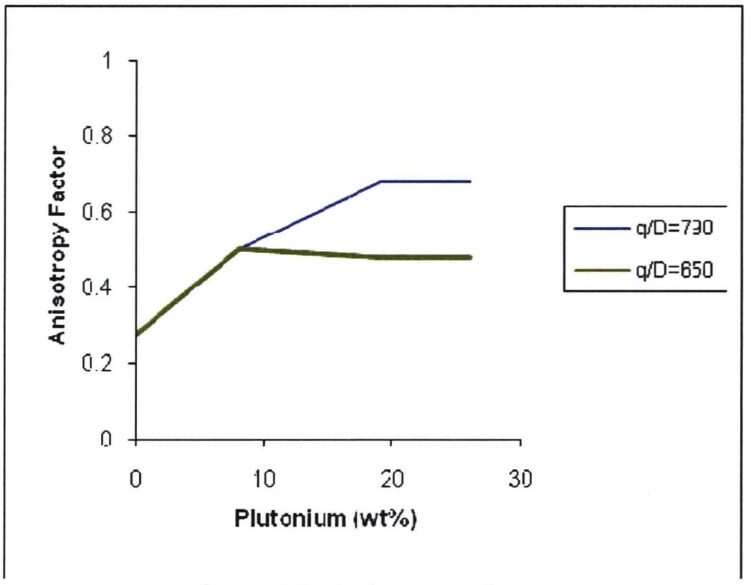


Figure-25: Anisotropy factor

Table-15 shows several experimental data for axial fuel elongation. FEAST predictions are in reasonable agreement with the experimental data.

Table-15: Slug axial elongation

Fuel Composition	Fuel Smear Density (%)	$\frac{q}{D_o}$ (W/cm²)	Axial Elongation (%)	
			Experimental Data	FEAST Predictions
U-10Zr	76 [54]	790	6.2	6.0
U-19Pu-10Zr	76 [54]		1.5	1.8
U-10Zr	72 [53]	830	8.5	7.2
U-8Pu-10Zr	72 [53]		6.5	5.7
U-19Pu-10Zr	72 [53]		2.5	2.3
U-10Zr	75 [33]	650	8	9.0
U-8Pu-10Zr	75 [33]		5.8	6.1
U-19Pu-10Zr	75 [33]		6.5	6.6

2.6.11. Verification of the Mechanical Analysis Module against the Analytical Solution for the Radial Distribution of Thermal Stresses

To verify the accuracy of the numerical algorithm that solves Eq-2.6.11, the FEAST predictions were compared to the close analytical solution for a very simple case. Consider an infinitely long cylinder fuel pin of radius R operating at linear power, q'. Creep and swelling strains are assumed to be zero. Assuming the material properties such as thermal conductivity, k, thermal expansion coefficient, α, Young's Modulus, E, and Poisson's ratio, ν, are constant as given in Table-16, the radial, hoop and axial stresses become [2]:

$$\sigma_r = -\frac{\alpha E q'}{16\pi(1-\nu)k}\left[1-\left(\frac{r}{R}\right)^2\right] \tag{2.6.40}$$

$$\sigma_\theta = -\frac{\alpha E q'}{16\pi(1-\nu)k}\left[1-3\left(\frac{r}{R}\right)^2\right] \tag{2.6.41}$$

$$\sigma_z = -\frac{\alpha E}{8\pi(1-\nu)}\frac{q'}{k}\left[1-2\left(\frac{r}{R}\right)^2\right] \tag{2.6.42}$$

Table-16: Approximate metal fuel properties

Fuel Properties	Value
$\alpha(^{o}C^{-1})$	2E-05
E (GPa)	150
ν	0.3
k (W/mK)	25
q'(kW/m)	40

Figure-26, 27 and 28 show the comparison of the FEAST results and the analytical solution of the radial variation of thermal stresses. The agreement is very good.

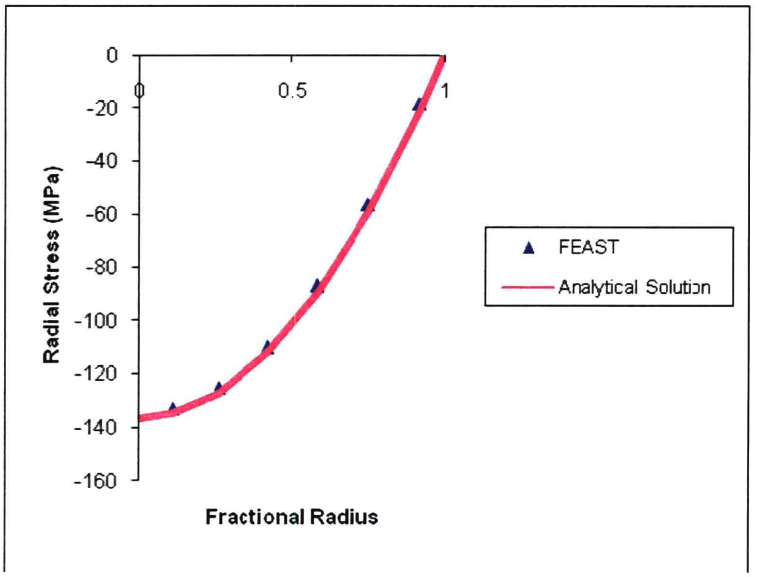


Figure-26: Radial stress distribution in radial direction

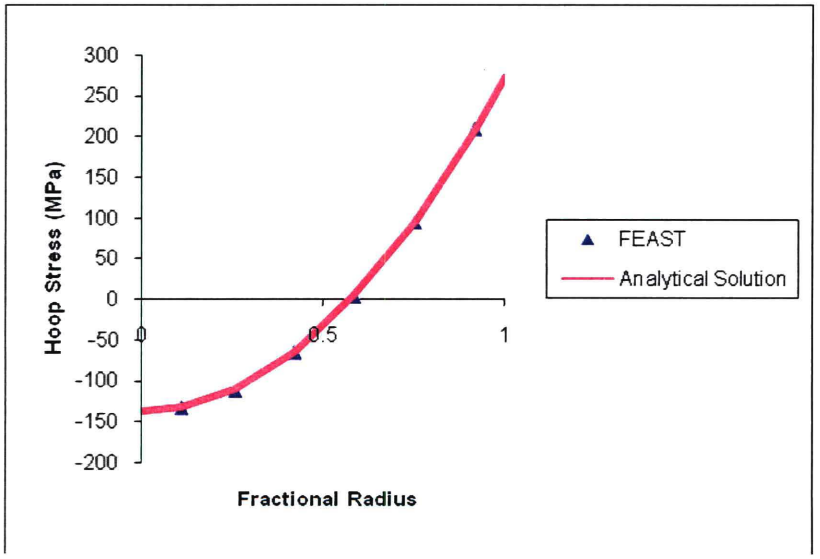


Figure-27: Hoop stress radial distribution

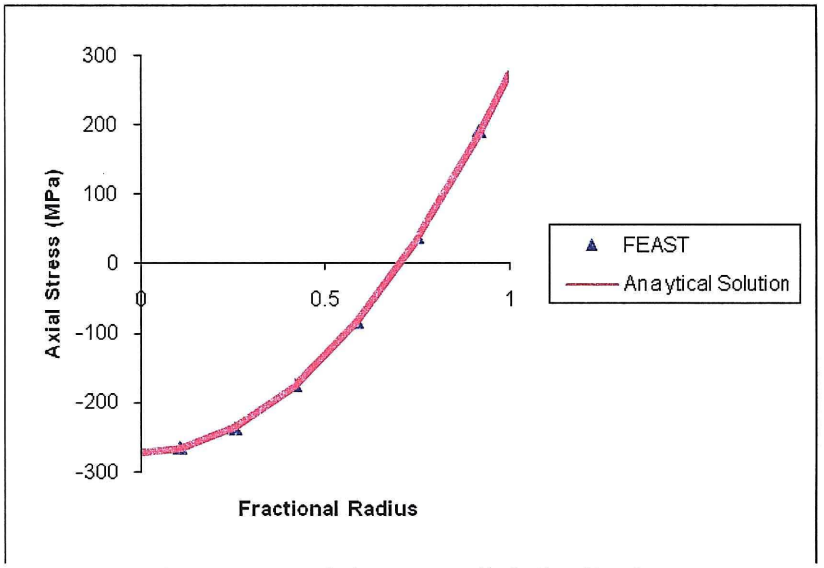


Figure-28: Axial stress radial distribution

2.7. Transient Creep Fracture Modeling

During transients, cladding temperatures may rise to levels where the thermal creep rate becomes excessive. Hence, the main fuel pin failure mechanism becomes the thermal creeping of the clad. Figure-29 shows a typical ferritic martensitic stainless steel creep-fracture map [55]. Typically, transient scenarios for the Sodium Fast Reactors lie in the intergranular creep fracture regime.

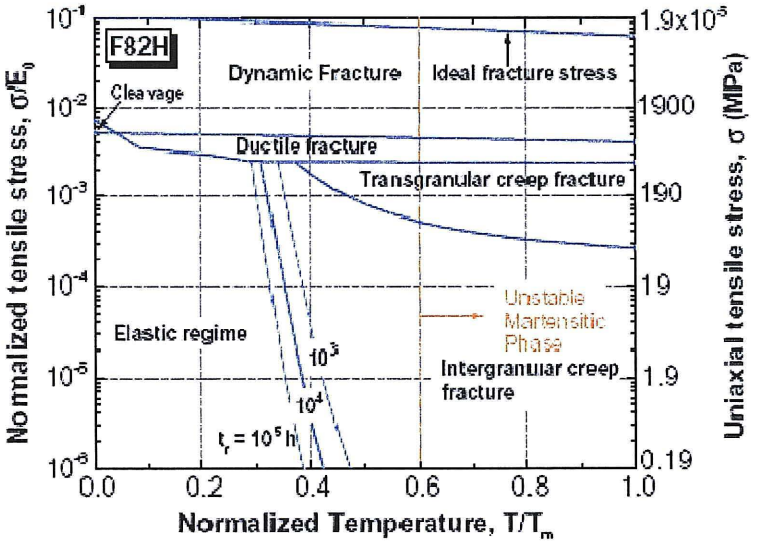


Figure-29: Creep fracture map of a typical ferritic-martensitic stainless steel [55]

The Cumulative Damage Fraction (CDF) model has widely been used to predict creep-rupture of the fast reactor cladding. In addition, a physical based model has been introduced in this work. It is the constrained diffusional cavity growth model, which reflects the basic intergranular creep fracture mechanism.

2.7.1. Cumulative Damage Fraction Model

During a transient scenario, the stress and the temperature of the cladding may vary as a function of time. Cumulative damage fraction is an empirical model which predicts the time to rupture by using the constant stress and constant temperature creep-rupture database. The model is given as follows:

$$CDF(t_n) = \sum_{i=1}^{n} \frac{\Delta t}{t_r(\sigma_i, T_i)} \tag{2.7.1}$$

$CDF(t_n)$: Cumulative damage fraction at time, t_n

Δt: Magnitude of a time step (sec)

$t_r(\sigma_i, T_i)$: Failure time calculated with the stress and temperature at time step (i) (sec)

n: Number of time steps

If the CDF reaches unity at any time, it is assumed that failure occurs.

2.7.2. Constrained Diffusional Cavity Growth Model

A physics based method describing intergranular creep-fracture could improve the accuracy of the transient simulations in which the temperature and stress cannot be assumed to be constant in time. Intergranular creep fracture can occur by nucleation and growth of grain boundary cavities [56]. Impurity particles present at grain boundaries may nucleate cavities due to lack of cohesion with the lattice. In case of ferritic/martensitic steels, grain boundary carbides are responsible for cavity nucleation [57], [58]. Once nucleated, voids grow by vacancy diffusion and condensation, dislocation pile-up when the applied stress is sufficiently large to overcome the tendency for the void to shrink by surface tension.

The idea of constrained cavity growth is that, if the material surrounding a cavitating facet were rigid, the excess volume of cavities could not be accommodated in the material and cavitation should come to a standstill [59]. This constraint may be relieved by creep of surrounding material. Then, the rate at which cavitation proceeds may be controlled by the creep rate (accommodation control) or, if the material creeps readily, cavitation is controlled by the rate of grain boundary diffusion (diffusion control, or unconstrained limit). The susceptibility of a grain boundary to cavitation depends on its orientation to the applied stress and on the microstructure [56].

The idea was quantified first by Rice [59], who described the cavitating facet as a penny-shaped crack which is embedded in an infinite body of power-law creeping material and is subjected to a remote stress σ_{ij}^{∞} (Figure-30).

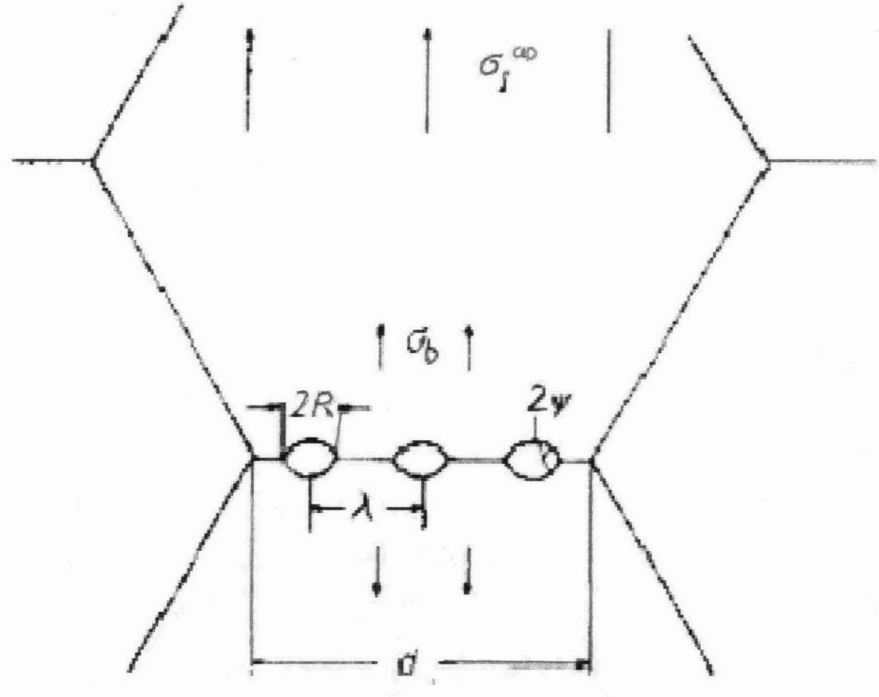


Figure-30: Cavitating polycrystalline [59]

A result of the penny-shaped crack model is an expression for the cavity growth rate which, for multi-axial loading, takes the following form:

$$\frac{da}{dt} = \frac{\sigma_I^{\infty} - (1-w)\sigma_0}{h(\psi)a^2\left[\frac{q(w)kT}{2\Omega\partial D_b} + \frac{q'\sigma_{eq}}{\dot{\varepsilon}_{eq}\lambda^2 d}\right]} \tag{2.7.2}$$

$$q(w) = -2\ln w - (3-w)\times(1-w) \tag{2.7.3}$$

$$h(\psi) = \frac{1}{\sin\psi}\left[\frac{1}{1+\cos\psi} - \frac{\cos\psi}{2}\right] \tag{2.7.4}$$

$$w = \frac{(2a)^2}{\lambda^2}$$

$$\cos\psi = \frac{\gamma_b}{2\gamma_s}$$

$$\sigma_0 = \frac{2\gamma_s \sin\psi}{a}$$

$$q' = \pi^2\left(1+\frac{3}{n}\right)^{0.5}$$

d: grain boundary diameter (m)

σ_I^{∞}: Applied hoop stress (Pa)

σ_{eq}: Equivalent stress (Pa)

σ_0: Sintering stress (Pa)

λ: Uniform spacing (m)

a: Cavity radius (m)

∂: Grain boundary thickness (m)

Ω: Atomic Volume (m^3)

D_b: Grain boundary diffusion coefficient (m^2/s)

n: Dislocation Creep exponent

γ_b: Grain boundary free energy (J/m^2)

γ_s: Free surface energy (J/m^2)

$\dot{\varepsilon}_{eq}$: Equivalent creep strain rate (1/s)

Table-17: Parameters [57]

N	5
Ω (m^3)	1.18E-29
∂D_{bo} (m^3/s)	1.1E-12
Q_b (J/mol)	1.74E+5
γ_s (J/m^2)	2.1
γ_b (J/m^2)	0.85
D (m)	20E-06
λ (m)	7E-06

The first term in the denominator is due to grain boundary diffusion. This term is neglected in the model given in Ref. [58] which is an application to the ferritic/martensitic stainless steel. However, Ref. [58] analyzed a narrow range of stress and temperature conditions, whereas we are seeking a very wide range in our model. As a consequence, this term has not been neglected in the FEAST implementation of the model.

The original model proposes that the coalescence of the neighboring cavities could be used to predict failure time of a material. However, this approach tends to highly overestimate the failure times [56], [57].

No compelling reason exists for this joining mechanism to be delayed until the cavities have coalesced [56]. Rather, as soon as cavity growth becomes accommodation controlled by a sufficient increase of "w", it starts to behave mechanically as a traction-free microcrack. It seems logical that the final joining of microcracks is triggered by the loss of mechanical strength rather than by the metallographic "appearance".

In conclusion, the time to cavity coalescence is irrelevant for the rupture lifetime in the limit of accommodation controlled growth, since the relevant process on the cavitating facet, namely the loss of mechanical strength occurs much earlier, and the coalescing microcracks are barely affected by the ongoing cavity growth.

As a result of the description above, the critical cavity radius has been calculated for HT9 at constant stress and constant temperature (Table-18) by using the available experimental data given in Figure-31 and 32 for HT9 based on Ref. [60] and [61].

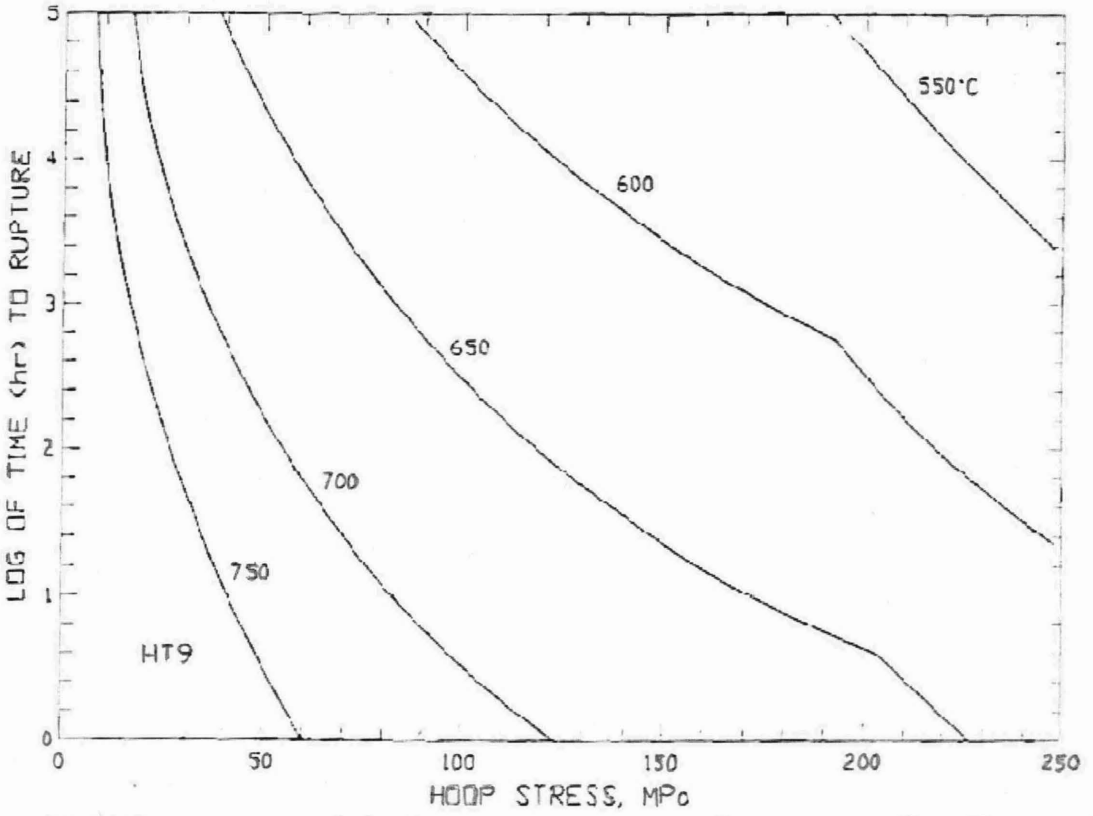


Figure-31: HT9 creep rupture behavior at constant stress and temperature (Low Temperature)

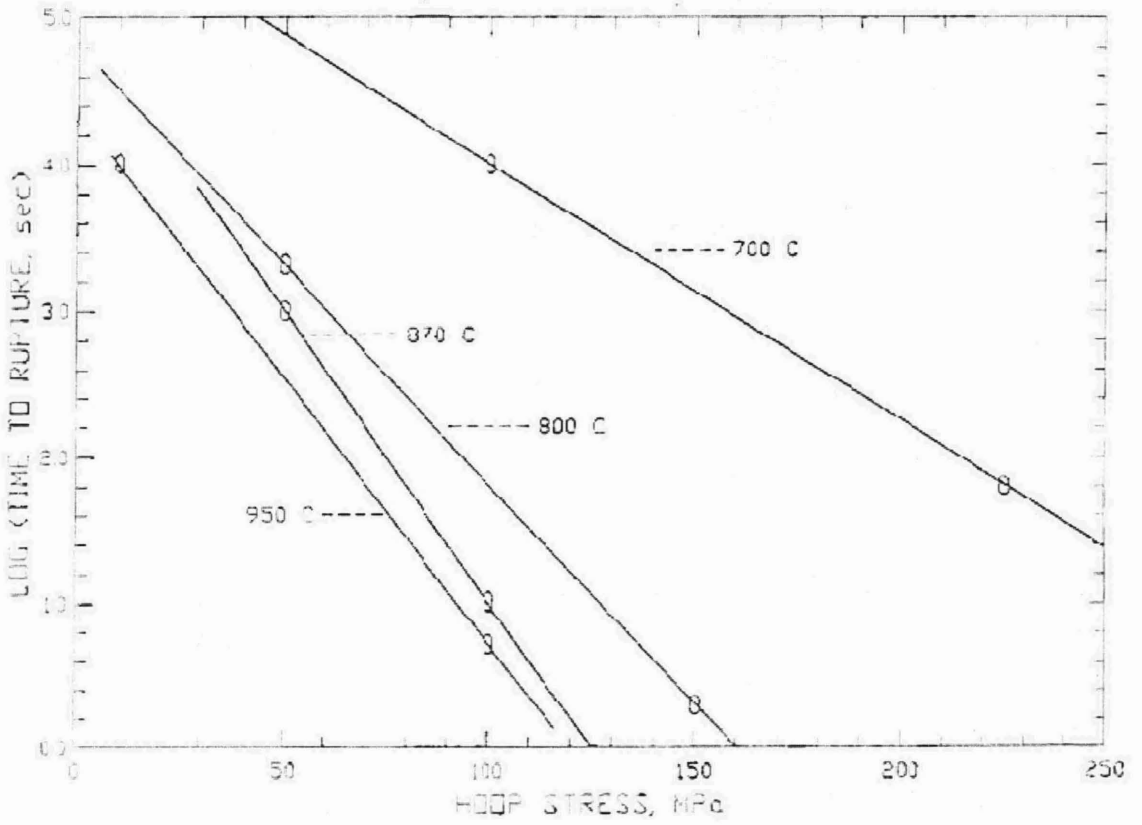


Figure-32: HT9 creep rupture at constant stress and temperature (High Temperature)

Table-18: Critical crack radius (microns) (HT9)

	Temperature (^{0}C)					
Hoop Stress (MPa)	675	700	725	750	800	870
10	33.5	10.89	6.854	4.599	1.299	3.418
25	3.863	2.589	1.923	1.577	0.788	1.753
50	2.756	1.533	1.052	0.677	0.668	0.903
75	1.599	1.083	0.687	0.397	0.397	0.384
100	1.272	0.795	0.456	0.247	0.219	0.155
125	1.001	0.572	0.312	0.166	0.114	0.0
150	0.767	0.417	0.226	0.120	0.051	0.0
175	0.587	0.315	0.170	0.090	0.0	0.0
200	0.458	0.246	0.134	0.070	0.0	0.0

Table-18 is now a look-up table. Cavity growth can be simulated by numerically integrating Eq-2.7.2. When the actual cavity size reaches the critical cavity radius, for the stress and temperature at that time step, it is assumed that fracture occurs.

3. VERIFICATION OF FEAST-METAL

3.1. Steady State

To validate the FEAST-METAL code, its predictions are compared to the irradiation database available from the EBR-II reactor experience, and to the predictions of the ALFUS and LIFE-METAL codes. The EBR-II test assemblies designated as X430 [54], X425 [19], [53], [62], [63] and X447 [37], [45] are used for the validation exercise as sufficient information is available for these assemblies.

Some metal fuel rods are currently being irradiated in the PHENIX reactor in France under the auspices of Japan's CRIEPI. The irradiation history has been reported up to 7.2 at % burnup [64]. These data are also used in the validation of the FEAST-METAL code.

There also exists a Russian report on metal fuels [65]; however, it contains no original irradiation data.

3.1.1. X430 Benchmark

Table-19 shows the fuel composition and geometry for the X430 benchmark. The peak assembly burnup is 11.9 at %. The coolant outlet temperature and peak linear heat rate as functions of burnup (i.e., the irradiation history) are the input required to run FEAST. Figure-33 is the irradiation history of the rod T-654. The thermo-mechanical behavior is predicted by FEAST for this particular rod and for four other high-burnup rods for which a similar irradiation history was assumed.

Table-19: X430 fuel data

Parameter	Value
Fuel Composition	U-19Pu-10Zr
Cladding Material	HT-9
Fuel slug radius (mm)	2.86
Clad inner radius (mm)	3.28
Clad outer radius (mm)	3.68
Fuel Active Length (cm)	34.3
Fuel Smear Density (%)	76.1
Plenum to Fuel Ratio	1.4

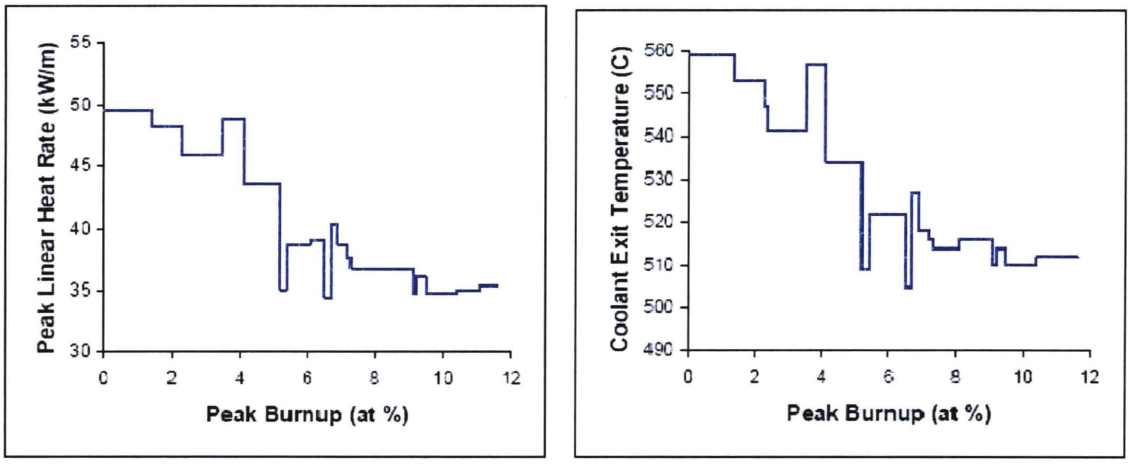


Figure-33: Irradiation history of T-654.

Figure-34 shows the average axial power profile given for EBR-II, and is used for all X430 rods. The fuel pin was divided into seven axial nodes. Furthermore, the fuel slug and cladding material in each axial node were divided into six and three radial nodes, respectively.

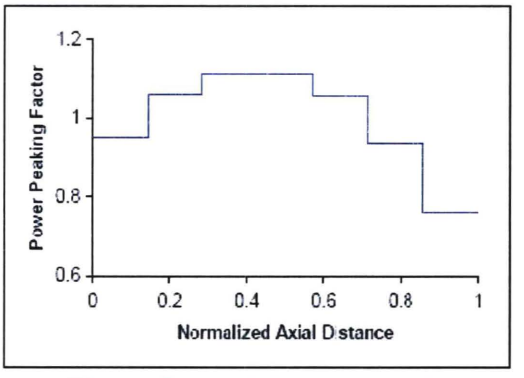


Figure-34: Axial power profile

The following relation between the neutron flux and the volumetric heat generation rate is assumed in order to match the neutron fluence data reported in Ref. [1].

$$\phi = Cq''' \qquad (3.1.1)$$

ϕ = Neutron Flux (n/cm²/s)

C=840000

q''' = Volumetric Heat Generation Rate (W/m³)

In Figure-35 the fission gas release behavior of the T-654 fuel rod is shown, and compared to the reported peak fission gas release at the end of life [54]. The agreement is very satisfactory. Figure-35 also shows generic data for U-19Pu-10Zr at lower burnup from Figure-3.

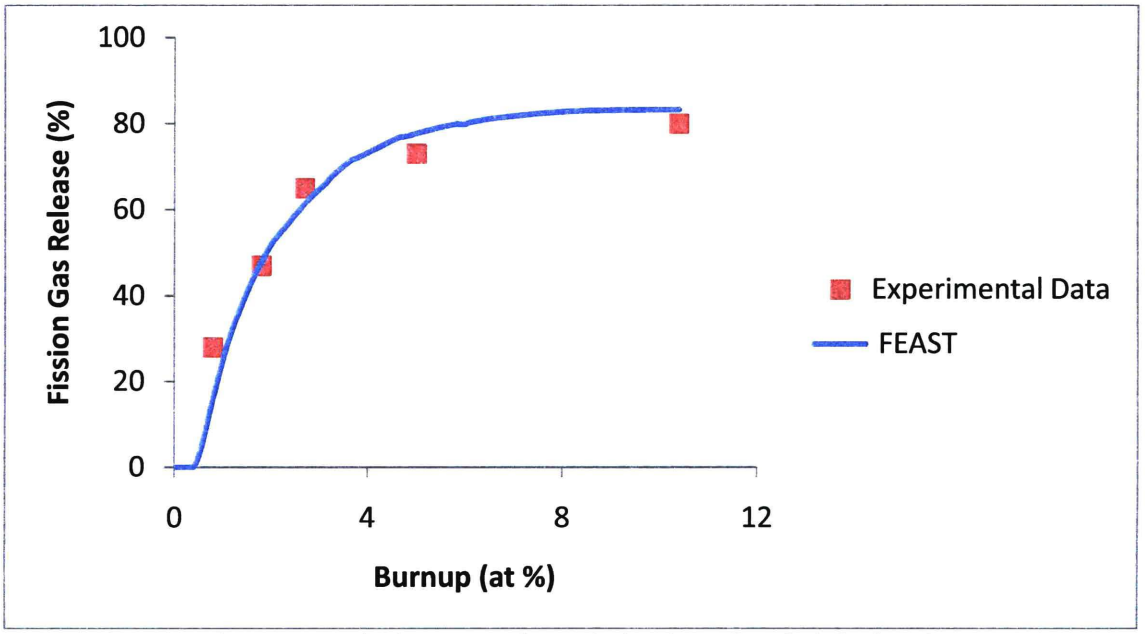


Figure-35: Fission gas release behavior of T-654 fuel rod.

Figure-36 shows the swelling behavior of the T-654 fuel rod. The fuel hot spot (located at 93% of the fuel slug length) touches the clad at ~1 at % burnup (Figure-36(b)). However, the fuel located at 50 % of the fuel slug length, which is cooler, is not radially restrained by the clad until it reaches 3.5 at % (Figure-36(a)). Therefore, temperature has a significant effect on the swelling behavior of the metal fuel, as expected.

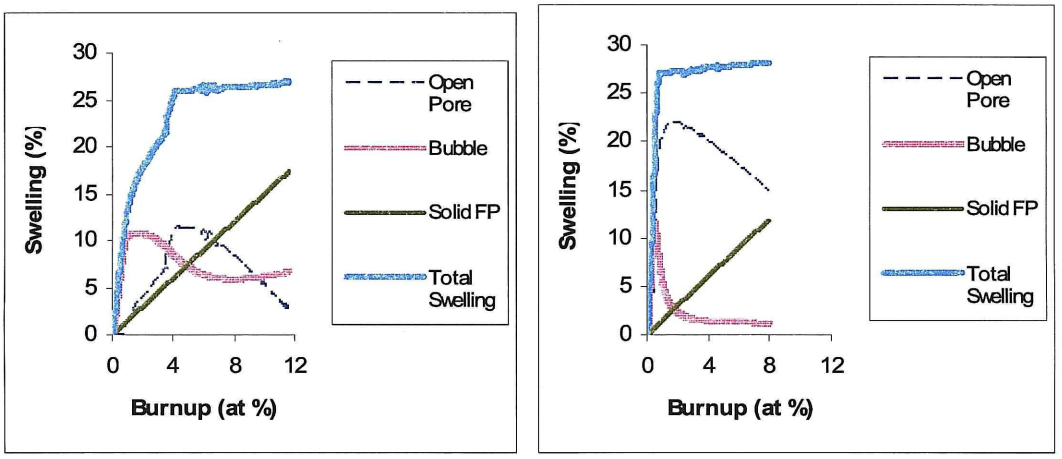


Figure-36: (a) Swelling at 50 %, (b) Swelling at 93 % of the fuel slug length for T-654 fuel rod

The fuel/clad contact pressure starts to increase after the fuel becomes radially restrained. As can be seen in Figure-37, FCMI is practically negligible at the hot spot of the fuel slug, thanks to the very high fuel creep rate at these temperatures. On the other hand, FCMI in the fuel cooler section becomes non-negligible shortly after the fuel becomes radially restrained. This is due to two effects; first, the lower temperature makes the fuel less compliant (i.e., compressing the open pores requires higher stresses); second, the somewhat high linear heat rate generates more solid fission products, which makes the fuel even stiffer.

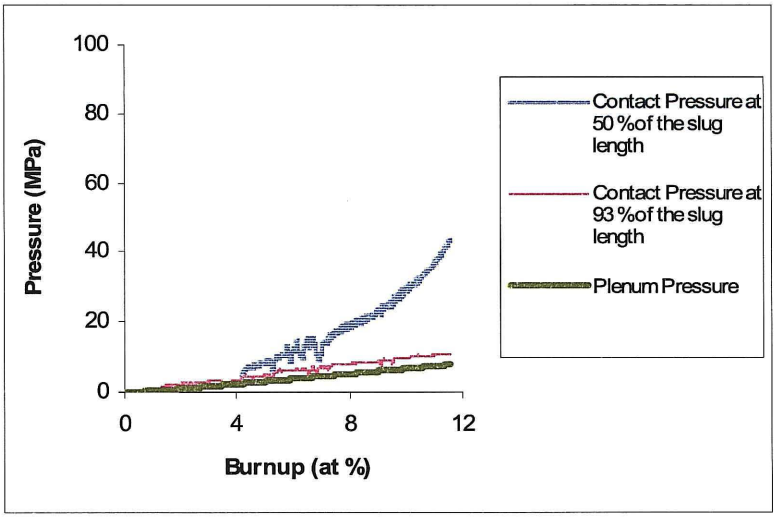


Figure-37: Contact and plenum pressure for T-654 fuel rod

Note that the oscillations in the contact pressure are directly related to the creep properties of the metal fuel. The creep rate of the gamma phase is two orders of magnitude higher than that of the

alpha and beta phases. When the phase boundary moves the compressibility of the fuel changes drastically and oscillations arise.

In parallel with the rise in contact pressure, the peak cladding strain rises as shown in Figure-38(a). Figure-38(b) shows the cladding strain axial distribution at the End of Life. Since irradiation creep dominates within the operating history, the peak cladding strain occurs at the peak power location.

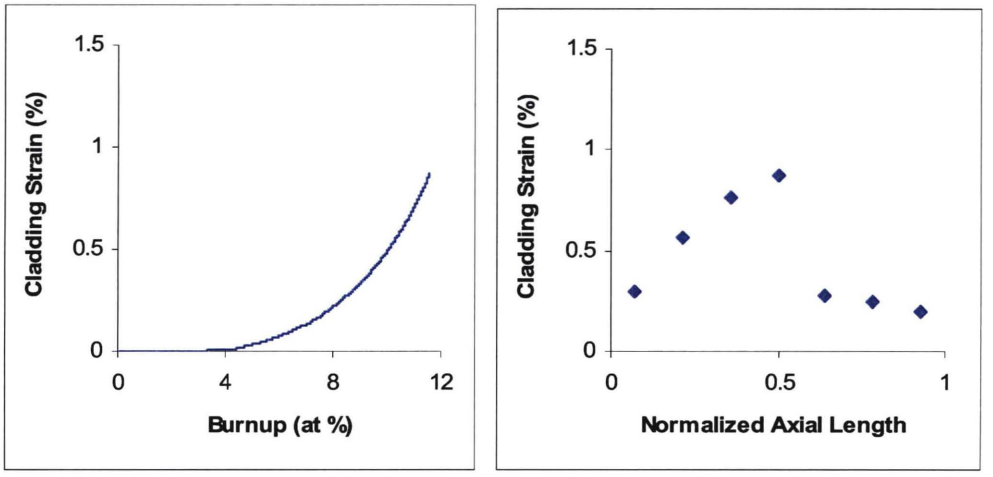


Figure-38: (a): Peak cladding strain for T-654 fuel rod (b): Axial distribution of the cladding strain at EOL

Finally, note that the maximum cladding wastage reported in Ref. [54] is of the order of 20 microns and the FEAST prediction is 29 microns; therefore the agreement is again reasonable.

Comparison of Predicted and Measured Peak Cladding Strain:

Experimental data for peak cladding strain are available for both low- and high-burnup cases.

Table-20 shows the experimental and predicted cladding strain data at low burnup. FEAST appears to underestimate considerably the cladding strain at these conditions. However, the low-burnup experimental data reported here are unusually high and are not consistent with the low-burnup cladding strain values reported in many other sources. A brief discussion of this issue is given next.

Table-20: X430 assembly peak cladding strain at low burnup

Fuel Rod ID	Burnup (at %)	Experimental Data	FEAST Prediction	Relative Error (%)
T-654	7.4	0.28	0.16	-43
T-655	7.2	0.38	0.14	-63
T-659	7.4	0.28	0.17	-39
T-660	7.2	0.41	0.16	-61

The Evidence for low Burnup HT-9 cladding creep behavior:

Figure-39 shows the clad strain of HT9 cladding [20]. The fuel composition is U-10Zr. At 7 at % the cladding strain should not exceed about 0.2 % whereas the experimental values for X430 are well in excess of 0.2 %.

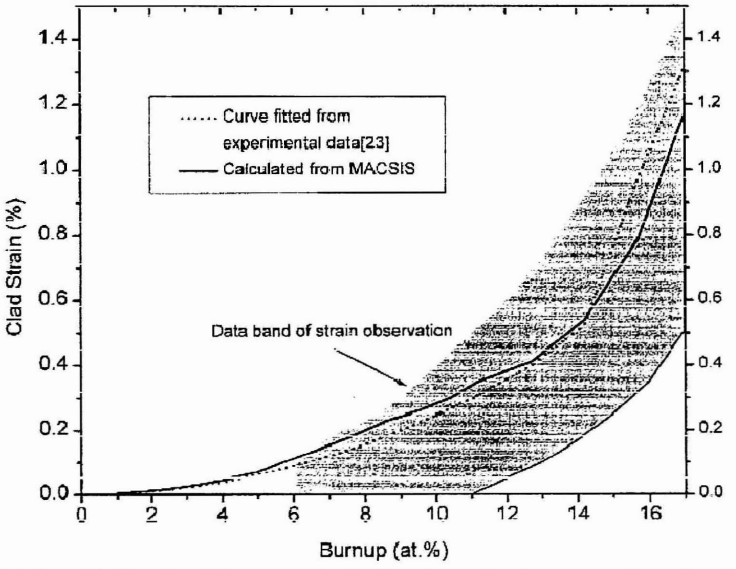


Figure-39: U-10Zr/HT9 cladding strain behavior (fuel smear density is ~75 %) [20]

Figure-40 shows a typical behavior of U-19Pu-10Zr fuel given by Ref. [21]. At 7 at %, the expected cladding strain is virtually zero for HT9 cladding.

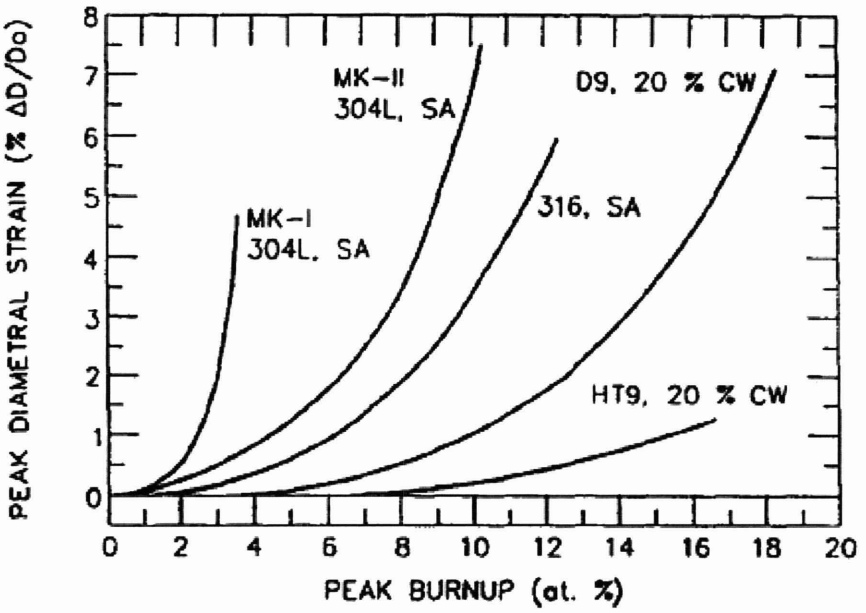


Figure-40: U-19Pu-10Zr/HT9 clad strain data (72 % smear density) [21]

Figure-41 and 42 show other cladding strain data for U-19Pu-10Zr given in Ref. [19]. Cladding strains at 5 at % burnup are relatively low even for 85 % smear density.

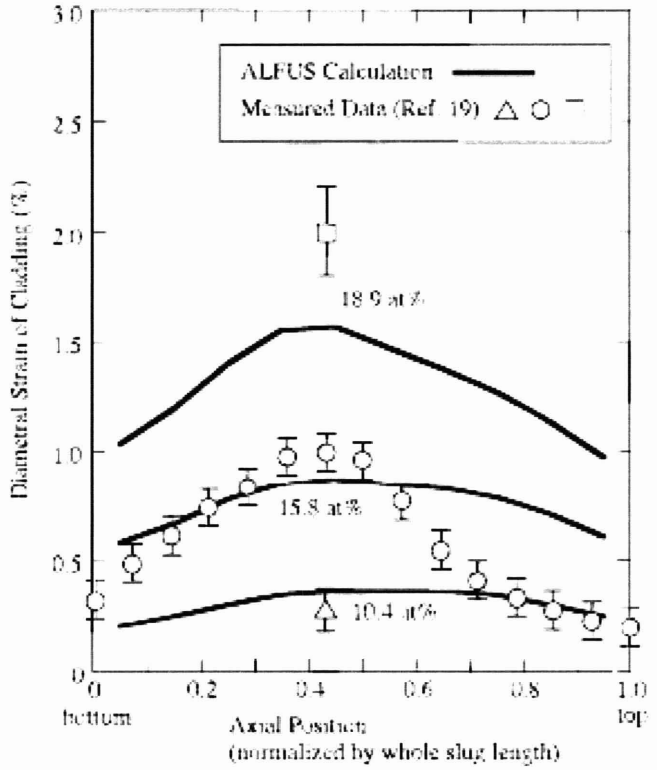


Figure-41: U-19Pu-10Zr/HT9 clad strain data (72 % smear density) [19]

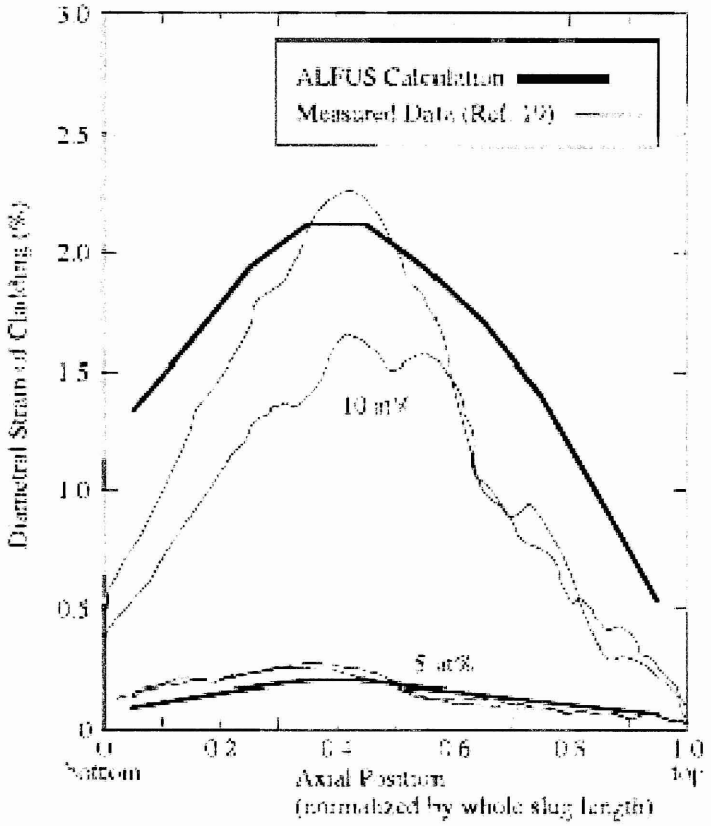


Figure-42: U-19Pu-10Zr/HT9 clad strain data (85 % smear density) [19]

It seems that the clad strains predicted by FEAST for fuel rods at low burnup are consistent with the trends described in most sources in the literature. However, this is clearly an area that warrants further investigation.

On the other hand, the FEAST predictions match reasonably well the cladding strain values at high burnup, as shown in Table-21.

Table-21: X430 assembly peak cladding strain at high burnup

Fuel Rod ID	Burnup (at %)	Experimental Data	FEAST Prediction	Relative Error (%)
T-654	11.6	0.97	0.87	-10.3
T-655	11.8	0.86	0.93	8.1
T-659	11.7	1.17	1.04	-11.1
T-660	11.9	1.03	1.19	15.5

3.1.2. X425 Benchmark

Table-22 shows the X425 fuel data. The irradiation history for X425 assembly unfortunately is not available in the open literature. Therefore, it was approximated by the X430 irradiation history as follows. The peak coolant exit history of the X425 assembly is assumed to be identical to that of the X430 assembly, as they were irradiated at same time and their locations in the core were very close to each other. Then, assuming a constant mass flow rate and knowing the initial peak linear heat rate given in Table-22, the power history given in Figure-43 was generated.

Table-22: X425 fuel data

Parameter	Value
Fuel Composition	U-19-Pu-10Zr
Clad Material	HT-9
Fuel slug radius (mm)	2.16
Clad inner radius (mm)	2.54
Clad outer radius (mm)	2.92
Fuel Smear Density (%)	72.4
Fuel Active Length (cm)	34.3
Plenum to Fuel Ratio	1.0
Peak Linear Heat Rate (kW/m)	40
Peak Clad Temperature (^{o}C)	590

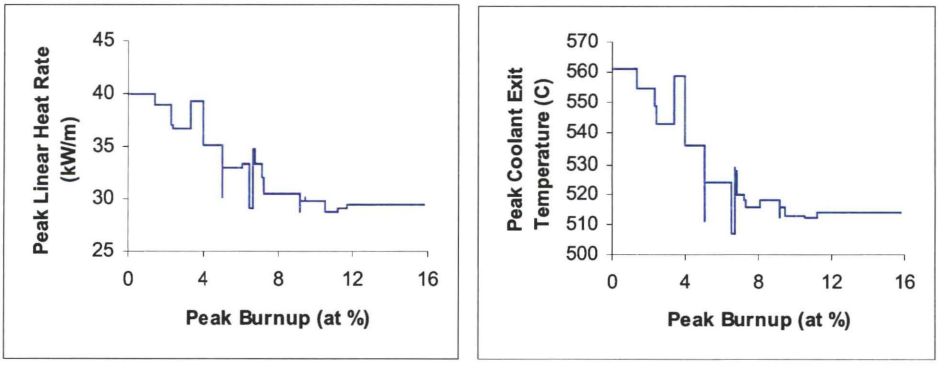


Figure-43: Approximate irradiation history of X425 assembly

The axial power profile given in Figure-34 has been adopted for X425 as well. The fuel pin was divided into seven axial nodes. Furthermore, the fuel slug and cladding material in each axial node were divided into six and three radial nodes, respectively. The fast flux is again calculated by means of Eq-3.1.1.

In Figure-44, the fission gas release for the X425 peak fuel rod is shown. Comparing it with Ref. [53] which states that the fission gas release for the peak fuel rod of this assembly is 80 % at the end of life, the agreement is excellent. Figure-44 also shows generic data for U-19Pu-10Zr at lower burnup from Figure-3.

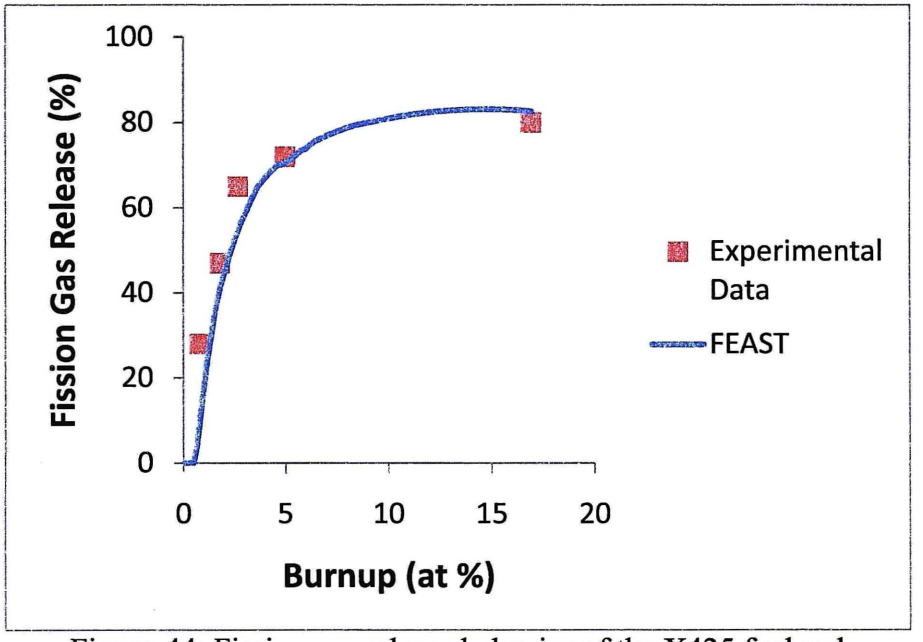


Figure-44: Fission gas release behavior of the X425 fuel rod

Figure-45 shows the swelling behavior of the X425 peak fuel rod. The fuel touches the clad at the hot spot at ~2 at % burnup (Figure-45 (b)). Due to X425 lower linear heat rate compared to X430, the fuel temperature and thus the swelling rates are somewhat lower. The fuel located at 36 % of the fuel slug length is not radially restrained by the clad at up to 5 at % (Figure-45(a)).

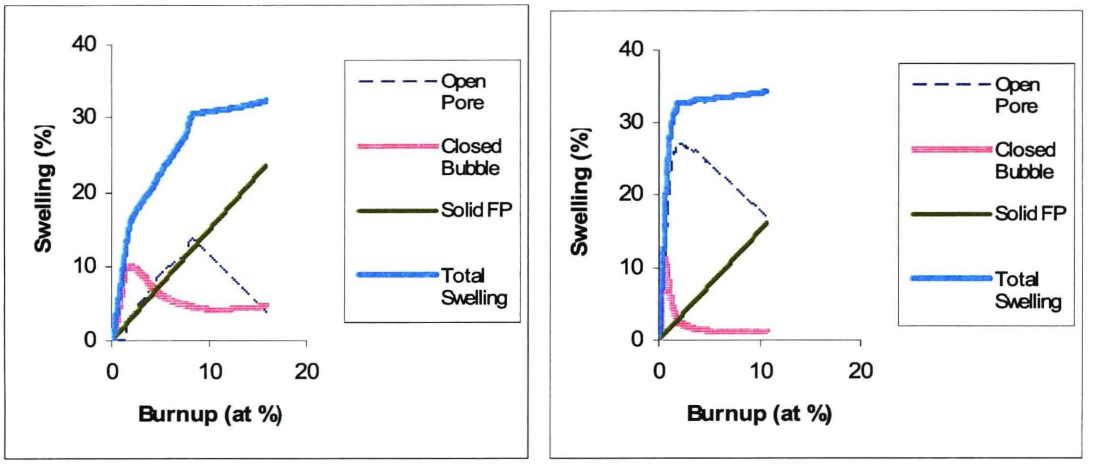


Figure-45: (a) Swelling at 36 %, (b) Swelling at 93 % of the fuel slug length for X425 peak fuel rod

Here too, the contact pressure starts to increase after the fuel becomes radially restrained. As can be seen in Figure-46, FCMI is negligible in the hot section of the fuel slug, and more significant in the cooler section of the fuel slug.

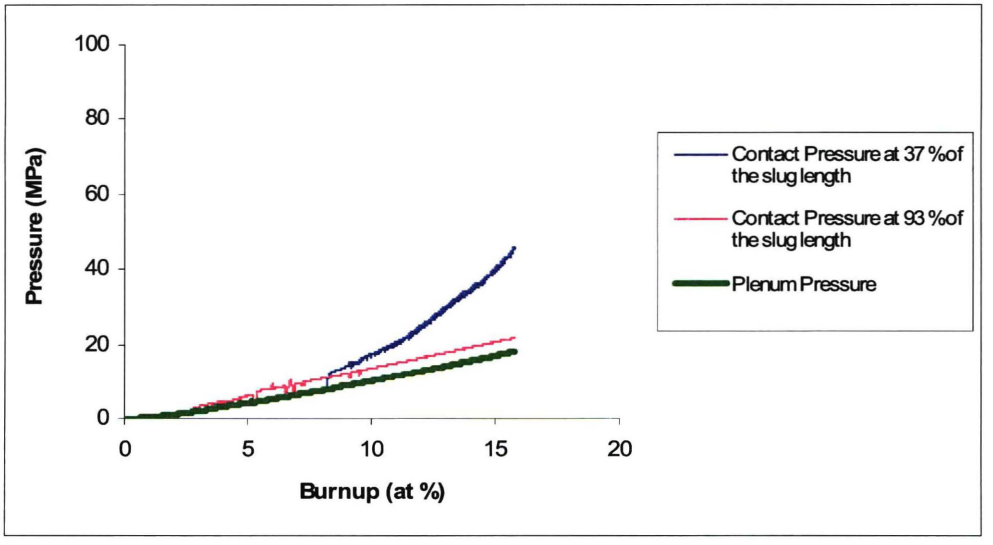


Figure-46: Contact and plenum pressure for X425 assembly

The cladding strain increases rapidly after 10 at % burnup as given in Figure-47.

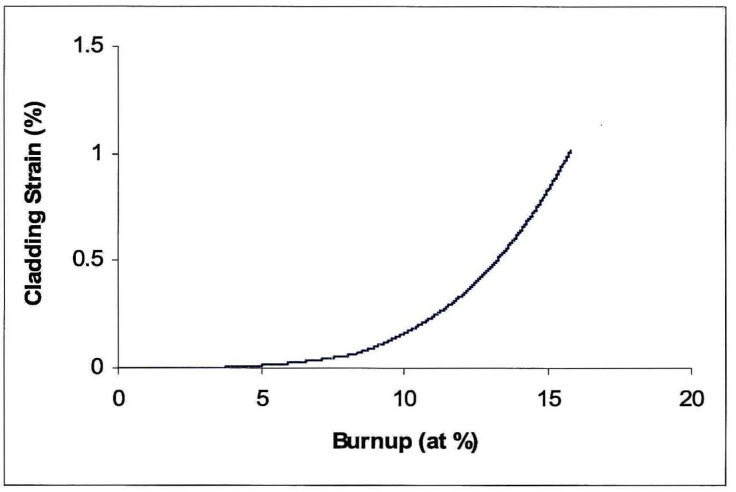


Figure-47: Peak cladding strain for X425 assembly

The cladding strain profile at 15.8 at % peak burnup predicted by FEAST is compared to the ALFUS predictions and the experimental data in Figure-48. Both codes give reasonable results, with FEAST predicting the correct bottom-peaked profile and a closer peak clad strain.

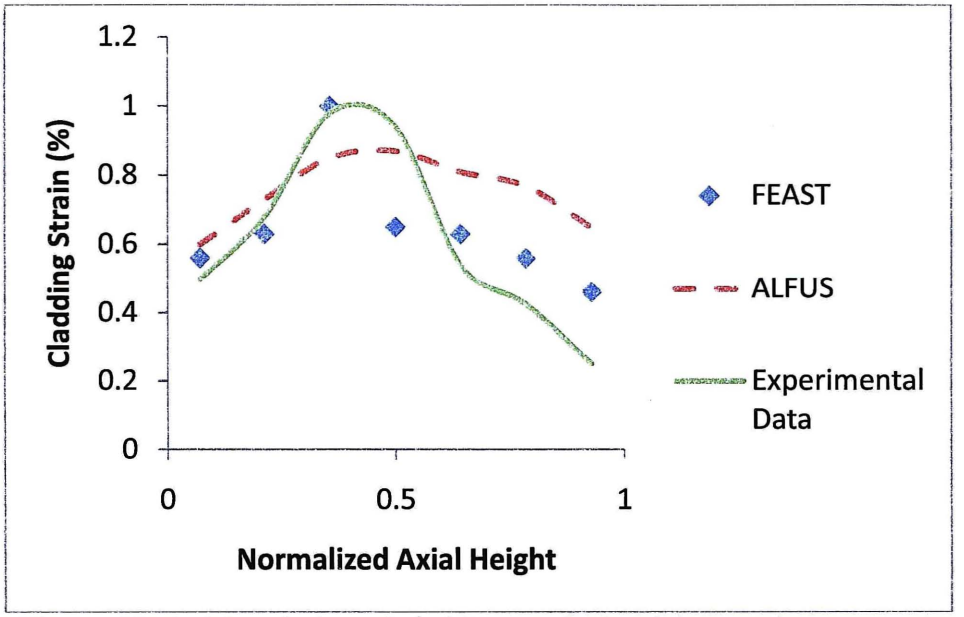


Figure-48: Axial variation of cladding strain (peak burnup is 15.8 at %)

Table-23 gives a comparison of the FEAST, ALFUS and also LIFE-METAL predictions with respect to the experimental data. It is important to note that the spectacular agreement of LIFE-METAL with the experimental data is due to the fact that X425 (and X441) were used for calibration of the various empirical coefficients in that code.

Table-23: X425 Peak cladding strain (%)

Peak Burnup (at %)	Experimental Data	FEAST		ALFUS [5]		LIFE-METAL [63]	
		Cladding Strain (%)	Relative Error (%)	Cladding Strain (%)	Relative Error (%)	Cladding Strain (%)	Relative Error (%)
10.4	0.25	0.22	-12.0	~0.37	48	~0.25	0.0
15.8	0.98	1.0	2.0	~0.86	-14	~0.98	0.0
18.9	2.0	2.23	11.5	~1.55	-22.5	~2.4	20

3.1.3. X447 Benchmark

Table-24 gives the fuel specifications for X447 assembly and Figure-49 shows the irradiation history.

Table-24: X447 fuel data

Parameter	Value
Fuel Composition	U-10Zr
Clad Material	HT-9
Fuel slug radius (mm)	2.16
Clad inner radius (mm)	2.54
Clad outer radius (mm)	2.92
Fuel Smear Density (%)	75.0
Fuel Active Length (cm)	34.3
Plenum to Fuel Ratio	1.4
Peak Linear Heat Rate (kW/m)	33
Peak Clad Temperature (^{0}C)	660

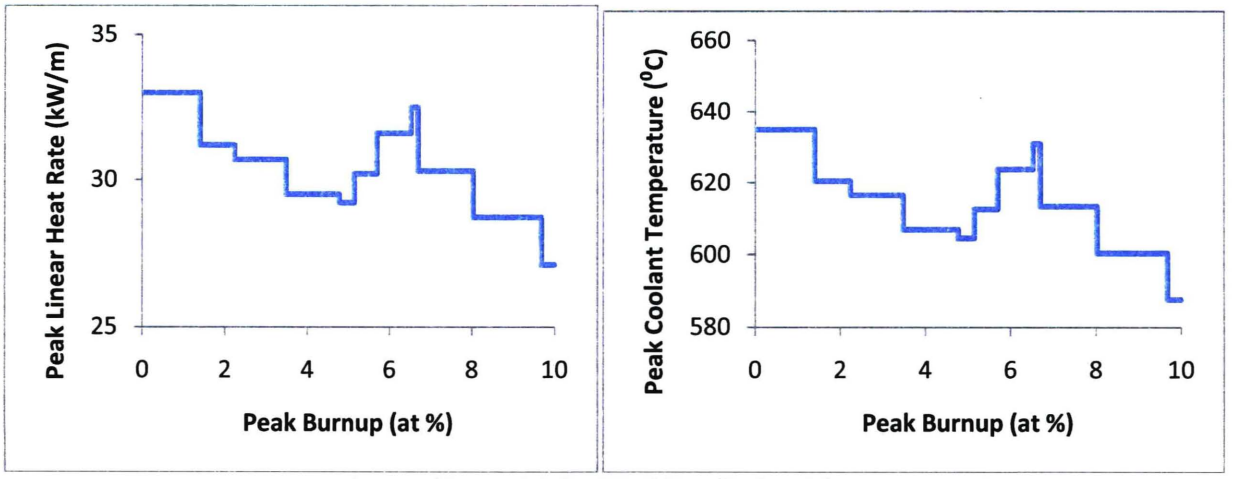


Figure-49: DP04 fuel rod irradiation history

The axial power profile given in Figure-34 and the fluence correlation for EBR-II given in Eq-3.1.1 are again adopted in the analysis. As can be seen in Figure-49, X447 cladding material temperature is quite high. In this temperature range, HT9 thermal creep becomes very significant and it has high dependency on temperature. To improve the accuracy, the fuel was first divided in seven axial nodes, and then, the top axial node was divided into four smaller axial nodes. As a result, the accuracy of the clad strain prediction was improved significantly, without increasing the computational time significantly. Furthermore, the fuel slug and cladding material in each axial node were divided into six and three radial nodes, respectively. The fast flux is again calculated by means of Eq-3.1.1.

Fission Gas Release

The fission gas release at the end of life for the X447 fuel assembly is reported by Ref. [45] to be between 72-76 %. The FEAST prediction for the peak fuel rod is 75 %. The agreement is satisfactory (Figure-50). Figure-50 also shows generic data for U-10Zr at lower burnup from Figure-3.

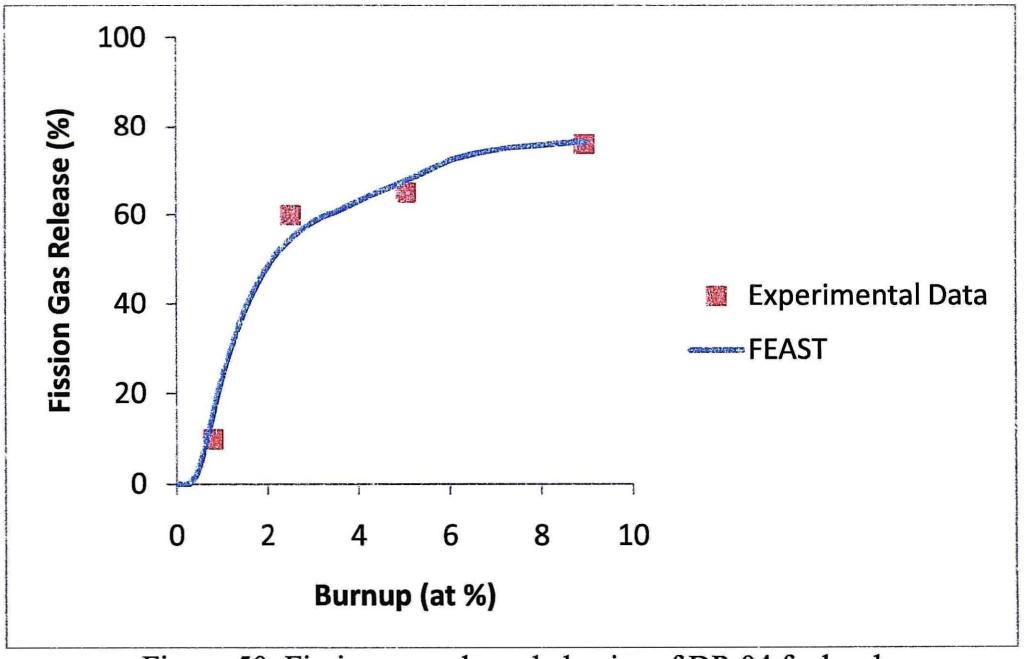


Figure-50: Fission gas release behavior of DP-04 fuel rod

The FEAST-predicted cladding strain for the DP-04 fuel rod matches well with the experimental cladding strain data, as shown in Figure-51.

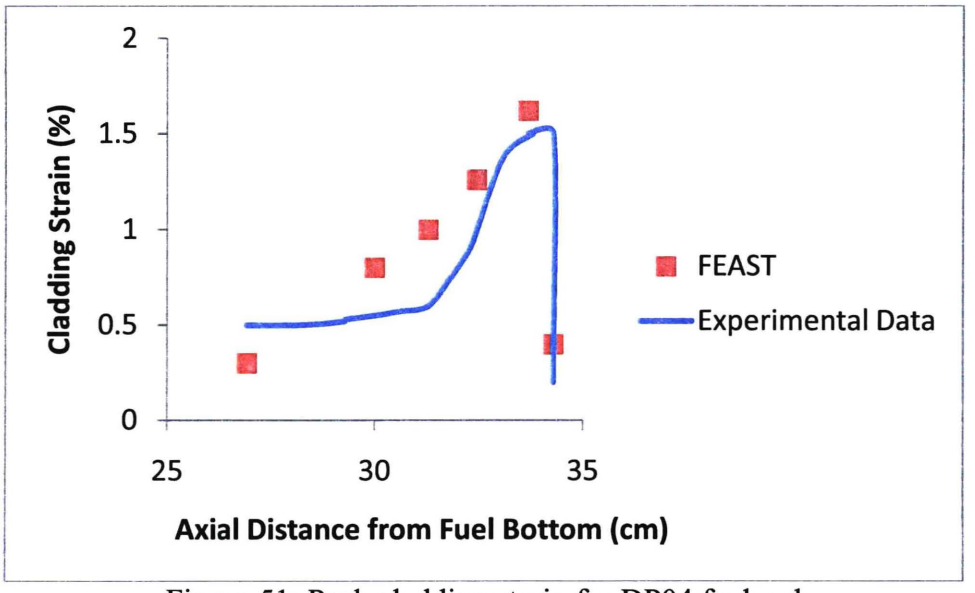


Figure-51: Peak cladding strain for DP04 fuel rod

3.1.4. Comparison with the ALFUS Code for the Current Metal Fuel Irradiation in the PHENIX Reactor

Fast reactor metal fuel rods containing minor actinides (MAs) and rare earths (REs) have been irradiated in the fast reactor PHENIX. The fuel specifications are given in Table-25. A code-to-code benchmark was accomplished against ALFUS, assuming the amount of minor actinides are small and their effect on the fuel performance is negligible [64].

Table-25: Fuel specifications

Fuel	U-19Pu-10Zr/U-19Pu-10Zr-5MA/U-19Pu-10Zr-5MA-5RE
Clad	CW 15-15Ti Steel
Pin length (mm)	1793
Outer cladding diameter (mm)	6.55
Cladding thickness (mm)	0.45
Fuel stack length (mm)	485
Fuel rod diameter (mm)	4.9
Fuel smear density (%TD)	75.2

Sodium level above fuel (mm)	10
Plenum length (mm)	464

The irradiation history of the metal fuel samples is given in Figure-52 [64]. Note that the total neutron flux was reported whereas the fast flux (>0.1 MeV) is actually needed for the irradiation creep calculation. According to Ref. [66] the PHENIX reactor cladding receives 18 dpa per cycle. Since three cycles were completed, the flux term is converted into dpa so that the cladding dose at the end of the irradiation is 54 dpa. The axial power profile given in Figure-53 was assumed to be unchanged during the irradiation. The fuel pin was divided into fourteen axial nodes. Furthermore, the fuel slug and cladding material in each axial nodes was divied into six and three radial nodes, respectively.

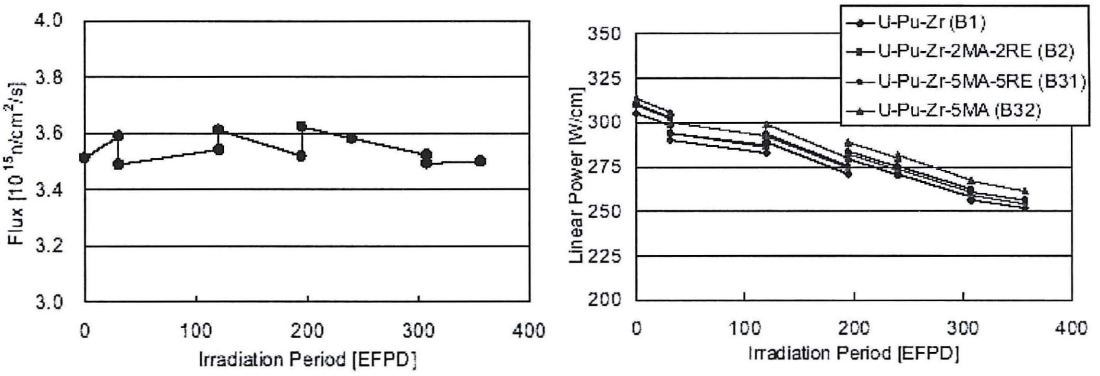


Figure-52: (a): Total peak neutron flux (b): Peak linear power [64]

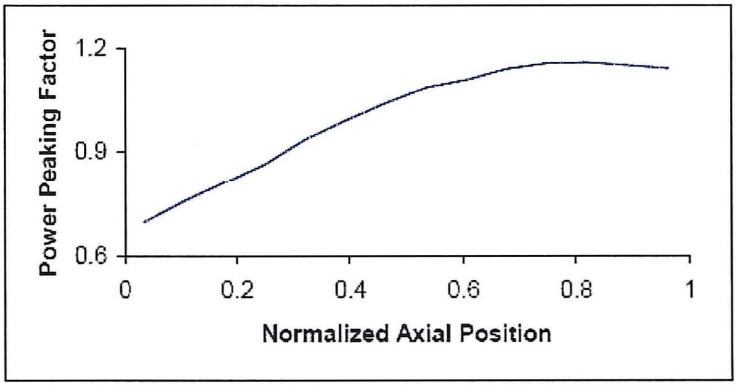


Figure-53: Axial power profile [64]

Irradiation Creep:

The irradiation creep of CW 15-15Ti steel is given by following correlation [67]

$$\varepsilon_\theta(creep) = \frac{3}{4} A(dpa^{-1}MPa^{-1}) \times \sigma_\theta(MPa) \times \phi t(dpa) \qquad (3.1.2)$$

where

ϕt **:** The dose,

$\varepsilon_\theta(creep)$ **:** The circumferential creep strain component (total deformation minus one-third volume swelling), and

σ_θ: The average hoop stress

A = Creep Modulus (Figure-54)

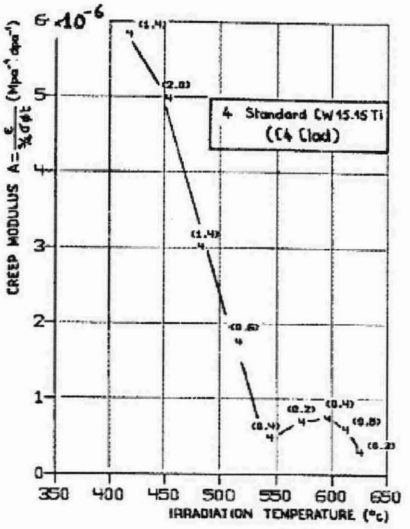


Figure-54: Creep modulus [67]

The correlation given in Eq. (3.1.2) is given only for the ϑ-component of the strain. According to the benchmark cases for X430, X425 and X447 assemblies the z-component of the creep strain remains negligibly small compared to the r- and ϑ-components. As a consequence, the r-component of the irradiation creep strain is assumed to be the opposite of the ϑ-component and the z-component is assumed to be zero in this analysis.

Note that thermal creep of this material is assumed to be negligible within the temperature range of interest [64].

Swelling:

The temperature- and dose-dependent swelling behavior is given in Figure-55 and Figure-56. A best fit of this data was performed in order to obtain the swelling strain at each time interval of the calculation. Since the maximum dose is 54 dpa, no swelling is expected for clad temperatures above 500 ^{0}C (Figure-55 and Figure-56).

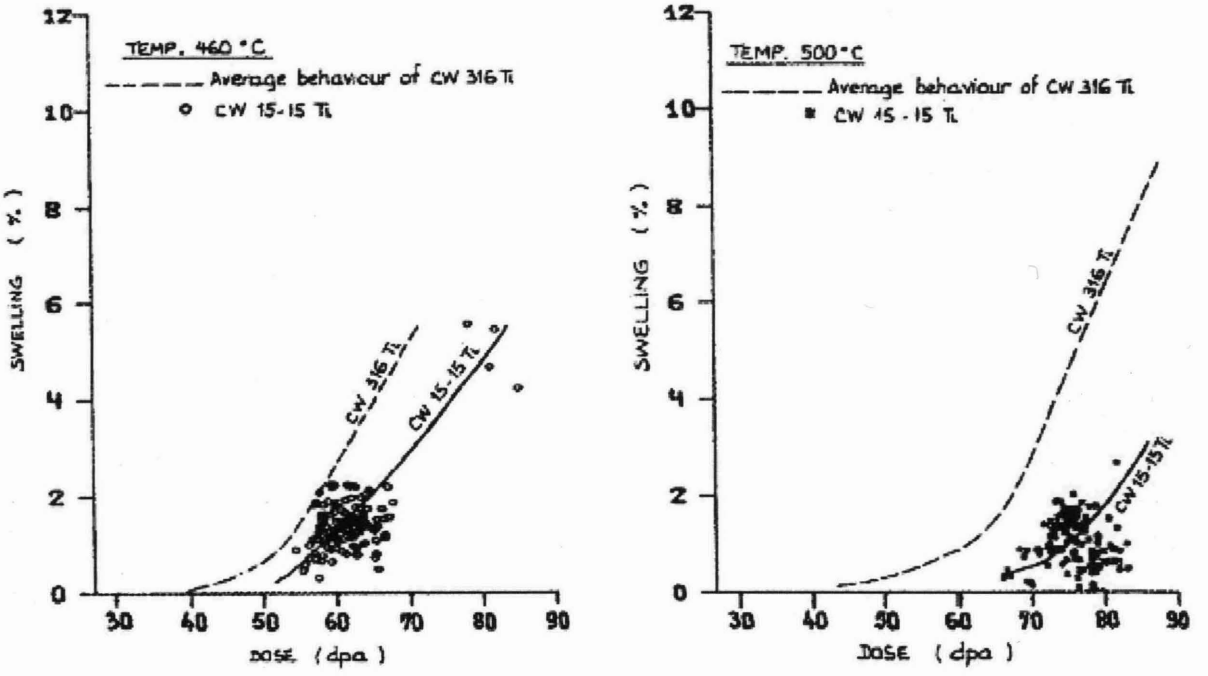


Figure-55: Swelling behavior of CW 15-15Ti at 460 ^{0}C and 500 ^{0}C [67]

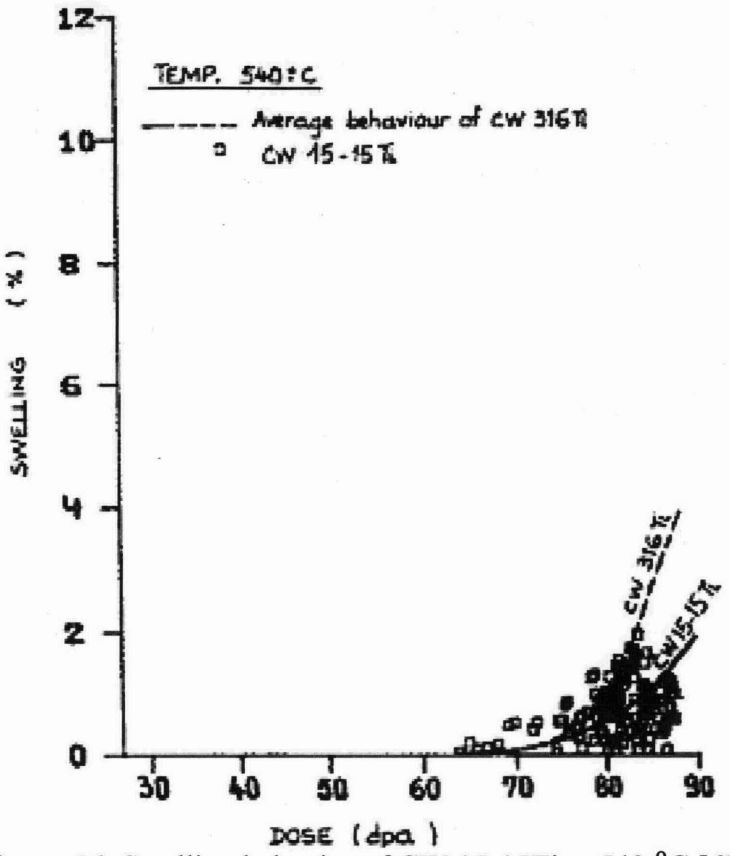


Figure-56: Swelling behavior of CW 15-15Ti at 540 ^{0}C [67]

Results:

The fuel swelling predictions at peak axial power location are given in Figure-57, and the code-to-code agreement is rather good. In Figure-58 it is shown that FEAST somewhat underestimates the contact pressure with respect to ALFUS predictions. The axial elongations shown in Figure-59 agree reasonably well. The discrepancy in cladding strain predictions shown in Figure-60 could be related to the lower predicted contact pressure of the fuel element.

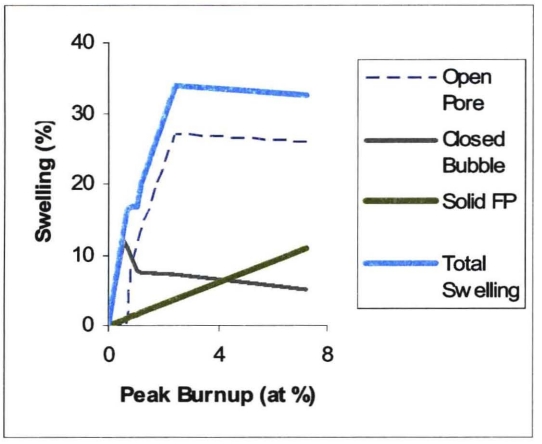
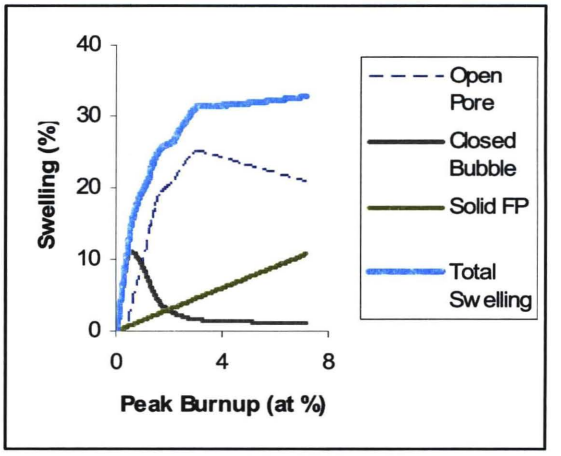


Figure-57: (a) ALFUS prediction



(b): FEAST prediction

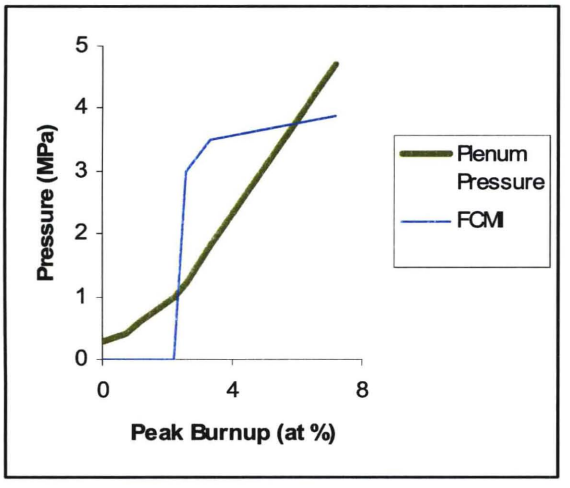
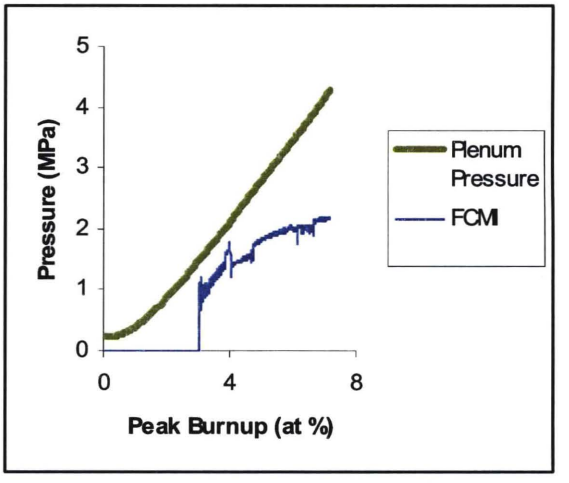


Figure-58: (a) ALFUS prediction



(b): FEAST prediction

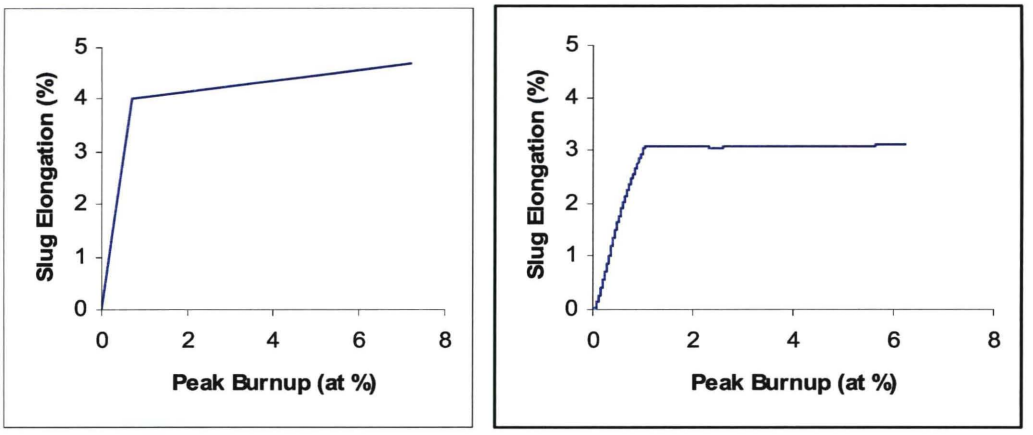


Figure-59: (a) ALFUS prediction (b): FEAST prediction

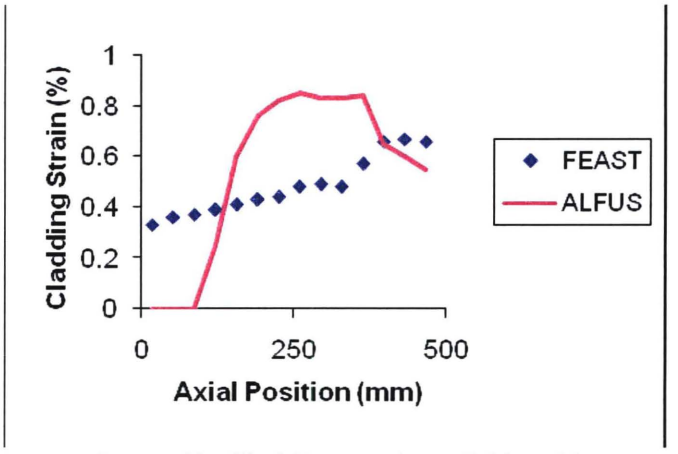


Figure-60: Cladding strain at 7.23 at %

3.2. Transients

FEAST-METAL has been used to simulate all the pin furnace tests performed at Argonne National Laboratory [61], [68]. The experiments were performed at the alpha-gamma hot cell facility. The furnace is radiant and computer controlled. It is able to heat intact irradiated fuel pins to the point of cladding breach.

Key pin parameters and test conditions are summarized in Table-26. FM-1, 2, 3, 4 and 6 are ramp-and-hold tests while FM-5 is a ramp-and-cool test. FM-5 has been performed to simulate the worst possible Loss of Flow Accident in EBR-II. Note that the steady operating conditions of these fuel pins are unknown. It is assumed that the operating condition is the same as the peak X425 fuel rod.

Although the database has some variety in burnup and plenum-to-fuel ratio, plutonium content and test temperature, the number of tests is too low to draw general conclusions about the code performance .

Therefore, additional code-to-code benchmarking with the LIFE-METAL and FPIN2 code predictions are performed.

Table-26: Key pin parameters

Test no.	Fuel type	Plenum to fuel ratio	Burnup (at %)	Test temperature (^{o}C)	Test duration (min)
FM1	U-10Zr/HT9	1.0	3	820	67
FM2	U-19Pu-10Zr/HT9	1.0	3	820	112
FM3	U-26Pu-10Zr/HT9	1.4	2.2	820	146
FM4	U-19Pu-10Zr/HT9	1.5	11.4	770	68
FM5	U-19Pu-10Zr/HT9	1.5	11.4	Ramp to 780; cool	3
FM6	U-19Pu-10Zr/HT9	1.0	11.3	650-670	2160

Table-27 shows the predictions and the experimental data for the failure time, cladding wastage and peak clad strain.

Failure time predictions are performed according to the Cumulative Damage Fraction (CDF) method (top) and Constrained Diffusional Cavity Growth model (bottom). It seems that the Constrained Diffusional Cavity Growth model is somewhat conservative with respect to the CDF model. FEAST predictions for FM1, FM3, FM5 and FM6 are satisfactory. Note that FM1 and FM2 are similar fuel pins and the difference in Plutonium concentration is not likely to cause a very significant difference. FEAST errs on the conservative side with respect to the FM1 and FM2 fuel pin failure times. On the other hand, FM4 fuel pin is an odd case. During the test, balooning of the plenum region was observed [61]. None of codes predicted this behavior. It is hypothesized that plenum balooning resulted in decreased plenum pressure, so pin breach was delayed significantly compared to the code predictions [61].

The clad wastage predictions of FEAST are also satisfactory.

It is not possible to compare the cladding strain of the breached fuel pins with the FEAST prediction because significant straining could result during the breach. FEAST prediction is given for the clad strain prior to clad breach. No failure is observed in FM5 and FM6 fuel pins, thus, the clad strain experimental data match well with the FEAST predictions.

Table-27: Furnace test results and comparison

Test	Failure Time (min)				Cladding Wastage (%)				Peak Strain (%)			
	FPIN	LIFE	FEAST	TEST	FPIN	LIFE	FEAST	TEST	FPIN	LIFE	FEAST	TEST
FM1	36	79	69 58	67	30	53	51 47	64	6.0	1.1	0.7 0.5	3.3
FM2	42	75	56 48	112	37	50	45 42	67	6.0	1.0	0.7 0.5	2.3-4.3
FM3	108	217	129 110	146	86	50	70 64	65	6.0	1.0	0.7 0.4	1.2
FM4	16	9	12 10	68	8.2	3	10 10	24	15.0	0.7	0.4 0.3	10-15
FM5	No failure	No failure	No failure No Failure	No Failure	0.15	0	5.0 5.0	0	0.6	0.0	0.2	0.1
FM6	222	1320	No Failure No Failure	No failure	0.0	0.0	5.0 5.0	0	4.5	1.0	1.0	0.89

4. METALLIC FUEL DESIGN AND PARAMETRIC STUDIES

4.1. Metal Fuel Parametric Study

4.1.1. Steady State

A parametric study that shows the variation of the fuel behavior upon variation of the major input parameters may improve the confidence in the FEAST-METAL code. In this section, the effect of the plenum to fuel ratio, fuel smear density and coolant outlet temperature on the metal fuel behavior will be examined. The simulations assume typical EBR-II conditions. The results are reported at 10 at % burnup.

Plenum-to-Fuel Volume Ratio:

The clad strain decreases with increasing plenum to fuel ratio (Figure-61), as expected. However, this effect becomes less pronounced for plenum-to-fuel volume ratios above 0.7, where the stress is so low that neither irradiation nor thermal creep are significant (at 10 at% burnup). The clad strain vs plenum-to-fuel volume ratio curve would shift to the right for higher values of the burnup and clad temperatures.

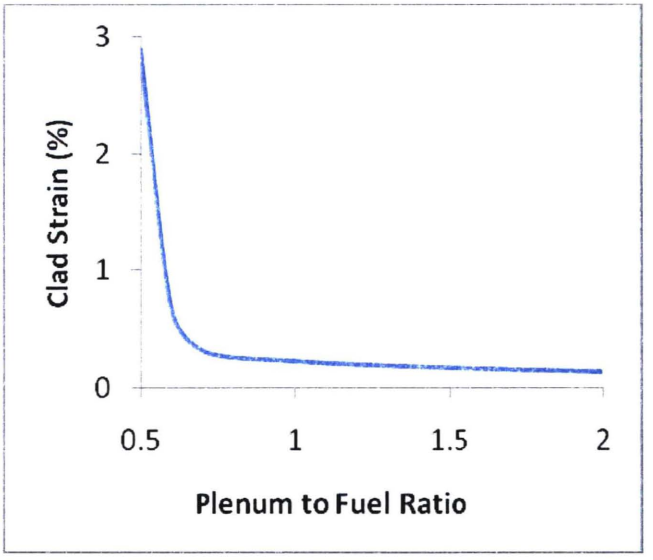


Figure-61: The effect of plenum to fuel ratio on clad strain

Smear Density:

Figure-62 shows that the clad strain increases with increasing smear density, as expected. Low smear density fuel has room for gas swelling. As a consequence, the interconnected open porosity forms, which results in low FCMI up to 10 at %. As the smear density increases, FCMI may appear before the formation of a siginificant interconnected open porosity, as the solid fission products are incompressible and need to be accomodated for by a compression of the open porosity within the fuel. Operation with a low amount of porosity (or high smear density) may result in a very rapid rise in FCMI and significant straining of the clad results.

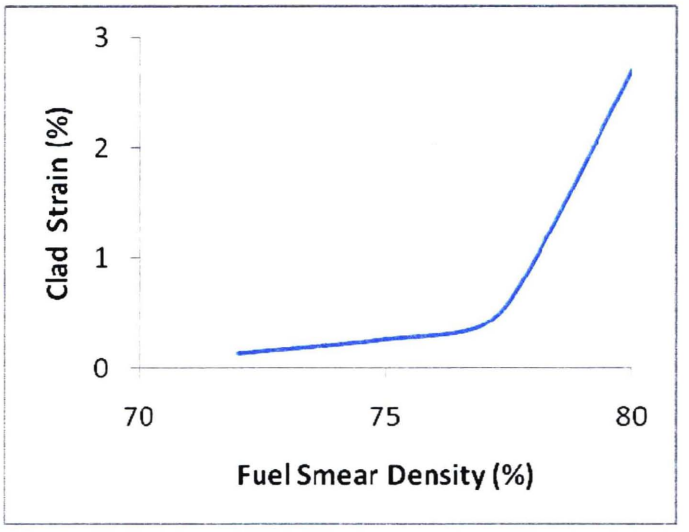


Figure-62: The effect of fuel smear density on clad strain

Coolant Outlet Temperature:

Figure-63 shows that fission gas release increases with increasing coolant outlet temperature, which is also expected. Everything else being the same, low coolant outlet temperatures lead to low average fuel temperatures. As a result of reduced gas diffusivity and bubble growth (surface diffusion), significant amounts of the fission gases remain in the fuel matrix. If the coolant outlet temperature is above 500 ^{0}C, the fission gas release behavior of the fuel tends to saturate because only the bottom (cold) part has significant amounts of retained gases, while the middle and the top parts release almost 100 % of their fission gases.

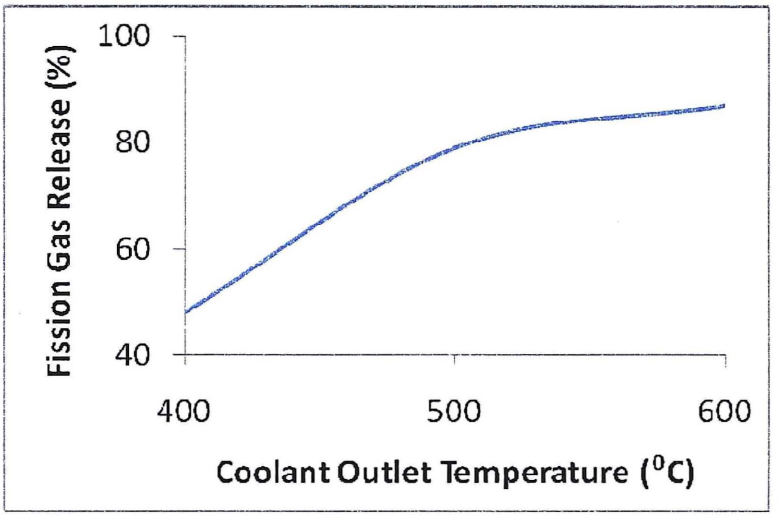


Figure-63: Variation of fission gas release with coolant outlet temperature

4.1.2. Transients

To improve the confidence in the transient capabilities of the code, a parametric study has been performed with simplified transient scenarios to simulate hypothetical Unprotected Transient Overpower (UTOP), Unprotected Loss of Flow (ULOF) and Unprotected Loss of Heat Sink accidents (ULOHS).

Unprotected Transient Over Power:

Reference [69] shows that simulated UTOP accident for the S-PRISM is similar to Case-1 in Figure-64. Furthermore, we examined the effect of increased peak power as shown in Figure-64. It is assumed that the coolant temperature rises proportionally to the rise in power, and therefore so does the clad temperature (Figure-65).

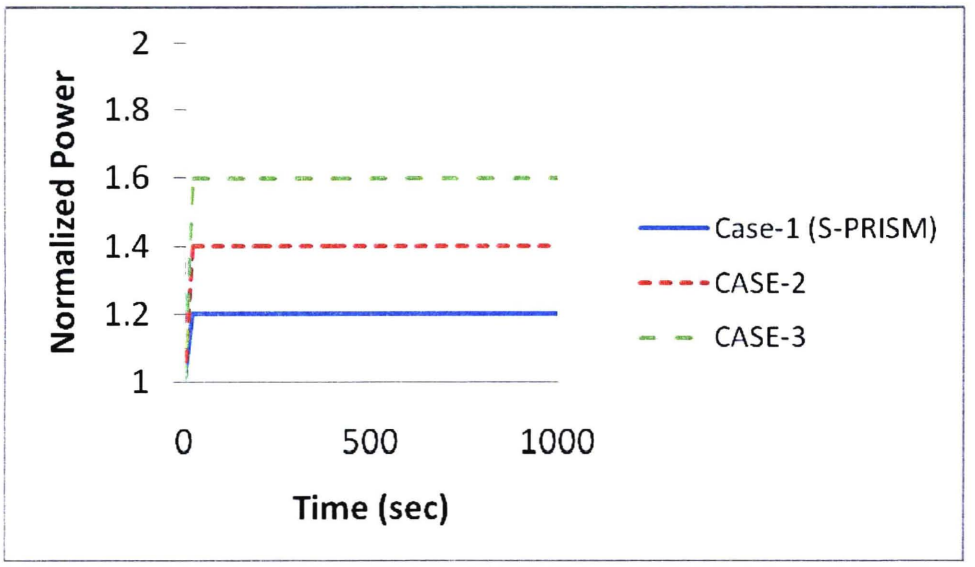


Figure-64: Power history in simulated UTOP scenarios

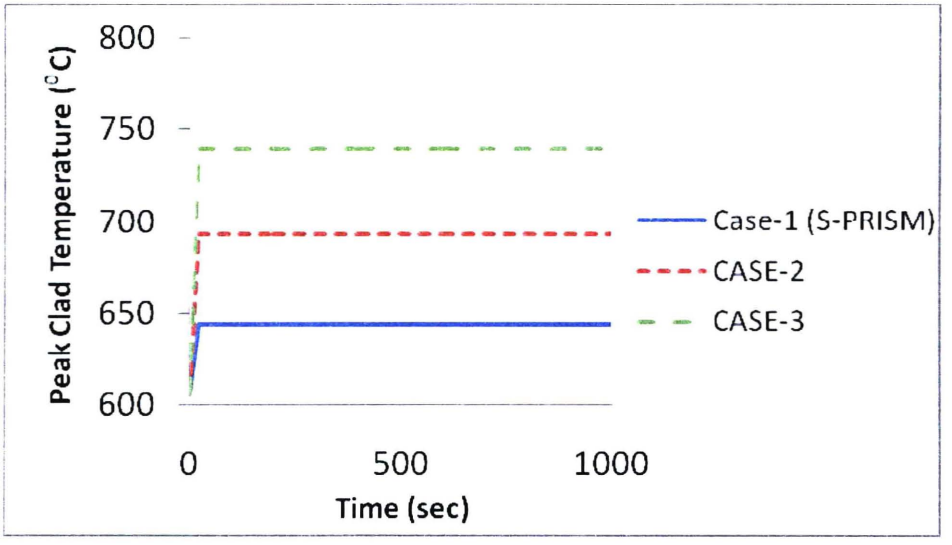


Figure-65: Peak clad temprature history in simulated UTOP scenarios

Figure-66 shows that the initial rise in power causes a high FCMI, due to fuel thermal expansion. Because the metal fuel is fairly compliant at high temperatures, the initial FCMI pressure spike disappers quickly. This ability to limit FCMI during overheating trasients is one of the unique features of the metal fuel, which makes it advantageous compared to fuel types with a higher melting temperature (such as oxides).

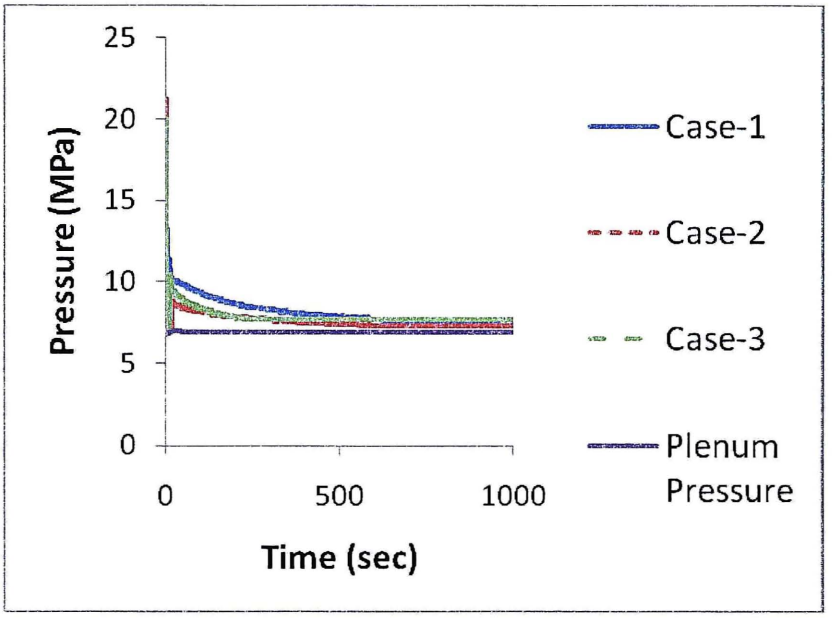


Figure-66: Fuel clad mechanical interaction and plenum pressure in simulated UTOP transients

Table-28 shows that the fuel pins survived for all three simulations with a duration of 1000 seconds. CDF of Case-3 is much higher with respect to the Case-1 and Case-2 simulation. Furthermore, the clad wastage of Case-1 is similar to its steady state wastage because the clad temperature for Case-1 remains below the eutectic temperature; hence, the clad wastage that occurs in 1000 seconds is negligible. On the other hand, Case-2 and Case-3 simulations are above the fuel liquefaction temperature; hence, a non-negligible clad wastage occurs due to eutectic penetration. Although the eutectic forms, the resulting clad wastage is acceptably low, as also suggested by the low clad strain accumulated during the transient.

Table-28: UTOP analysis results at 1000 seconds

Parameter	CASE-1 (S-PRISM)	CASE-2	CASE-3
Cumulative Damage Fraction	0.004	0.006	0.2
Crack Radius/Critical Crack Radius (micron)	N/A	0.14/1.7	0.30/0.77

Clad Wastage / Clad Thickness (micron)	58/381	80/381	82/381
Transient Clad Strain (%)	<0.01	<0.01	0.03

Unprotected Loss of Flow and Loss of Heat Sink Accidents (ULOF/ULOHS):

Unprotected Loss of Flow and Unprotect Loss of Heat Sink transient scenarios are simulated based on the S-PRISM description [70]. CASE-1 shows the S-PRISM characteristics [70]; whereas CASE-2 and CASE-3 were made up to see the performance of the fuel at more severe situations. In these accidents the reactor power decreases due to the reactivity feedback (Figure-67). However, the clad temperature rises because of the reduction in flow (ULOF) and/or loss of the heat sink (ULOHS), as shown in Figure-68.

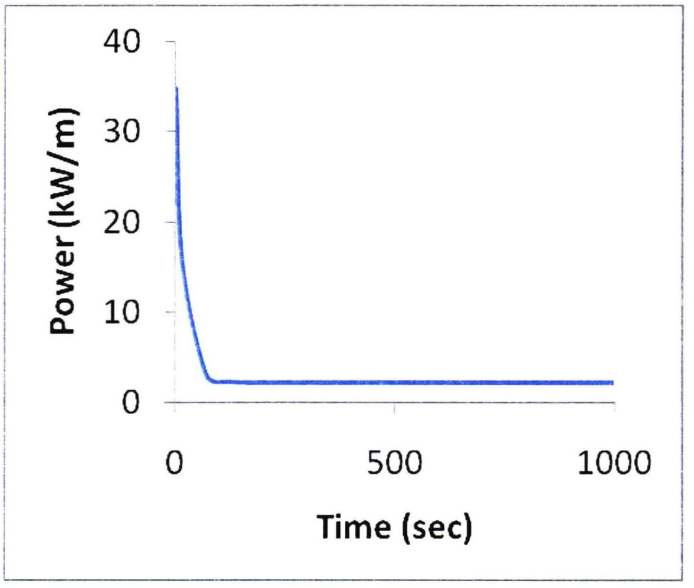


Figure-67: Power history in the simulated ULOHS/ULOF scenarios

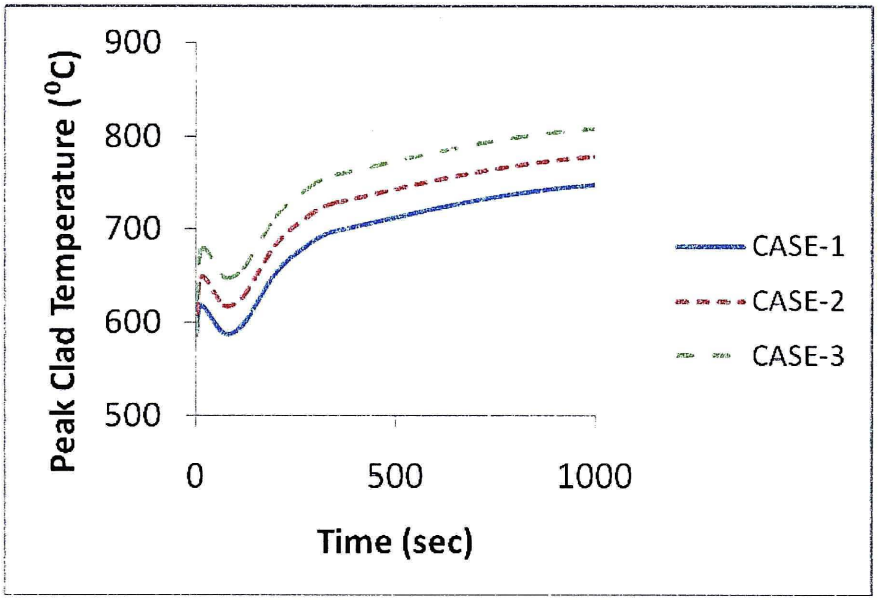


Figure-68: Peak clad temprature history in simulated ULOHS/ULOF scenarios

As can be seen in Figure-69, the FCMI pressure acts for a short period of time at the beginning of the transient due to thermal expansion of the fuel. Later in the event, the FCMI pressure is negligible in Cases-2 and 3 because the fuel temperature is very high and so the fuel is compliant. On the othr hand, Case-1, which has lower fuel temperatures and thus a stiffer fuel, experiences a non-negligible FCMI pressure.

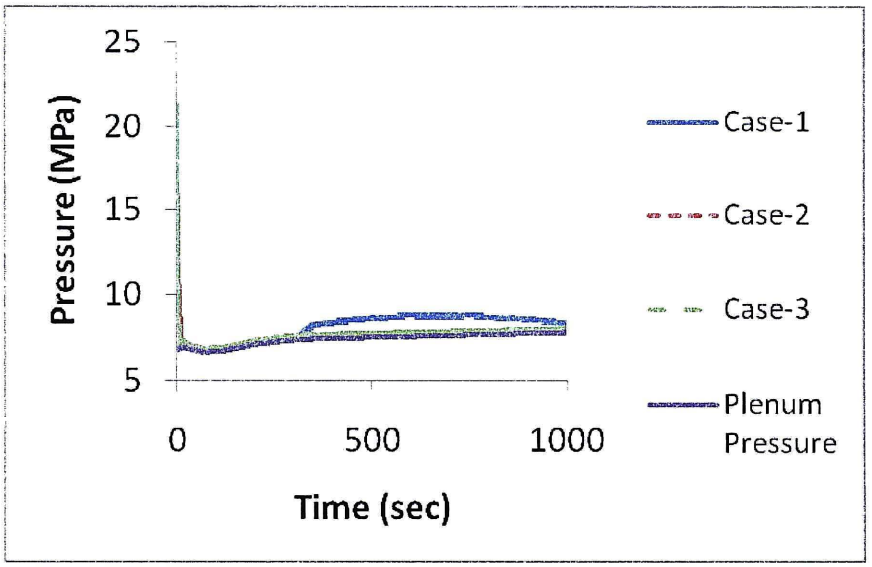


Figure-69: Fuel clad mechanical intereaction in simulated UTOP transients

Table-29 shows that Case-1 and Case-2 fuel pins survived after 1000 seconds, whereas the constrained diffusional cavity model predicts a failure at 1000 seconds for Case-3. All three cases exceeds the eutectic temperature, hence clad wastage appears for all cases.

Table-29: ULOHS/ULOF analyses results at 1000 seconds

Parameter	CASE-1	CASE-2	CASE-3
Cumulative Damage Fraction	0.11	0.32	0.76
Crack Radius/Critical Crack Radius (micron)	0.24/0.48	0.31/0.45	0.44/0.43
Clad Wastage / Clad Thickness (micron)	77/381	80/381	86/381
Transient Clad Strain (%)	0.01	0.05	0.24

4.2. A Breed and Burn Reactor Design, an Application of FEAST-METAL

A breed and burn sodium fast reactor design concept has been analyzed as an application of FEAST-METAL. The selected fuel specifications are given in Table-30. There are two types of fuels. The driver fuel consists of enriched uranium, and provides the criticality before enough plutonium breeds in the seed fuel. The seed fuel assemblies consist of depleted uranium. As the time progresses, the plutonium breeds in the seed fuel pins and seed assemblies start to drive the system.

The postulated limit for these simulations is a 3 % clad strain to avoid excessive clad embrittlement. Note that the thermal creep remains small for the operating condition given in Table-30.

Table-30: The selected breed and burn reactor design fuel pin specifications

Parameter	Driver Fuel	Seed Fuel
Clad OD (mm)	8.36	8.8
Clad thickness (mm)	0.475	0.5
Clad ID (mm)	7.41	7.8
Smear density (%)	70	70
Fuel meat OD (mm)	6.20	6.526
Fuel pin to clad ID radial gap (mm)	0.605	0.637
Wire wrap OD (mm)	1.2	0.800
Pin heated length (m)	2.5	2.5
Gas plenum length (m)	2	2
Fuel type	Metallic U-Zr	Metallic U-Zr
Clad type	HT9	HT9
Fuel density (g/cc)	15.8	15.8
Heavy metal wt%	92.50	92.50
Zr wt%	7.50	7.50
Axial power peaking factor	1.6	1.7
Peak linear heat rate (kW/m)	30	17.5
Peak clad temperature (^{0}C)	550	550
Peak fast flux (n/cm^2/s)	2.0E+15	1.9E+15

4.2.1. Driver Fuel

The driver fuel reaches 23.6 at % peak burnup. At this burnup the peak clad strain is 3 % due mainly to irradiation creep and the simulation was terminated. The peak dose is 319 dpa. Note that 319 dpa could be beyond the HT9 dose limit for swelling.

Temperature Distribution:

Temperature distribution for BOL and EOL is reported in Figure-70 and Figure-71, respectively. The figures show the axial distribution of the fuel centerline and inner clad temperatures. Note that the fuel microstructure is $\alpha+\delta$ phase. Since there is no gamma phase, only a mild fuel constituent redistribution has been observed due to the plutonium formation with burnup. Furthermore, the zirconium content of the fuel increases from 7.5 wt % to 9.5 wt % at the peak power location, due to fission production, i.e., Zr is a fission product (see Figure-72).

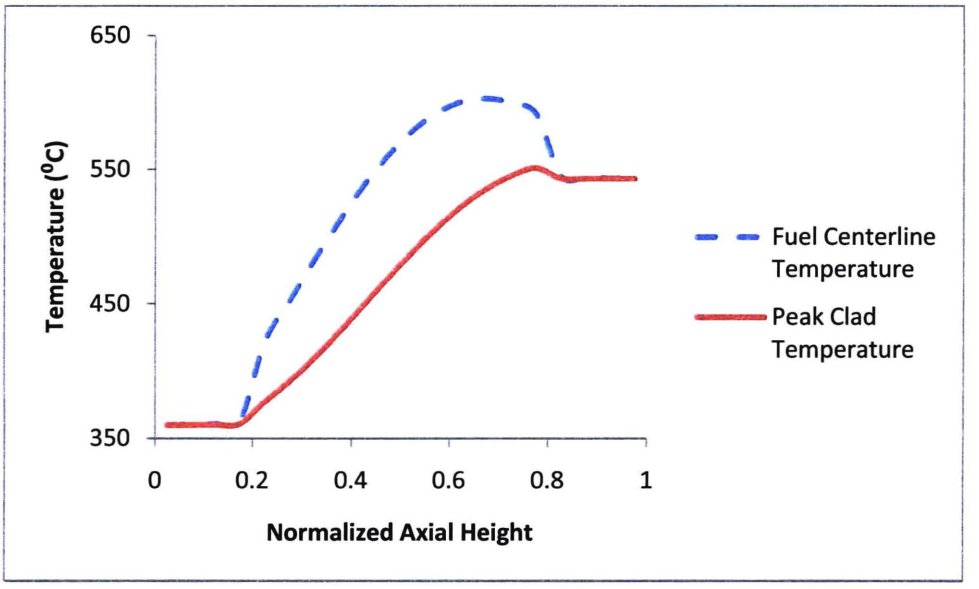


Figure-70: Driver fuel centerline and inner clad temperature distribution at BOL

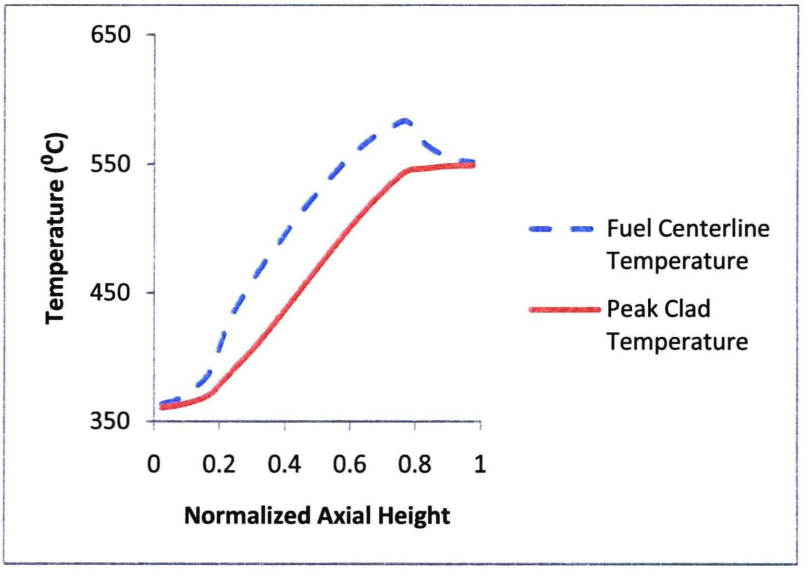


Figure-71: Driver fuel centerline and inner clad temperature distribution at EOL

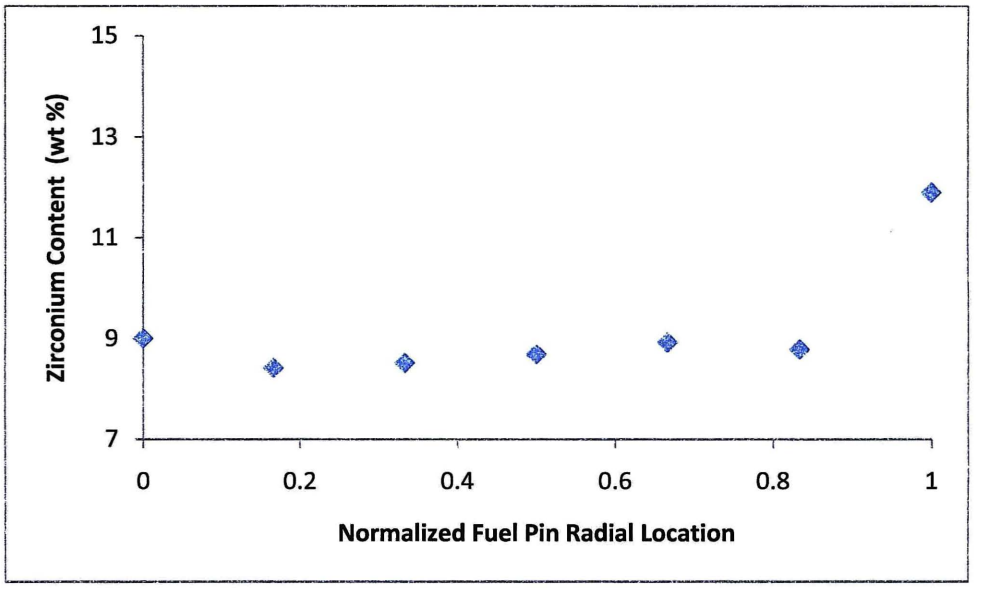


Figure-72: Zirconium radial distribution at EOL (the axial location is 63 % from the bottom of the fuel)

Fission Gas Release:

The driver fuel fission gas release is shown in Figure-73 as a function of average burnup. It starts to increase at 1-2 at % burnup and levels off at 76 % at EOL.

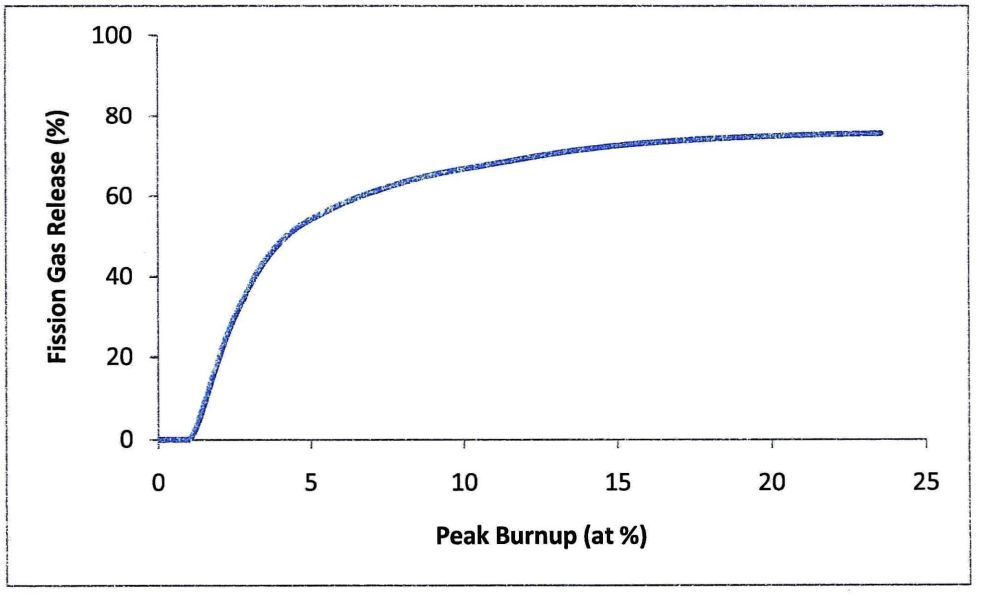


Figure-73: Driver fuel fission gas release

Fuel Axial Elongation:

Figure-74 shows the axial fuel slug elongation for the driver fuel. The fuel slug touches the clad and becomes axially restrained around 4 at %. After this point, the fuel and clad are axially locked.

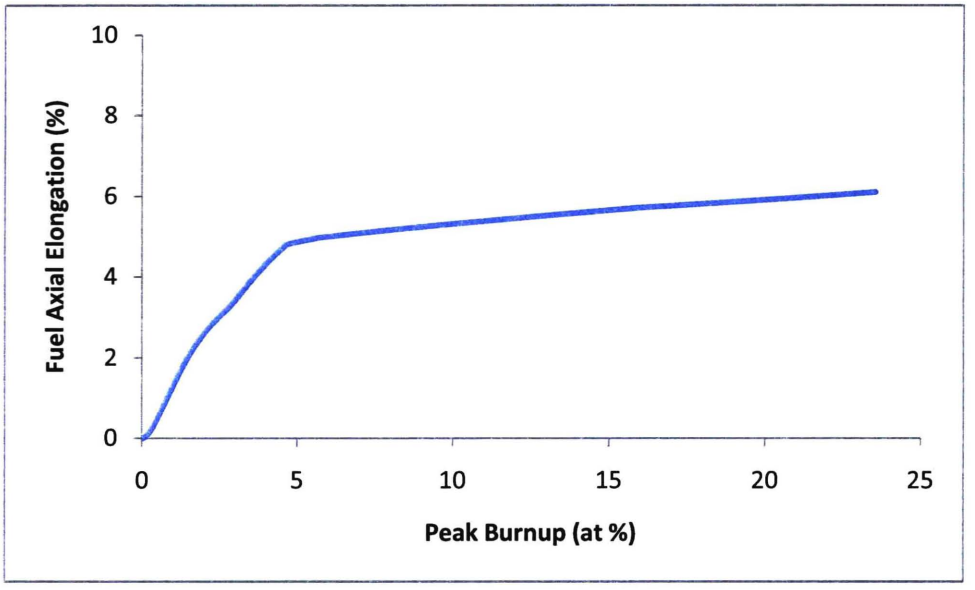


Figure-74: Driver fuel axial elongation

Contact Pressure and Plenum Pressure:

Figure-75 shows the variation of the plenum pressure, as well as, the contact pressure at the peak clad strain location. The peak location is at 35 % height from the fuel slug bottom. The fuel at this axial location becomes radially restrained at around 13 at %. After that, the contact pressure rises because of fuel swelling due to solid fission product accumulation in the fuel, only partially compensated for by fission gas porosity compression.

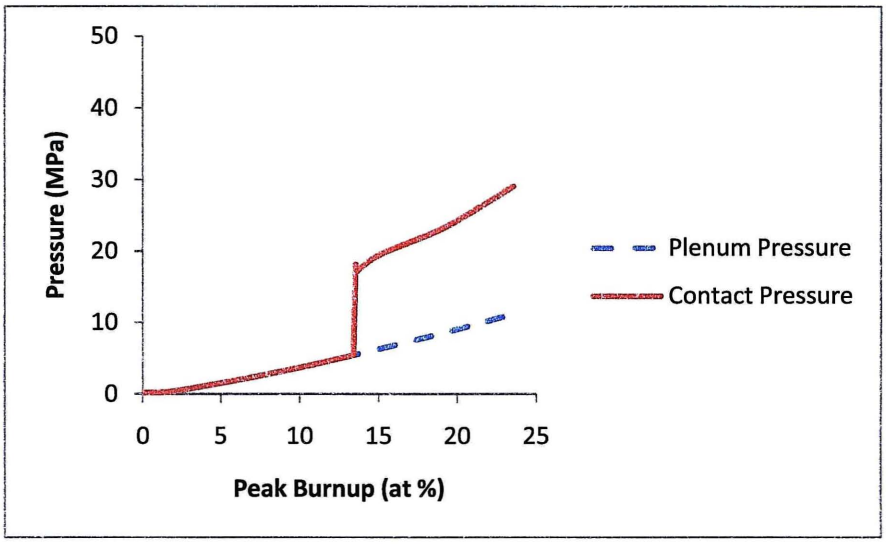


Figure-75: Driver fuel contact pressure variation at peak clad strain location and plenum pressure

Fuel Swelling:

Figure-76 shows the driver fuel swelling behavior at the peak clad strain location. The fuel becomes both axially and radially constrained at around 13 at %. After that, the open porosity content of the fuel diminishes.

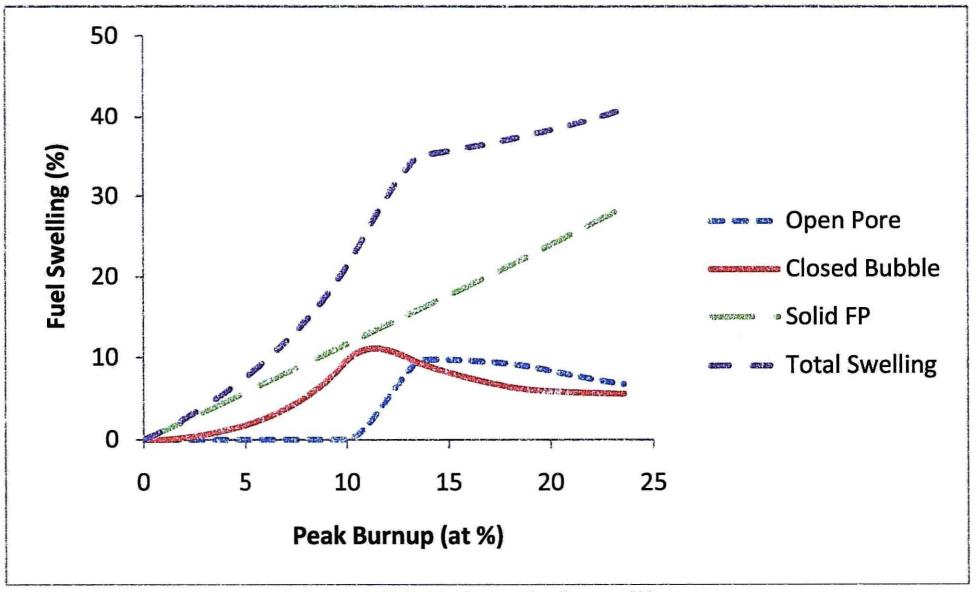


Figure-76: Driver fuel swelling

Clad Strain:

Figure-77 shows the clad strain axial variation with burnup. With the start of FCMI at around 13 at %, the clad strain rises significantly. At 3 % clad strain the simulation is stopped. Almost all of the clad strain is due to irradiation creep. Thermal creep remains small, as the clad temperatures remain relatively low throughout the irradiation cycle.

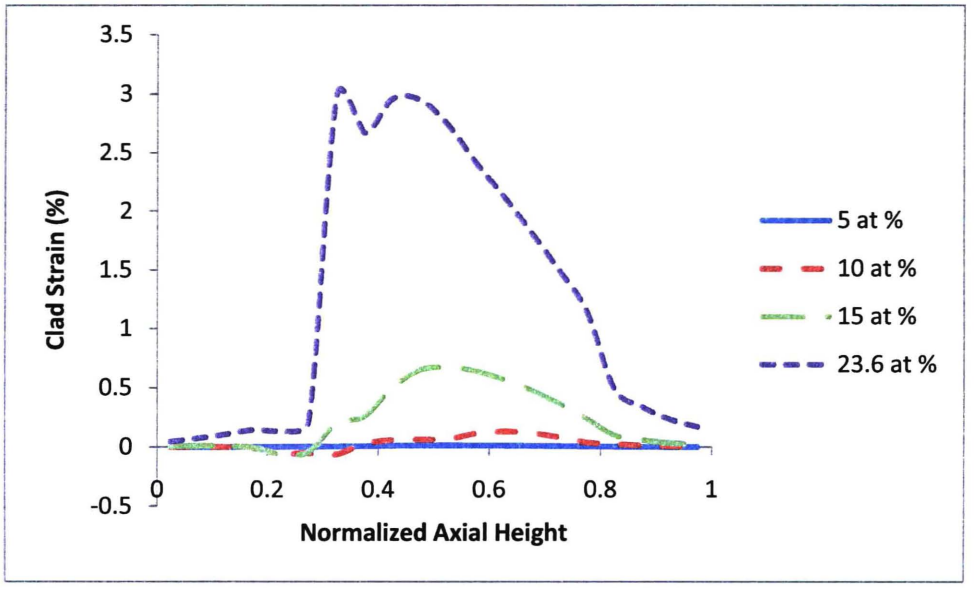


Figure-77: Driver fuel clad strain axial variation with burnup

Clad Wastage:

The clad wastage occurs at the inner and outer surfaces of the clad. Clad wastage at inner surface occurs mainly due to the lanthanide diffusion and formation of a brittle layer at the fuel/clad interface. Figure-78 shows the clad wastage at the inner surface of the clad. As FCCI is driven by temperature, the peak wastage occurs in the region of maximum clad temperature. At the outer surface, sodium corrosion is the main wastage mechanism. Maximum wastage layer due to sodium corrosion is 5 microns at EOL.

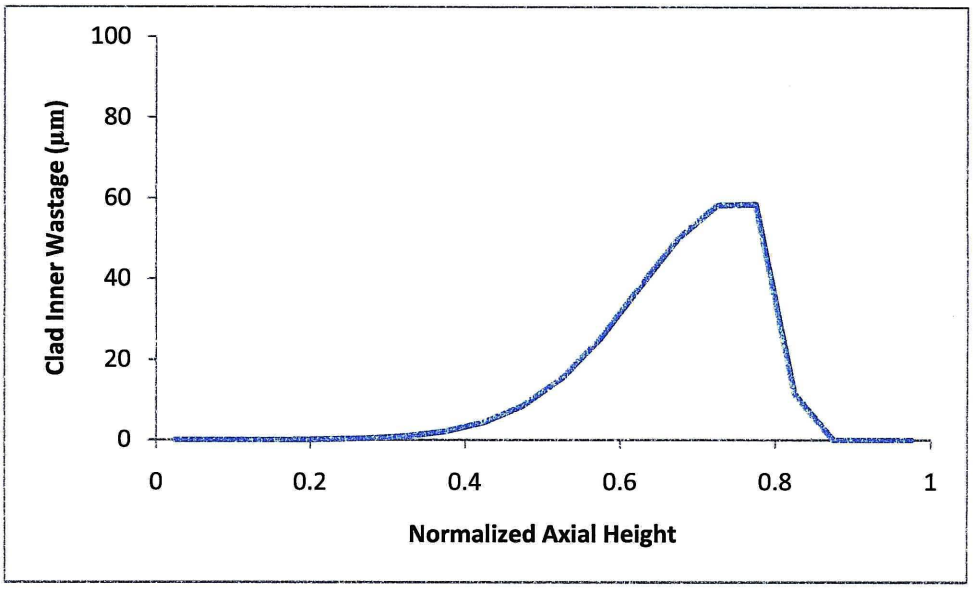


Figure-78: Driver fuel inner clad wastage at EOL

Clad Dose:

Figure-79 shows the peak fluence variation with burnup. The driver fuel peak dose is 319 dpa at the end of life, which is higher than the expected HT9 dose limit to prevent clad swelling.

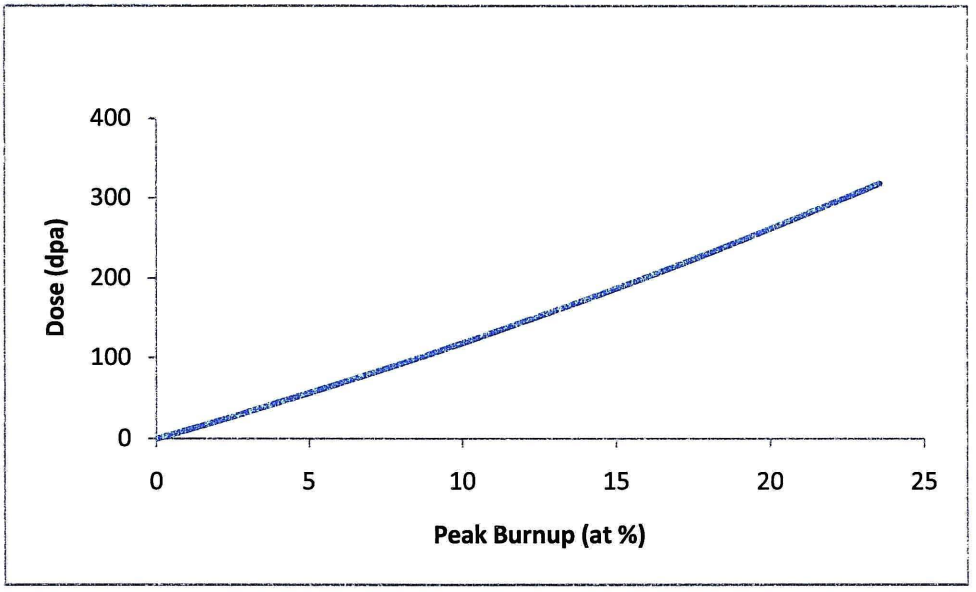


Figure-79: Driver fuel cladding dose increase with burnup

4.2.2. Seed Fuel

The seed fuel reaches 3% peak clad strain at 19.1 at % peak burnup. At this burnup, the clad strain is due mainly to irradiation creep. The corresponding peak dose is 370 dpa, which is well beyond the HT9 dose limit for swelling.

Temperature Distribution:

Seed fuel temperature distribution for the BOL and EOL is reported in Figure-80 and Figure-81, respectively. The figures show the axial distribution of the fuel centerline and inner clad temperatures. During the first few atom percent burnup, the seed fuel linear heat rate is low. Thus, the temperatures are low. The clad and fuel centerline temperatures increase with increasing linear heat rate during the irradiation cycle. However, the temperatures remain below the phase transition temperatures. The fuel microstructure is $\alpha+\delta$ phase. Since there is no gamma phase, a mild fuel constituent redistribution has been observed, similarly to the driver fuel situation. The zirconium content of the fuel increases from 7.5 wt % to 9.1 wt % at peak power location at EOL, again due to production from fission (see Figure-82).

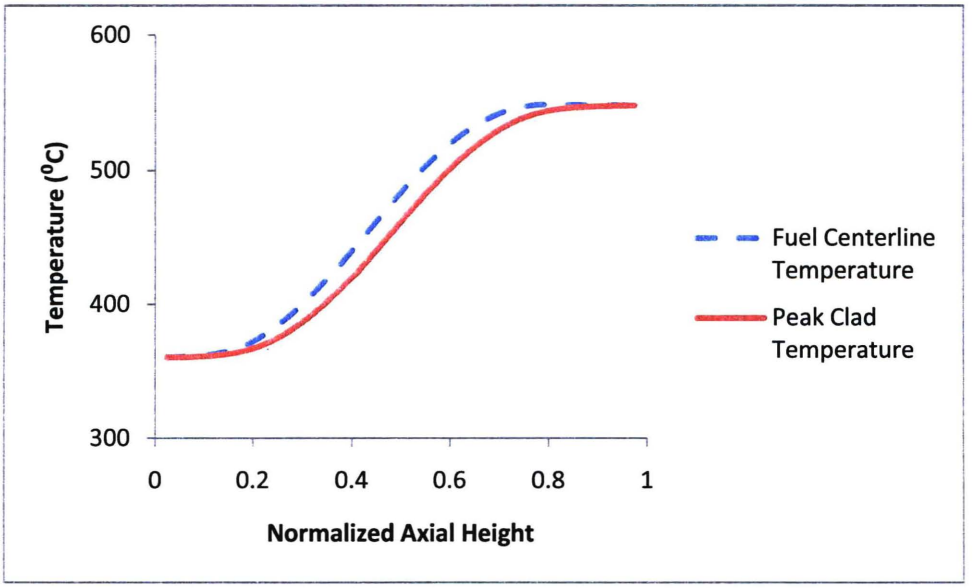


Figure-80: Seed fuel centerline and inner clad temperature distribution at BOL

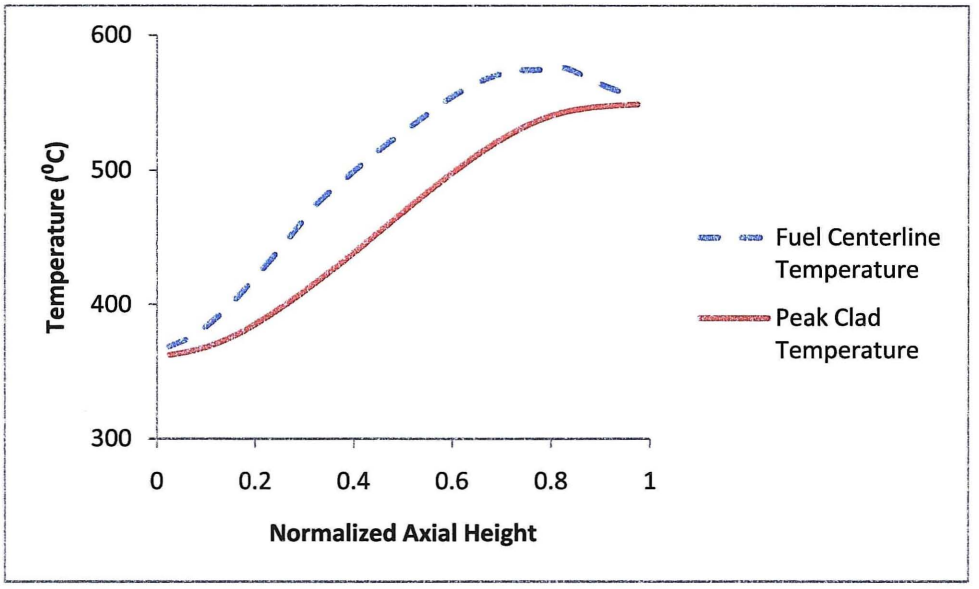


Figure-81: Seed fuel centerline and inner clad temperature distribution at EOL

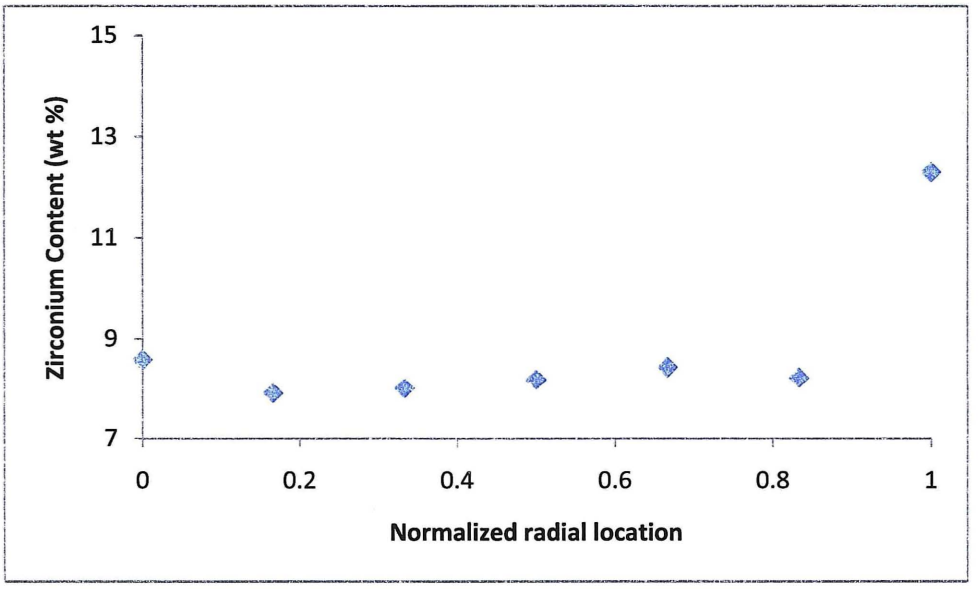


Figure-82: Zirconium radial redistribution at EOL (the axial position is 63 % from the fuel bottom)

Fission Gas Release:

The seed fuel fission gas release is shown in Figure-83 as a function of average burnup. It starts to increase at 2 at % average burnup and monotonically approaches 70 % at EOL.

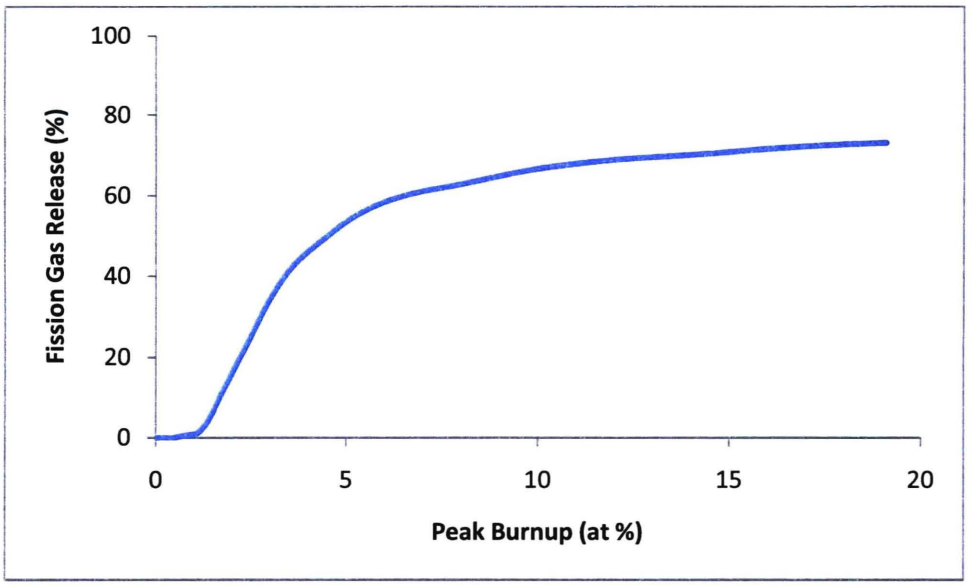


Figure-83: Seed fuel fission gas release

Fuel Axial Elongation:

Figure-84 shows the axial fuel slug elongation for the seed fuel. The fuel touches the clad and becomes axially constrained around 1-2 at % average burnup. After this point, the fuel and clad become axially locked. The fuel elongation at the end of life is 3.0 %, which is much lower than that of the driver fuel, due to the lower temperatures resulting in low gas diffusion rates and thus low swelling.

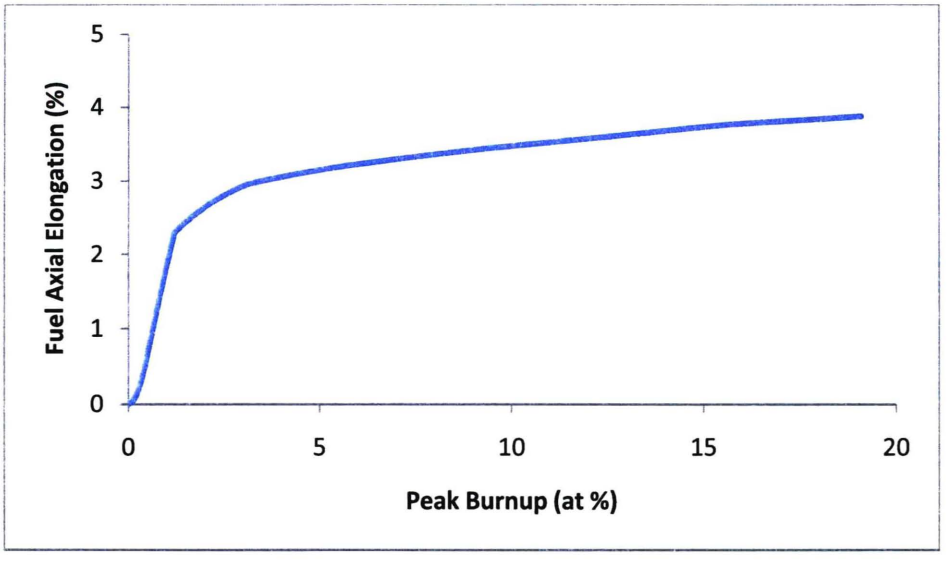


Figure-84: Seed fuel axial elongation

Contact pressure and Plenum Pressure:

Figure-85 shows the variation of the plenum pressure, as well as, the contact pressure at the peak clad strain location. Again the peak location is at 45 % height from the fuel slug bottom. The fuel at this axial location becomes radially constrained at around 6 at %. After that, the contact pressure rises due to the effect of solid fission product accumulation.

The difference in contact pressure and plenum pressure is of the same order of the driver fuel case despite having a lower linear heat rate. Because the seed fuel operates with lower temperature, the fuel creep rate is much lower, so the fuel is less complaint and the FCMI remains signficant.

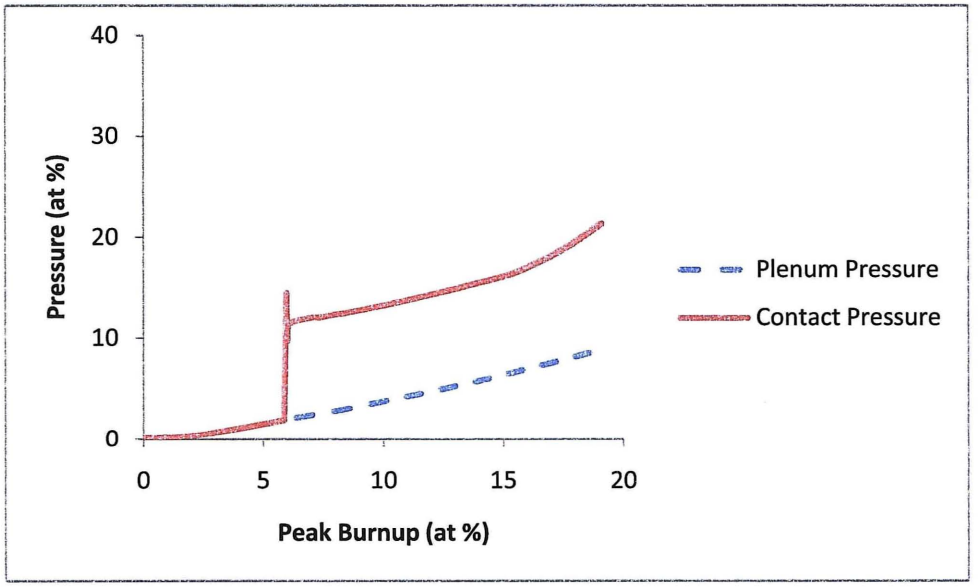


Figure-85: Seed fuel contact pressure variation at peak clad strain location and plenum pressure

Fuel Swelling:

Figure-86 shows the seed fuel swelling behavior at the peak clad strain location. At BOL the fuel temperature is too low for bubble formation and growth. The gas atoms remain in the fuel matrix and bubbles remain small. When the linear heat rate (and fuel temperature) starts to increase at around 4 at % peak burnup, the activation energy for the gas atom diffusion and the bubble growth is available and a significant gas swelling and open pore formation occurs. Note the

linear heat rate of the seed fuel is much lower and the fuel residence time is much higher than the driver fuel. Thus, for a given burnup, the seed fuel gas atoms have more time for diffusing into the gas bubbles. As a consequence, the fuel becomes radially constrained at around 6 at %, which is much earlier (burnup-wise) than the driver fuel.

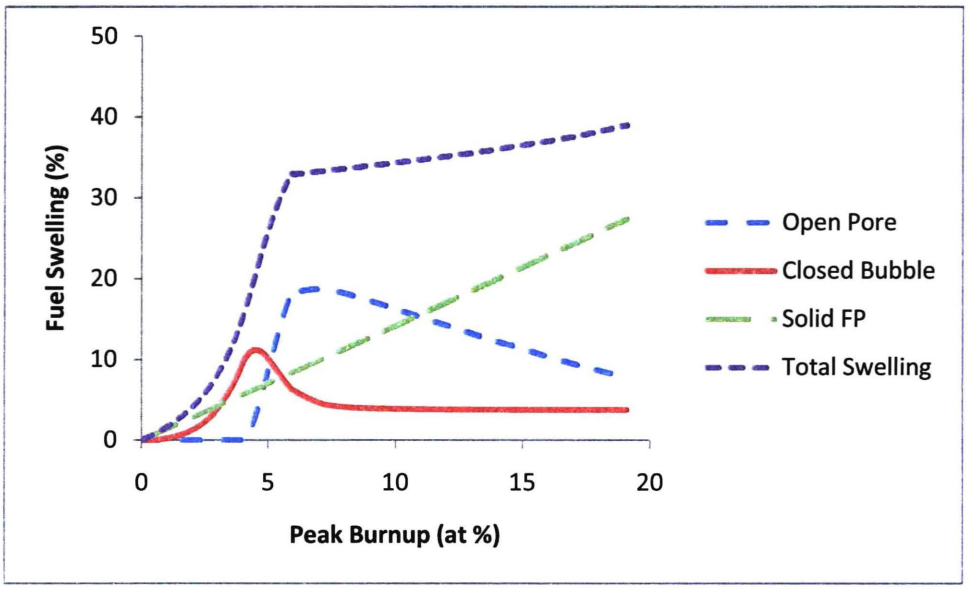


Figure-86: Seed fuel swelling

Clad Strain:

Figure-87 shows the clad strain axial variation with burnup. The fuel becomes axially constrained above 2 at % burnup. The axial friction force acting on the clad is significant because the fuel porosity is zero at this time (see Figure-86). As the clad is strained axially, it shrinks radially (because the total volume change due to creep must be zero, per Prandtl-Reuss flow law), so Figure-87 reports a slight negative clad hoop strain at low burnup. With the start of radial fuel clad mechanical interaction at around 6 at %, the clad hoop strain rises significantly in the positive direction. At 3 % clad strain, the simulation is stopped. Almost all of the clad strain is again due to the irradiation creep, as temperatures are too low for thermal creep to be significant.

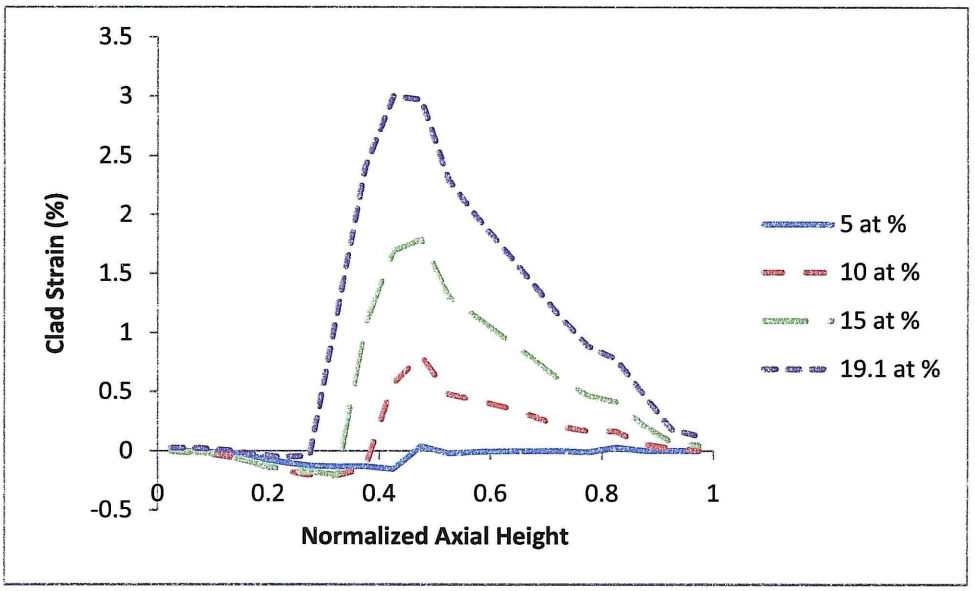


Figure-87: Seed fuel peak clad strain variation with burnup

Clad Wastage:

Figure-88 shows the clad wastage at the inner surface of the clad. Maximum wastage layer due to sodium corrosion at the outer surface of the clad is 5 microns at EOL.

The seed fuel clad wastage is lower than that of the driver fuel. Although the clad temperature of these two fuel pins are the same, the lanthanide contents are different at the time at which fuel clad interaction starts. Due to lower lanthanide content of the seed fuel, a cladding wastage is predicted. This behavior is consistent with the explanation given in Ref. [48].

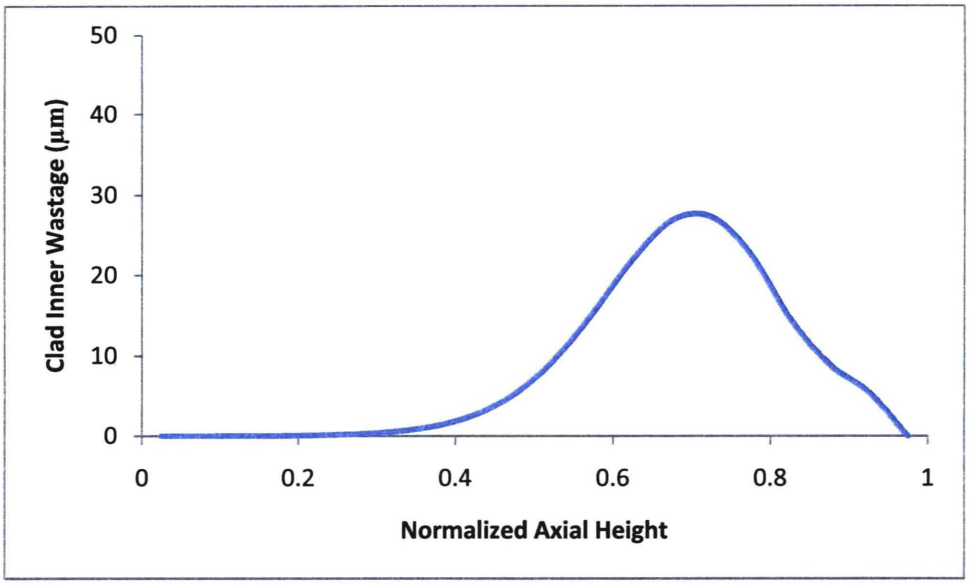


Figure-88: Seed fuel inner clad wastage at EOL

Dose:

Figure-89 shows the peak fluence variation with burnup. The seed fuel peak dose reaches 370 dpa. It is not sure that HT9 can sustain such damage without excessive swelling.

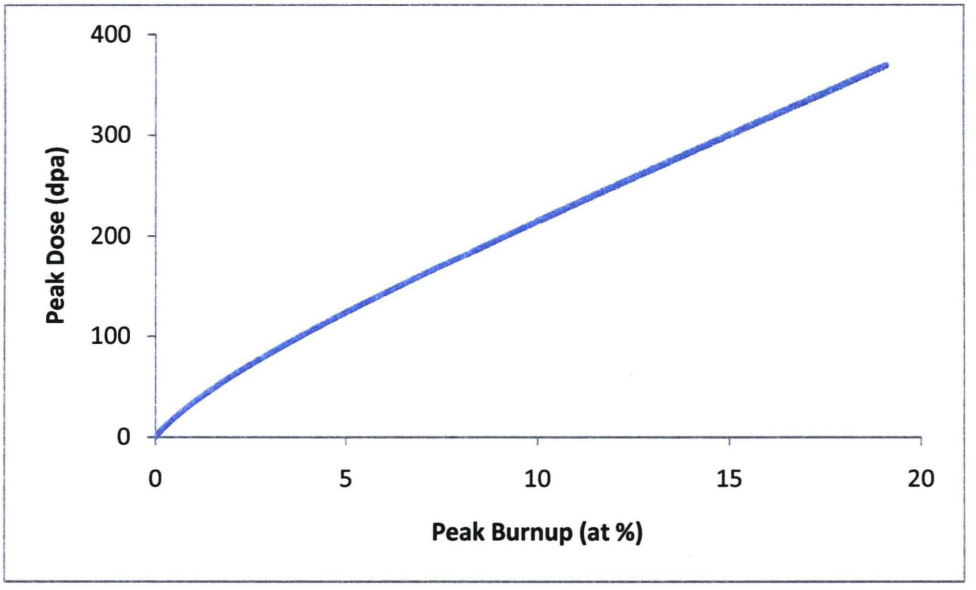


Figure-89: Seed fuel cladding dose variation with burnup

2.11.3.Comments on the Analyzed Breed and Burn Fuel Design

A typical breed and burn fuel pin design concept was analyzed in this work. The combination of high fast neutron flux and high residence time lead to an excessive dose level on the cladding material. Such a high dose may cause void swelling and embrittlement of the cladding.

Based on Ref. [71] and [72], 5 % volumetric swelling of HT9 is expected at 400 dpa if the saturated swelling does not occur. Note that 5 % volumetric swelling of the fast reactor clad material could be acceptable [73]. The channeling fracture may occur at 10 % volumetric swelling. Ref. [73] shows that the clad failure probability is only 10^{-4} when 5 % volumetric swelling is allowed. Typically, the swelling of the ferritic/martensitic steels is expected to saturate at a certain dose level and after that the swelling rate will increase by an order of magnitude. The saturation dose of HT9 is unknown. Hence, the design given here is based on operation with no saturation swelling up to 400 dpa. Embrittlement of the cladding material with the formation of the helium bubbles is another significant issue [74]. The helium embrittlement could reduce the creep-rupture strength as much as an order of magnitude [75]. Hence, it should be also be adressed as the future work.

In addition to void swelling and embrittlement of the clad, the coolant flow channel blockage due to straining of the cladding and hard contact between the wire and the cladding material should also be evaluated. To avoid these issues, the following approach is proposed. When the clad hoop strain reaches to 3 % (swelling and irradiation creep), wire can be replaced with a larger one and an acceptable clearance between the wire and cladding material; furthermore, some fuel pins should be taken out of the fuel assembly. By this approach, it may be possible to allow 3 % irradiation creep and about 5-10 % volumetric void swelling of the cladding with no hard contact between the wire and the cladding material and opearation with an acceptable coolant flow area.

Increasing the coolant inlet and outlet temperature should also be considered. Ferritic/martensitic steels are rather susceptible to embrittlement below 390 ^{0}C. The current coolant inlet temperature is 360^{0}C. It might be rather low to impede ductile to brittle transition. Furthermore, it may be possible to increase the coolant outlet temperature while allowing for 1 % thermal creep at the upper of the cladding. As a consequence, the thermal efficiency of the plant could be

increased. In addition to thermal efficiency, the fuel becomes more compliant at high temperatures. The compressiblity of Body Centred Cubic (BCC) γ phase is two orders of magnitude higher than the stiff $\alpha+\delta$ phase.

To increase the heavy metal inventory and the average discharge burnup, hourglass fuel concept could be introduced. Solid fission product swelling of the metallic fuel is very high compared to the oxide fuel. If the axial power profile of the reactor is having a high peaking at the middle region, it may be advantageous to increase the smear density at the low power regions and/or decrease it at high power regions. Hence, a flatter power profile, increased heavy metal inventory and discharge burnup could be achievable. Note that the upper part of the fuel slug is rather soft. The effect of an increase in power peaking in this region may not have a significant influence on the fuel clad mechanical interaction.

Vented fuel is another interesting concept that could help improving the performance of the breed and burn fuel design. Eliminating the plenum pressure may allow for operation with a very low FCMI at the upper part of the fuel. As a result, peak clad temperature can be increased further and transient performance of the fuel would increase by an order of magnitude. On the other hand, this concept would not help significantly on increasing the peak burnup because FCMI at the lower part of the fuel is much higher than the plenum pressure and it is the limiting factor.

To conclude, it may be possible to improve the breed and burn fuel performance by adopting hourglass fuel, increasing the inlet and outlet temperatures by ~20 ^{0}C and adopting the vented fuel approach.

4.3. Annular Metal Fuel Modeling

The FEAST-METAL capabilities were extended to model annular fuel pins with simultaneous internal and external cooling. This concept is being investigated at MIT, as a means to reduce fuel and clad temperatures and heat flux, thus enabling an increase of the power density in LWR

as well sodium-cooled fast reactor cores [76], [77]. Here we are interested in the sodium-coolled fast reactor application only. Figure-90 shows the typical annular fuel pin. Sodium coolant occupies the channels inside and outside the fuel annulus. The fuel slug is immersed into sodium bond and encapsulated with the stainless steel clad.

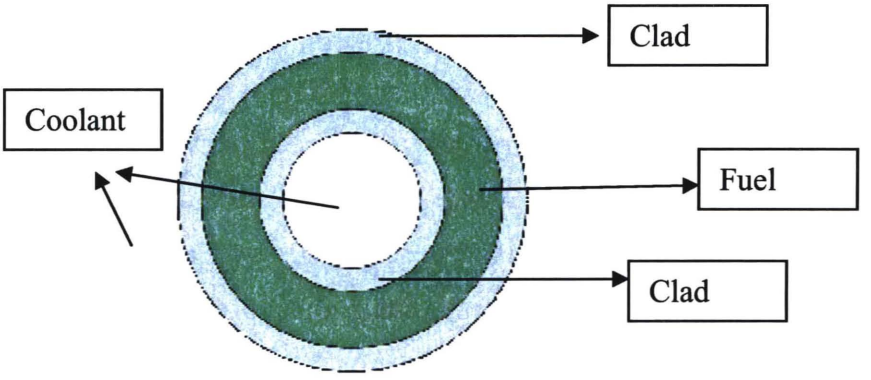


Figure-90: A typical annular fuel pin geometry

4.3.1. Temperature Distribution

The temperature distribution model has been updated to allow for the heat transfer to the inner coolant channel. Furthermore, the inner clad region and gap between the inner clad and the fuel inner surface have been modeled.

Boundary Conditions:

The energy balance equation for each axial node is solved given the coolant temperature and coolant heat transfer coefficient at the outer and inner nodes. The coolant temperature and heat transfer coefficient have been calculated by the thermalhydraulics module given the following boundary conditions:

a) Coolant inlet temperature
b) Mass flow rate of inner and outer channels

Calculation procedure for the temperature distribution for an axial node:

Because the heat splits between the inner and outer coolant channels, iteration is necessary as follows:

1- Initial guess for the coolant temperature and heat transfer coefficient for inner and outer channels
2- Calculate fuel pin temperature distribution.
3- Using the heat deposited into inner and outer channels, re-calculate coolant temperature and heat transfer coefficient for inner and outer channels.
4- If coolant temperature has converged, exit the loop, else continue iterations.

Verification of the temperature module:

Fuel temperature distribution has been calculated with the data given in Table-31. As can be seen in Figure-91, FEAST-METAL predictions match well with the analytical solution of the heat equation given the boundary conditions and the geometry in Table-31.

Table-31: Fuel specifications

Fuel inner radius (mm)	1.91
Fuel Outer radius (mm)	3.395
Linear Heat Rate (kW/m)	30
Fuel inner surface temperature (K)	873.15
Fuel outer surface temperature (K)	873.15

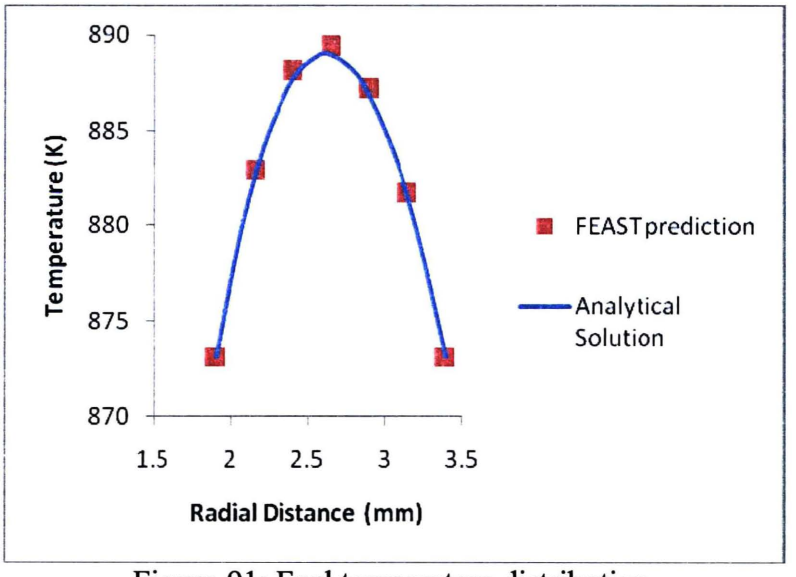


Figure-91: Fuel temperature distribution

4.3.2. Mechanical Analysis

The mechanical analysis model has been updated to include the inner clad region. Stress strain distribution and creep-fracture models are also applied to the inner region.

Boundary Conditions:

The boundary conditions for the mechanical analysis model have been updated as follows:

a) Inner clad inner surface is subject to the coolant pressure
b) Inner clad outer surface is subject to the plenum pressure, if the inner gap is open, plus contact pressure, if the inner gap is closed
c) Fuel inner surface is subject to the plenum pressure, if the inner gap is open, plus contact pressure, if the inner gap is closed
d) Fuel outer surface is subject to the plenum pressure, if the outer gap is open, plus contact pressure, if the outer gap is closed
e) Clad outer surface is subject to the coolant pressure

Verification of the Mechanical Module:

Analytical solution of the mechanical equilibirium equation for the simplified postulated temperature distribution shown in Figure-92 has been accomplished for the annular fuel. The geometry and the thermal expansion coefficient are given in Table-32.

Table-32: Fuel geometry and properties

Fuel inner radius (mm)	1.91
Fuel Outer radius (mm)	3.395
Young's Modulus (GPa)	150
Poisson's Ratio	0.3
Thermal Expansion (1/K)	2E-05

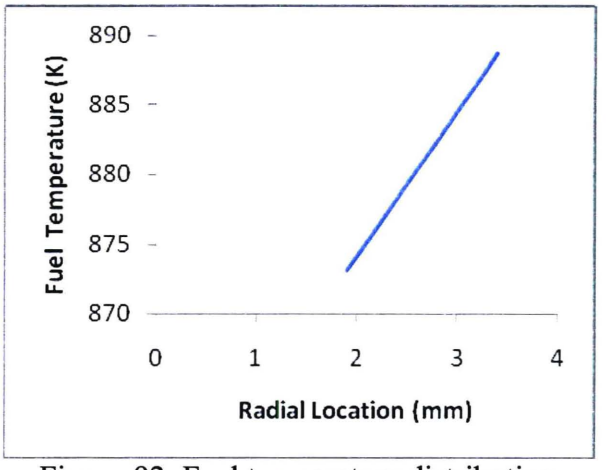


Figure-92: Fuel temperature distribution

As can be seen in Figure-93, 94 and 95, the analytical solution matches well with all components of the stresses.

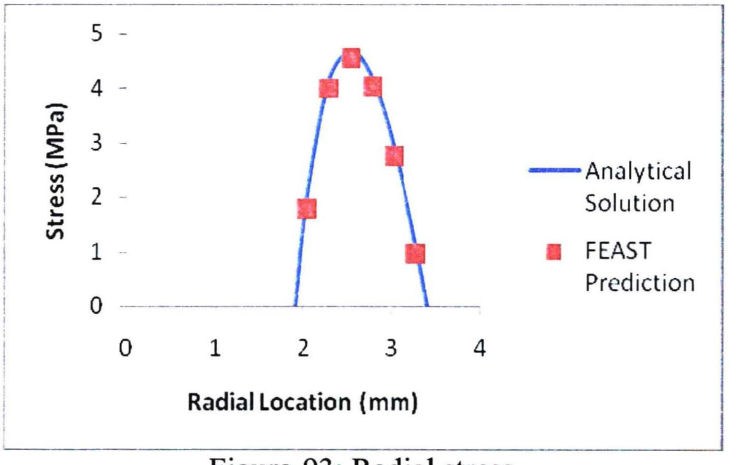


Figure-93: Radial stress

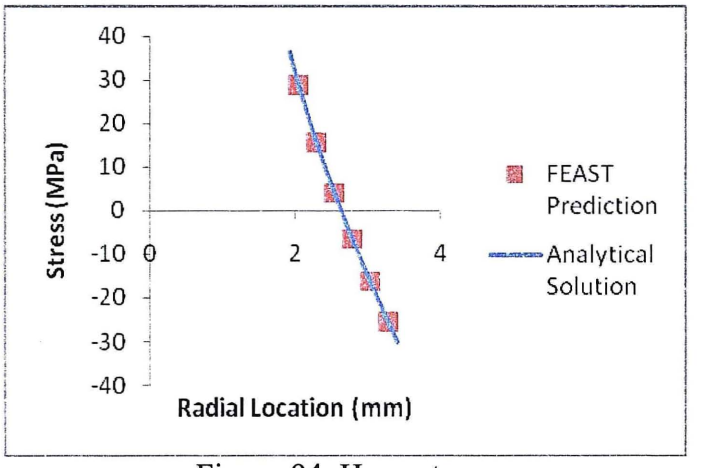


Figure-94: Hoop stress

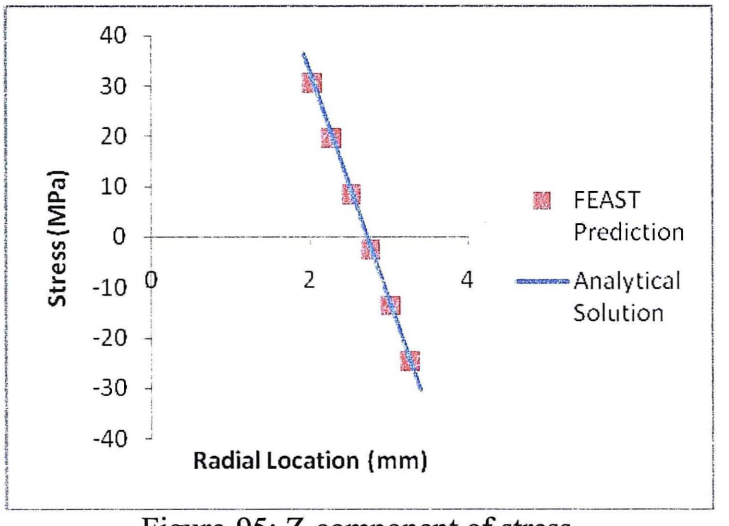


Figure-95: Z-component of stress

4.3.3. Fuel Clad Chemical Interaction

The Fuel Clad Chemical Interaction module is applied also to the inner clad.

4.3.4. Steady State Analysis

A steady state analysis was conducted first. Fuel specifications for three different cases are given in Table-33. Case-A is a data set based on a previous MIT work. In this work, we tried to optimize Case-A to improve the burnup and the heavy metal density. The simulation was terminated when 1 % clad strain limit is reached.

Table-33: Fuel specifications

Parameter	Case-A	Case-B	Case-C
Fuel active length (m)	1.016	1.016	1.016
Plenum to fuel ratio	1.5	1.5	1.5
Inner clad inner radius (mm)	1.7	1.7	1.7
Inner clad outer radius (mm)	2.259	2.0	1.9
Fuel inner radius (mm)	2.270	2.01	1.91
Fuel outer radius (mm)	3.485	3.366	3.395
Outer clad inner radius (mm)	3.796	3.796	3.855
Outer clad outer radius (mm)	4.355	4.355	4.355
Fuel smear density (%)	75	70	70
Peak linear heat rate (kW/m)*	29.24	29.24	29.24
Inner channel mass flow rate (kg/s)	0.0552	0.0552	0.0552
Outer channel mass flow rate (kg/s)	0.0388	0.0388	0.0388
Coolant inlet temperature (^{0}C)	370	370	370
Peak clad temperature (^{0}C)	~600	~600	~600

Table-34: Results at EOL

Parameter	Case-A	Case-B	Case-C
Inner Clad Peak Cladding Strain (%)	-0.39	-0.21	-0.31
Outer Clad Peak Cladding Strain (%)	**1.0**	**1.0**	**1.0**
Peak Burnup (at %)	11.4	16.6	15.6
Fission Gas Release (%)	54.5	57.3	57.2
Fuel Slug Axial Elongation (%)	0.77	1.14	1.08
Inner Clad Wastage (microns)	3.4	4.4	4.2
Outer Clad Wastage (microns)	39.6	58.1	53.7

Case-A:

Case-A is a 75 % smear density fuel. The inner and outer clads have identical thickness. Figure-96 shows the variation of FCMI as a function of peak burnup. At 5 at %, the fuel touches the outer clad. However, fuel swelling continues inward. At around 8 at % burnup, the fuel touches also the inner clad and becomes radially constrained in both directions; hence, FCMI increases rapidly. At 11.4 at %, clad strain reaches 1 % at the outer region and the simulation was terminated.

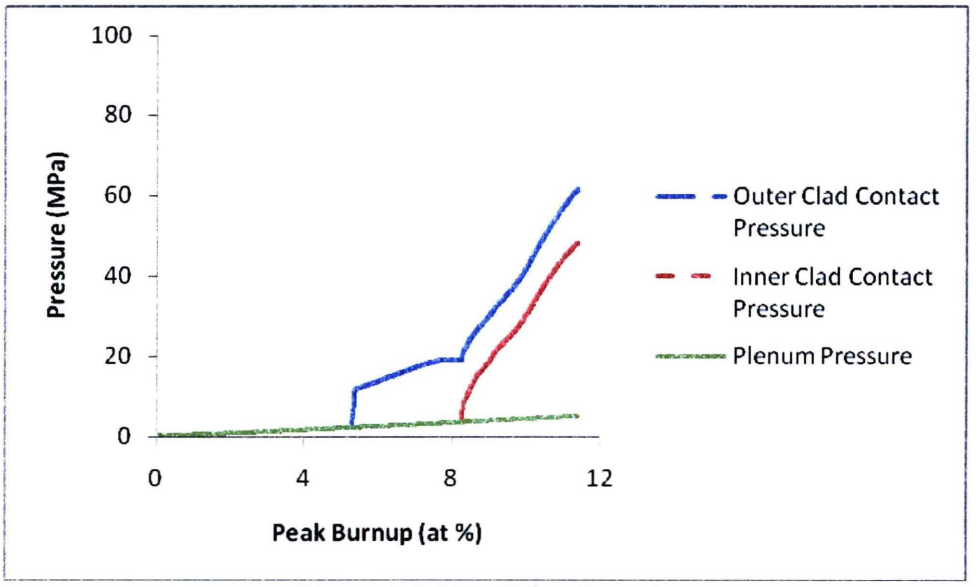


Figure-96: FCMI for Case-A

Case-B:

In Case-B, the fuel smear density has been reduced from 75 % to 70 %. As a result, the fuel does not touch the inner clad during the operation. Morever, the FCMI at the outer clad remains relatively low (Figure-97). As a consequence, a higher peak burnup (16.6 at %) coudl be achieved.

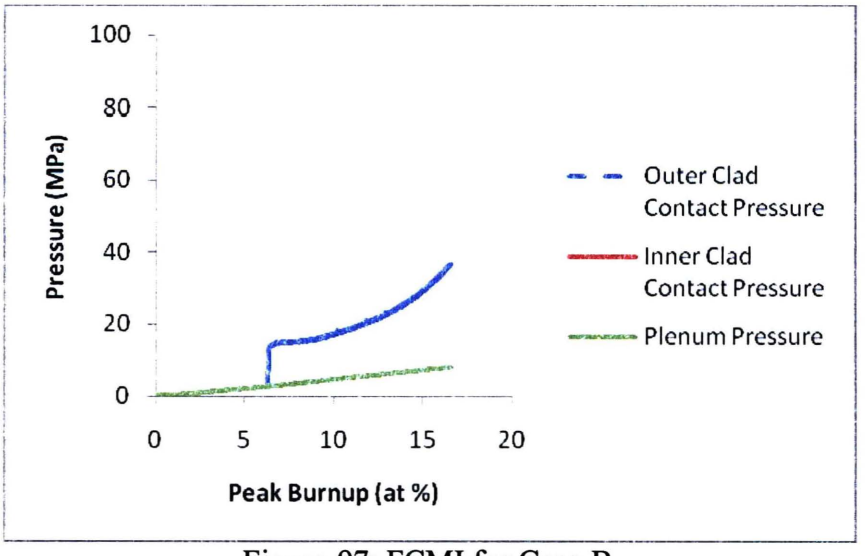


Figure-97: FCMI for Case-B

CASE-C:

In Case-C the inner and outer clad thickness was reduced, while the smear density was kept at 70 %. As a result, the heavy loading was increased by 13 %. Achievable burnup is now 15.6 at %. No FCMI is observed in the inner clad region (Figure-98).

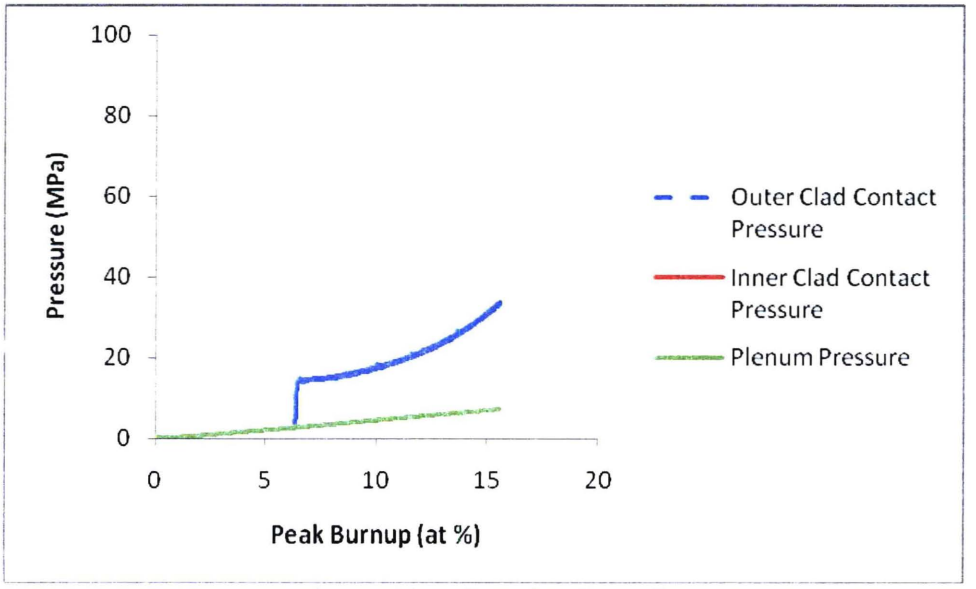


Figure-98: FCMI for Case-C

4.3.5. Transient Analysis

The ULOF transient analysis has been performed for CASE-C at 10 at % peak burnup. Figure-99 shows the normalized power and flow coastdown as functions of time. Consistently with the power and flow coast down, the peak coolant temperature rises as given in Figure-100. The resulting variation of the FCMI stress is given in Figure-101. Note that, no FCMI is observed at the inner clad region. After 40 seconds, the clad loading is identical to the plenum pressure.

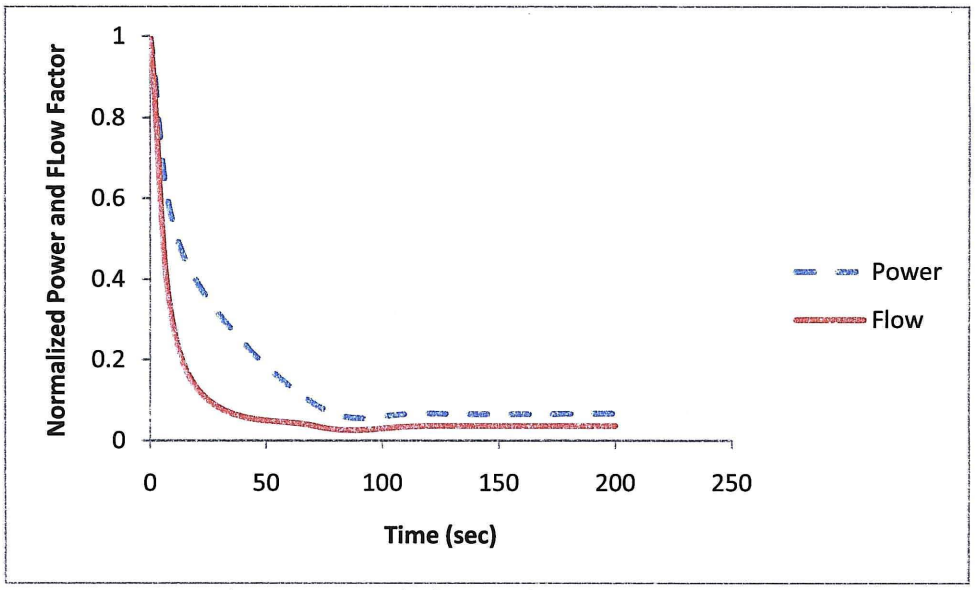


Figure-99: Variation of the power and flow

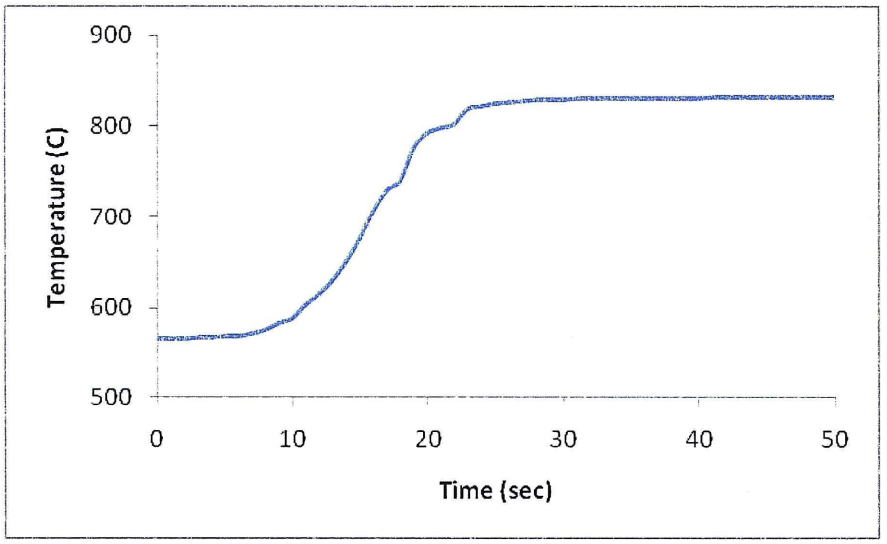


Figure-100: Variation of the coolant temperature

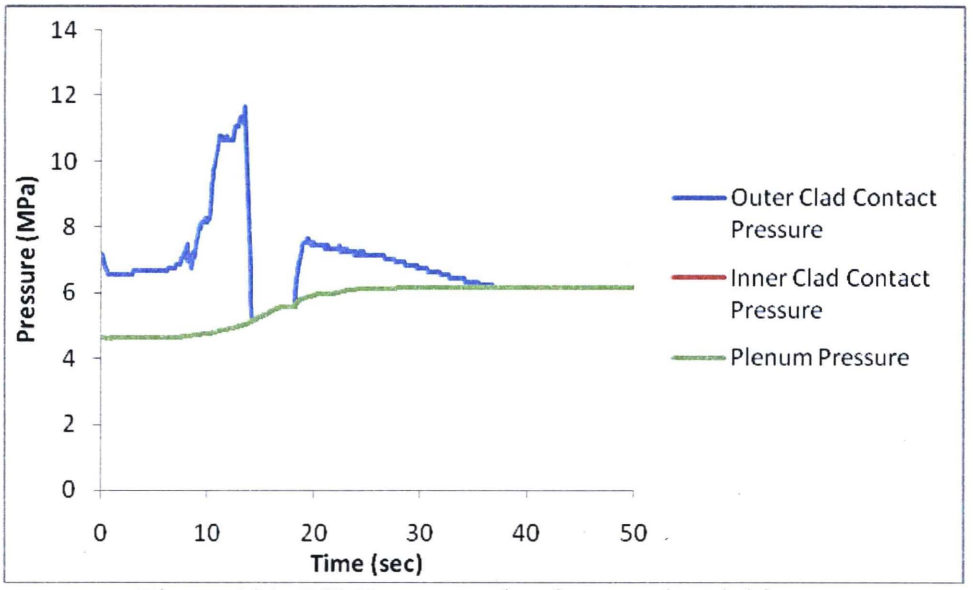


Figure-101: FCMI stress early after transient initiates

The results are also given for t = 1000 seconds in Table-35. No failure is predicted with CDF and Constraint Diffusional Cavity Growth models. Clad wastage of the inner region is only due to sodium corrosion because fuel and clad do not touch. On the other hand, significant wastage is predicted for the outer clad region due mainly to eutectic penetration in 1000 seconds.

Table-35: Transient results after 1000 seconds

Parameter	Value
Inner Clad CDF	0.20
Outer Clad CDF	0.15
Inner Clad Crack Radius/Critical Crack Radius (microns)	0.33/1.22
Outer Clad Crack Radius/Critical Crack Radius (microns)	0.27/1.57
Inner Clad Wastage (microns)	3.1
Outer Clad Wastage (microns)	85.9

4.3.6. Comments on the Annular Fuel Design

An internally and externally cooled annular fuel pin design was examined for Sodium Fast Reactors. Allowing for internal cooling reduces the surface heat flux, fuel centerline temperature and fission gas release; hence, it may provide more room for power uprate. On the other hand, allowing for an inner channel isolated from the outer channels could potentially cause problems

with the coolant flow distribution. The flow needs to be adjusted between inner and outer channels from BOL to EOL such that peak clad temperatures will be similar at the inner and outer channels. During the operation, the straining of the cladding at the inner and outer surfaces are not in equal magnitude, hence, the survey should be conducted in burnup dependent form to find the optimized geometry.

Lower fission gas release may allow for a smaller volume of plenum; hence, a lower core pressure drop. As a consequence, there could be room for power uprate while keeping the inlet and exit conditions same.

In this study, 1 % clad strain was used as a limit; however, up to 3 % could be acceptable for a typical fast reactor. Allowing for the straining for the cladding material may lead to a design with a much higher burnup.

Finally, the study shows that the fuel tends to swell outwards; hence since there is limited FCMI and FCCI for inner cladding, a design with unequal clad thickness could be feasable to increase the heavy metal inventory.

5. MODELS FOR MIXED OXIDE FUEL

5.1. Introduction

The oxide fuel has been widely used in the world in light water reactors, fast reactors and gas cooled reactors. Its maturity and ease of fabrication make it a very attractive candidate for future nuclear systems. First, the oxide fuel has good chemical stability with the stainless steel clad at high temperatures (up to 700 ^{0}C); in addition, it is possible to control the fuel-clad chemical interaction by adjusting the initial oxygen-to-metal ratio of the fuel. Its high melting temperature is also advantageous. However, a significant part of the fuel operates below half of the melting point. As a consequence, the fuel is very hard and stiff and Fuel Clad Mechanical Interaction (FCMI) becomes a significant life limiting issue, especially for the transient over-power scenarios. Developing highly creep resistant cladding materials, such as Oxide Dispersion Strenghened Ferritic/Martensitic Stainless Steel, may enable operation at higher temperature and burnup, thus rendering oxide fuel quite promising for fast reactor systems.

Liquid metal cooled fast reactors operate with a higher linear heat rate and higher coolant temperature compared to Light Water Reactors (LWRs). Furthermore, the fuel smear density and the initial oxygen to metal ratio is lower than LWRs. As a result, the operating fuel temperatures are much higher compared to light water reactors. The high temperatures and temperature gradients result in a complex chemical environment, in which migration of the fuel constituents, such as cesium, oxygen, molybdenum and plutonium has significant influence on the overall performance of the fuel pin.

In addition to chemistry, high temperatures affect fission gas release and swelling. Surface diffusion may allow bulk intra-granular bubble movement and direct discharge into the grain boundaries. Furthermore, fuel thermal creep plays a major role in grain boundary gas swelling, bubble interlinkage and gas release to the free volume (plenum) of the fuel pin.

Because of the complexity of the phenomena to be modelled, benchmarking of the oxide fuel code against experimental data is a most crucial step. However, the experimental fast-reactor

data readily available are limited. FFTF, JOYO and EBR-II available experimental database is used in this work to benchmark FEAST-OXIDE.

5.1.1. Description of the Mixed Oxide Fuel Pin

A typical mixed oxide fuel pin is shown in Figure-102. A solid cylindrical or annular oxide fuel slug is encapsulated by the cladding. The gap between the fuel and cladding is occuppied by a fill gas (Helium) at the beginning of life. Later, the noble fission gas concentration in the gap becomes significant. If oxygen is available and the fuel surface temperature is above 600 ^{0}C, Cesium Molybdenum Oxide (Cs_2MoO_4, also known as Joint Oxide Gain, or JOG) may also be present in the gap region.

Oxide Dispersion Strengthened (ODS) steels are being considered worldwide as cladding materials for the oxide fuels [78], [79]. However, ODS technology is not ready now. Low swelling austenitic steels are in use today, instead. HT9 clad, which is a good material with the metal fuel pin, is not convenient for the oxide fuel, because its thermal creep resistance at high temperatures is not high enough to sustain the FCMI load for steady state as well as transient scenarios, which are typical of oxide fuel pins.

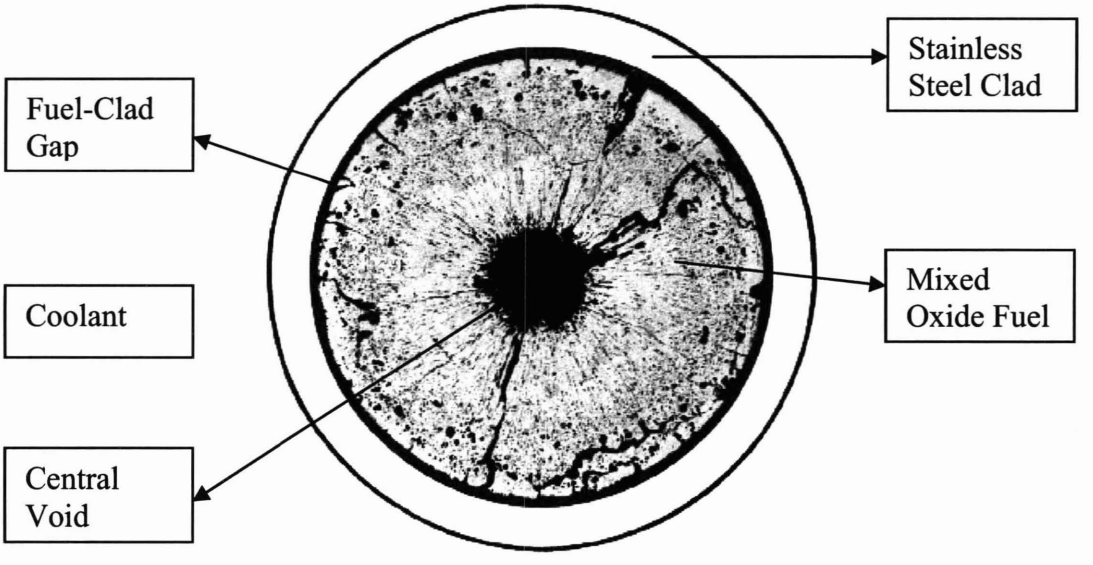


Figure-102: Cross-sectional view of a mixed oxide fuel pin [16]

5.1.2. Thermo-mechanical Behavior of the Oxide Fuel

Table-36 reports the sequence of key physical phenomena during the irradiation of a typical oxide fuel pin, as deduced from the operating experience in the Fast Flux Test Facility (FFTF) in Richland, Washington.

Table-36: Description of the burnup history of the typical FFTF fuel with no swelling clad.

Burnup (at %)	Relevant phenomena
0.0	Irradiation begins
0.0-0.5	Fuel Restructuring takes place (1) Brittle part of the fuel cracks due to the thermal stresses (1) Pores above 1300 ^{0}C migrate towards center of the fuel and form a central hole. (2) Pore shrinkage occurs due to irradiation induced densification (3) Grain growth takes place (4) Oxygen to metal ratio redistributes radially (fast process) (5) If the temperature is high enough (above 2000 ^{0}C), significant plutonium migration towards center of the fuel occurs. (5) Gas swelling rate due to fission gases is significant. (6) Fission gas release starts
1.0-2.0	(1) Fuel becomes axially and radially constrained by the clad at peak power location. (2) Radial contact pressure between fuel and clad rises to a level somewhat higher than plenum pressure. As-fabricated porosity and gas bubbles get compressed. Swelling due to the solid fission products, which are incompressible, continues.
5.0-7.0	(1) Joint Oxide Gain (JOG) forms at the fuel surface due to cesium and molybdenum diffusion and oxygen availability. Diffusion of the fission products generates internal stresses. As a consequence, the effective grain size drops due to transgranular fracture. As-fabricated porosity shrinkage occurs. Moreover, JOG improves the fuel clad gap conductance and significant fission gas release may result due to the reduced grain size at the peripheral region. (2) Fuel Clad Chemical Interaction (FCCI) starts, and increases for the next 5 at % burnup, then levels off. (3) Cesium axial migration may start causing a noticeably higher solid fission product swelling at top of the fuel.
15-20	Solid fission product swelling may lead to disapperance of all as-fabricated the gap is closed. Thus, FCMI rises and clad straining occurs. Clad breach may result.

5.1.3. Project Objectives and Review of Current Oxide Fuel Codes

The objective of this work is to develop a robust and reliable code, which we will call Fuel Engineering And Structural analysis Tool (FEAST-OXIDE), to model the irradiation behavior of mixed oxide fuels in sodium-cooled fast reactors. Given the fuel pin geometry, composition and irradiation history, FEAST-OXIDE can analyze the fuel slug and cladding thermo-mechanical behavior at both steady state and transient conditions. The ultimate goal is to use FEAST-OXIDE in the development, design and licensing process of oxide-fuelled fast reactors.

A literature review has been conducted to identify and assess the major oxide fuel codes in use or being developed to date.

LIFE-II is a thermo-mechanical analysis code developed at the Argonne National Laboratory in early 1970s to simulate the steady state behavior of the oxide fuel code [4]. It is designed to predict (1) Temperature distribution in the element, (2) Dimensions of the fuel and cladding, including length changes, (2) Extent of fuel restructuring, (3) Amount of gas released to the plenum, (4) Plenum pressure, (5) Distribution of the fuel constituents (6) Hot-pressing of the fuel (7) Stress-strain distribution including a breakdown into thermoelastic, thermal and irradiation creep and swelling deformations for each region of fuel and cladding, (7) Fuel/clad contact pressure and (8) Amount of cumulative damage that has occured in the cladding to reduce the expected fuel-element life time. The mechanical analysis model adopts a 1D approach. Cracking and healing is allowed in the brittle region (below 1300 ^{0}C) of the fuel. Fuel swelling and fission gas release models are purely empirical [4]. The effect of Joint Oxide Gain (JOG) formation on temperature distribution, stresses and strains, and fission gas release and swelling was not accounted for. However, ignoring JOG effects can result in a few hundred degrees of overestimation of the peak fuel temperature [80], thus resulting in inaccurately high fuel swelling and clad strains at high burnup. Finally, axial migration of cesium was not included in LIFE-II, which may lead to significant underestimation of the fuel clad mechanical interaction at top of the fuel pin.

COMETHE II computer program was formulated by Belgonucleaire [5] to predict the steady-state thermal and mechanical behavior of oxide fuel pins during their irradiation life. Fuel

swelling model is based on an empirical correlation; whereas fission gas release is based on Booth's diffusion model [81]. The mechanical analysis adopts a 1D approach similar to LIFE-II. The fuel chemistry model has not been included in this code; so the effects of fuel constituent migration are not considered.

FRUMP is a more detailed steady state code compared to the previous two [6]. It was developed by Harwell Institute in UK. It was the first code that included physically based fission gas release and swelling and fuel restructuring models. Similar to the previous codes, the fuel chemistry was not included. In the 1980s Harwell Institute decided to develop a new oxide fuel performance code for the following reasons: (1) It was desired to have a sophisticated code that can analyze both steady-state and transient behavior of the oxide fuel, (2) Incorporate new findings on fission gas release and swelling behavior of the fuel and advanced models developed in early 1980s. The name of that second code is TRAnsient Fuel Interpretive Code (TRAFIC) [11]. TRAFIC-1 has capabilities for analysis of several phenomena: (1) Fuel restructuring: cracking, porosity redistribution, grain growth, (2) Chemical effects: fission product behavior, plutonium and oxygen redistribution, (3) Temperature distribution: molten fuel generation, coolant boiling, (4) Fission gas behavior: fuel swelling and fission gas release, (5) fuel pin mechanics: cladding loading and failure limits. The OGRES model was used to predict the fission gas release and swelling behavior for steady state operation. The NEFIG model is activated for transients, up to the melting temperature. Molten fuel fission gas release and swelling behavior is described by the AFMOT and MINIMOT models [3]. TRAFIC-2 [82] has the following additional options: (1) An implicit treatment for the coupling of the stresses, temperatures and displacements is allowed, (2) Cladding plasticity is modeled, (3) The boiling model was inadequate in TRAFIC-1 once flow reversal (following dryout) had occured. Homsep multi-bubble model was combined with TRAFIC to improve the code performance. It allows for simulating the boiling even when the flow reversal (following dryout) occurs. Although the TRAFIC code has much better fuel chemistry model, the effects of the JOG formation on fission gas release and swelling and mechanical analysis models were not included in this code.

LIFE-IV was developed at Argonne National Laboratory in the 1980s for steady-state and transient behavior of the oxide fuel [13]. The code mechanical analysis model is based on a one-

dimensional generalized plane-stress strain analysis. The fuel part includes the followings: (1) Thermal and fission enhanced creep, (2) Hot pressing and sintering, (3) Cracking, fuel fragment relocation and crack healing, (4) Pore and gas bubble migration, (4) Swelling: fission gas and solid fission product, (5) Grain growth, (6) Oxygen and Plutonium redistribution, (7) Axial vapor phase transport and (8) Fuel melting and molten fuel axial migration. A physics based but less sophisticated fission gas release and swelling model [12] is adopted compared to OGRES model. Perphaps the most significant shortcoming of the code is that the JOG formation and its effect on thermal, fission gas release and swelling and mechanical performance were not included.

The GERMINAL code was developed by CEA/DEC to simulate the steady state and transient thermo-mechanical behavior of the oxide fuel for the fast reactor operating conditions [14], [15]. It includes (1) Fuel evolution (cracking, porosity redistribution, central hole and pellet surface diameter modifications, plutonium and oxygen radial migrations, swelling, etc.), (2) Fission gas production and release, (3) Clad evolution (thermal expansion, irradiation induced creep and swelling), (4) fuel/clad gap size and heat transfer coefficient, (5) Fuel clad mechanical interaction after gap closure, (6) Fuel melting and axial mass redistribution, (7) Effect of volatile fission products on gap heat transfer (JOG formation) and fission gas release and swelling behavior. The models are purely empirical but it is the first code that includes the impact of volatile fission products on fuel performance.

Note that none of the codes mentioned above includes the kinetics behavior of the clad wastage formation.

FEAST-OXIDE was developed as part of this thesis to simulate the behavior of the mixed oxide fuel in steady-state and design basis accident scenarios. The mechanical analysis module is modeled according to the LIFE algorithm, which is a one-dimensional generalized plane strain approach. The code adopts the OGRES and NEFIG models for fission gas release and swelling behavior of the fuel. Furthermore, the effect of JOG formation on the fission gas release and swelling has been included in the code. Unlike other codes, the kinetics of the FCCI is included to predict the time dependent behavior of the clad wastage. Thermal diffusion models are adopted to predict the important chemical effects, such as JOG formation, and oxygen, plutonium and cesium

radial and axial distribution. Fuel restructuring effects, such as pore migration, grain growth, hot pressing and irradiation induced densification are all included. Hence, FEAST-OXIDE includes all the known important phenomena of the oxide fuel with more mechanistic, physics-based approaches compared to the other codes in the literature.

This section provides a detailed description of the FEAST-OXIDE code structure (Section-5.1) and constitutive models (Section-5.2 through 5.6). Validation of the code using the available irradiation data is shown in Section-6, for steady state and transients.

5.1.4. FEAST-OXIDE Code Structure

The FEAST-OXIDE code is composed of several modules in coupled form to simulate oxide fuel thermo-mechanical behavior. The code is written in FORTRAN-90 language.

The code implements an explicit numerical algorithm. The flow sheet of the calculations is given in Figure-103. Note that the fission gas release and swelling module is quite sophisticated and requires short time steps, of the order of 5 seconds, therefore a typical irradiation simulation results in an execution time of the order of 5-10 hours, when run on a single CPU personal computer.

The input file for the code allows the specification of the operating conditions and the initial fuel pin and coolant flow path geometry.

The code performs the following steps for each axial node at each time step:

1- Radial power distribution within the fuel slug is calculated based on the actinide concentration and as-fabricated porosity concentration within each radial node.
2- Contact pressure between the fuel and clad is calculated as a function of displacement of fuel and cladding.
3- Temperature distribution of the fuel pin is calculated as a function of radial power profile. Furthermore, the coolant axial temperature distribution is calculated with the

Single Mass Velocity Model [27]. This calculation is performed every 100,000 seconds. The Gauss-Seidel matrix solver algorithm is used [28].

4- The code calculates the evolution of oxygen-to-metal ratio with burnup every 100,000 seconds. Oxygen-to-metal ratio increases with burnup due to heavy metal consumption.

5- Radial distribution of oxygen is calculated using the thermal diffusion model every 100,000 seconds.

6- Radial plutonium distribution is calculated using the thermal diffusion model.

7- Joint Oxide Gain formation at the fuel surface is calculated.

8- Migration of the as-fabricated porosity and central void formation (first 300 hours) is predicted

9- Calculation of the fuel grain growth is performed.

10- The fuel stress/strain analysis is performed. Using the creep strains and axial strains calculated at the previous step, the average radial displacement can be calculated for each radial ring by using the Gauss-Jordan matrix solver algorithm [29]. After that, the axial force balance is used to calculate either the axial strain if the gap between the fuel and the clad is open; or the axial friction force, if the gap between the fuel and the clad is closed. Finally, the creep and plasticity strains and hot pressing and irradiation induced densification strains are calculated which will be used in the next time step.

11- Cladding wastage is calculated.

12- Given the contact pressure between fuel and cladding and coolant pressure outside the cladding, the radial displacement for each radial ring in the cladding are solved using the Gauss-Jordan matrix solver. After that, the axial force balance is used to calculate the axial strain. Finally, cladding creep strains are updated again and used in the next time step.

13- Given the hydrostatic stress, temperature and fission rate of each radial ring, the fission gas release and swelling behavior of the fuel is calculated with OGRES Model. Swelling due to gas bubbles at grain edges and faces, intra-granular gas swelling and solid fission product swelling are accounted. If it is a transient situation, the NEFIG model is activated to describe the intra-granular gas behavior.

14- Axial migration of cesium is calculated.

15- The plenum pressure calculation is performed by assuming that the perfect gas law applies. The sum of the open porosity within the fuel slug and the plenum region at the top of the fuel slug is the volume occupied by gas.

16- Print Output.

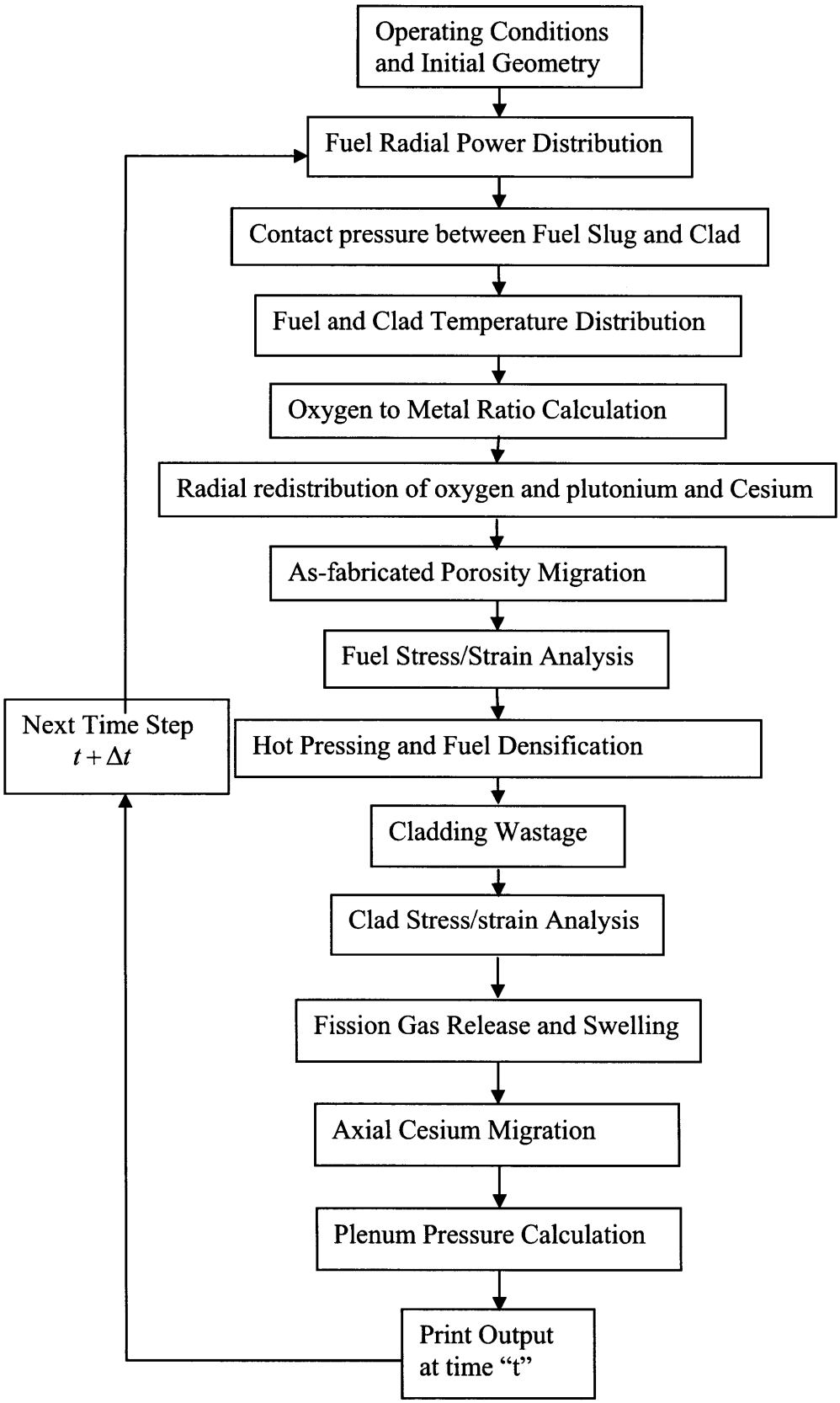


Figure-103: Flow sheet of FEAST-OXIDE

5.2. Fission Gas Release and Swelling

5.2.1. Introduction

The gas atoms produced during fission have very low thermodynamic solubility in UO_2 and similar oxide fuels during nuclear reactor operation [2]. The insolubility of fission gas and the high concentration of nucleation sites for bubbles have led to problems in constructing theories to explain the high rates of release of fission gases observed in UO_2 at temperatures above ~1300 ^{0}C.

The Operational Gas Release and Swelling (OGRES) model developed at Harwell is a mature model based on 20 year experimental and theoretical work (1960s – 1980s) [7-10]. It is incroporated into FEAST-OXIDE. The model treats intragranular and intergranular gas behavior, separately. The intragranular model describes the gas release to the grain boundary and the behavior of the intragranular bubbles. It simply superimposes all the relevant processes onto a system with one representative bubble size. This has the advantage of retaining the correct physical representation while producing a model that is sufficiently fast for use in larger fuel codes. The intergranular, or grain boundary, model describes the swelling behavior of grain boundary bubbles, interlinkage and release to the fuel pin free volume. It is a sophisticated model because (1) grain edge and face porosity are modeled separately, (2) partitioning of the gas between the faces and edges and its effect on release from the grains, as well as gas transfer between edge and face bubbles are modeled, (3) dynamics of vacancy flow on the grain boundaries are included.

5.2.2. Intragranular Gas Model (OGRES-I)

Normal Operation:

The intragranular gas model (OGRES-I) deals with four processes: nucleation of bubbles on vacancy clusters in fission tracks; complete destruction of bubbles by fission spikes; diffusion of gas from the interior of the fuel grains to the grain boundaries; and bubble movement towards the grain boundary under the temperature gradient driving force (only above 1600 ^{0}C).

The main premises are

(a) Gas migrates through the fuel matrix as single gas atoms, and gas release from the matrix is by diffusive flow to the boundaries of the spherical grains.

(b) Fission gas bubbles trap migrating gas atoms

(c) The gas bubbles are immobile up to 1600 ^{0}C, in accord with the experimental observations for bubbles existing in the unrestructured and low temperature equiaxed regions of the oxide fuel.

(d) Above 1600 ^{0}C, which corresponds to the high temperature region of the equiaxed grain growth zone and the columnar grain region, gas release is very high and is dominated by the migration of larger bubbles under the temperature gradient driving force. These bubbles are large enough for their temperature gradient driving force to overcome the dislocation pinning force, when they migrate, without further pinning towards grain boundaries.

(e) The passage of fission fragments through the fuel causes gas atoms to be knocked back into the fuel matrix, thus destroying individual bubbles.

The equations describing the fission gas and bubble behavior within the fuel grains are written as follows:

$$\frac{\partial c_g}{\partial t} = \frac{1}{r^2}\frac{\partial}{\partial r}\left(D_g r^2 \frac{\partial c_g}{\partial r} \right) + K_g - D_g k_b^2 c_g - K c_t + b c_{gb} \tag{5.2.1}$$

$$\frac{\partial c_{gb}}{\partial t} = D_g k_b^2 c_g + K c_t - b c_{gb} - \dot{G} \tag{5.2.2}$$

$$c_t = c_g + c_{gb} \tag{5.2.3}$$

$$\frac{dc_b}{dt} = K c_t - b c_b - \frac{\dot{G}}{n_b} \tag{5.2.4}$$

$$n_b = \frac{c_{gb}}{c_b} \tag{5.2.5}$$

$$p_{gas} = -\sigma + \frac{2\gamma}{r_b} \tag{5.2.6}$$

c_g: Gas atom density within the fuel matrix (atom/m³)

c_{gb}: Gas atom density within the gas bubbles (atom/m³)

c_t: Total gas atom density (atom/m³)

c_b: Bubble density (bubble/m³)

n_b: # of gas atoms per bubble

D_g: Gas atom diffusion coefficient (m²/s)

K_g: Gas atom generation rate due to fission (atom/m³/s)

k_b^2: Sink strength of bubbles for the migrating gas atoms (atom/m²)

K: Gas bubble nucleation rate constant (1/s)

b: Probability per unit time that a particular bubble will be completely destroyed by a fission fragment (1/s)

$\dot{G}$: Gas atom deposition rate to the grain boundary by bubble migration (atom/m³/s)

p_{gas}: Gas pressure in the bubble (Pa)

σ: External stress (Pa)

γ: Surface tension (1 J/m²)

r_b: Bubble radius (m)

The coupled equations above are solved for the average grain for each fuel radial node by using the finite difference procedure. The grain is divided into 15 spherical nodes as suggested in Ref. [83]. The following boundary conditions are adopted:

$\frac{dc_g}{dr} = 0$ at r = 0

$c_g = 0$ at r = R

R is the grain radius.

Solving the coupled equations given above, the net rate of change of the gas within the grains can be calculated. The amount of gas leaving the grain is assumed to deposit into the grain boundary bubbles.

The constitutive relations will be disscussed next.

Gas atom diffusion coefficient:

The trap free gas diffusion coefficient is given as a function of temperature and thermal rating (specific power) [32]. The thermal rating reflects the enhancement due to fission. The fission enhanced diffusion becomes significant at temperatures below half of the melting point.

$$D_g = 7.6\times10^{-10}\exp\left(-\frac{35000}{T}\right)+\left[2.3\times10^{-20}\exp\left(-\frac{15000}{T}\right)+3\times10^{-26}\right]R \qquad (5.2.7)$$

D_g : Gas diffusion coefficient (m^2/s)

R: Rating (W/kg)

T: Temperature (K)

Eq-5.2.7 is modified if the Joint Oxide Gain (JOG) forms at the fuel surface (see section-5.3.5). The formation of JOG and resulting intense diffusion of fission products and internal stresses generated in the fuel results in transgranular cracking of the grains. Hence, reduced grain size may lead to a higher fission gas release rate at the brittle peripheral region of the fuel ($T < 1300\ ^0C$). To account for the effect of JOG on the fission gas release, the gas diffusion coefficient has been increased as follows:

$$D_g = 7.6\times10^{-10}\exp\left(-\frac{35000}{T}\right)+\left[2.3\times10^{-20}\exp\left(-\frac{15000}{T}\right)+5\times10^{-25}\right]R \qquad (5.2.8)$$

Note that, the resulting low temperature diffusion coefficient is very similar to the reported gas diffusion coefficient for the OGRES at an earlier work [7]. The calibration study is given in Section-5.2.6.

Gas atom generation:

Gas atom generation occurs by fission. Only the stable gas atoms are modeled.

$$K_g = Y\dot{F} \tag{5.2.9}$$

K_g: Gas atom generation rate (atoms/m³/s)

Y: Fission yield of gas atoms generated by fission (0.25 for U and Pu in fast reactors) [2]

$\dot{F}$: Fission rate (fission/m³/s)

Gas diffusion into the bubbles:

Gas diffusion into the bubbles is given as a function of the gas diffusion coefficient, gas atom density in fuel matrix and the sink strength of bubbles $\left(D_g k_b^2 c_g\right)$

Sink strength of the bubbles for the migrating gas atoms is taken as spatially independent and slowly varying function with time, in accord with the normal rate theory prescription.

$$k_b^2 = 4\pi r_b c_b \tag{5.2.10}$$

Thus, as bubbles size and population increase, the sink strength increases.

Bubble resolution:

Bubble destruction by fission fragments is given as proportional to the bubble resolution coefficient and gas atom density in intragranular bubbles $\left(bc_{gb}\right)$

Bubble resolution coefficient is defined in terms of fission spike radius and length and fission rate:

$$b = 2\pi R_f^2 l_f \dot{F} \tag{5.2.11}$$

R_f: Radius of the fission spike (6 nm)

l_f: Length of the fission spike (6 μm)

The factor 2 arises because there are two fission fragments per fission.

Gas bubble nucleation:

The bubble nucleation rate is Kc_t. It is controlled by the total gas concentration (c_t) because the new bubbles are nucleated in the wake of the fission tracks in which the remains of bubbles annihilated in the re-solution process are dissolved.

The gas bubble nucleation constant, K, is defined in terms of a fraction of the resolution coefficient.

$$K = 0.027 \times b \tag{5.2.12}$$

Gas bubble migration to the grain boundary:

The large release of gas found above 1600 ^{0}C is due to migration of fission gas bubbles under the temperature gradient driving force.

At high temperatures there is a tendency for large gas bubbles to nucleate at dislocations and other types of defects. It is asserted that these bubbles nucleate heterogeneously at a characteristic volume concentration ($c_b \sim 10^{18}$/m^3) and they grow at their nucleation sites, by the accumulation of gas atoms, until they are large enough for the temperature gradient driving force to overcome the dislocation pinning force, so they migrate, without further pinning, towards the grain boundaries. The rate of gas migration associated with bubble movement is given as follows [9]:

$$\dot{G} = 4\pi D_g' R_c c_t c_b F \tag{5.2.13}$$

$$D_g' = 0.973 \frac{D_g b}{D_g k_b^2 + b} \tag{5.2.14}$$

R_c is the effective capture radius of the bubbles for gas (40 nm).
F is the fraction of bubbles which survive their journey to the grain boundaries, this is given by:

$F = h/a \quad h \leq a$

$F = 1 \quad h > a$

a is the effective grain size in the columnar grain region (32 μm)

h is the distance a bubble moves before being destroyed, and is given by $h = v_b/p$

v_b is the bubble velocity given as follows:

$$v_b = \frac{3\delta_s D_s Q_s \nabla T}{40\times10^{-9} RT^2} \tag{5.2.15}$$

δ_s: Effective surface thickness = 0.34 nm

D_s: Surface diffusion coefficient = $50\exp\left(-\frac{45280}{T}\right)$ (m²/s)

Q_s: Heat of transport = 0.42 MJ/mol

∇T: Temperature gradient (K/m)

R: Gas constant = 8.314 J/mol/K

p is the probability per unit time that a particular bubble is destroyed.

$$p = \frac{b}{\beta}$$

b is the resolution coefficient. The parameter β is included to provide a rough measure of the effectiveness of bubble destruction (for large bubbles) by a fission fragment. Its value is 7.

The Equation of State:

Carnahan-Starling hard sphere equation of state model [84] is applied to calculate the radius of the intra-granular gas bubbles. At high pressures (above 0.1 GPa), the reduced Van der Waals equation of state is shown to be seriously in error with respect to the experimental data while the hard sphere model is in good agreement [84]. Note that the pressure of the intragranular gas bubbles is usually significantly above 0.1 GPa.

$$\frac{PV}{n_b kT} = \frac{1+y+y^2-y^3}{(1-y)^3} \tag{5.2.16}$$

$$y = \frac{\pi d^3}{6}\frac{n_b}{V} \tag{5.2.17}$$

P: Bubble Pressure (Pa)

V: Bubble Volume (m^3)

n_b: Gas atoms per bubble

k : Boltzmann constant = 1.3806×10^{-23} J/K

T: Temperature (K)

Hard sphere radius is given as follows:

$$d = 0.445\left(0.8542 - 0.03996\ln\left(\frac{T}{231.2}\right)\right) \text{ (nm)} \qquad (5.2.18)$$

Grain Size:

The OGRES model assumes constant effective grain size during the simulation. The grain size as a function of the fuel temperature is given in Figure-104. Grain growth occurs in fast reactor oxide fuel during the early operation. The temperature distribution calculated at the end of the restructuring period is used to calculate the effective grain size for each radial node. Further discussion about the grain growth mechanism and its effect on mechanical properties are given in Section-5.3.8 and 5.6.2, respectively.

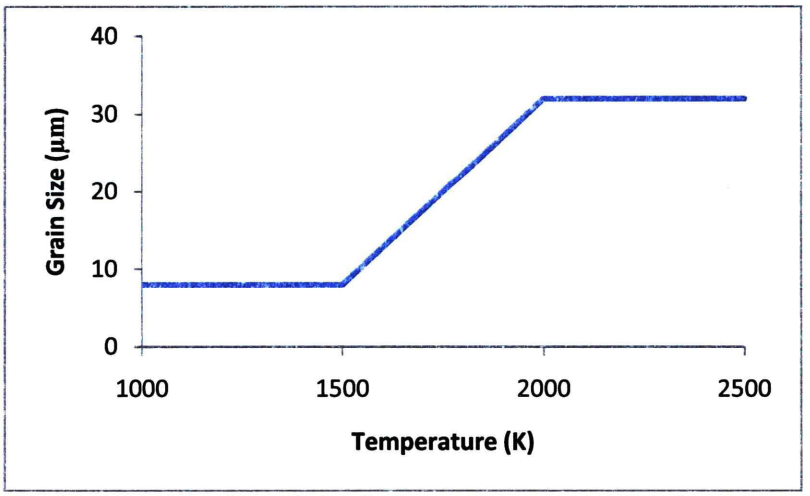


Figure-104: Grain size as a function of the fuel temperature (as-fabricated grain size is 8 µm)

Intragranular gas modeling for the transient scenarios:

Fission gases play an important role in the development of any hypothetical transient overpower accident. The Non-Equilibrium Fission Gas (NEFIG) model was developed as a part of OGRES model to describe intragranular gas behavior during rapid heating of the fuel [10], [83].

NEFIG follows the transfer of gas from solution into gas bubbles; the coalescence of the bubbles arising from their uni-directional drift in a temperature gradient; the change in bubble radius arising from bubble coalescence, the time-dependent acquisition of vacancies from the grain boundaries and the release of gas in the form of gas bubbles.

Consistently with OGRES, the bubble population is represented by a single bubble size. The dissolved gas concentration decreases with time due to (1) pick-up of single gas atoms by bubbles migrating under the influence of a temperature gradient driving force, and (2) the collection of single gas atoms into the bubbles by both gas atom and bubble random motion. Hence, the change in the dissolved gas atom concentration, c_g, is then given by

$$\frac{dc_g}{dt} = -\pi r_b^2 v_b c_g c_b - 4\pi r_b c_g c_b \left(D_g + D_b\right) \tag{5.2.19}$$

$$D_b = \frac{3D_s \lambda \Omega}{2\pi r_b^4}$$

D_b: Bubble diffusion coefficient (m^2/s)

Ω: Atomic volume = 4.09E-29 m^3

λ: Thickness of the diffusivity layer = $\Omega^{1/3}$ (m)

Gases in the fuel matrix are trapped by the bubbles. Hence, the balance equation is as follows:

$$\frac{d\left(c_{gb}\right)}{dt} = -\frac{dc_g}{dt} \tag{5.2.20}$$

Gas bubble population decreases with time due to coalescence of the gas bubbles:

$$\frac{dc_b}{dt} = -\alpha_c r_b^2 c_b^2 v_b - 8\pi r_b c_b^2 D_b \tag{5.2.21}$$

The first term is due to unidirectional (temperature-driven) bubble motion and the second to random bubble motion. Because bubbles are travelling with the same uni-directional velocity cannot coalesce, the parameter α_c has been introduced to simulate the behavior of a size distribution of bubbles exhibiting such motion. The value of α_c is 2π.

The representative bubble radius, r_b, varies during a transient through coarsening of the bubble population by coalescence, the accretion of single gas atoms into bubbles, and the influx of vacancies to the bubbles, arising from their non-equilibrium disposition.

$$\frac{dr_b}{dt} = \frac{D_U p^{ex} \Omega}{r_b kT\left[1+\frac{a(\pi r_b c_b)^{0.5}}{3}\right]} - \frac{r_b \frac{dc_b}{dt}}{3c_b} - \frac{\nu\Omega\frac{dc_b}{dt}}{4\pi r_b^2 c_b} \tag{5.2.22}$$

$$p^{ex} = p_g - \sigma - \frac{2\gamma}{r_b} \tag{5.2.23}$$

D_u : Cation self-diffusion coefficient $= 2\times10^{-4}\exp\left(-\frac{55650}{T}\right)$ (m²/s)

p^{ex} : The effective bubble excess pressure (Pa)

ν: The number of atomic volumes associated with each gas atom in solution (2)

a: Grain size (m)

The fraction of the released gas is calculated by the following relation, assuming the grain is spherical:

$$f(t) = 1 - h(t)^2 \frac{(3a - h(t))}{2a^3} \tag{5.2.24}$$

$$h(t=0) = a \text{ and } \frac{dh}{dt} = -v_b$$

The number of gas atoms per gas bubble is given as follows:

$$n_b = \frac{c_{gb}}{c_b} \times \left(1 - f(t)\right) \tag{5.2.25}$$

Finally, the gas bubble pressure, p_g is calculated using the hard sphere equation of state (Eq-5.2.16.).

5.2.3. Grain Boundary Gas Behavior (OGRES-II)

When the gas is released from the fuel grains it collects initially at the grain boundaries before being released to the pin free volume. It is generally accepted [8], [83] that the major process leading to gas release is the growth (Figure-105) and subsequent interlinkage of grain boundary bubbles (Figure-106) for a typical Sodium Fast Reactor operating condition. Experimental evidence shows that interconnected channels exist along the edges of grains after relatively modest burn-ups (Figure-106) and temperatures, and that these can permit continuous gas release [8].

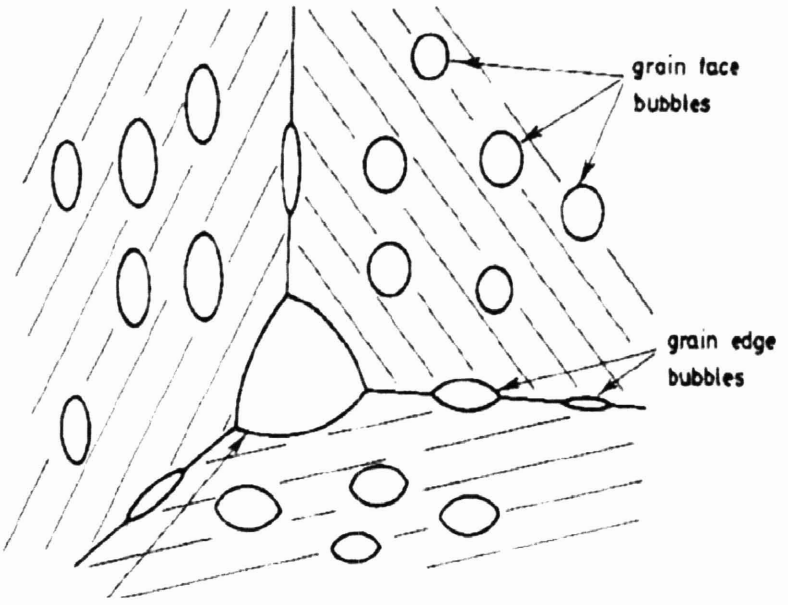


Figure-105: Edge and face bubbles before interlinkage [83]

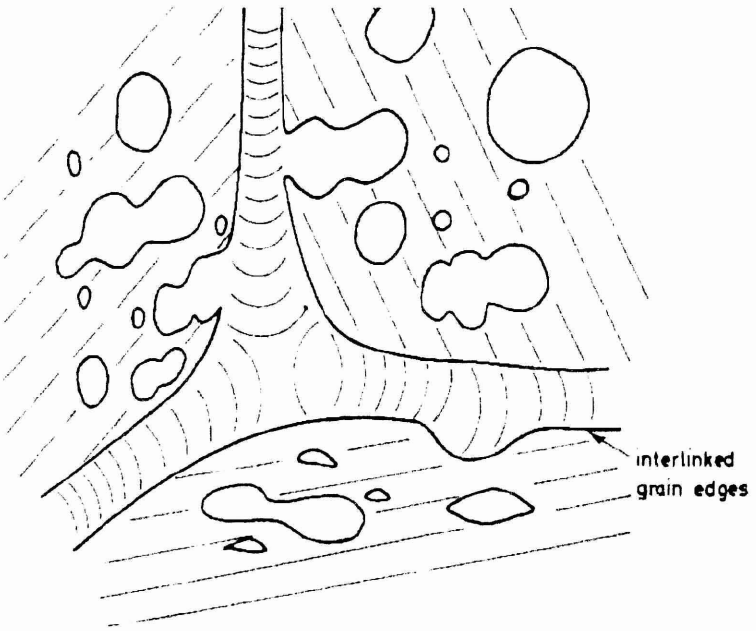


Figure-106: Face and Edge bubbles, after interlinkage [83]

The model geometry:

Grain edge and face porosity types have different geometries as depicted in Figure-105; hence they are defined separately. The edge porosity geometry is described with a toroid model [8]. The relation between the volume fraction of the edge porosity and the radius of curvature becomes as follows:

$$S_e = 0.51\left(\frac{r_e}{a_r}\right)^2 - 0.161\left(\frac{r_e}{a_r}\right)^3 \tag{5.2.26}$$

$$K_e = \frac{1}{r_e} - 11\frac{S_e}{a_r} \tag{5.2.27}$$

S_e: Swelling due to the grain edge bubbles

K_e: Geometric curvature of the grain edge bubbles

r_e: Edge bubble radius of curvature (m)

a_r: Grain radius (m)

The following relation is adopted for the swelling behavior of the face bubbles [8]:

$$S_f = 1.18\left(\frac{e}{s}\right)^2\left(\frac{r_f}{a_r \sin\theta}\right)^3 \tag{5.2.28}$$

$$e = h_r - 0.3798 r_e$$

$$h_r = 0.5557 a_r$$

$$s = \frac{1}{\sqrt{\pi c_b}}$$

S_f: Swelling due to the grain face bubbles

r_f: Face bubble radius of curvature (m)

θ: 50^0

e: Radius of the grain face not occupied by the grain edge porosity (m)

h_r: Radius of the grain face (m)

c_b: Face bubble concentration ($1/m^2$)

s: Half distance between the bubbles (m)

The growth of the edge and face bubbles:

A model which attempts to describe the grain-boundary swelling requires two features: (i) a representation of the accumulation of gas on the grain faces and edges by diffusion from the grain interior and its division between the face and edge porosity, together with a description of the subsequent loss of gas from the edge porosity into the free volume of the fuel pin (fission gas release) and (ii) a treatment of the growth of the edge and face porosity driven by accumulation of gas (swelling).

Interaction and competition between edge and face porosity during their growth is described by emission and absorption of vacancies on the grain boundary. The driving force is the difference in chemical potential for vacancies between the cavity surface and the grain boundary.

The balance of vacancy emission and absorption in the grain boundary may be represented by the steady state rate equation for the mean vacancy volume concentration, c_v, over the grain face:

$$\beta_s + \beta_f + \beta_e - \delta_b D_b \left(k_e^2 + k_f^2\right) c_v = 0 \qquad \text{(per unit volume)} \qquad (5.2.29)$$

$$k_f^2 = \frac{8\left(1 - \frac{r_f^2}{s^2}\right)}{s^2\left[\left(\frac{r_f^2}{s^2} - 1\right)\left(3 - \frac{r_f^2}{s^2}\right) + 4\ln\left(\frac{s}{r_f}\right)\right]}$$

$$k_e^2 = \frac{2k_f}{e}$$

$$\beta_f = \delta_b D_b k_f^2 c_f$$

$$\beta_e = \delta_b D_b k_e^2 c_e$$

where β_s is the rate of production of vacancies on the grain face, β_f and β_e are the rates of vacancy emission from face bubbles and edge bubbles or tunnels respectively, k_f^2 and k_e^2 are the sink strengths of face and edge bubbles respectively, δ_b is the grain boundary width in meters and D_b is the vacancy migration coefficient in the boundary.

c_f and c_e are the local vacancy volume concentrations adjacent to face and edge bubbles, respectively. These are defined in terms of the local differences in the vacancy chemical potentials at the surface of the bubbles by

$$c_f = c_o \exp\left(\frac{\mu_f}{kT}\right) \cong c_o\left(1 + \frac{\mu_f}{kT}\right) \qquad (5.2.30)$$

$$c_e = c_o \exp\left(\frac{\mu_e}{kT}\right) \cong c_o\left(1 + \frac{\mu_e}{kT}\right) \qquad (5.2.31)$$

Where c_o is the equilibrium thermodynamic vacancy volume concentration in the boundary and μ_f and μ_e are the face and edge bubble vacancy chemical potentials, respectively.

$$\mu_f = \Omega\left(\frac{2\gamma_s \sin\theta}{r_f} - \sigma - p_f\right)$$

$$\mu_e = \Omega\left(K_e\gamma_s - \sigma - p_e\right)$$

Where K_e is given by Eq-5.2.27 and p_f and p_e are the internal gas pressures of face and edge porosity in Pascal, respectively. σ is the external stress, Ω is the atomic volume (m^3) and γ_s is the surface tension (J/m^2).

The remaining unknown is the rate of production of vacancies on the grain boundary, β_s. This is determined from the observation that the total force acting on a grain face, made up of components from external restraint, capillary force and gas pressure acting on the bubble surfaces, equals the chemical potential per unit volume integrated over the grain face, which may be found, for example, by using the principle of virtual work [8].

$$\beta_s = \delta_b \frac{D_{gb}}{kT}\left\{\begin{array}{l}\dfrac{\left(k_e^2 + k_f^2\right)}{\left(s^2 - r_f^2\right)}\left[A\dfrac{s^2}{e^2}r_e p_e + r_f^2 p_f + h_r^2\dfrac{s^2}{e^2}\sigma - 2\gamma_s \sin\theta\left(r_f + \dfrac{s^2}{e}\right)\right] \\ -k_e^2\left(K_e\gamma_s - \sigma - p_e\right) - k_f^2\left(\dfrac{2\gamma_s \sin\theta}{r_f} - \sigma - p_f\right)\end{array}\right\} \quad (5.2.32)$$

The volume change rate per grain face for each type of porosity has two components: a component from the rate of emission or absorption of vacancies at the bubbles and a component from the "jacking" apart of the boundary. Taking into consideration that there are 14 faces per grain and each face is shared by two grains, the rate of change of the total volume fraction for grain boundary porosity is given as follows:

$$\frac{dS_t}{dt} = 21\beta_s\Omega\frac{h_r^2}{4a_r^2} \quad (5.2.33)$$

The rate of change of volume fraction of the edge porosity is then

$$\frac{dS_e}{dt} = X\frac{dS_t}{dt} + \frac{dS_c}{dt} \tag{5.2.34}$$

And the rate of change of volume fraction of the face porosity is

$$\frac{dS_f}{dt} = (1-X)\frac{dS_t}{dt} - \frac{dS_c}{dt} \tag{5.2.35}$$

Where

$$X = 1 - \frac{e^2}{h_r^2}\frac{\left(k_f^2 + \frac{r_f^2 k_e^2}{s^2}\right)}{\left(k_f^2 + k_e^2\right)}$$

And the effective flow of volume from the face bubbles to the edge is

$$\frac{dS_c}{dt} = \frac{21\delta_b D_{gb}}{4a_r^2}\frac{e^2}{s^2}\left(s^2 - r_f^2\right)\frac{k_f^2 k_e^2}{\left(k_f^2 + k_e^2\right)}\frac{\left(\mu_f - \mu_e\right)}{kT} \tag{5.2.36}$$

Combining the bubble swelling rate equations (Eq-5.2.34 and Eq-5.2.35) with the geometric swelling relations (Eq-5.2.26 and Eq-5.2.28):

$$\frac{dr_f}{dt} = \left(1.18\left(\frac{e^2}{s^2}\right)\frac{3r_f^2}{\left(a_r \sin\theta\right)^3}\right)^{-1}\frac{dS_f}{dt} \tag{5.2.37}$$

$$\frac{dr_e}{dt} = \left(1.02\frac{r_e}{a_r^2} - 0.483\frac{r_e^2}{a_r^3}\right)^{-1}\frac{dS_e}{dt} \tag{5.2.38}$$

The dynamics of fission gas on the grain boundary:

The description of gas transfer on the grain boundary may be split into two problems: the partition of gas arriving onto the boundary between face bubbles and the edges; and the more difficult problem of the subsequent release of gas from the face to the edge and finally out of the

fuel. Consider the simpler problem first: A fraction X of gas goes to the edge and (1-X) to the face bubbles.

The OGRES model adopts the "snake-like" interlinkage model to describe the gas release behavior [8]. In this model, gas arrives at the face so rapidly that surface diffusion is not rapid enough to allow interlinked bubbles to coalescence properly and snake-like chains of bubbles persist until the chain touches the edge. If at this stage the edge porosity has already interlinked the chain of face bubbles will break up into individual bubbles.

If F is the fraction of bubbles on the grain face interlinked to the edge, the rate of accumulation of gas in face bubbles is represented as follows:

$$\frac{dn_f}{dt} = (1-F)(1-X)\frac{dn_b}{dt} - \frac{(n_f - n_{f1})}{(1-F)}\frac{dF}{dt} + \frac{n_f}{A_f}\frac{dA_f}{dt} \tag{5.2.39}$$

Where n_f is the concentration of gas in face bubbles, n_b is the concentration of gas atoms released in total to the grain boundary, $A_f = \pi e^2$ is the area of a grain face available for face bubbles, and n_{f1} is a measure of the final concentration of gas atoms on faces after complete interlinkage.

$$n_{f1} = S_f \frac{n_f + n_e}{S_f + S_e}$$

n_e is the concentration of gas atoms on the grain edges. The three terms on the right hand side of Eq-5.2.39 correspond respectively to direct acquisition of gas by face bubbles, loss of gas to the edges by the growth of edge porosity reducing the area of grain faces. When Eq-5.2.39 is applied, the term involving dF/dt is suppressed for dF/dt < 0, similarly when $\frac{dA_f}{dt} > 0$, the final term is omitted.

If E is the fraction of edge porosity connected to a free surface, the rate of accumulation of gas on the grain edges is represented in our model by

$$\frac{dn_e}{dt}=(1-E)\left(\left[F(1-X)+X\right]\frac{dn_b}{dt}+\frac{(n_f-n_{f1})}{(1-F)}\frac{dF}{dt}-\frac{n_f}{A_f}\frac{dA_f}{dt}\right)-\frac{(n_e-n_{e1})}{(1-E)}\frac{dE}{dt} \quad (5.2.40)$$

Where n_e is the concentration of the gas in edge bubbles or tunnels, and n_{e1} is a measure of the final gas concentration per unit current volume after complete interlinkage and is given by

$$n_{e1}=\frac{p_b S_e}{kT}$$

p_b is the pressure to which the gas is vented in Pascal.

The expression for the release of gas from the fuel then as follows:

$$\frac{dn_r}{dt}=E\left(\left[F(1-X)+X\right]\frac{dn_b}{dt}+\frac{(n_f-n_{f1})}{(1-F)}\frac{dF}{dt}-\frac{n_f}{A_f}\frac{dA_f}{dt}\right)+\frac{(n_e-n_{e1})}{(1-E)}\frac{dE}{dt} \quad (5.2.41)$$

Where n_r is the concentration of gas released from the fuel. The release fraction is then given simply by the ratio of n_r and the time-integrated gas production rate in the fuel.

The expression suggested in Ref. [8] for the face bubble interlinkage:

$$F=\frac{0.1975\frac{r_f}{s}}{1-0.8475\frac{r_f}{s}} \quad (5.2.42)$$

Similarly for the edge bubble interlinkage:

$$E=\frac{4S_e}{(0.27-S_e)} \quad (5.2.43)$$

Finally, the face bubble concentration is given as follows:

$$c_b=1928\exp\left(\frac{33120}{T}\right)/\ \mathrm{m}^2$$

which is consistent with experimentally observed concentrations. At low temperatures the concentration was given an upper limit value of 10^{14}. Similarly, above 2000 K, mainly in the columnar grain region, c_b is assumed to be constant. In parallel with the grain size, face bubble concentration in each fuel node is assigned at the end of the restructuring period and held

constant during the operation. We note that the effect of the possible variations in c_b in fission gas release and swelling is negligibly small.

5.2.4. Gas Bubble Swelling

The gas bubble swelling has three contributions: intragranular gas bubble, grain face bubble and grain edge bubble swelling.

$$S_g = S_{\text{int}} + S_f + S_e \tag{5.2.44}$$

The swelling for each group is defined as the bubble concentration multiplied by the bubble volume. This is actually the bubble volume.

5.2.5. Swelling due to solid fission product swelling

Swelling due to cesium is given as 0.47% / at.% burnup at low temperatures. However, significant amount of cesium releases at high temperatures. A balance equation has been adopted to calculate the net swelling per at % burnup.

$$\frac{dS_{Cs}}{dt} = 5.55\times10^{-15} R - 2\times10^{-4} \exp\left(-\frac{12280}{T}\right) S_{Cs} \tag{5.2.45}$$

S_{Cs} : Fuel swelling due to cesium

R: Rating (W/kg)

t: Time (sec)

where the second term on the right-hand side of the equation represents cesium evaporation. Swelling due to solid fission products excluding cesium is given as 0.19 %/ at.% burnup.

5.2.6. Benchmarks

The FEAST-OXIDE model for swelling has been benchmarked against the available experimental data at 1250, 1500, 1750 and 2000 K and the preliminary OGRES model predictions given in Ref. [8]. In the late 1970s and early 1980s, such complex simulations were severely limited by the avaiable computational power. OGRES model equations were linearized before solving, as stated in Ref. [8]. Such an approach allows for significant gain in

computational time but it may also hurt the accuracy of the calculation. In this study, the equations were solved directly in an explicit manner. In addition to the solution method, some important constitutive relations, such as the diffusion coefficients reported in Ref. [8], were not the latest models suggested by Harwell. FEAST adopts the latest and the most reliable constitutive relations. Because of these differences, OGRES and FEAST predictions do not match well on Figure-107, 108, 109 and 110. On the other hand, FEAST predictions are satisfactory compared to the experimental data.

Figure-107 shows that the fuel irradiated at 1250 K has a much higher fission gas release fraction compared to the FEAST model prediction when the effect of JOG formation is neglected. JOG formation starts with the availability of excess oxygen around 2 at % burnup. As a consequence, fission gas release increases significantly due to transgranular fracture and resulting decrease in effective grain size. This behavior is modeled by increasing the fission enhanced gas diffusion coefficient. Note that the experimental data given in Figure-107 is used to fit the effect of JOG formation on fission gas release.

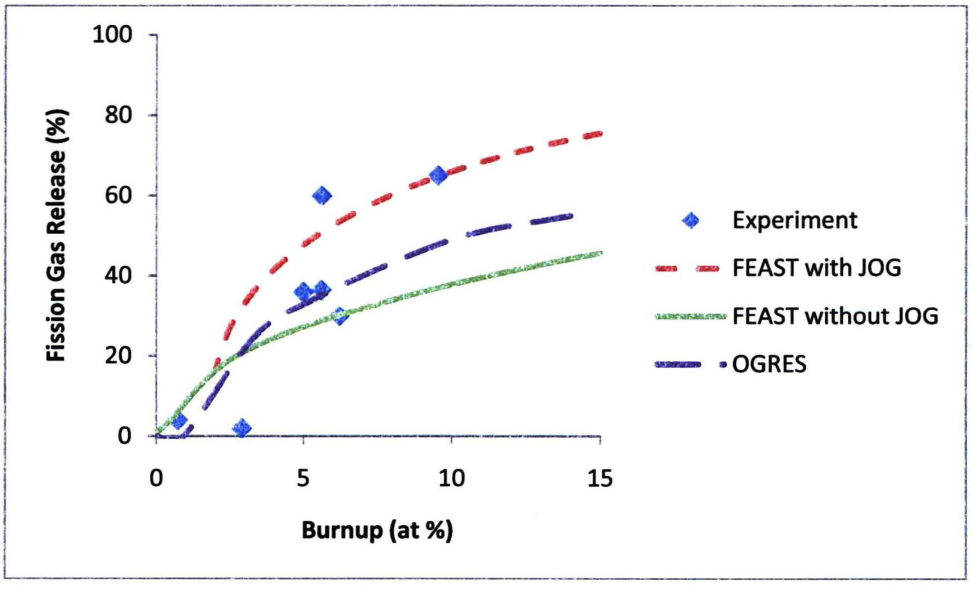


Figure-107: Fission gas release from fuel irradiated at 1250 K (grain size is 10 μm)

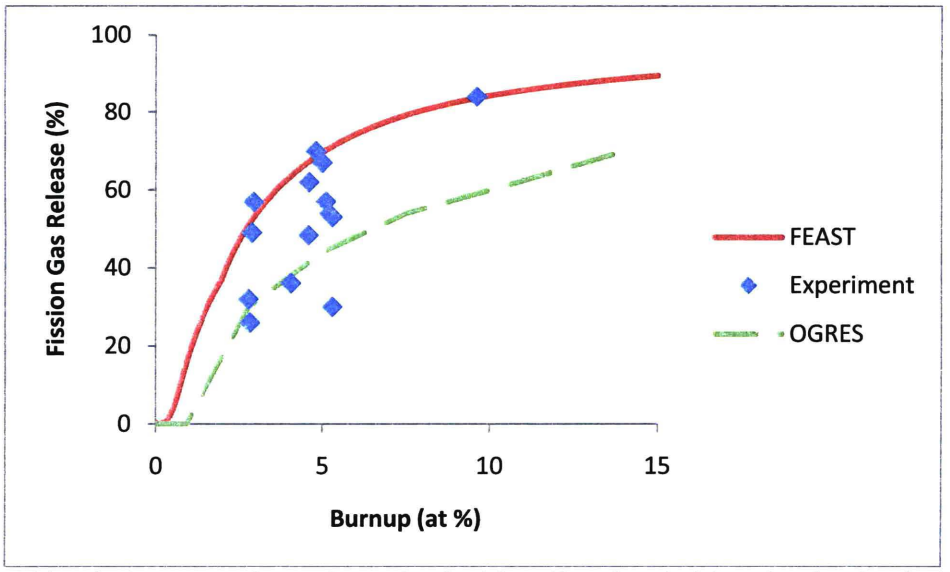


Figure-108: Fission gas release from the fuel irradiated at 1500 K (grain size is 10 μm)

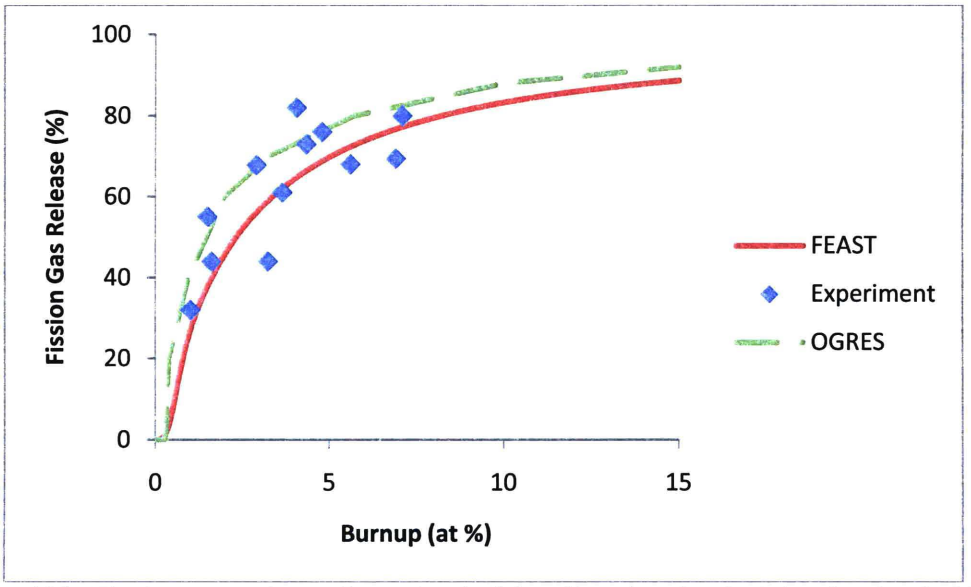


Figure-109: Fission gas release from the fuel irradiated at 1750 K (grain size is 23μm)

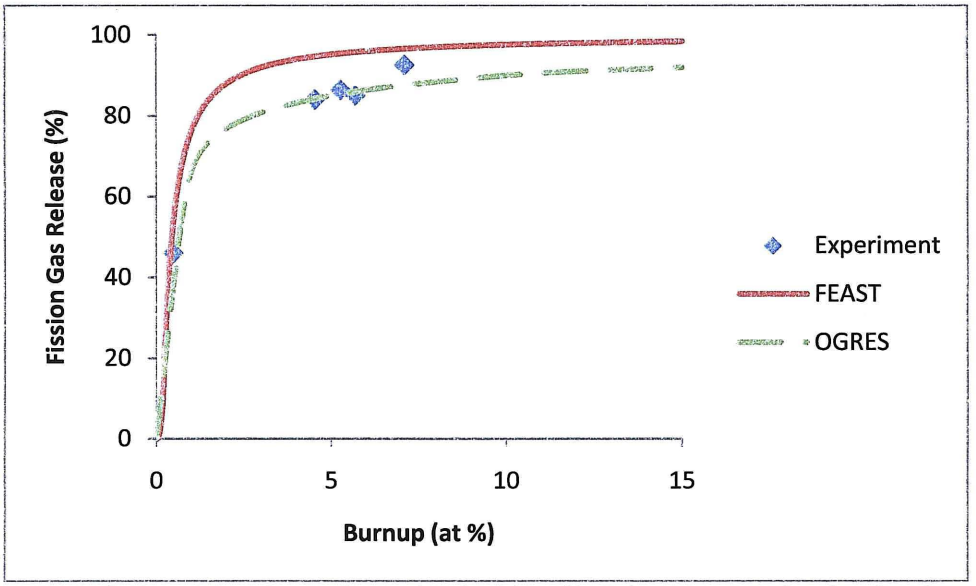


Figure-110: Fission gas release from the fuel irradiated at 2000 K (grain size is 32 μm)

5.3. Fuel Chemistry and Restructuring

5.3.1. Introduction

A significant part of the oxide fuel in fast reactors operates at high centerline and surface temperatures, together with a steep temperature gradient. As a consequence, the diffusion of the fuel constituents under the temperature gradient driving force becomes very active. Oxygen and plutonium tend to redistribute radially through the fuel pellet. This behavior affects the fuel temperature distribution and power distribution. The excess oxygen evolved during the irradiation increases the valence of the fuel. In addition, volatile fission products, specifically cesium, tend to migrate to the colder regions within the fuel pin, both radially and axially. If excess oxygen is available, cesium can combine with oxygen and molybenum to form the Joint Oxide Gain (JOG) at the fuel surface. This behavior affects the fuel performance significantly, as explained in Section 5.2. Finally, fuel restructuring includes the migration of as-fabricated porosity and the resulting formation of a central void, as well as grain growth and irradiation-induced densification of the as-fabricated porosity. Predicting the fuel restructuring and fuel chemistry behavior in an accurate manner is very critical to building an oxide fuel performance code.

5.3.2. Modeling the Burnup Dependency of the Oxygen to Metal Ratio

The fission process produces about twice as many atoms of fission products as the number of uranium and plutonium atoms destroyed. The oxygen atoms, however, are not affected by fission. Thus, as a result of fission, two atoms of oxygen are released for each heavy-metal atom destroyed. Some of the oxygen so liberated may combine with fission products and form oxides as shown in Table-37. Not all the fission products accept oxygen, however, and those that do may form oxides of lower valence than that of the actinide metals (for which the valence is 4). As a result, the oxygen-to-metal ratio in the fuel increases with burnup. The excess oxygen dissolves in the fuel matrix where it increases the valence of the uranium or the plutonium; thus, fission can be regarded as an oxidizing process. The net effect of burnup is to render the fuel more hyperstoichiometric than the fresh fuel or to increase the oxygen potential of the fuel [2].

Table-37: Probable chemical and physical states of fission products in near stoichiometric mixed oxide fuel [2]

Chemical Group	Physical State	Probable Valence
Zr and Nb	Oxide in fuel matrix; some Zr in alkaline earth oxide phase	4+
Y and rare earths	Oxide in fuel matrix	3+
Ba and Sr	Alkaline earth oxide phase	2+
Mo	Oxide in fuel matrix or element in metallic inclusion	4+ or 0
Ru, Tc, Rh, and Pd	Elements in metallic inclusion	0
Cs and Rb	Elemental vapor or separate oxide phase in cool regions of fuel	1+ or 0
I and Te	Elemental vapor; it may be combined with Cs as CsI	0 or 1-
Xe and Kr	Elemental gas	0

The objective of the analysis of the effect of burnup on the chemical state of the fuel is to permit prediction of the evolution of the oxygen potential, ΔG_{O_2}, during the irradiation.

Concentration changes during burnup:

Figure-111 shows a unit volume of unirradiated mixed oxide fuel material that contains N_U^o atoms of uranium and N_{Pu}^o atoms of plutonium. The number of oxygen atoms in the fresh fuel is

$$N_O^o = \frac{O}{M}\left(N_U^o + N_{Pu}^0\right) \tag{5.3.1}$$

where O/M is the oxygen-to-metal ratio of the as-fabricated fuel.

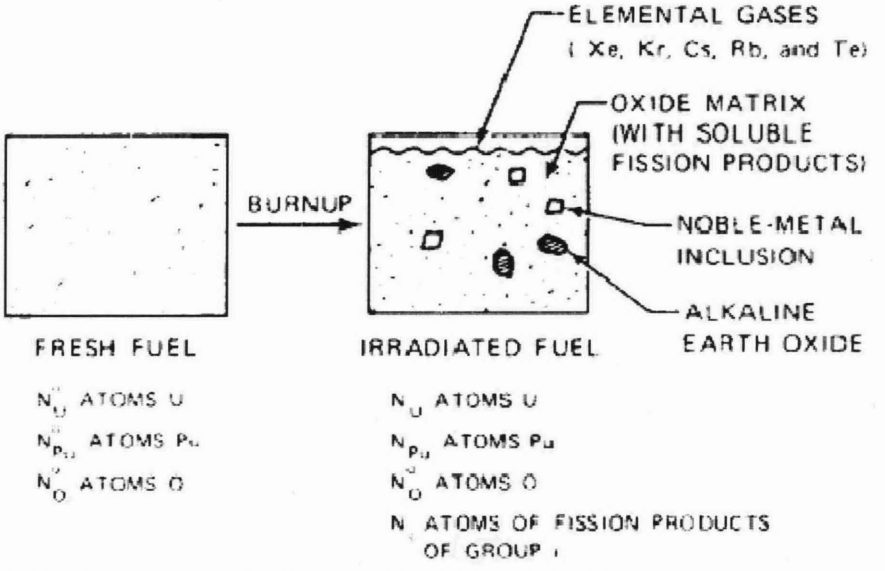


Figure-111: A unit volume of mixed oxide fuel irradiated as a constant mass system [2]

The initial cation fraction of plutonium is

$$q_o = \frac{N_{Pu}^o}{N_U^o + N_{Pu}^o} \tag{5.3.2}$$

During irradiation, fission product phases forms. Figure-111 depicts the process. The fraction of the initial heavy metal atoms after burnup β. is given as follows:

$$\frac{N_U + N_{Pu}}{N_U^o + N_{Pu}^o} = 1 - \beta \tag{5.3.3}$$

and the ratio of plutonium to heavy metal atoms is

$$q = \frac{N_{Pu}}{N_U + N_{Pu}} = \frac{q_0}{1-\beta} \tag{5.3.4}$$

Fission products are collected into groups characterized by particular chemical states. The concentration of fission product in a particular group present after burnup β is

$$N_i = Y_i \beta \left(N_U^o + N_{Pu}^o \right) \tag{5.3.5}$$

Where Y_i is the sum of the elemental yields of all fission products in group i and N_i includes all of group-i that has been formed in the unit volume of fuel.

Partitioning molybdenum:

The free energy of formation of MoO_2 is so close to the oxygen potential of nearly stoichiometric fuel that this fission product cannot be unambiguously assigned to the elemental or the oxide chemical state. Rather, it is distributed between the oxide matrix (as dissolved MoO_2) and the metallic inclusions as Mo in the solid solution with the noble metal fission products) in the concentrations that satisfy the equilibrium.

Mo (solution in metal) + O_2 = MoO_2 (solution in fuel matrix)

Application of the law of mass action to this equilibrium results in

$$\frac{a_{Mo}^f}{a_{Mo}^m p_{O_2}} = \exp\left(-\frac{\Delta G_{Mo}^o}{RT} \right) \tag{5.3.6}$$

Where ΔG_{Mo}^o is the free energy of formation of MoO_2, which is:

$$\Delta G_{Mo}^o = -574 + \frac{164T}{1000} \text{ (kJ/mole)} \tag{5.3.7}$$

The quantities of a_{Mo}^f and a_{Mo}^m are the thermodynamic activities of molybdenum in the fuel matrix and in the metallic inclusions, respectively. If it is assumed that molybdenum forms ideal solutions in these two phases, the activities can be replaced by the cation fraction of Mo in the fuel matrix (y_f^{Mo}) and by the atom fraction of Mo in the metal phase (y_m^{Mo}).

$$\Delta G^{o}_{Mo} = RT \ln p_{O_2} - RT \ln \frac{y^{f}_{Mo}}{y^{m}_{Mo}} \tag{5.3.8}$$

$$\Delta G_{O_2} = RT \ln p_{O_2} \tag{5.3.9}$$

ΔG_{O_2} is given in Appendix-B. Attainment of equilibrium within the control mass depicted in Figure-111 requires the following relation:

$$\Delta G^{o}_{Mo} = \Delta G_{O_2} - RT \ln \frac{y^{f}_{Mo}}{y^{m}_{Mo}} \tag{5.3.10}$$

The partitioning of molybdenum between the fuel matrix and the metallic inclusions can be described by the quantity f_{mo}, which is defined as the fraction of the total molybdenum present which is oxidized to MoO_2. In terms of f_{mo} and the concentrations of the other species present, the cation fraction of molybdenum in the oxide matrix is

$$y^{f}_{Mo} = \frac{f_{Mo} N_{Mo}}{N_U + N_{Pu} + N_{Y-\mathrm{Re}} + f_{Mo} N_{Mo} + N_{Zr-Nb} - N_{Ba-Sr}} \tag{5.3.11}$$

where N_U and N_{Pu} are the concentrations of uranium and plutonium, N_{Y-Re} is the sum of concentration of yttrium and the rare earths, and N_{Mo} is the total concentration of molybdenum, irrespective of whether it is in the fuel matrix or in the inclusions. The difference between N_{Zr-Nb} and N_{Ba-Sr} represents the amount of zirconium that is dissolved in the fuel matrix. It is the total amount of zirconium less the amount contained in the alkaline earth oxide phase as $BaZrO_3$ or $SrZrO_3$.

Similarly, the atom fraction of molybdenum in the metallic inclusions is

$$y^{m}_{Mo} = \frac{(1 - f_{Mo}) N_{Mo}}{N_{NM} + (1 - f_{Mo}) N_{Mo}} \tag{5.3.12}$$

Where N_{NM} stands for the sum of the concentrations of the noble metal ruthenium, technetium, rhodium and palladium.

Combining Equations 5.3.10, 5.3.11 and 5.3.12 gives the following relation:

$$\Delta G^{o}_{Mo} = \Delta G_{O_2} - RT \ln \left[\left(\frac{f_{Mo}}{1-f_{Mo}} \right) \times \frac{Y_{NM} + (1-f_{Mo}) Y_{Mo}}{\frac{1-\beta}{\beta} + Y_{Y-\mathrm{Re}} + f_{Mo} Y_{Mo} + Y_{Zr-Nb} - Y_{Ba-Sr}} \right] \quad (5.3.13)$$

Charge Balance:

If the final state of the fuel matrix is such that $V_U = 4$ and $V_{Pu} < 4$, the charge balance on the fuel oxide phase can be written as follows:

$$2N_O^f = 4N_U + V_{Pu} N_{Pu} + 4\left(N_{Zr-Nb} - N_{Ba-Sr}\right) + 3N_{Y-\mathrm{Re}} + 4 f_{Mo} N_{Mo} \quad (5.3.14)$$

The analogous charge balance for the case of $V_U > 4$ and $V_{Pu} = 4$ is

$$2N_O^f = 4N_{Pu} + V_U N_U + 4\left(N_{Zr-Nb} - N_{Ba-Sr}\right) + 3N_{Y-\mathrm{Re}} + 4 f_{Mo} N_{Mo} \quad (5.3.15)$$

Substituting equations:

For $V_U = 4$ and $V_{Pu} < 4$:

$$2\left(\frac{O}{M}\right) = 4(1-q)(1-\beta) + V_{Pu} q (1-\beta) + \left(2Y_{Ba-Sr} + 4Y_{Zr-Nb} + 3Y_{Y-\mathrm{Re}} + 4 f_{Mo} Y_{Mo}\right)\beta \quad (5.3.16)$$

For $V_U > 4$ and $V_{Pu} = 4$

$$2\left(\frac{O}{M}\right) = 4q(1-\beta) + V_U (1-q)(1-\beta) + \left(2Y_{Ba-Sr} + 4Y_{Zr-Nb} + 3Y_{Y-\mathrm{Re}} + 4 f_{Mo} Y_{Mo}\right)\beta \quad (5.3.17)$$

V_U: Probable charge of the Uranium atoms

V_{Pu}: Probable charge of the Plutonium atoms

Y_{Ba-Sr}: Elemental yield of Ba-Sr group

Y_{Zr-Nb}: Elemental yield of Zr-Nb group

Y_{Y-Re}: Elemental yield of Y-Re group

Y_{Mo}: Elemental yield of Molybdenum

Simultaneous solution of Eq-5.3.16 or 5.3.17 and Eq-5.3.13 yields f_{Mo} and V_U or V_{Pu}.

Benchmark is accomplished between FEAST and Ref. [2] for $(U_{0.85}Pu_{0.15})O_{1.96}$ fuel for 2000 K. The agreement is satisfactory (Figure-112).

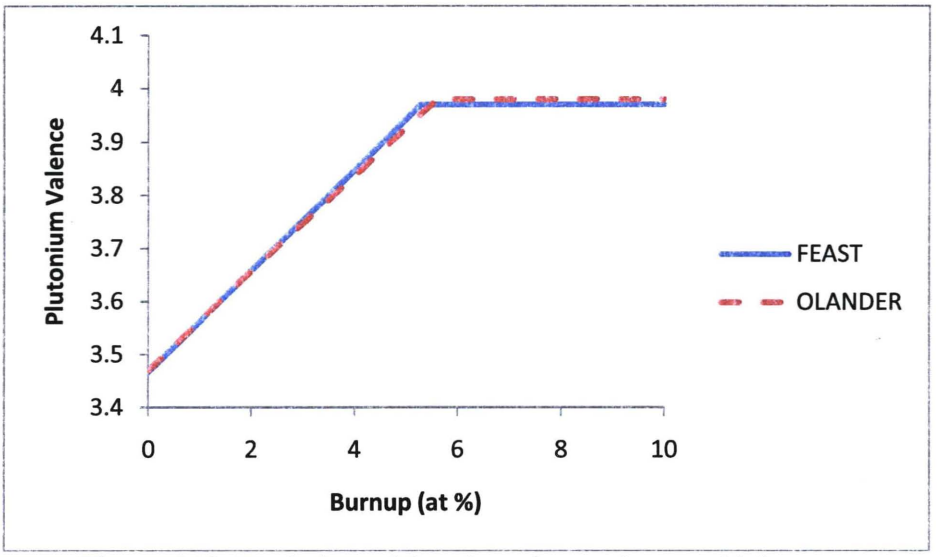


Figure-112: Variation of the plutonium valence with burnup

Figure-112 shows that plutonium valence holds constant just below 4, at 3.97. At this level, oxidation of the molybednum is favorable. Once all the molybdenum gets oxidized, the valence of the uranium starts to increase. Note that we would like to control the initial oxygen-to-metal ratio of the fuel so that the valence of the uranium will not exceed 4 significantly throughout the irradiation cycle, which will limit the fuel clad chemical interaction (FCCI).

5.3.3. Radial Redistribution of the Oxygen to Metal Ratio

The initial oxygen-to-metal ratio of the mixed-oxide fuel for fast reactor use is selected to be less than 2 to control fuel clad chemical interaction. During the irradiation, in addition to the increase in average oxygen-to-metal ratio as described in Section-5.3.2, a radial redistribution of oxygen occurs due to the very large temperature gradient in the fuel. The OXIRED model is adopted to describe the radial redistribution of oxygen [85].

The deviation from the stoichiometry is designated as x:

$$x = \frac{O}{U + Pu} - 2 \tag{5.3.18}$$

$c_i = x$ (hyperstoichiometric state)

$c_v = -\frac{x}{2}$ (hypostoichiometric state)

c_i and c_v are atomic fraction of interstitial atoms and oxygen vacancies, respectively.

In the following discussion, the i and v indices are omitted.

The net current of oxygen atoms driven by temperature gradient is given as follows based on the thermo-transport theory:

$$J = -D\left(\Delta c + c\frac{Q}{RT^2}\nabla T\right) \tag{5.3.19}$$

Q: Molar effective heat of transport of oxygen

T: Fuel temperature (K)

D_O : Diffusion coefficient of oxygen (m^2/s)

The equation of continuity is:

$$\frac{\partial c}{\partial t} = -\nabla . J \tag{5.3.20}$$

J: Oxygen current ($atom/m^2/s$)

The finite-difference discretization of Eq-5.3.20 gives the following relation:

$$c_t^i = c_{t-1}^i + 2\Delta t \frac{J_+^{i-1} \times rc^{i-1} - J_+^i \times rc^i + J_-^i \times rc^i - J_-^{i+1} \times rc^{i+1}}{\left(r_i^2 - r_{i-1}^2\right)} \tag{5.3.21}$$

rc^i: Center of node i (m)

r_i: Outer boundary of node-i (m)

J_+^i: Positive oxygen current emerging from node-i towards the outer part of the fuel. Its sign is positive ($atom/m^2/s$)

J_{-}^{i}: Negative oxygen current emerging from node-i towards the inner part of the fuel. Its sign is negative (atom/m²/s)

Boundary Conditions:

$J_{+}(R) = 0$
$J_{-}(0) = 0$ where R is the fuel pellet radius

Molar effective heat of transport:

The heat of transport of the oxygen vacancies is given as a function of the valence of the plutonium [85]:

$$Q_v = -8.12 \times 10^{-4} exp(4.85 V_{Pu}) \text{ (J/mol)} \qquad V_{Pu} < 3.3 \tag{5.3.22}$$

$$Q_v = -3.96 \times 10^6 + 2.37 \times 10^6 V_{Pu} - 3.6 \times 10^5 V_{Pu}^2 \text{ (J/mol)} \quad 3.3 \leq V_{Pu} < 4.0 \tag{5.3.23}$$

For the hyperstoichiometric fuel, the heat of transport of the oxygen interstitial atoms is given as follows:

$$Q_i = -3.5 \times 10^{34} exp(-17 V_U) \text{ (J/mol)} \qquad V_U \geq 4.0 \tag{5.3.24}$$

Diffusion coefficient:

The diffusion coefficient is reported in Ref. [85] for the OXIRED description:

$$D_O = 1.39 \times 10^{-6} \times \exp\left(-\frac{9128}{T}\right) \text{ (m²/s)} \tag{5.3.25}$$

However, with this expression for the diffusion coefficient, integration of Eq-5.3.25 does not re-produce the results in Figure-113, which is taken from Ref. [85]. We suspect there is a typo or inconsistency in Eq-5.3.25. Therefore, the diffusion coefficient was found by fitting the results given in Figure-113 and the following updated diffusion coefficient was obtained:

$$D_O = 3.5 \times 10^{-9} \times \exp\left(-\frac{7500}{T}\right) \text{ (m²/s)} \tag{5.3.26}$$

Comparing Figures-113 and 114, it can be seen that the updated expression does reproduce the correct O/M distribution in space and time. At r=R, the slope of the distribution is different likely due to differences in the temperature gradients between the two simulations.

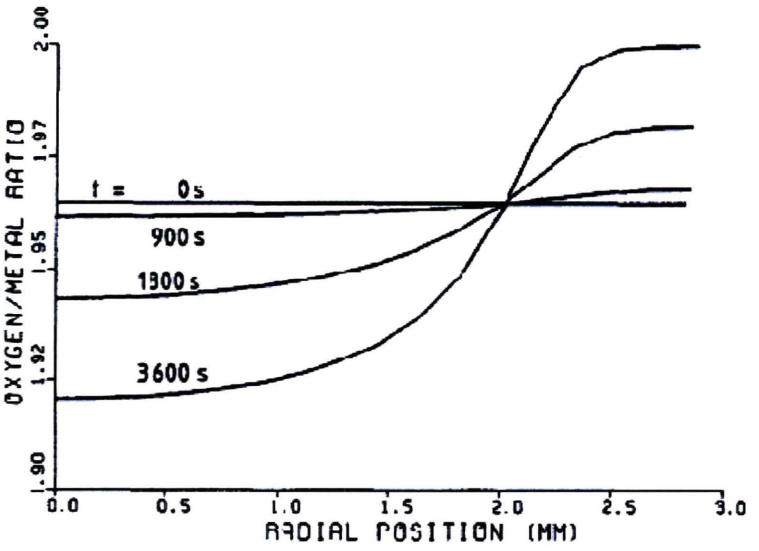


Figure-113: Oxygen to metal ratio as a function of radius for a typical sodium fast reactor condition (OXIRED predictions) [85]

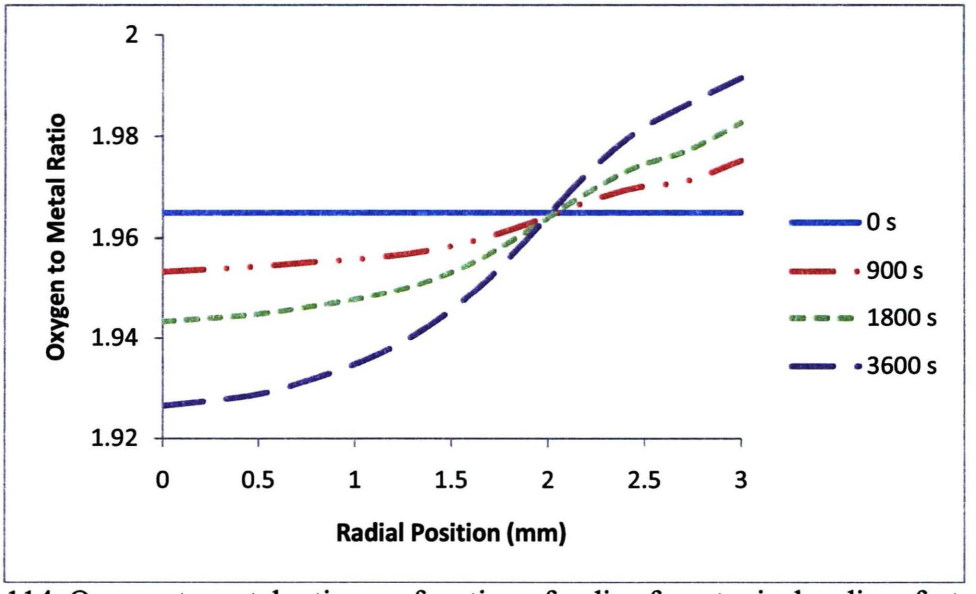


Figure-114: Oxygen to metal ratio as a function of radius for a typical sodium fast reactor condition (FEAST predictions)

5.3.4. Radial Migration of the Actinides

It is a well-known fact that uranium and plutonium migrate up the temperature gradient during irradiation, particularly in the radial direction under high temperature gradients [80]. This migration leads to local Pu concentration variations that affect the fuel material properties and power distribution. Hence, the impact on the fuel thermal performance may be considerable.

Plutonium migration has been modeled by using the thermo-transport theory given in Ref. [80] and [86]. The diffusion current has concentration gradient and thermal diffusion terms. It is given as follows:

$$J = -D_{Pu}\left(\frac{\partial C}{\partial r} + C(1-C)\frac{Q_{Pu}}{RT^2}\frac{dT}{dr}\right) \tag{5.3.27}$$

Q_{Pu} : Heat of transport = 35000 cal/mol

R : Universal Gas Constant = 1.987 cal/mol/K

C: Pu atom fraction

D_{Pu} : U-Pu interdifusion coefficient (m^2/s)

The continuity equation and its discretization is the same as the radial oxygen redistribution model:

$$\frac{\partial C}{\partial t} = -\nabla . J \tag{5.3.28}$$

$$c_t^i = c_{t-1}^i + 2\Delta t \frac{J_+^{i-1} \times rc^{i-1} - J_+^i \times rc^i + J_-^i \times rc^i - J_-^{i+1} \times rc^{i+1}}{\left(r_i^2 - r_{i-1}^2\right)} \tag{5.3.29}$$

rc^i: Center of node i (m)

r_i: Outer boundary of node-i (m)

J_+^i: Positive Plutonium current emerging from node-i towards the outer part of the fuel. Its sign is positive (atom/m^2/s)

J_-^i: Negative Plutonium current emerging from node-i towards the inner part of the fuel. Its sign is negative (atom/m^2/s)

Inter-diffusion coefficient is given as follows [86]:

$$D_{Pu} = 0.34\times10^{-4}\exp\left(-\frac{55351}{T}\right) \quad (\text{m}^2/\text{s}) \tag{5.3.30}$$

Benchmarking is accomplished for the MOX fuel with 27 wt % Plutonium with the approximate irradiation history given in [80]. The agreement is reasonably good (Figure-115).

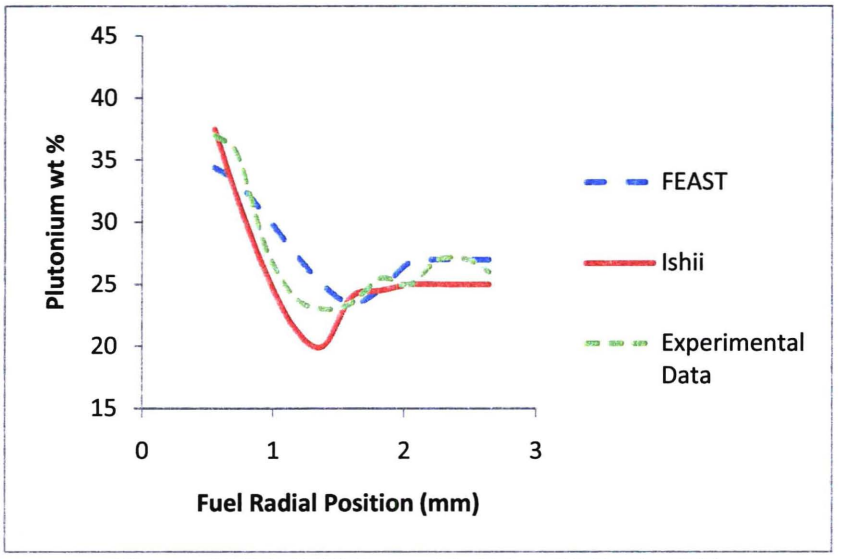


Figure-115: MOX fuel with 27 wt % PuO_2 [80]

5.3.5. Cesium Migration

Cesium, an abundant and mobile/reactive fission product in irradiated oxide fuel pins, plays an important role in fuel pin performance due to its participation in both mechanical and chemical interactions that are potentially life-limiting [87]. Because of these involvements, it is important to develop a detailed understanding of the behavior of cesium in irradiated oxide fuel pins, particularly the mechanism and kinetics of cesium thermo-migration and the mechanism of cesium-oxide fuel reaction swelling.

Cesium Radial Migration and Joint Oxide Gain Formation:

In the high burnup fuel rods, solid fission product oxide deposit, whose major composition is cesium molybdenate (Cs_2MoO_4), is observed in the gap between the fuel pellet and the cladding. This deposit is called Joint Oxide Gain (JOG), but the specific mechanism of its formation is not

yet understood [88]. JOG improves gap conductance, because it has a high thermal conductivity. Due to excessive stresses generated with the diffusion of Cesium and Molybdenum, localized transgranular fracture of the fuel, as-fabricated porosity shrinkage and significant release of fission gases were reported in Ref. [17]. Furthermore, Figure-116 and Figure-117 reported in Ref. [15] show that the start of JOG formation and reduction in fission gas retention in the fuel is simultaneous (The increase in fission gas release is due to the transgranular fracture occuring at the brittle part of the fuel). The pore shrinkage and the resulting decrease in fuel swelling is expected to mitigate FCMI, while the improvement of the gap conductance reduces fuel centerline temperatures. Therefore, it is very important to estimate the effect of JOG formation in the thermal computation.

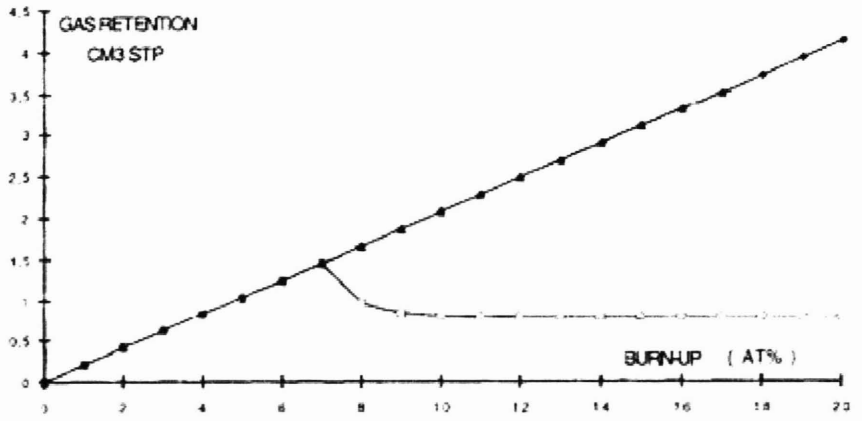


Figure-116: Evolution of fission gas retention [15] (When the effect of JOG formation is considered, fission gas retention decreases around 7 at % and saturates. On the other hand, the calculation ignoring the effect of JOG formation predicts a continuous increase in fission gas retention.

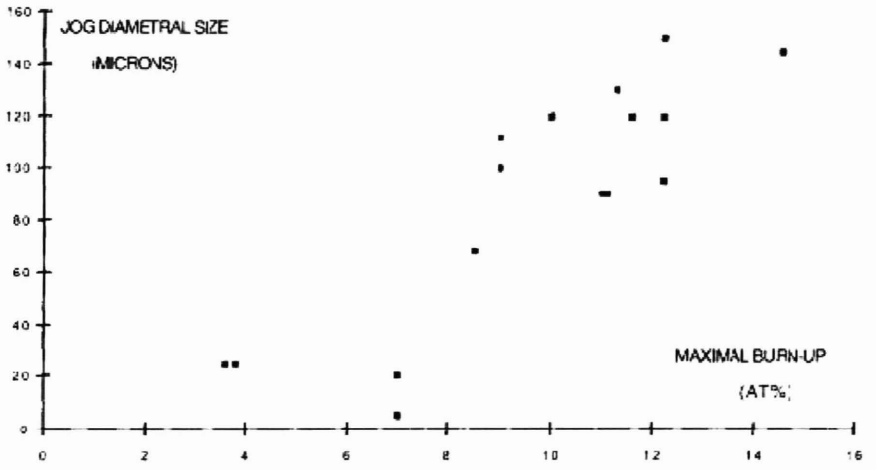


Figure-117: Evolution of the JOG size [15]

Cesium, which is one of the volatile fission products and migrates to the outer low-temperature region in the fuels, is a necessary element to create the JOG (Figure-118). Half as much Molybdenum is needed for JOG formation in accord with the chemical formula (Cs_2MoO_4) and the yield of Mo is somewhat higher than the yield of Cs [2]; hence, enough molybdenum as a solid fission product is assumed to exist when cesium migrates and reaches the outer region, so the process is considered Cs limited. Therefore, only cesium migration need to be computed to estimate the JOG formation. In this code the cesium generated in the fuel is assumed to migrate by thermo-diffusion as per Ref. [88].

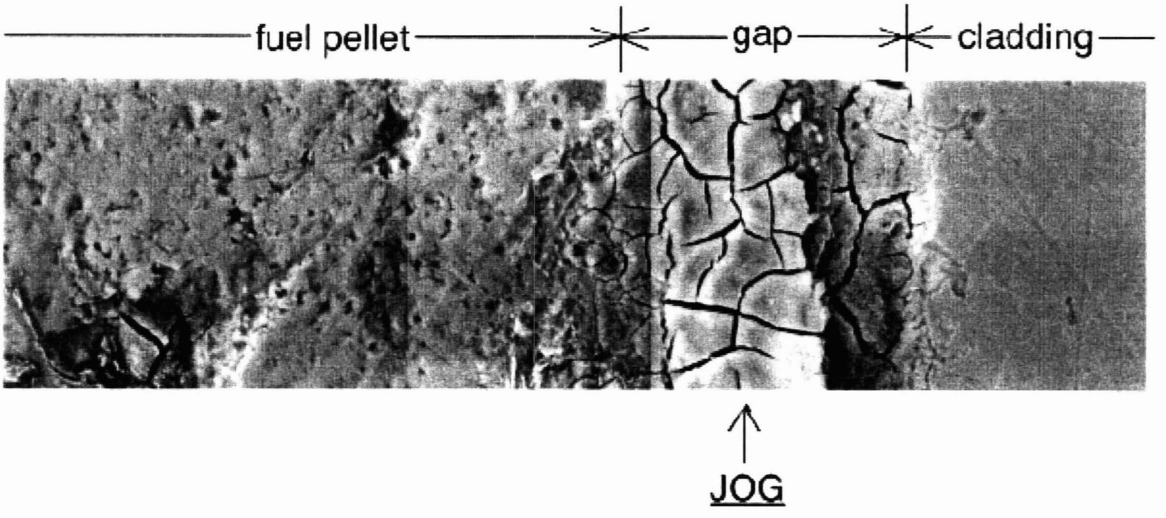


Figure-118: Aspect of JOG formation in pellet cladding gap [88]

This can be computed from the following equation:

$$J = -D_{FP}\left[\frac{\partial X_{Cs}}{\partial r} + \frac{Q_{Cs}X_{Cs}}{RT^2}\frac{\partial T}{\partial r}\right] \tag{5.3.31}$$

J : Radial cesium current (atom/m²/K)

X_{Cs}: Cesium atom fraction

Q_{Cs}: Cesium Heat of transport = 60000 cal/mol

R: Gas constant = 1.987 cal/mol/K

T: Temperature (K)

D_{FP} is the diffusion coefficient for monoatomic molecule fission product gas in m²/s. It is given as

$$D = D_1 + D_2 + D_3 \tag{5.3.32}$$

$$D_1 = 7.6\times10^{-10}\exp\left[-\frac{6.95\times10^4}{RT}\right] \tag{5.3.33}$$

$$D_2 = S^2 J_v c_v^0 \tag{5.3.34}$$

Where

S: Jump distance of fission product gas atoms, corresponding to = 3.45×10^{-10}m

J_v: Jump frequency $=10^{13}\exp\left(-\frac{5.48\times10^4}{RT}\right)$ (5.3.35)

c_v^0 : Content of vacancy calculated as follows:

$$c_v^0 = \frac{\alpha_s S^2 + ZV_0}{2Z}\times\left[\sqrt{1+\frac{4K'Z}{J_v\left(\alpha S^2 + ZV_0\right)}} - 1\right] \tag{5.3.36}$$

α_s : Sink intensity

Z: Number of sites surrounding a defect (=2)

K': Generation rate of a defect (= 10^4)

V_0: Value calculated from $\exp\left(-\frac{5.52\times10^4}{RT}\right)$

$$D_3 = 2 \times 10^{-40}\dot{F} \tag{5.3.37}$$

Where $\dot{F}$ is the fission rate in fissions/m³/s

The form of the continuity equation and its discretization is the same as the oxygen redistribution model. It is given as follows:

$$\frac{\partial c}{\partial t} = -\nabla . J \tag{5.3.38}$$

$$c_t^i = c_{t-1}^i + 2\Delta t \frac{J_+^{i-1} \times rc^{i-1} - J_+^i \times rc^i + J_-^i \times rc^i - J_-^{i+1} \times rc^{i+1}}{\left(r_i^2 - r_{i-1}^2\right)} \tag{5.3.39}$$

rc^i: Weight center of node i (m)

r_i: Outer boundary of node-i (m)

J_+^i: Positive cesium current emerging from node-i towards the outer part of the fuel. Its sign is positive (atom/m²/s)

J_-^i: Negative cesium current emerging from node-i towards the inner part of the fuel. Its sign is negative (atom/m²/s)

The diffusion coefficient D_1 represents the diffusion through vacancies of uranium and plutonium above 1400 ^{0}C, and D_2 represents the diffusion through vacancies produced due to irradiation damage in the range of 1000 to 1400 ^{0}C. D_1 and D_2 are the diffusion coefficients with the fuel temperature dependence, but D_3 is the diffusion coefficient that depends only on fission rate, without the fuel temperature dependence.

The JOG layer thickness is computed in accordance with the amount of released cesium, which has migrated to the outer region of the fuel pellet.

The pre-requisite for JOG formation is the existence of a surplus of oxygen, so the minimum oxygen-to-metal ratio in the pellet should be 1.985 [88]. A second condition for JOG formation is cesium migration from the hot inner region of the fuel to the cooler outer surface of the pellet. These phenomena can occur only if the fuel surface temperature is below 600 ^{0}C and the inner

region is above 1100 ^{0}C [88]. In addition, only if the cladding inner temperature is less than 600 ^{0}C the released cesium remains in the gap [88]. The JOG density is 4 g/cm^3 [88]. It is assumed that the JOG has mechanical properties like those of a liquid and thus no influence on the cladding stress even when FCMI is taking place. Any lubrication effect of the JOG on axial friction when the pellet and clad make contact is also neglected.

Comparison of the experimental data [15] and FEAST prediction is given in Figure-119. FEAST calculation was performed with the typical MK-II type oxide fuel operating conditions [89]. It is not a direct comparion because the exact fuel specifications are not reported in Ref. [15]. However, Figure-119 shows that the agreement is satisfactory.

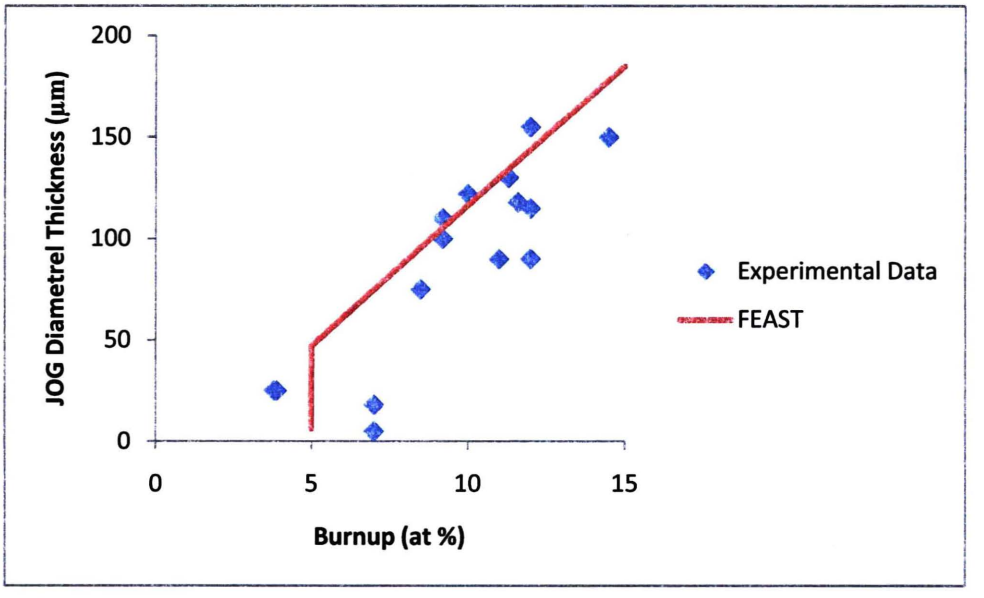


Figure-119: Comparison of the JOG thickness predictions between FEAST and PHENIX experimental data

Cesium Axial Migration:

A number of studies on axial cesium migration in mixed oxide fuel pins have shown that cesium migrates down the temperature gradient, resulting in accumulation of cesium and subsequent swelling of cesium compounds at the interface between the core and blanket fuel pellets [87] [90], [91], [92]. Transport of cesium is based on evaporation/condensation process, and the total flux of cesium, ϕ, across the interface between each axial nodes can be expressed by the following equation [87]:

$$\phi = k\left[N(h) - N(c)\right]\exp\left(-\frac{\Delta H_v}{RT}\right) \tag{5.3.40}$$

Where N(h) and N(c) are the concentration of cesium on the hotter and cooler side, k is the mobility of cesium vapor (1/s), left as a calibration constant and found to be equal to 3.5 for best fit with the experimental data base (see Section-6). ΔH_v , the partial molar heat of vaporization of cesium, is 177.7 kJ/mol [87]. The average fuel temperature is assigned to the exponential term. In addition, the axial gradient of the direction of the cesium current is specified by the fuel centerline temperature.

The cesium vapor reaching the top fuel node is assumed to deposit to the outer radial node and causes swelling. The effect of cesium axial migration in Fuel Clad Mechanical Interaction and clad straining could be very significant if the clad does not have good creep strength (see Section-6).

5.3.6. As-fabricated Porosity Migration

Typically, the oxide fuel includes as-fabricated porosity which is filled with helium gas. Because they are large and remains at low pressure, the shape of these pores is lenticular [2]. At power, the pores move to the inner regions of the fuel up the temperature gradient. The mechanism is based on the vapor transport. The fuel evaporates at the hot surface of the pore and condenses to the cold surface. As a consequence, the pores migrate to the center of the rod where they form a central void.

Pore velocity:

Pore migration velocity is a highly uncertain quantity. The following relation is suggested in Ref. [93]:

$$V_p = 0.3376\exp\left(-\frac{66490}{T}\right) \tag{5.3.41}$$

V_p: Pore velocity (m/s)

T: Fuel Temperature

Redistribution kinetics:

The following assumptions are made based on Ref. [2]:

1- Pores are closed and migrate only in the radial direction under the influence of the temperature gradient.
2- All pores are of the same size, and their volume is independent of radial position and time. Collisions between migrating pores and the resulting coalescence to form larger pores are not considered.

We would like to determine porosity distribution function, $N_p(r,t)$, which gives the number of pores per unit volume at radial position r in the fuel rod at time t.

$$\frac{\partial N_p}{\partial t} = -\frac{1}{r}\frac{\partial}{\partial r}\left(rV_pN_p\right) \tag{5.3.42}$$

Which has an initial condition

$$N_p(r,0) = N_{p0}$$

Where N_{p0} is the pore concentration in the as-fabricated fuel.

Eq-5.3.42 requires a boundary condition at the outer fuel region. However, because of the low temperatures near periphery of the fuel rod, pore migration ceases well before r = R. It is assumed that 1300 ^{0}C is the limiting temperature for the pore migration. Therefore, the pore current is set equal to zero at the location where T= 1300 ^{0}C.

Discretization of the continuity equation is given as follows:

$$P_i^{t+1} = P_i^t + 2\times dt \times \frac{V_p^{i+1}P_{i+1}^t r_{i+1} - V_p^{i}P_i^t r_i}{\left(rr_{i+1}^2 - rr_i^2\right)} \tag{5.3.43}$$

P_i^t: Porosity fraction at radial node-i and at time t

V_p^i: Pore velocity at node i (m/s)

r_i: Node-i radial location (m)

rr_i: Inner boundary of node-i (m)

rr_{i+1}: Outer boundary of node-i+1 (m)

Perfect sintering (= zero porosity) is however not possible, so there is a minimum residual porosity, which is a function of the local temperature, as shown in Figure-120, from which it is clear that sintering becomes more effective as the temperature increases [93], [94]. The minimum residual porosity assigned in this simulation is 3 % based on Ref. [88]. Hence, pore velocity vanishes if the pore concentration reaches 3 %. Furthermore, Refs. [93] and [2] show that some porosity piles up at the interface between central void and the fuel. FEAST also allows for the accumulation of the pores at the interface. Once an inner node reaches unity porosity fraction, it is assumed to contribute to the central void. The maximum allowed accumulation of the porosity is 20 %. Hence, if a node at central void-fuel interface has a porosity fraction that is higher than 20 %, the excess porosity directly contributes to the central void.

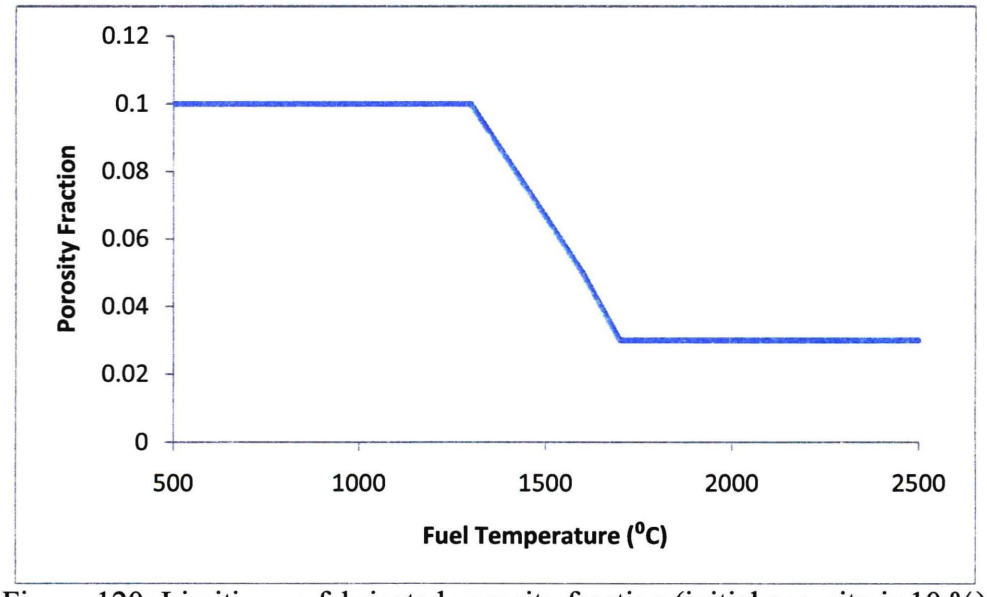


Figure-120: Limiting as-fabricated porosity fraction (initial porosity is 10 %)

Benchmarking has been accomplished against the Ref. [93] model prediction for mixed oxide fuel operating at 44.2 kW/m. Initial O/M is 1.99 and fuel surface temperature is 560 ^{0}C. The FEAST prediction for the central void radius and fuel temperature distribution matches well with Lackey model prediction (Figure-121 and Figure-122).

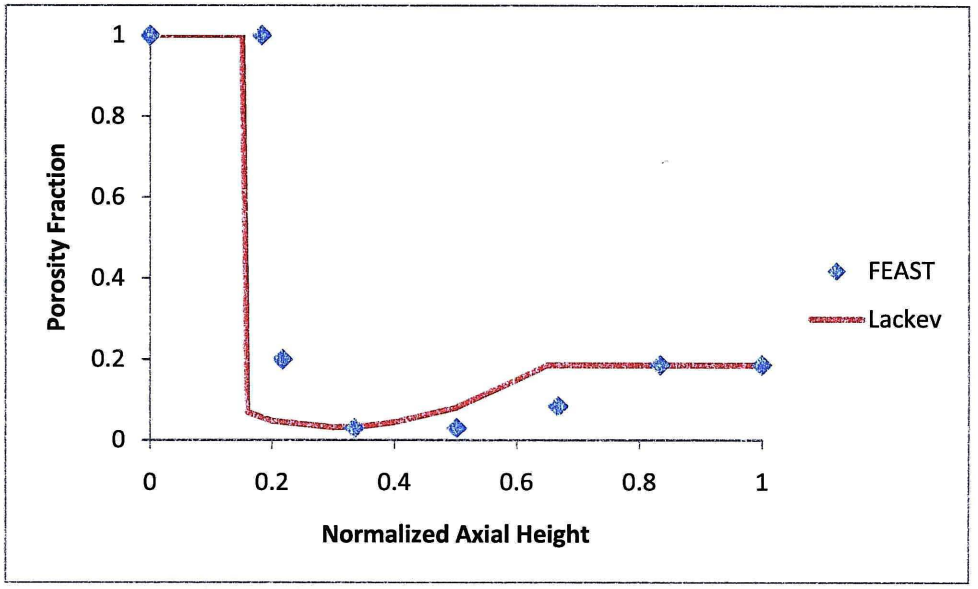


Figure-121: Comparsion of the porosity distribution predicted by Ref. [93] and FEAST

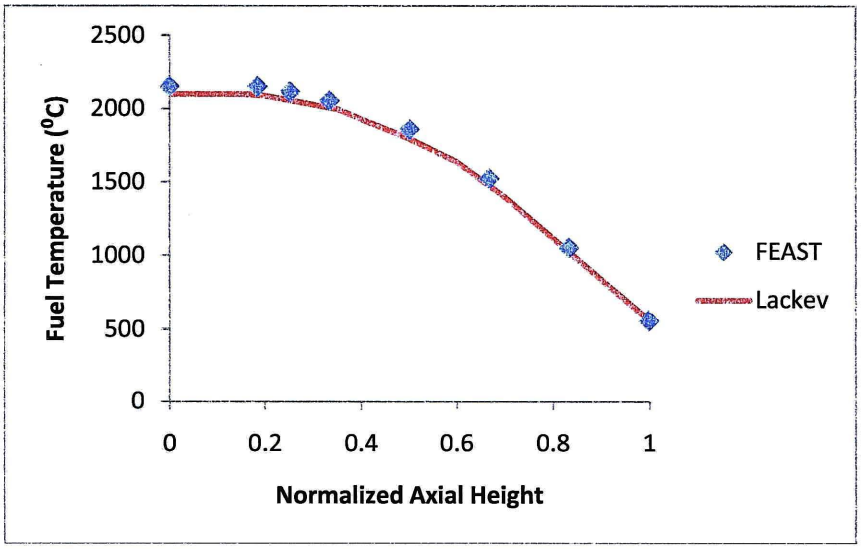


Figure-122: Comparison of the fuel temperature distribution predicted by Ref. [93] and FEAST

Note that code-to-code comparison of the central void radius predictions of FEAST and LIFE-4 is also given in Section-6.

5.3.7. Irradiation-induced Fuel Densification

A significant fraction of the as-fabricated pores disappears early in the irradiation due to the irradiation induced-fuel densification. Vacancies leave the pores and enters the adjacent solid by

distruptive action of fission fragments passing through or near a pore. It may result in a dramatic axial shortening of the fuel stacks in some light water reactors. However, in fast reactors it is not such an effective mechanism due to pore migration and central void formation and rapid gas swelling. Irradiation induced pore shrinkage is given in Ref. [94] as follows:

$$\rho = \rho_o + (0.96 - \rho_o)\left(1 - \exp\left(-\frac{Bu}{0.6}\right)\right) \tag{5.3.44}$$

ρ: Fuel density fraction

ρ_o: Initial fuel density fraction

Bu: Burnup (at %)

In addition to irradiation effects, as-fabricated porosity shrinkage has been observed if Joint Oxide Gain formation occurs at the fuel surface [16], [17]. Migration of the fuel constituents, cesium, molybdenum and oxygen to the brittle (cold) region of the fuel causes excessive internal stresses, transgranular fracture occurs extensively and as-fabricated porosity shrinkage results. FEAST assumes that solid fission product swelling replaces as-fabricated pores at the axial locations where JOG formed.

5.3.8. Grain Growth

Grain growth is observed in the mixed oxide fuel at typical fast reactor operating conditions. It affects the creep behavior of mixed oxide fuel. The experimental database shows a large scatter between measurements [95], [96], [97]. In addition to time and temperature variables, the presence of the radiation field may significantly affect the growth kinetics. The generation of large numbers of vacancies due to fission cascades might be a reason for the enhancement of grain growth, while the production of fission products tends to retard it. The driving force for the equiaxed grain growth is the decrease in surface free energy of grain boundaries (or decrease of the total grain boundary surface area).

Ref. [95] suggests the following grain growth relation:

$$D^3 - D_o^3 = 1.11 \times 10^{12} \exp\left(-\frac{445870}{RT}\right) t \tag{5.3.45}$$

Furthermore, the maximum allowed grain size is suggested by Ref. [2] as follows:

$$D_m = 2200 \exp\left(-\frac{63000}{RT}\right) \tag{5.3.46}$$

Constant grain size is assigned above 2000 K in columnar grain zone. These relations are used to estimate the diffusional creep behavior of the mixed oxide fuel.

5.3.9. Fuel Cracking and Relocation

Fuel pellet cracking and relocation significantly influences the fuel pin performance particularly at the beginning of life. The following empirical correlation is suggested to model the relocation behavior of the sodium fast reactor fuel pins, specifically for typical JOYO reactor driver fuel [98]:

$$DR = 0.111GD_{ci} - 45 \tag{5.3.47}$$

DR: Diameter relocation (μm)

G: Diameter gap size (μm)

D_{ci}: Clad inner diameter (mm)

Diameter relocation is defined as the difference between as-fabricated and residual diameter gap size. The relocation behavior will effectively reduce the gap size and improve the heat transfer across the gap. The effect of cracking on mechanical properties are described in Section-5.6.

5.4. Temperature Distribution

5.4.1. Introduction

Due to its low thermal conductivity, oxide fuel operates with a high temperature gradient in a sodium fast reactor environment. Furthermore, a low gap conductance in the gas filled gap region adds to the fuel centerline temperature. It is obviously very critical to calculate the temperature distribution to estimate the oxide fuel performance. First, fission gas release and gas swelling have a strong dependence on the temperature distribution. Second, as-fabricated pore

migration, fuel compressiblity, plutonium and oxygen migration are influenced significantly by the temperature distribution. Finally, the cesium evaporation, which affects solid fission product swelling, is also a strong function of temperature.

The Energy Balance Method, the same numerical technique described in Section-2.4, is applied for the oxide fuel code for both steady state and transient scenarios.

5.4.2. Heat Generation Rate

Linear heat rate is the input to the code simulation. The radial variation of the specific heat is expected due to as-fabricated porosity migration, fuel densification and plutonium radial redistribution [2]. The heat generation is assumed to be directly proportional to the local plutonium concentration only if the depleted uranium is loaded in MOX fuel. The contribution of uranium atoms to fission is simply neglected while calculating the normalized radial power distribution. Hence, the radial heat generation rate is given as follows:

$$q'''(r) = q_o''' \frac{1-P}{1-P_o} \times \frac{x_{Pu}}{x_{Puo}} \tag{5.4.1}$$

q''': Volumetric heat generation at a radial position r (W/m³)

q_0''': Radially average (nominal) volumetric heat generation rate (W/m³) obtained from the specified linear heat generation rate at the axial location fo interest

P: Porosity at a radial position r

P_o: As-fabricated porosity

x_{Pu}: Atomic fraction of Plutonium at a radial position r

x_{Pu0}: Pin average atomic fraction of plutonium

5.4.3. Numerical Algorithm to Simulate the Melting

If melting initiates at a fuel radial node, the fuel temperature holds at the melting temperature. The the melt fraction becomes the unknown. The energy balance equation (Eq-2.4-13) was modified as follows:

$$\rho A_i h_m \frac{x_i^{t+1} - x_i^t}{\Delta t} = \frac{1}{2}\left(\frac{T_{i-1}^{t+1} - T_i^{t+1}}{\frac{1}{2\pi k_{i-1,i}} \ln \frac{r_i}{r_{i-1}}} + \frac{T_{i-1}^{t} - T_i^{t}}{\frac{1}{2\pi k_{i-1,i}} \ln \frac{r_i}{r_{i-1}}} \right)$$

$$+ \frac{1}{2}\left(\frac{T_{i+1}^{t+1} - T_i^{t+1}}{\frac{1}{2\pi k_{i+1,i}} \ln \frac{r_{i+1}}{r_i}} + \frac{T_{i+1}^{t} - T_i^{t}}{\frac{1}{2\pi k_{i+1,i}} \ln \frac{r_{i+1}}{r_i}} \right) + q_i''' A_i \qquad (5.4.2)$$

Where x_i^t is the melt fraction at time t at the radial node-i; h_m is the heat of fusion, it is 274 kJ/kg.

5.4.4. Melting Temperature

The melting temperature of mixed oxide (MOX) fuel used in fast reactors is an essential property of the fuel that determines its limit of applicability. Early measurements of the melting temperature of the oxide fuel shows large scatter [99]. Figure-123 shows the difference in two measurements by the same scientist. The results are given in burnup dependent form.

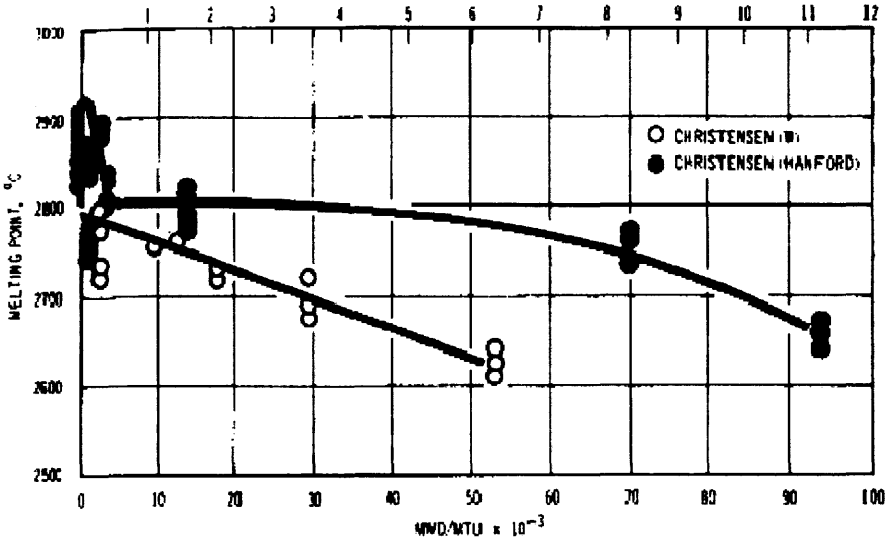


Figure-123: Melting temperature of the oxide fuel in burnup dependent form for two different measurements [99]

In this study, the Ref. [100] approach has been adopted to estimate the mixed oxide fuel melting temperature. It is a relatively recent model. The correlation displays dependency on plutonium and americium content, burnup and oxygen to metal ratio of the fuel. When no minor actinides are loaded in the fuel, X_2 is set to zero.

$$T_m = 3138 - 497X_1 + 60X_1^2 - (1000 - 2850X_1)|2 - X_4| - (1206 - 782X_1)X_2$$
$$-(1.06 - 1.43X_1)X_3 + 0.0008\left(\frac{(1.06 - 1.43X_1)}{0.66}\right)^{1.5} X_3^2 \qquad (5.4.3)$$

T_m: Melting temperature (K)

X_1: Plutonium fraction $\frac{Pu}{Pu+U}$ (wt %)

X_2: Americium fraction $\frac{Am}{Pu+U+Am}$ (wt %)

X_3: Burnup (GWd/t)

X_4: O/M ratio

The correlation is valid for

- Pu concentration from 10 to 40 wt %
- Am concentration up to 2 wt %
- O/M ratio from 1.94 to 2.00
- Burnup from 0 to 250 GWd/t

The plot of an experimental data base and its comparison with this correlation is given in Figure-124 [100]. The match is satisfactory.

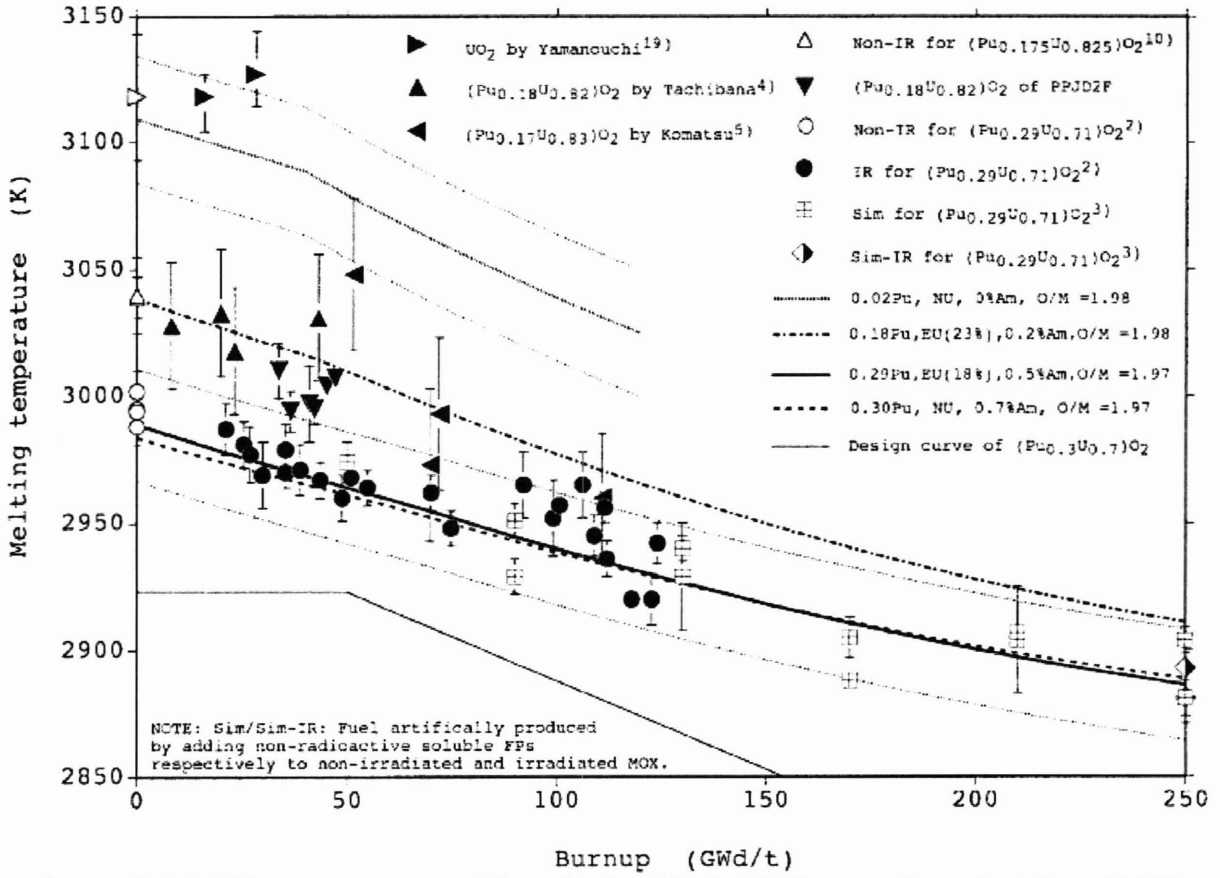


Figure-124: Melting temperature of the mixed oxide fuel in burnup dependent form [100]

5.4.5. Fuel Thermal Conductivity

Martin in Ref. [101] comprehensively reviewed the thermal conductivity of oxide fuels and established the basic approaches to their characterization. Philipponneau in Ref. [102] reviewed Martin's work and developed an equation for fast reactor MOX fuel; the major difference between Ref. [101] and Ref. [102] was an O/M ratio dependence. Based on the fuel pin thermal analysis for the short-term irradiation experiments in the experimental fast reactor JOYO, Philipponneau's equation tends to underestimate the thermal conductivity. The fuel thermal conductivity given in Ref. [17], [103] was developed based on Martin's approach in Ref. [101] and JOYO experimental database.The experimental data set used to build the thermal conductivity equation was systematically selected to minimize experimental uncertainty [103].

Ref. [17] description of the mixed oxide fuel thermal conductivity correlation is adopted in this study. As-fabricated mixed oxide fuel thermal conductivity (k_0) is given as the sum of phonon

and electron conduction. In addition, the correction factors are included to describe the effect of dissolved solid fission products (F_1), precipitated solid fission products (F_2), radiation damage (F_3) and porosity (F_4).

$$k = F_1 F_2 F_3 F_4 k_o$$

(5.4.4)

$$k_o = \frac{1}{0.06059 + 0.2754\sqrt{|2 - O/M|} + 2.011\times10^{-4}T} + \frac{4.715\times10^{9}}{T^2}\exp\left(-\frac{16361}{T}\right)$$

$$F_1 = \left(\frac{1.09}{\beta^{3.265}} + \frac{0.0643}{\sqrt{\beta}}\sqrt{T}\right)\arctan\left(\frac{1}{\frac{1.09}{\beta^{3.265}} + \frac{0.0643}{\sqrt{\beta}}\sqrt{T}}\right)$$

$$F_2 = 1 + \frac{0.019\beta}{(3 - 0.019\beta)}\frac{1}{1+\exp\left(-\frac{T-1200}{100}\right)}$$

$$F_3 = 1 - \frac{0.2}{1+\exp\left(\frac{T-900}{80}\right)}$$

$$F_4 = 1 - \alpha P$$

Where,

k: Mixed oxide fuel thermal conductivity (W/m/K)

O/M: Oxygen to metal atomic ratio

T: Temperature (K)

β: Burnup (at %)

P: Fuel Porosity

α: Porosity factor (1.5 or 2.5 as explained below)

Two different values are allowed for the porosity factor, α. Reference [104] suggests that 1.5 is appropriate for the large pores (above 30 μm) and 2.5 is appropriate for the small pores. For the migration of the as-fabricated porosity in early irradiation, 1.5 is assumed during the restructuring period. After the restructuring period, the as-fabricated porosity decreases due to

densification, furthermore, gas bubbles are much smaller than 30 μm. Therefore, 2.5 is assumed conservatively, to calculate the fuel temperature distribution after the restructuring period.

5.4.6. Gap Heat transfer

Gap heat transfer is an essential part of thermal modeling of the oxide fuel. High thermal resistance of the gap region may lead to a significant temperature difference between the fuel outer surface and the clad inner surface. On the other hand, the formation of the Joint Oxide Gain (JOG) may improve the thermal resistance significantly.

In this study the gap heat transfer model accounts for conduction and radiation heat transfer through the fill gas, as well as conduction through the JOG.

Heat Transfer through the JOG:

JOG thermal conductivity is given as follows [88]:

$$K_{JOG} = \frac{1}{0.895} \times \left(\frac{132.56}{T_{gap}} + 0.03 + 3.2 \times 10^{-10} T_{gap}^{3} \right) \tag{5.4.5}$$

K_{JOG} : Thermal conductivity of JOG (W/m/K)

T_{gap} : Gap Temperature (K)

The resulting JOG heat transfer coefficient is given as follows:

$$h_{JOG} = \frac{K_{JOG}}{D_{JOG}} \tag{5.4.6}$$

D_{JOG} : JOG thickness (m)

Gas Heat Transfer:

It is assumed that the gap has helium and xenon gases only [2]. Note that the yield of Krypton is much lower than Xenon for Pu-239 fission (U235 and Pu-239 have different fission yields). Note that the fission yield of Krypton is 8 % of the fission yield of Xenon. Initially, helium gas

occupies the gap and with the initiation of fission gas release, xenon fraction starts to increase. Helium and Xenon thermal conductivity is given in Ref. [2] as follows:

$$k_{He} = 15.8 \times 10^{-4} T^{0.79} \tag{5.4.7}$$

$$k_{Xe} = 0.72 \times 10^{-4} T^{0.79} \tag{5.4.8}$$

k_{He}: Helium thermal conductivity (W/m/K)

k_{Xe}: Xenon thermal conductivity (W/m/K)

T: Temperature (K)

Thermal conductivity of the mixed gas is given as follows:

$$k_g = k_{He}^{x} \times k_{Xe}^{1-x} \tag{5.4.9}$$

x: The mole fraction of the helium gas

k_g: Mixed gas thermal conductivity (W/m/K)

Then, the gap conductance is given as follows:

$$h_{gas} = \frac{k_g}{D_{gap} + Ro} \tag{5.4.10}$$

D_{gap} : Gas filled gap thickness (m)

Ro: Fuel and clad roughness (typical value is reported in [17] as 4 μm)

Heat transfer due to conduction through the gas and JOG is modeled as two thermal resistances in parallel as given in Ref. [88]:

Heat transfer coefficient:

$$H_{G+J} = \frac{h_{gas} \times h_{JOG}}{h_{gas} + h_{JOG}} \tag{5.4.11}$$

Heat transfer due to conduction:

$$q'_{G+J} = 2\pi r_{gap} H_{G+J} \left(T_{fo} - T_{ci} \right) \tag{5.4.12}$$

Radiation Heat Transfer:

The contribution of the radiation heat transfer through the gap is quite small during steady state and design basis accidents.

It is however modeled with the following relation [38]:

$$q'_{rad} = \sigma_s \left(T_{fo}^4 - T_{ci}^4\right) \frac{2\pi r_{gap}}{\frac{1}{\varepsilon_f} + \frac{1}{\varepsilon_c} - 1} \tag{5.4.13}$$

q'_{rad} : Linear heat rate transferred from the fuel to the clad via radiation

σ_s : Stefan-Boltzman constant = 5.6710^{-8} W/m²/K⁴

ε_f : Fuel surface emissivity = 0.79

ε_c : Clad surface emissivity = 0.79

T_{fo}: Fuel outer surface temperature (K)

T_{ci}: Clad inner surface temperature (K)

r_{gap}: Average gap radius (m)

5.4.7. Specific Heat of Fuel

Specific heat of the fuel is modeled according to the description given in Ref. [105] as follows:

$$c_p^f = \frac{K_1 \theta^2 \exp\left(\frac{\theta}{T}\right)}{T^2\left[\exp\left(\frac{\theta}{T}\right) - 1\right]} + K_2 T + \frac{Y K_3 E_D}{2RT^2} \exp\left(-\frac{E_D}{RT}\right) \tag{5.4.14}$$

c_p^f: Fuel specific heat capacity (J/kg/K)

T: Temperature (K)

Y: Oxygen to metal atomic ratio

R: Universal gas constant = 8.314 (J/mol/K)

θ: The Einstein temperature (K) (given in Table-38)

And the constants are given in Table-38 for UO_2 and PuO_2 fuels.

Table-38: Constants for the Equation-5.4.14

Constant	UO_2	PuO_2	Units
K_1	296.7	347.4	J/kg/K
K_2	2.43×10^{-2}	3.95×10^{-4}	J/kg/K²
K_3	8.745×10^{7}	3.86×10^{7}	J/kg
θ	535.285	571.0	K
E_D	1.577×10^{5}	1.967×10^{5}	J/mol

The specific heat of the molten fuel (which is needed in the analysis of severe trasient overpower events) is 503 J/kg/K.

5.4.8. Verification of the Thermal Analysis Model

The temperature distribution model has been benchmarked against the analytical solution including transient effects, under simplified assumptions. The fuel specifications are given in Table-39. Given the initial temperature and linear heat rate, converged steady state temperature distribution is compared with the analytical results. Figure-125, 126 and 127 shows that, the agreement below the melting point as well as above the melting point is satisfactory.

Table-39: Fuel properties

Property	Value
Composition	UO_2/Helium/HT9
Fuel Pellet Radius (mm)	2.85
Clad Inner Radius (mm)	2.87
Clad Outer Radius (mm)	3.43
Coolant Temperature (^{0}C)	377
Fuel Thermal Conductivity (W/m/K)	2
Melting Point(K)	2900
Initial Fuel Temperature (K)	1000

$$T(r) = \frac{q''' r_o^2}{4k}\left(1 - \frac{r^2}{r_o^2}\right) + T_s \qquad (5.4.15)$$

q''': Volumetric heat generation rate (W/m³)

r: Fuel radial location (m)

r_o: Fuel pellet outer radius (m)

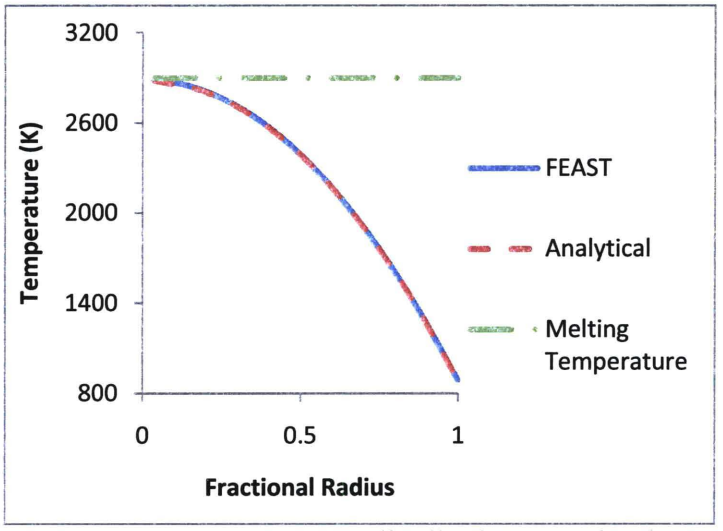


Figure-125: Temperature distribution at 66 kW/m

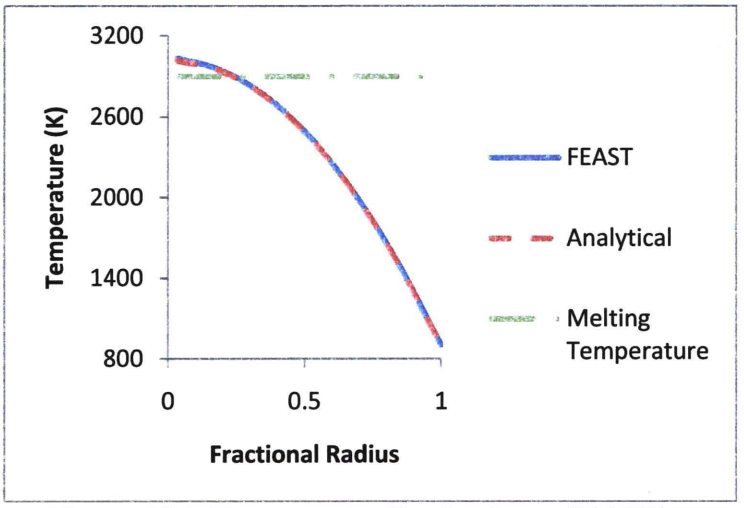


Figure-126: Temperature distribution at 70 kW/m

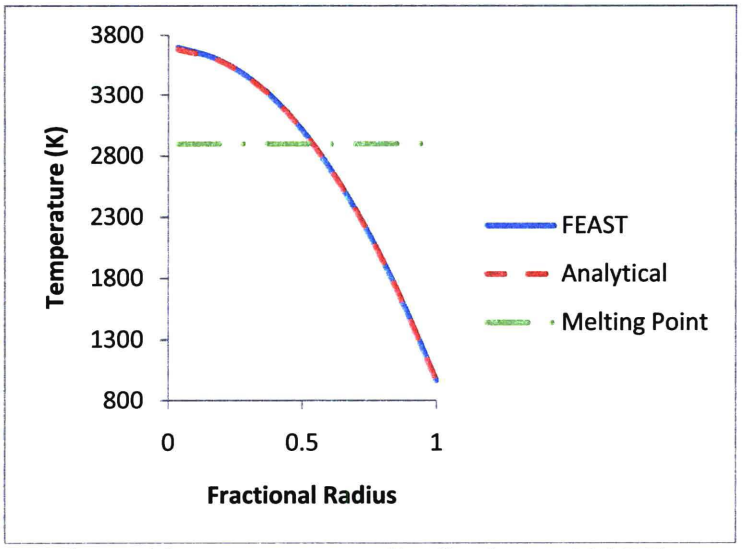


Figure-127: Temperature distribution at 90 kW/m

A parametric study has also been performed to check the numerical stability of the code. Case-1, Case-2 and Case-3 are assigned for the low medium and high linear heat rates, repectively. Setting the initial fuel temperature as 1000 K and given the linear heat rate as a function of time in Figure-128, the temperature distribution is calculated up to t=40 seconds (Figure-129). As the linear heat rate goes up, the centerline temperature increases, as expected. Melting occurs for all three cases.

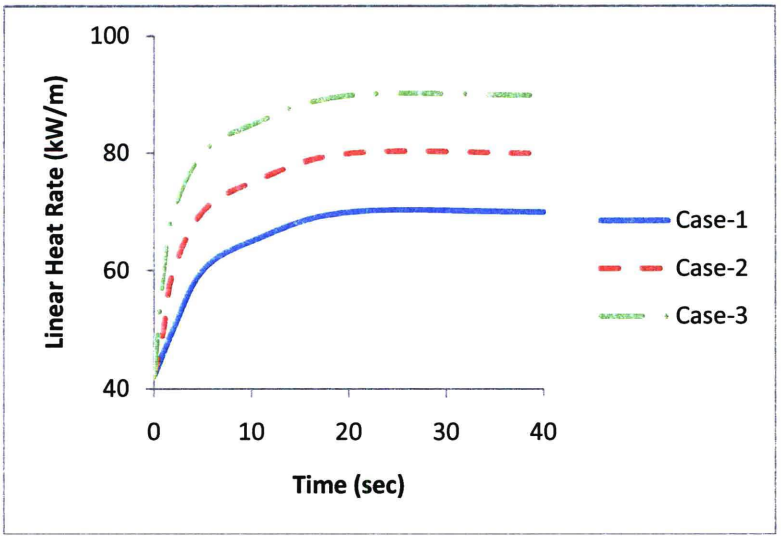


Figure-128: Linear heat rate history

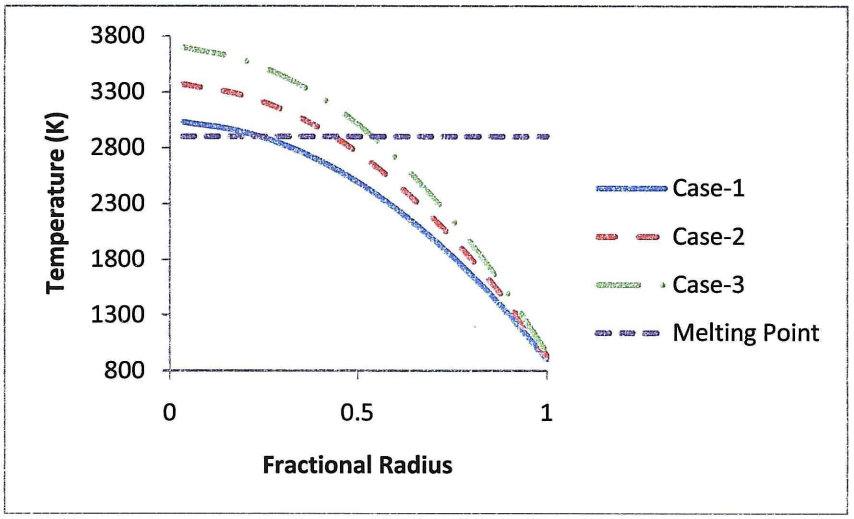


Figure-129: Temperature distribution at 40 seconds

5.5. Fuel Clad Chemical Interaction

5.5.1. Introduction

Fuel Clad Chemical Interaction (FCCI) has been observed in post irradiation examinations of fast reactor oxide fuel pins. The reaction between uranium-plutonium mixed oxide fuel containing fission products and stainless steel cladding affects the in-reactor fuel performance. Chemical attack of the cladding may limit the life of the fuel pins through reduction in cladding thickness. Cesium is universally observed in the attack region and is usually bonded with chromium from the cladding. Iodine is observed almost as frequently and is generally bonded with cesium. Tellurium is observed more sporadically [106].

Based on results of micrographic examinations, the observed FCCI data were separated into three groups: matrix attack, intergranular attack and combined attack. Matrix attack is a uniform transgranular corrosion, and is usually observed in a wide region of the cladding surface. Intergranular attack is restricted to the grain boundaries of the cladding, and is observed in a localized region of the inner surface. The occurrence of the intergranular attack is sporadic. Combined attack is a mode that includes both the above types of attack.

Attempts have been made to correlate the depth of attack with the fuel pin operating parameters, chiefly the temperature of the cladding inner surface, the initial O/M ratio of the fuel and the extent of burnup of the fuel. These parameters have been incorporated to a greater or lesser extent into various models and correlations of cladding attack; however, even with their inclusion, these models appear to be of limited applicability. None of these correlations could reflect the kinetic behavior appropriately, as described below. On the other hand, the model given in Ref. [107] and [108] is able to reflect the kinetic behavior of cladding wastage growth and its saturation. The model is based on the data obtained from JOYO and MONJU-type fuel pins irradiated in the Doureay Fast Reactor (DFR) and Rapsodie, with supplementary data obtained from pins irradiated in JOYO.

5.5.2. Model Description

Figure-130 illustrates the kinetic model for FCCI in a simplified way. The corrosion process consists of two stages. In the first stage, the corrodants are released from the fuel; in the second stage, they react with the cladding. The corrodants are those portions of the reactive fission products, such as cesium, tellurium, iodine and oxygen, that are available to react with the cladding. To simplify the current model, a single effective corrodant is assumed in [107] and [108]. The evolution of the quantity of corrodant in the fuel/cladding gap is described by:

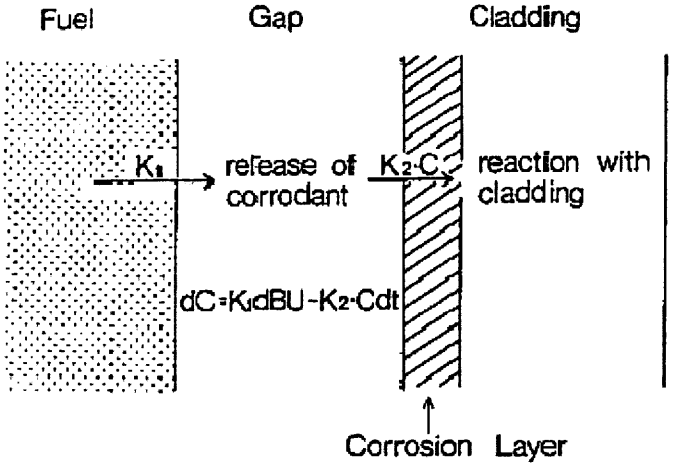


Figure-130: Fuel clad chemical interaction model [108]

The resulting equation for the thickness of the clad wastage layer is given in Ref. [107] as follows:

$$D = K_1 B - \frac{K_1}{K_2}\left\{1 - \exp\left(-K_2\left(B - B_o\right)\right)\right\} \tag{5.5.1}$$

The equation has the following differential form:

$$dD = K_1 dB - K_1 \exp\left(-K_2\left(B - B_o\right)\right) dB$$

$$K_1 = 1.33 \times 10^{-3}$$

$$K_2 = 1.12 \times 10^{8} \exp\left(-\frac{47200}{RT}\right)$$

D: Clad wastage (μm)

B: Burnup (MWd/t)

T: Temperature (K)

R: Gas Constant (1.987 cal/mol/K)

B_o: Burnup at which O/M=1.994 (Oxidation of the Molybedum starts)

5.5.3. Other FCCI Models

Three other clad wastage models appear in the literature and are also considered here.

HEDL Model:

The Hanford Engineering Development Laboratory (HEDL) correlation based on EBR-II data. It has explicit dependency on fuel oxygen to metal ratio of the as-fabricated fuel, clad inner temperature and burnup [107].

$$D = 0.3198\left(\frac{O}{M} - 1.935\right)\left(BU + 4.33\right)\left(T - 739\right) \tag{5.5.2}$$

D: Clad wastage layer (μm)

O/M: As-fabricated fuel oxygen to metal atom ratio

BU: Local Burnup (at %)

T: Clad Inner Temperature (K)

United Kingdom Model:

The United Kingdom Model is based on experimental data from DFR and the Materials Testing Reactor [107]. It accounts only for the clad inner temperature dependency.

$$D = 560 - 2.22T + 2.21\times10^{-3}T^2 \tag{5.5.3}$$

D: Clad wastage layer (μm)

T: Clad Inner Temperature (^{0}C)

SNR Model:

The SNR correlation is based on DFR and Rapsodie data [107]. It is developed for use in the design of Schneller Natriumgekühlter Reactor (SNR) 300.

$$D = \left[96.97 - 2.922\times10^{7}\left(2 - O/M\right)^{4}\right]\times\exp\left[-\frac{76.92}{T-769}\right] \tag{5.5.4}$$

D: Clad wastage layer (μm)

T: Clad Inner Temperature (^{0}C)

O/M: As-fabricated fuel oxygen to metal atom ratio

5.5.4. Model Verification

Comparison and verification of the predicted clad wastage at 50 MWd/kg with an initial O/M of 1.985 at various clad temperatures were conducted. Figure-131 shows the Ref [107] calculation and the calculation performed in this study. The results show that our calculations are able to match very well with Ref. [107] calculation.

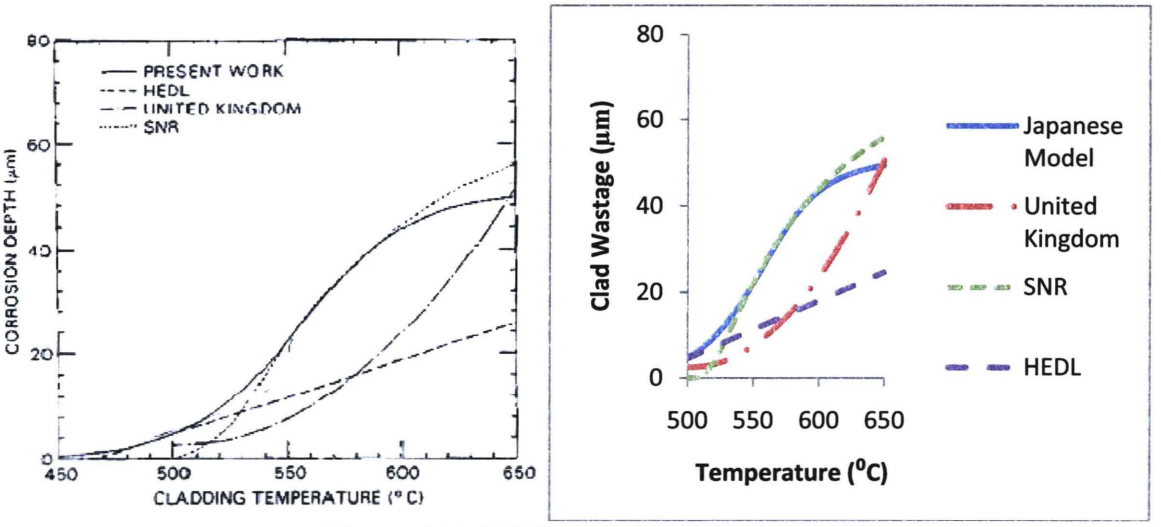


Figure-131: FCCI model verification

5.5.5. Parametric Study

Clad wastage is influenced by the clad temperature, fuel oxygen-to-metal ratio and burnup. The effect of these parameters on clad wastage has been examined and compared with SNR, UK and HEDL correlations.

Temperature:

The clad inner temperature is varied between 500 ^{0}C to 650 ^{0}C for two different burnups (see Figure-132). Initial oxygen to metal ratio is taken as 1.98. The results show that at low burnups the Japanese model underestimates the clad wastage with respect to other correlations because the Japanese model has a threshold oxygen-to-metal ratio for the start of wastage, whereas other correlations do not have such a feature. Note that this behavior is consistent with the observed experimental data [108]. At high burnup it seems that the Japanese Model is conservative compared to other correlations.

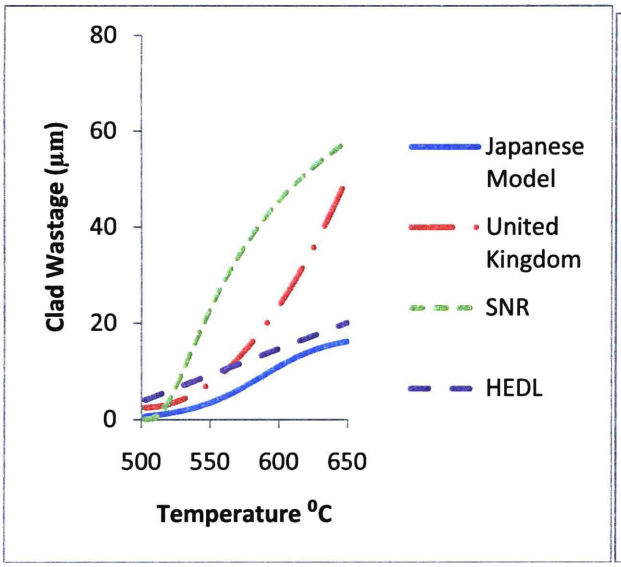
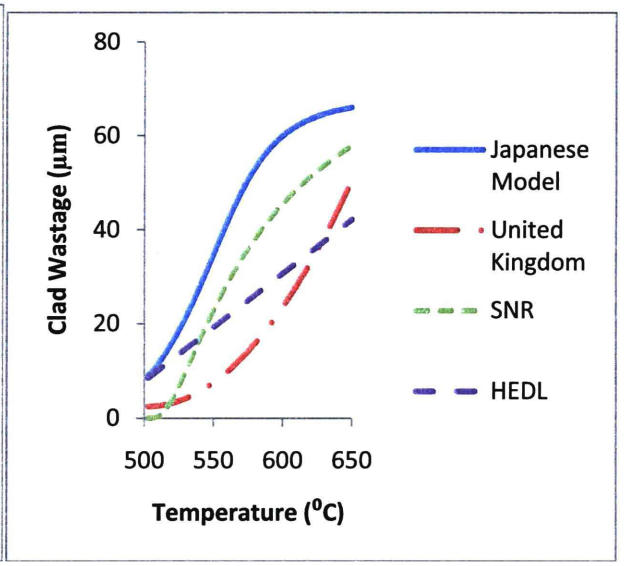


Figure-132: Burnup= 25 MWd/kg



Burnup = 100 MWd/kg

Oxygen-to-Metal Ratio:

The effect of oxygen to metal ratio on the clad wastage is investigated for the four correlations at low and high burnups (Figure-133 and Figure-134). Note that the UK model does not have an O/M dependency. The simulations are performed at 650 °C. At low burnup the Japanese model tends to underestimate the clad wastage. On the other hand, at high burnups the Japanese model appears to be conservative.

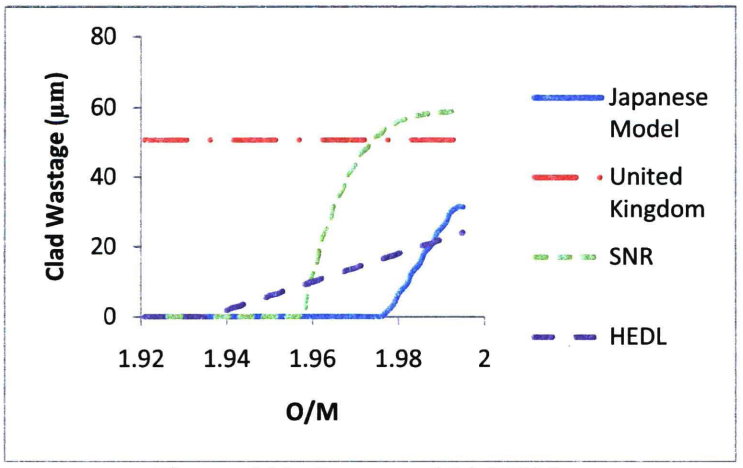


Figure-133: Burnup=25 MWd/kg

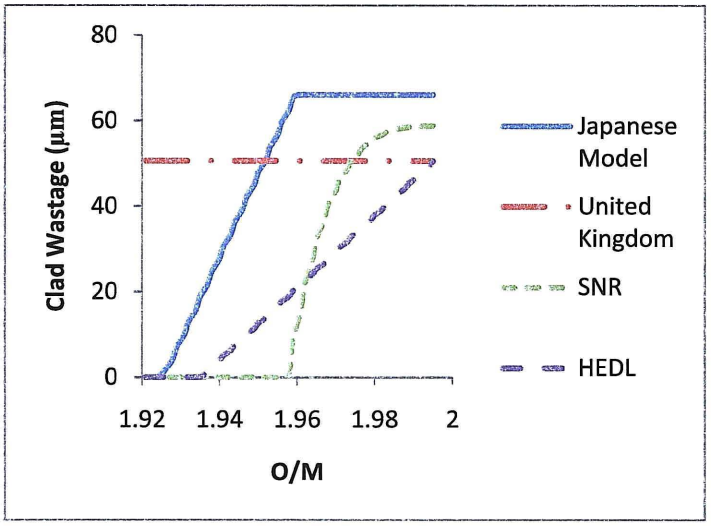


Figure-134: Burnup = 100 MWd/kg

Burnup:

Burnup dependency of the clad wastage layer evolution has been compared for 650 ^{0}C inner clad temperature and 1.98 oxygen-to-metal ratio (Figure-135).

The Japanese model has a threshold oxygen-to-metal ratio for the start of clad wastage, and has a saturation burnup for the termination of clad wastage growth. As a consequence, at low burnups it tends to underestimate whereas at high burnups it tends to overestimate. United Kingdom and SNR models do not have a clad wastage dependency on burnup.

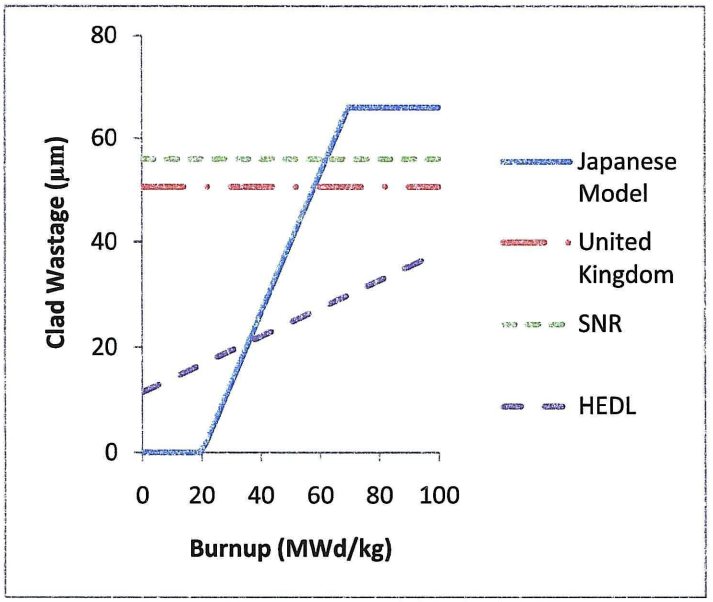


Figure-135: Burnup = 100 MWd/kg

5.6. Mechanical Analysis

5.6.1. Introduction

Mechanical analysis model of FEAST-OXIDE adopts the LIFE algorithm as described in Section 2.6. Unlike metal fuel, a significant part of the oxide fuel operates at temperatures below half of the melting temperature. As a consequence, extensive cracking may result, which is a major difference between oxide and metal fuel mechanical analysis models.

The constitutive relations for the oxide fuel mechanical analyis and the material properties will be given in this section.

5.6.2. Fuel Material Properties

Fuel Thermal Creep:

Predicting the fuel creep in a correct way is key to estimating the Fuel Clad Mechanical Interaction stress for steady state and transient scenarios.

The compressive creep rate for mixed UO_2 -25% PuO_2 is given in Ref. [109]. It was measured between 1300 ^{o}C and 1700 ^{o}C. In this study, it is extrapolated to the higher temperatures. The creep correlation has two components: (1) Diffusional creep and (2) Dislocation creep

$$\dot{\varepsilon} = \frac{3.23\times10^{9}}{d^{2}}\sigma\exp\left(-\frac{92500}{RT}\right)+3.24\times10^{6}\sigma^{4.4}\exp\left(-\frac{136800}{RT}\right) \tag{5.6.1}$$

$\dot{\epsilon}$: Fuel Creep Rate (h^{-1})

d: Grain size (μm)

R:Universal gas constant = 1.987

σ: Stress (MPa)

Fuel Iradiation Creep:

At temperatures below 45 % of the melting temperature, the thermal creep is no longer an effective strain mechanism. Irradiation creep becomes dominant. Ref. [110] suggests the following relation to model the mixed oxide fuel irradiation creep behavior:

$$\dot{\varepsilon}_f = 1.78\times10^{-26}\sigma\phi \tag{5.6.2}$$

$\dot{\varepsilon}_f$: Fuel irradiation creep rate (h^{-1})

σ : Stress (MPa)

ϕ : Fission rate (Fission/m³/s)

Young's Modulus:

Young's Modulus of ceramic fuels is affected by the temperature, density, and, to a lesser extent, the oxygen-to-metal ratio (O/M) and burnup of the fuel. It is given in Ref. [105] as follows:

$$ES = 2.334\times10^{11}\left[1-2.752\left(1-D\right)\right]\left[1-1.0915\times10^{-4}T\right] \tag{5.6.3}$$

ES: Young's Modulus of the stoichiometric UO_2 fuel

D: Fuel density (fraction of the theoretical density)

T: Fuel Temperature (K)

For nonstoichiometric fuel or mixed oxide fuel. The Young's Modulus is given as follows:

$$E = ES\exp\left(-Bx\right)\left[1+0.15f\right] \tag{5.6.4}$$

E: Young's Modulus (N/m²)

B: 1.34 for hyperstoichiometric fuel or 1.75 for hypostoichiometric fuel

x: The magnitude of the deviation from stoichiometry in $MO_{2\mp x}$ fuel

f: PuO_2 content of the fuel (weight fraction)

Poisson's Ratio:

Poisson's ratio of Uranium and Plutonium is given in [2] and [105] as follows:

$$\nu_U = 0.316 + \frac{T-300}{2800}(0.5-0.316) \tag{5.6.5}$$

$$\nu_{Pu} = 0.276 + \frac{T-300}{2800}(0.5-0.276) \tag{5.6.6}$$

ν_U: Poisson's Ratio of UO_2

ν_{Pu}: Poisson's Ratio of PuO_2

T: Fuel Temperature (K)

The Poisson's Ratio of the mixed oxide is given as follows:

$$\nu = (1-x_{Pu})\nu_U + x_{Pu}\nu_{Pu} \tag{5.6.7}$$

x_{Pu} : PuO_2 weight fraction

Thermal Expansion:

Thermal expansion of the oxide fuel below the melting point is given in [105] in the following form:

$$\frac{\Delta L}{L_o} = K_1 T - K_2 + K_3 \exp\left(-\frac{E_D}{kT}\right) \tag{5.6.8}$$

$\frac{\Delta L}{L_o}$: Linear strain caused by thermal expansion

T: Temperature (K)

E_D: Energy of formation of a defect (J)

k: Boltzmann Constant (1.38×10^{-23}) (J/K)

and K_1, K_2 and K_3 and E_D are given in Table-40 for UO_2 and PuO_2. Given the concentration, $\frac{\Delta L}{L_o}$ values for UO_2 and PuO_2 are interpolated.

Table-40: Constants for the fuel thermal expansion

Constant	UO_2	PuO_2	Units
K_1	1.0×10^{-5}	9.0×10^{-6}	K^{-1}
K_2	3.0×10^{-3}	2.7×10^{-3}	Unitless
K_3	4.0×10^{-2}	7.0×10^{-2}	Unitless
E_D	6.9×10^{-20}	7.0×10^{-20}	J

During melting, an expansion equal to a linear strain of 0.043 occurs. If the fuel is partially molten, the strain due to thermal expansion is given by:

$$\frac{\Delta L}{L_o} = \frac{\Delta L}{L_o}(T_m) + 0.043 X_m \tag{5.6.9}$$

$\frac{\Delta L}{L_o}(T_m)$: Linear strain of the solid fuel at the melting point

X_m: Fraction of the molten fuel

Fracture Stress:

Cracking occurs in the oxide fuel when any principal stress exceeds the fracture stress below 1300 ^{0}C, where the fuel is brittle. The fracture stress is defined following Ref. [105].

Below 1000 K, the fracture stress is 130 MPa and is constant. Above 1000 K, the following relation is adopted:

$$\sigma = 1.58 \times 10^8 \exp\left(-\frac{1590}{RT}\right) \tag{5.6.10}$$

σ: Fracture stress (MPa)

R: 8.314 J/mol/K

T: Fuel Temperature (K)

Yield Stress:

The fuel gains ductility above 1300 ^{0}C. Hence, the fuel yielding without fracture becomes possible.

The Ref. [105] description is adopted for the oxide fuel yield strength.

For the fuel temperatures above 1573 K and below 2250 K the following relation is adopted:

$$\sigma_y = \frac{2250 - T}{2250 - 1573} \times 120 + 10 \qquad \text{(MPa)} \tag{5.6.11}$$

For temperatures above 2250 K, the fuel weakens significantly. The Yield strength drops linearly. At temperatures close to the melting point, it approaches zero.

$$\sigma_y = \frac{2800 - T}{2800 - 2250} \times 10 \qquad \text{(MPa)} \tag{5.6.12}$$

T: Temperature (K)

5.6.3. Fuel Cracking and Healing

Immediately upon startup and before swelling or creep has occurred to any appreciable extent, the fuel develops a network of cracks oriented either along radial planes passing through the fuel pin axis (teta cracks) or along horizontal planes perpendicular to z-axis (z cracks). These cracks appear because the thermoelastic stress components exceed the fracture strength of the fuel in tension [2].

When any principal stress exceeds the fracture stress at a fuel radial node below 1300 ^{0}C, Young's modulus and Poisson's ratio must be modified as decribed in Ref. [2], to account for the cracks:

$$E' = \left(\frac{2}{3}\right)^N E \tag{5.6.13}$$

$$\nu' = \left(\frac{1}{2}\right)^N \nu \tag{5.6.14}$$

N: Number of cracks (Each time any pricinple stress exceeds the fracture stress, N increases by 1 at the brittle part of the fuel.)

As a result of cracking, the principle stresses fall below the fracture stress.

When the cracked region of the fuel is under compressive stresses and the temperature is above 1400 ^{0}C, the cracks heal and the Young's Modulus and Poisson's Ratio turn back to their original form (N = 0).

5.6.4. Hot Pressing

Under the application of an external stress, a fraction of the as-fabricated porosity shrinks. Hot pressing is correlated as a function of creep rate, external stress and the amount of porosity within the fuel. The Ref. [2] model is adopted in this study as follows:

$$\frac{dP}{dt} = -\frac{9}{4}\alpha_1 \sigma P - \left(\frac{3\sigma}{2n}\right)^n \frac{3\alpha_2}{2} \frac{(1-P)P}{\left(1-P^{1/n}\right)^n} \tag{5.6.15}$$

α_1: Diffusional creep coefficient $= \dfrac{3.23\times10^9}{d^2}$ $(1/MPa)$; where d is the grain size (μm)

α_2: Dislocation creep coefficient $= 3.24\times10^6$ $(1/MPa^{4.4})$

n: Stress exponent for the dislocation creep = 4.4

σ: External stress (MPa)

P: As-fabricated porosity fraction

6. VERIFICATION OF FEAST-OXIDE

6.1. Steady State

Preliminary benchmarking of the FEAST-OXIDE steady-state capabilities has been accomplished by using FFTF, EBR-II and JOYO experimental data. Clad strain, fission gas release, fuel central void diameter, clad wastage and fuel failure time (breach) have been benchmarked against the experimental data, as well as against LIFE-4 and SIEX fuel performance codes.

6.1.1. FFTF Bencmarks

The driver fuel of the Fast Flux Test Facility was a mixed oxide fuel. The experimental data for the Core Demonstration Experiment (CDE) lead assemblies [111], [112], [113] and [13] have been used to benchmark the FEAST-OXIDE code. These assemblies consist of mixed oxide fuel pins with annular pellets. The clad and duct materials are HT9. The as-fabricated fill gas is at a pressure of 300 kPa. The experimental data reported for the ACO-1 fuel assembly will be benchmarked against FEAST-OXIDE [111], [112]. Furthermore, LIFE-4, SIEX and FEAST-OXIDE code predictions will be compared for the ACO-3 [13] and CDE [113] fuel assemblies.

The approximate axial power profile of the FFTF core is given in Figure-137 [114]. The fuel pin was divided into eight axial nodes. Furthermore, fuel pellets and cladding material in each axial node were divided into six and three radial nodes, respectively.

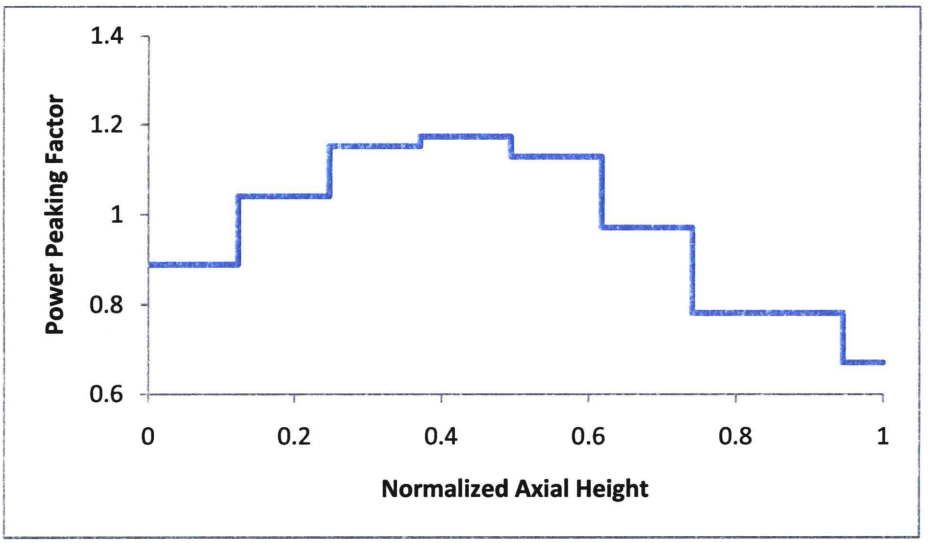


Figure-136: FFTF axial power profile

ACO-1 Fuel Assembly:

Table-41 shows the fuel specifications for the ACO-1 fuel assembly [111], [112], [13]. Furthermore, Figure-138 shows the approximate power history of the ACO-1 fuel assembly [111], [113]. The simulation was performed for the peak operating fuel pin. FEAST-OXIDE results are compared with the experimental data.

Table-41: Fuel specifications for ACO-1 fuel pins

Property	Value
Clad	HT9
Fuel pellet density (%)	92.5
Fuel smear density (%)	80
Fuel pellet inner diameter (mm)	1.47
Fuel pellet outer diameter (mm)	5.55
Clad thickness (mm)	0.56
Clad outer diameter (mm)	6.86
Active fuel height (cm)	91.44
Plenum to fuel ratio	1.0
Oxygen to metal ratio	1.95
Peak linear heat rate (kW/m)	42
Peak time average cladding midwall temperature (^{0}C)	627
Peak burnup (MWd/kg)/ (at %)	123/ 12.5
Peak fluence ($\times 10^{22}$) (n/cm^2)	19

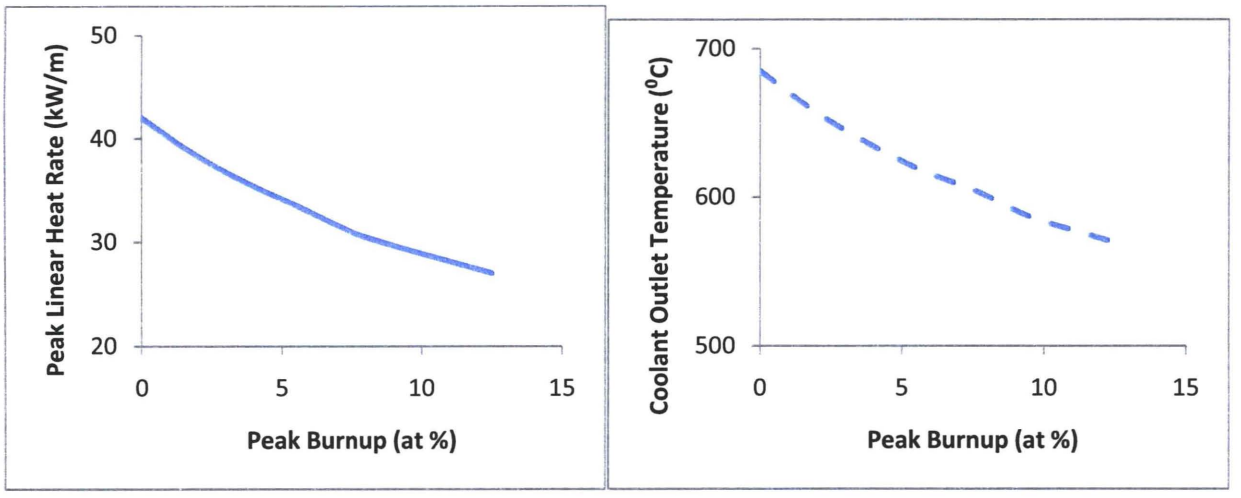


Figure-137: (a): Linear heat rate (b): Peak coolant temperature

Figure-138 shows that FEAST-OXIDE clad strain predictions are matching well with the experimental data. Furthermore, FEAST-OXIDE predictions seem to be more conservative at the middle region. This is the peak power region. The low clad strain at the middle regions could be due to the JOG formation and resulting excessive pore shrinkage. Note that, FEAST-OXIDE models this behavior in a conservative way (see Section 5.3).

High straining of the clad is observed at the top region. First, a significant solid fission product swelling occurs in this region due to cesium axial migration. Second, the operating clad temperature is too high for good HT9 thermal creep performance. Hence, a moderately high fuel clad mechanical interaction (Figure-139) would be enough to strain the cladding. If a more thermal creep-resistant-clad material were to be used (e.g., an ODS), the fuel would have been compressed rather than the clad strained.

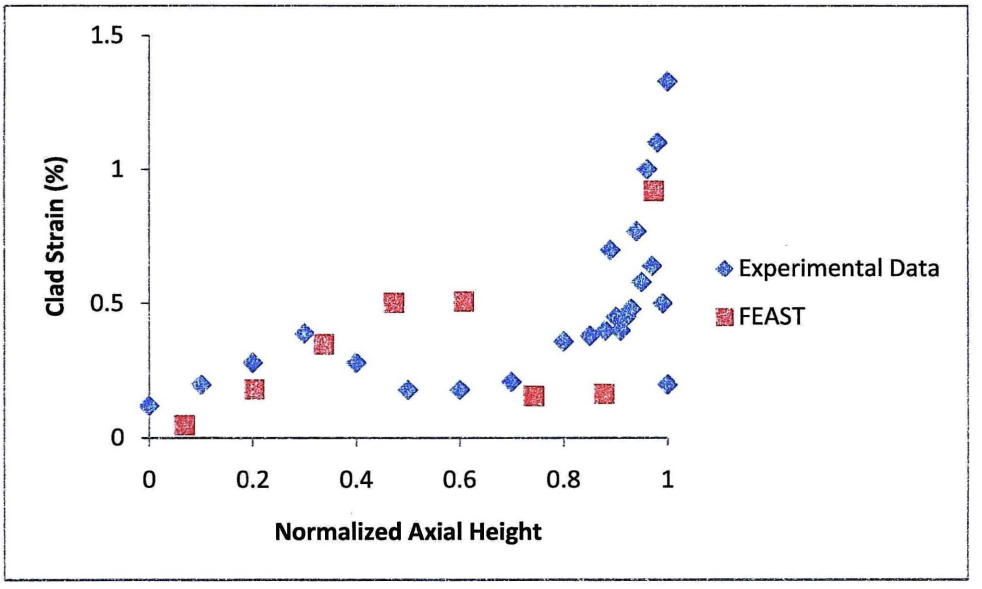


Figure-138: Comparison of the ACO-1 clad strain data with FEAST-OXIDE

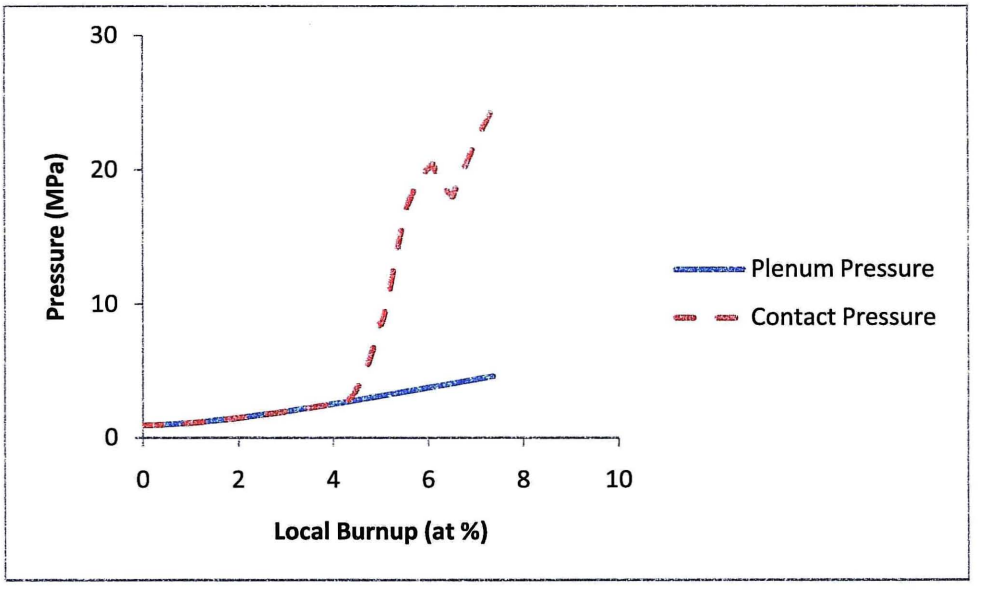


Figure-139: Variation of the contact pressure with local burnup at 97 % height from the bottom of the fuel

Maximum predicted wastage layer is 37 μm at the End Of Life (EOL). The experimental data shows that maximum wastage is 38 μm [111].

ACO-3 Fuel Assembly:

Table-42 shows the fuel specifications for ACO-3 fuel pins. The calculations have been performed with an approximate irradiation history (Figure-140) [13], [113]. The FEAST-OXIDE and LIFE-4 predictions are compared.

Table-42: Fuel specifications for ACO-3 fuel pins [13]

Property	Value
Clad	HT9
Fuel pellet density (%)	92.5
Fuel smear density (%)	80
Fuel pellet inner diameter (mm)	1.47
Fuel pellet outer diameter (mm)	5.55
Clad thickness (mm)	0.56
Clad outer diameter (mm)	6.86
Active fuel height (cm)	91.44
Plenum to fuel ratio	1.0
Oxygen to metal ratio	1.95
Peak linear heat rate (kW/m)	42.6
Peak time average clad outer diameter temperature (^{0}C)	574
Peak burnup (at %)	16.3
Peak fluence ($\times 10^{22}$) (n/cm^2)	19

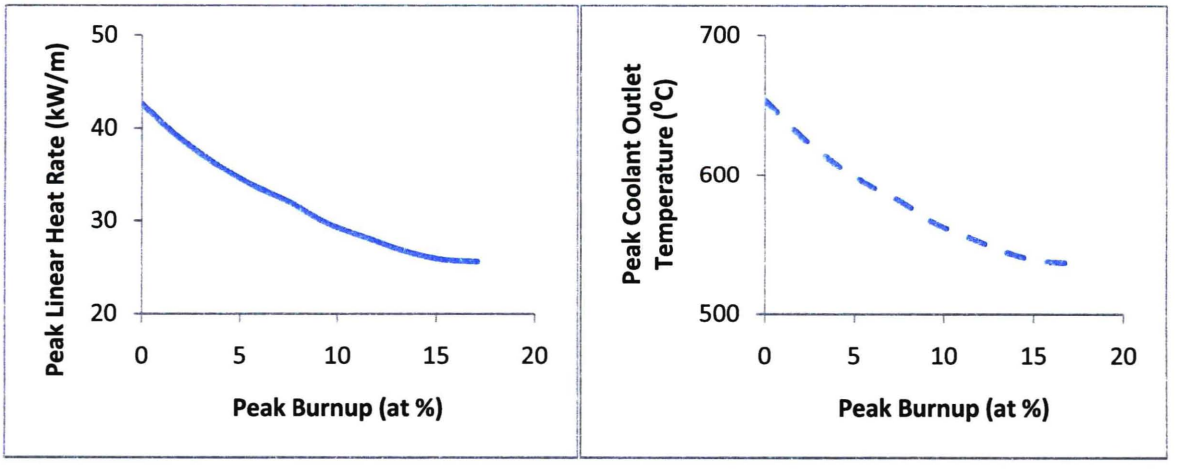


Figure-140: (a): Linear heat rate (b): Peak coolant temperature

The ACO-3 clad operated with a much lower temperature compared to the ACO-1 clad; hence the clad was more resistant to thermal creep. The fuel and clad became radially and axially

restrained at 1-2 at % burnup at the peak power location (Figure-141). A significant increase in contact pressure occurs at the top of the fuel due to the cesium axial migration (Figure-142). Figure-143 shows the effect of cesium axial migration on the solid fission product swelling.

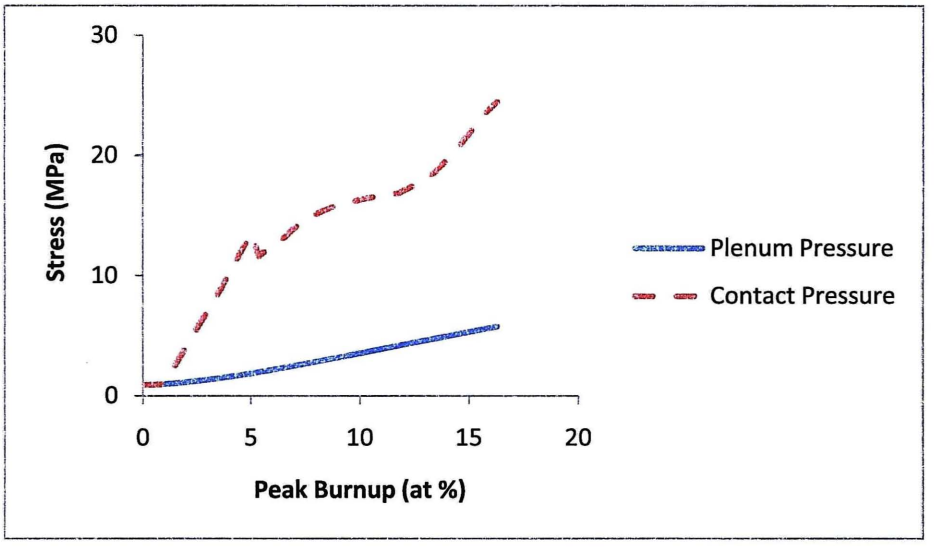


Figure-141: The variation of the contact pressure with peak power location (middle region)

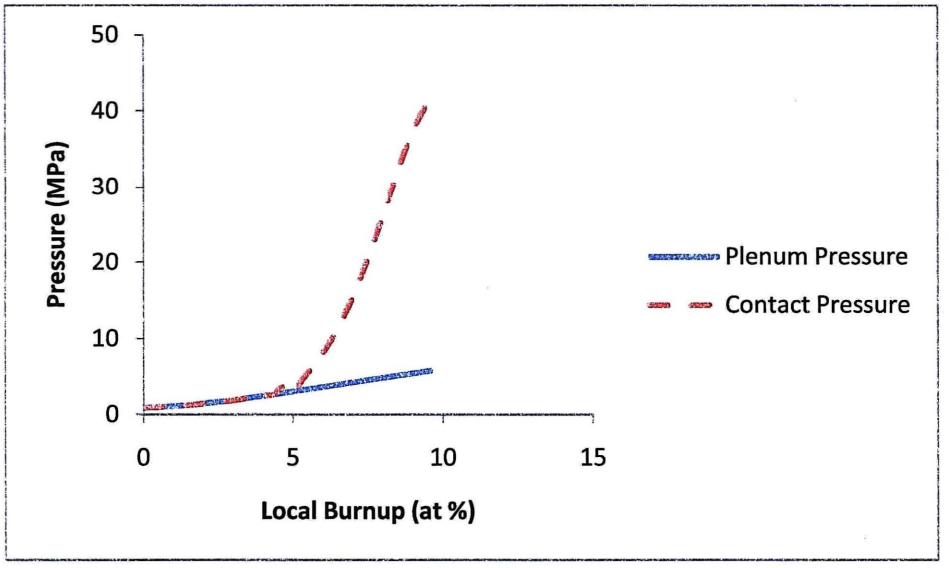


Figure-142: The variation of the contact pressure with local burnup at 97 % height from the bottom of the fuel

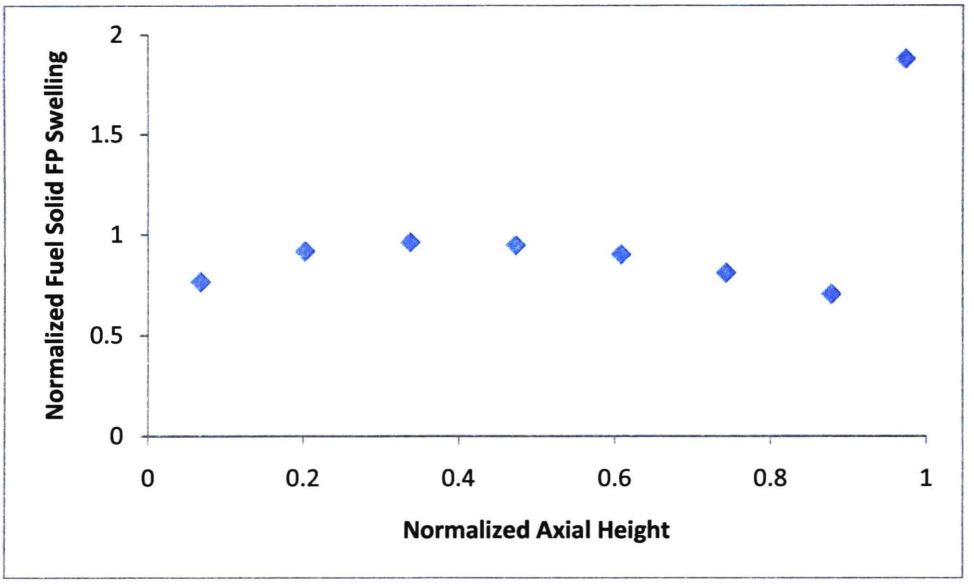


Figure-143: Normalized fuel solid fission product swelling

Figure-144 shows the clad strain comparison between LIFE-4 and FEAST-OXIDE at the End of Life (EOL). The agreement is reasonable. FEAST appears to be conservative at the critical locations, which are the peak power location (middle) and top of the fuel.

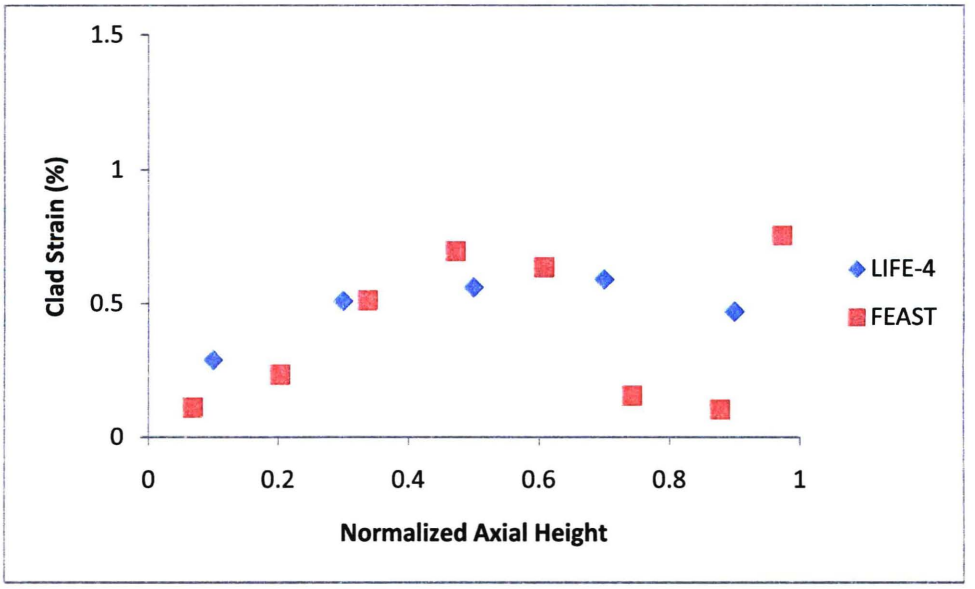


Figure-144: Comparison of the ACO-3 clad strain predictions between FEAST-OXIDE and LIFE-4 at End of Life

Figure-145 shows a comparison of the central void diameter predictions of LIFE-4 and FEAST-OXIDE at the End of Life. FEAST-OXIDE somewhat overestimates the void radius at the bottom of the fuel. However, the predictions match well at the middle and the upper regions.

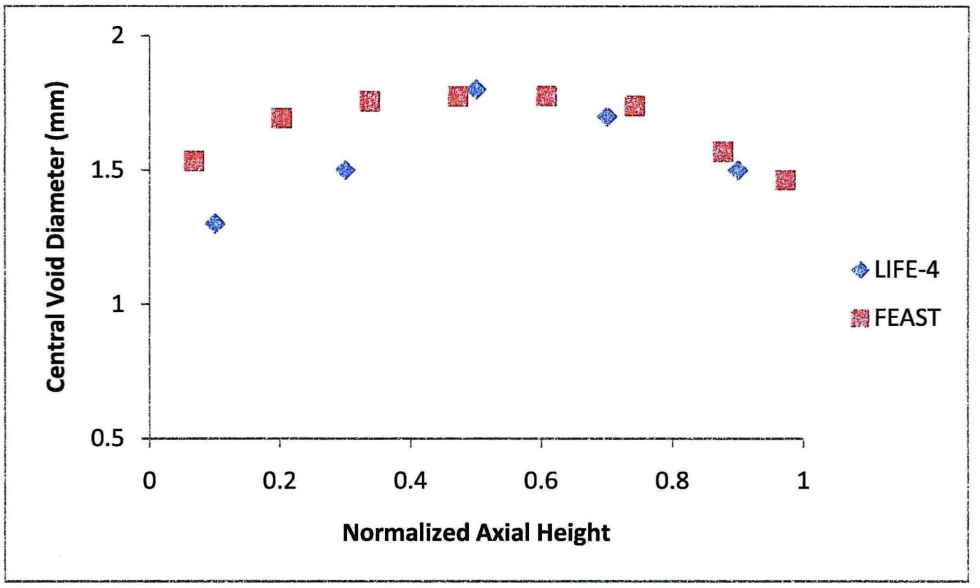


Figure-145: Comparison of the ACO-3 fuel pin central void diameter predictions between FEAST-OXIDE and LIFE-4 at End of Life

CDE Fuel Assembly:

The Core Demonstration Experiment (CDE) fuel assembly is one of the most successful mixed oxide fuel assembly operated in FFTF [111]. LIFE-4 analysis was performed up to 17.1 at %. Similarly, FEAST-OXIDE analysis has been performed up to 17.1 at % and comparisons have been made. Fuel specifications for the CDE fuel pin are given in Table-43. The operating history is given in Figure-146 [113].

Table-43: Fuel specifications for CDE fuel pins [111], [112] [113]

Property	Value
Clad	HT9
Fuel pellet density (%)	92.5
Fuel smear density (%)	80
Fuel pellet inner diameter (mm)	1.47
Fuel pellet outer diameter (mm)	5.55

Clad thickness (mm)	0.56
Clad outer diameter (mm)	6.86
Plenum to fuel ratio	1.0
Fill gas initial pressure (kPa)	300
Active fuel axial height (cm)	91.44
Peak linear heat rate (kW/m)	44.5
Oxygen to metal ratio	1.95
Peak coolant temperature (^{0}C)	588
Peak burnup (MWd/kg) / (at %)	168 / 17.1
Peak fluence ($\times 10^{22}$) (n/cm^2)	25.6

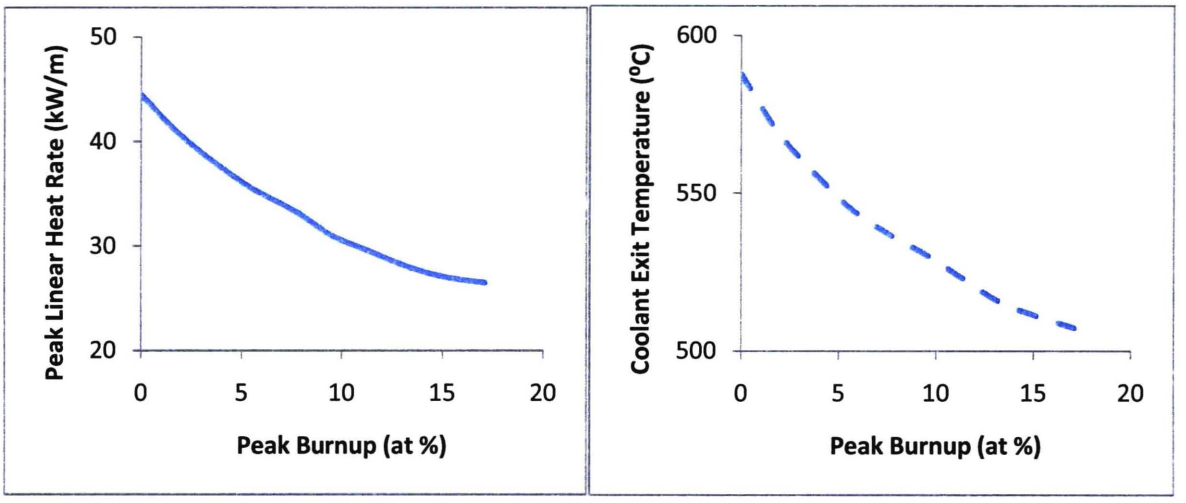


Figure-146: (a): Linear heat rate (b): Peak coolant temperature

The cladding of the CDE fuel pin operated at lower temperatures that the ACO-1 and ACO-3 cases; hence, the clad strain remained low at the top region up to the end of the simulation. The critical location is the middle region. Figure-147 shows the variation of the contact pressure at the peak power location (middle region).

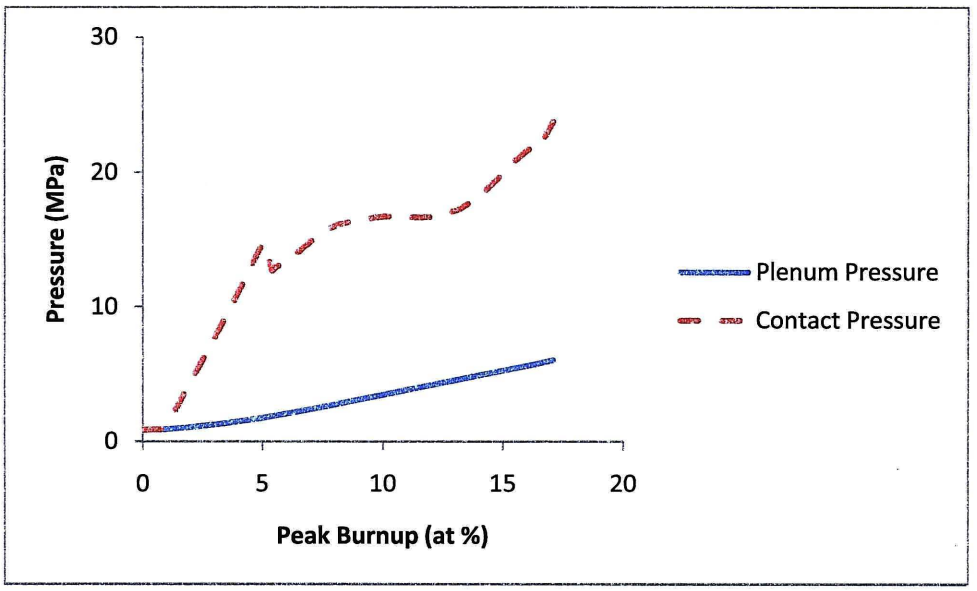


Figure-147: The variation of the contact pressure with peak power location (middle region)

Due to increased contact pressure, clad straining occurs. Figure-148 shows a comparison of the clad strain predictions by different codes. SIEX does not account for the Fuel Clad Mechanical Interaction; hence, it significantly underestimates the clad strain. FEAST-OXIDE lies on the conservative side compared to LIFE-4 and SIEX code predictions.

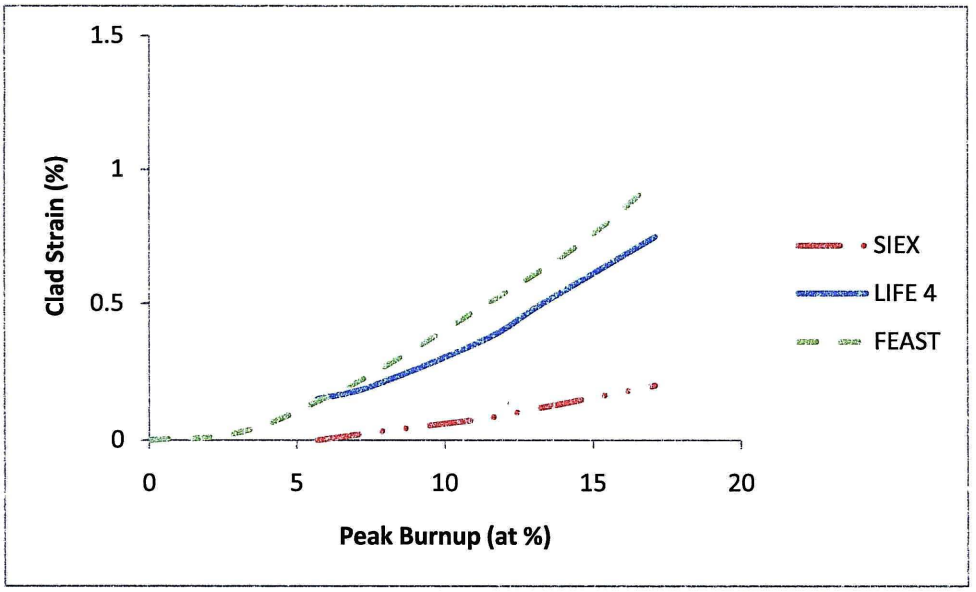


Figure-148: Comparison of the clad strain predictions between LIFE-4, SIEX and FEAST-OXIDE

6.1.2. EBR-II Benchmarks

The breached fuel pins operated in the P42R test in EBR-II are benchmarked against FEAST-OXIDE [115]. These fuel pins possessed a high smear density, high linear heat rates and a thinner clad. Fuel specifications, burnup at which the breaches were observed, and FEAST-OXIDE predictions are given in Table-44. Note that, EBR-II axial power profile is given in Figure-34. The fuel pin was divided into seven axial nodes. Furthermore, fuel pellets and cladding material in each axial node wer divided into six and three radial nodes, respectively.

The experimental data for the time to failure for 316 SS given in Figure-149 were used to predict the time for failure [116]. Note the data is for the clad tempertures above 575 ^{0}C. Sample-3 clad temperature is significantly lower than 575 ^{0}C. Hence, the CDF model is extrapolated to the low temperature region.

Table-44 also shows the predicted burnup at which clad rupture occurs and the experimental data. The Sample-3 failure burnup is somewhat overestimated. It is likely due to the extrapolation of the CDF model to the low temperature regime. The Sample-1 and Sample-2 failure burnups are well predicted.

Table-44: EBR-II high smear density fuel specifications

Property	Sample-1	Sample-2	Sample-3
Fuel smear density (%)	92.3	92.3	92.3
Fuel pellet as-fabricated porosity (%)	6.6	6.6	6.6
Clad material	316SS	316SS	316SS
Clad thickness (mm)	0.28	0.28	0.28
Clad outer diameter (mm)	6.86	6.86	6.86
Active fuel height (cm)	34.3	34.3	34.3
Plenum to fuel ratio	1.0	1.0	1.0
Oxygen to metal ratio	1.945	1.916	1.916
Peak linear heat rate (kW/m)	40.4	45.6	47.3
Peak clad temperature (^{0}C)	574.0	621.0	560.0

Peak Fluence ($\times 10^{22}$)	3.7	2.1	2.2
Peak burnup at rupture (at %) **FEAST Prediction (at %)**	**3.9** **3.9**	**2.5** **2.6**	**1.8** **2.5**

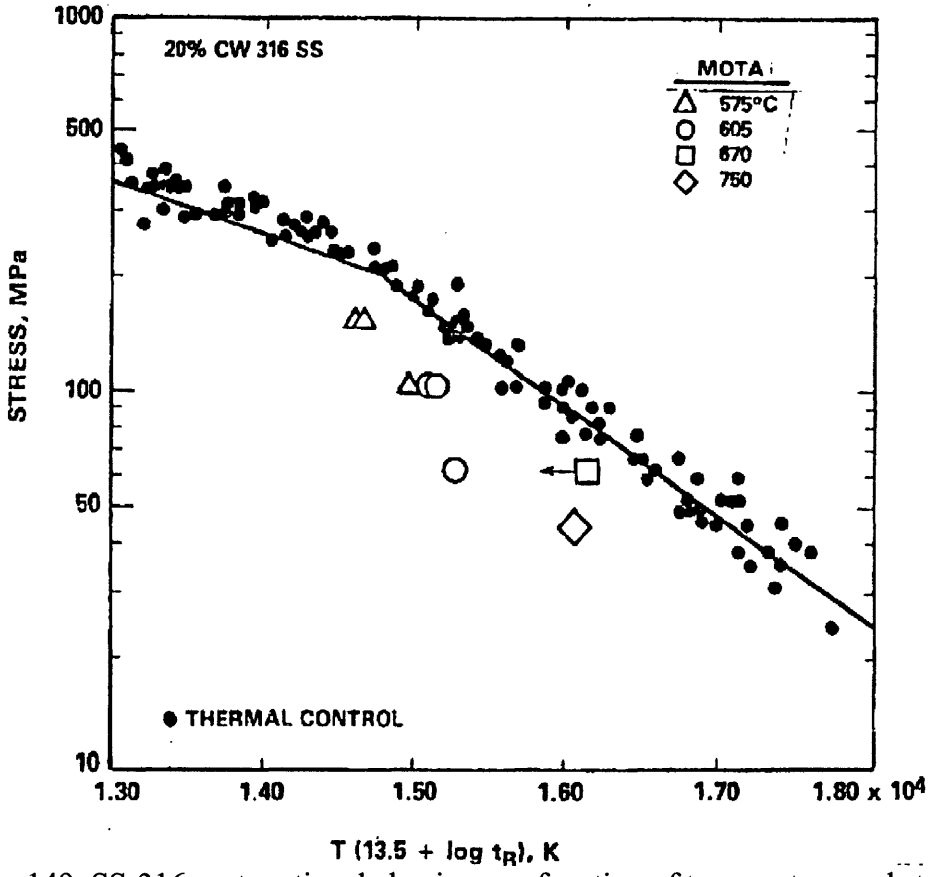


Figure-149: SS-316 rupture time behavior as a function of temperature and stress [116]

Sample-1:

Sample-1 contact pressure, clad strain and cumulative damage fraction variation with burnup are given in Figure-150, 151, and 152, respectively. Operation with a high linear heat rate results in rapid gas swelling due to high operating temperatures. Also, the smear density is high; hence there is not much room to accommodate fuel swelling, so fuel clad mechanical interaction rises significantly and clad straining occurs. The contact pressure increases less rapidly with time, as the stresses are partially relieved by clad straining. The predicted burnup at which a breach occurs (CDF=1) and the experimental data are in perfect agreement in this case (see Table-44).

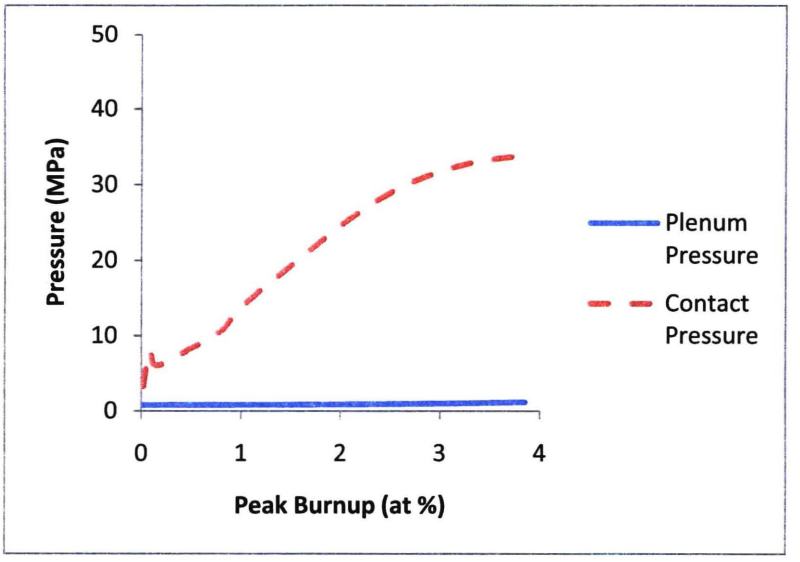


Figure-150: Sample-1 contact pressure variation with burnup at peak power location

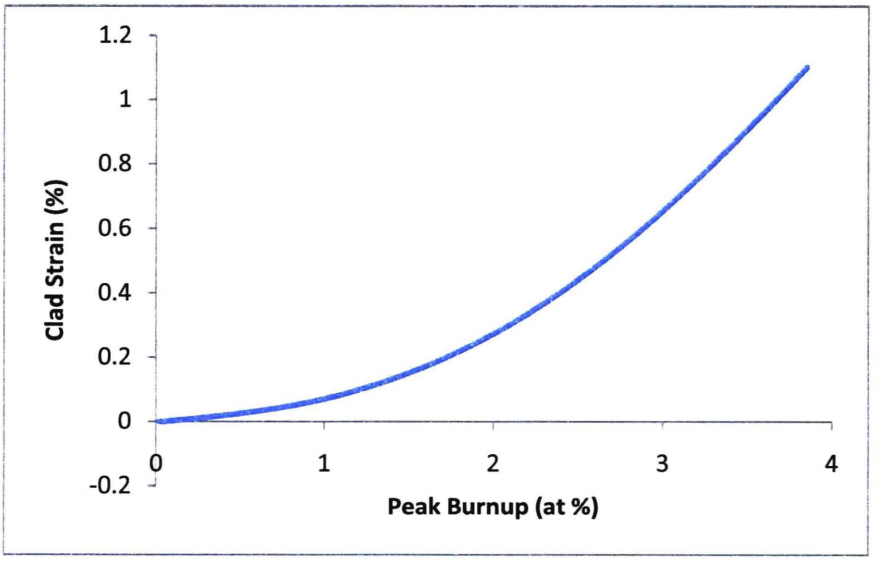


Figure-151: Sample-1 clad Strain at peak power location

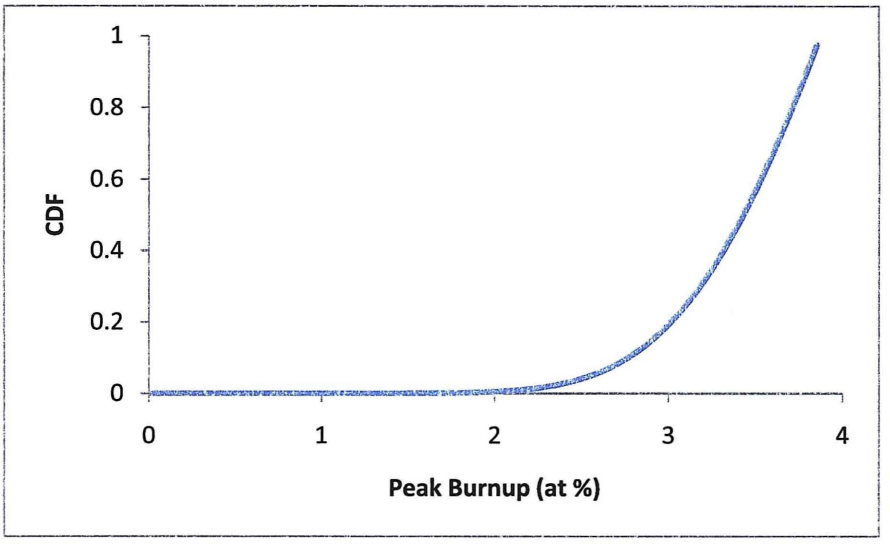


Figure-152: Sample-1 cumulative damage fraction

Sample-2:

Sample-2 operated with a higher clad temperature and linear heat rate. As a result, the predicted burnup at which a breach occurs is much earlier compared to Sample-1. The oxygen-to-metal ratio in sample-2 is lower than in Sample-1. Figure-153, 154 and 155 show variation of the contact pressure, clad straining and cumulative damage fraction, respectively. The match between the predicted burnup (CDF=1) and experimental data for the breach is again excellent.

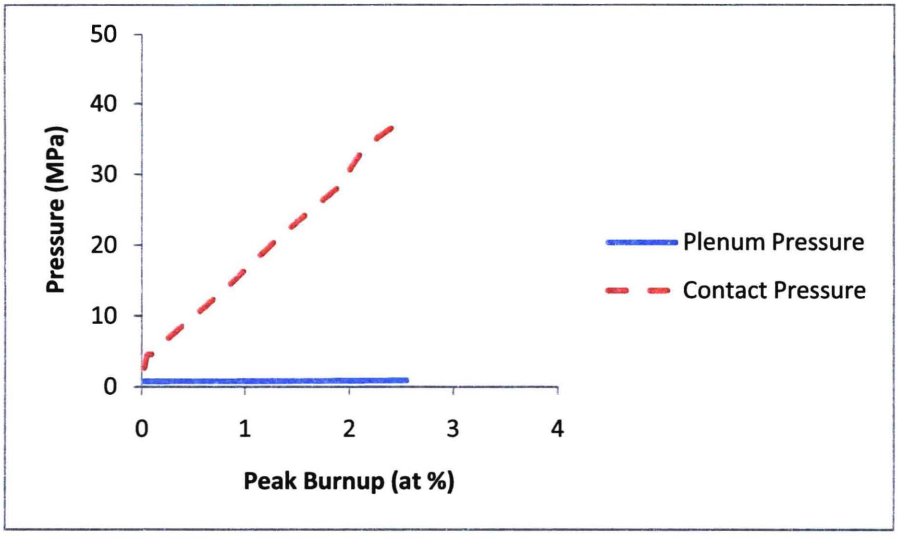


Figure-153: Sample-2 contact pressure variation with burnup at peak power location

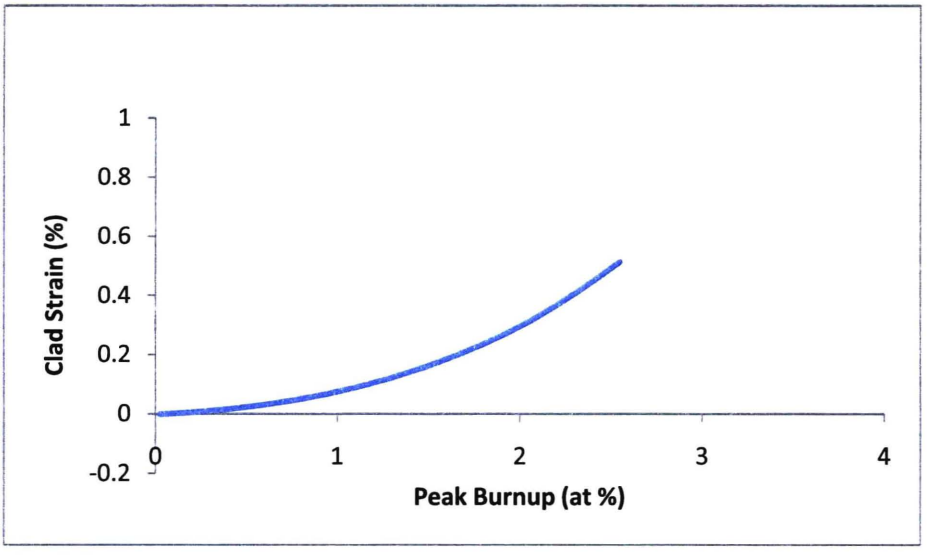


Figure-154: Sample-2 clad strain at peak power location

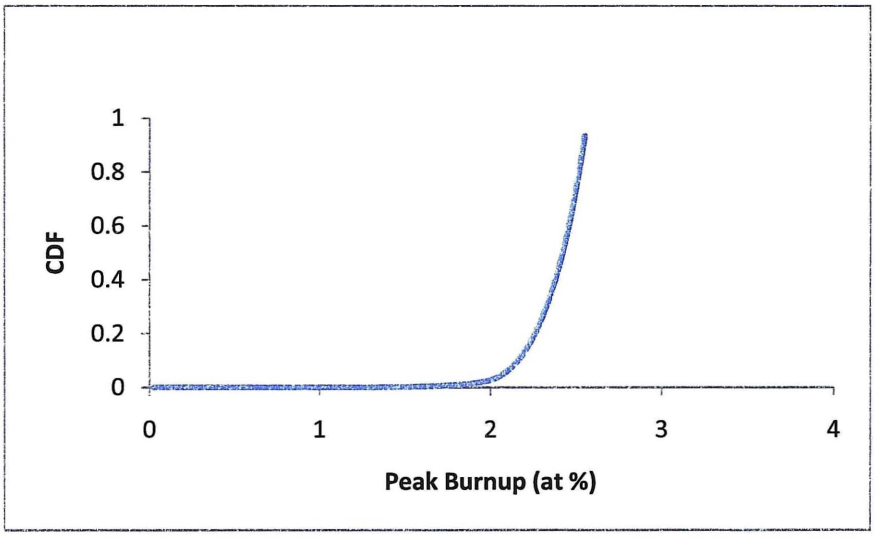


Figure-155: Sample-2 cumulative damage fraction

Sample-3:

Sample-3 has the highest linear heat rate. Furthermore, its oxygen-to-metal ratio is lower; hence, the fuel centerline temperature and corresponding thermal expansion strain is higher than Sample-1 and identical to sample-2. On the other hand, the clad temperature is lower than both Sample-1 and Sample-2, outside the failure database given in Ref. [116] and used in developing the failure model in this thesis. Figure-156, 157 and 158 show the variation of the contact pressure, clad strain and cumulative damage fraction, respectively. The predicted burnup at which breach occurs is 2.5 at %, whereas the experimental data is 1.8 at %. The agreement in this case is reasonable.

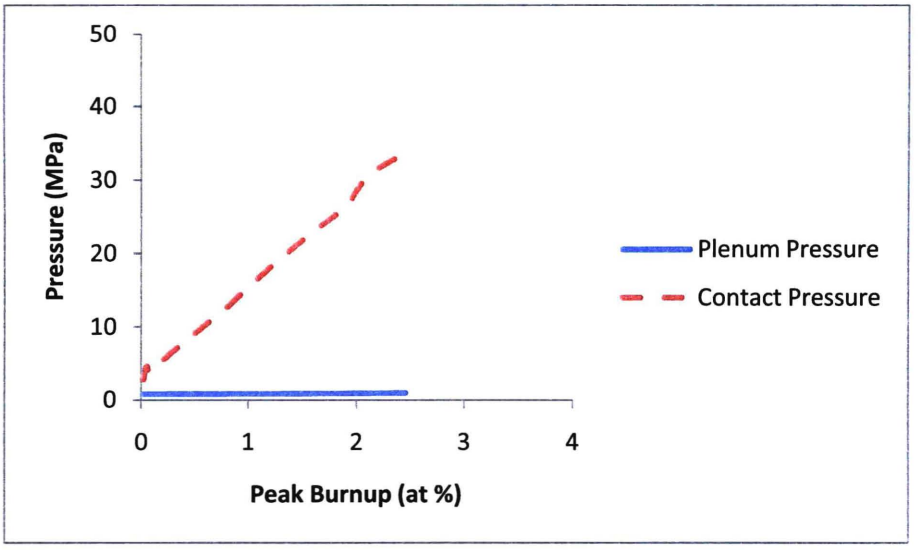


Figure-156: Sample-3 contact pressure variation with burnup at peak power location

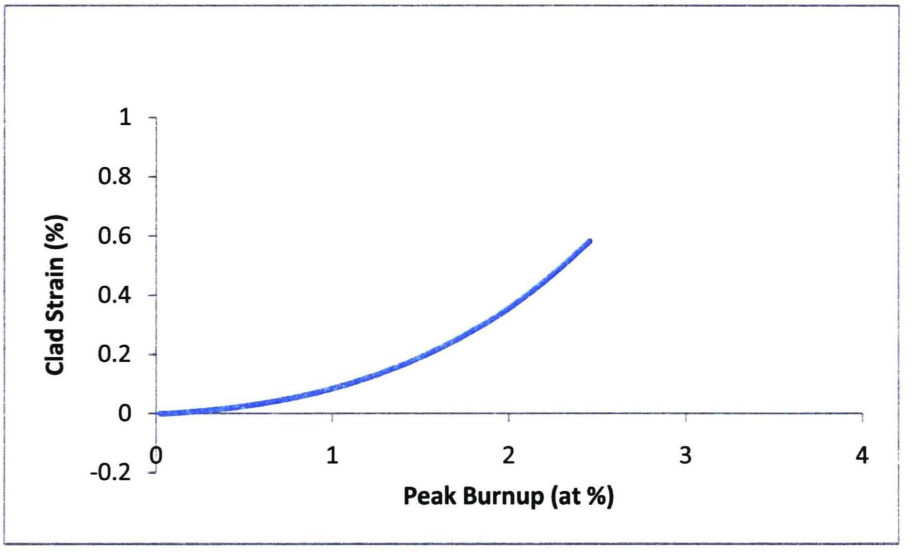


Figure-157: Sample-3 clad strain at peak power location

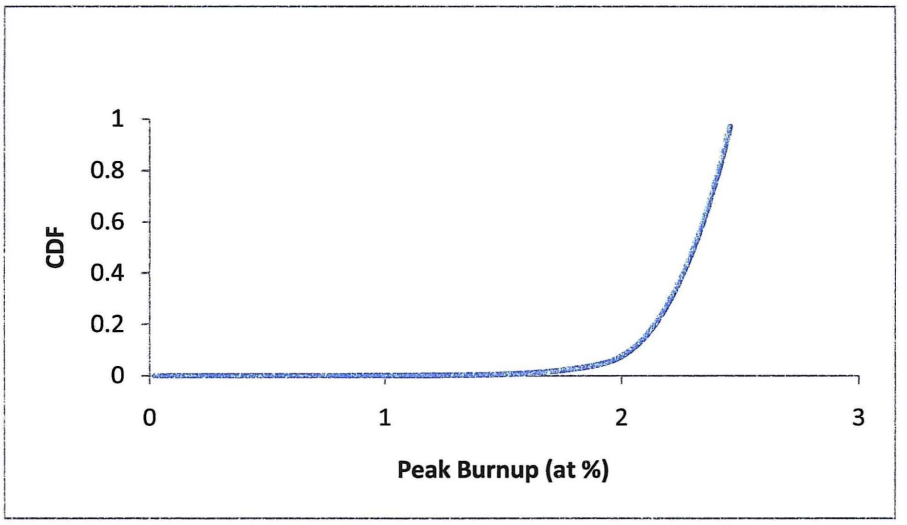


Figure-158: Sample-3 cumulative damage fraction

6.1.3. JOYO Benchmarks

The liquid-metal-cooled experimental fast reactor JOYO was constructed as the first step in the FBR development program in Japan [117]. The initial criticality was estabilished in April 1977 with the MK-I type core. Later the MK-I core was replaced with the MK-II core accompanied by a reactor power uprate. The MK-I and MK-II fuel specifications are given in Table-45. The approximate axial power profile of the FFTF core given in Figure-136 is used also for JOYO. The fuel pin was divided into eight axial nodes. Furthermore, the fuel pellet and the cladding material in each axial node were divided into six and three radial nodes, respectively.

Table-45: JOYO MK-1 and MK-II fuel specifications

Property	MK-I	MK-II
Pellet diameter (mm)	5.4	4.63
Pellet Density (%)	93.5	93.0
Wire diameter	1.2	0.9
Clad Material	316SS	316SS
Clad thickness (mm)	0.35	0.35
Clad outer diameter (mm)	6.3	5.5
Plenum to fuel ratio	1.0	1.0

Active core height (m)	0.6	0.55
Oxygen to metal ratio	1.98	1.98
Peak linear heat rate (kW/m)	32	40
Reactor coolant inlet temperature (^{0}C)	370	370
Peak coolant exit temperature (^{0}C)	470.0	500.0
Peak Flux (n/cm^2/s)	3E+15	5.1E+15
Maximum Average Burnup (MWd/kg)/ (at %)	42 / 4.3	50 / 5.1

Comparison of the experimental fission gas release data for MK-I and MK-II are given in Figure-159 and Figure-160, respectively.

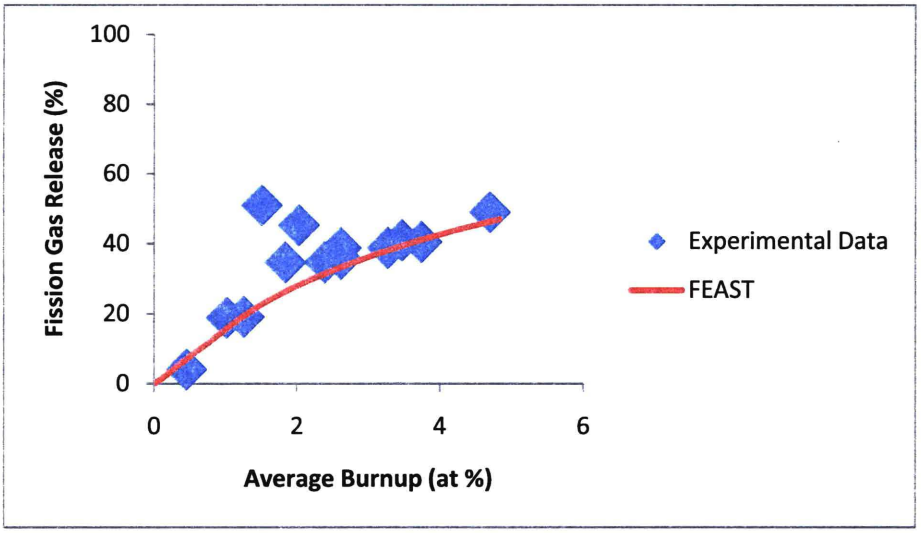


Figure-159: Fission gas release behavior of MK-I type fuel

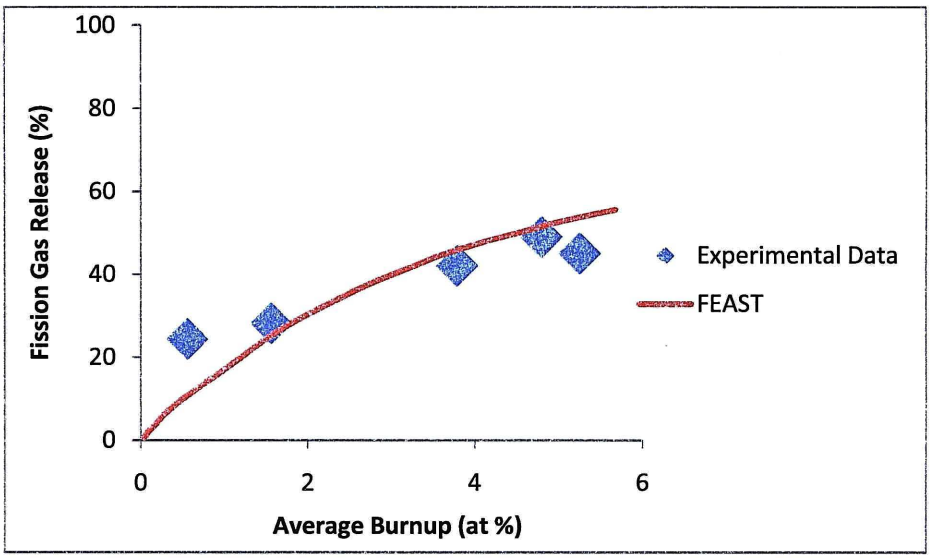


Figure-160: Fission gas release behavior of MK-II type fuel

6.2. Transients

A slow-ramp extended overpower test was conducted in EBR-II for mixed oxide fuel pins [118]. Table-46 shows the fuel specifications. The clad materials are the modified austenitic stainless steels D9 and SUS-316 [118]. The transient scenario for each fuel pin is given in Table-47 and Figure-161. The reactor power linearly increased from 38.5 MWt to 73.3 MWt. The scenario was simulated with FEAST-OXIDE and benchmarked against the experimental data.

The analysis has been accomplished assuming fuel and clad are locked to each other if the fuel is constrained by the cladding. It is stated in Ref. [118] that few fuel pins show significant elongation axially; whereas others remain axially constrained by the clad. Significant axial elongation may occur due to the transverse fuel cracking and lifting of the fuel with the molten part. Neglecting them and assuming the fuel and clad are axially locked is a conservative assumption.

After the steady state operation, the reactor operating conditions were adjusted at a different level than the End of Life Condition and the reactor was operated with the new conditions

approximately for a week period prior to the transient initiation. This period is called pre-conditioning.

Table-46: Fuel specifications for TOP-1D test elements

Test Element	Time averaged Clad ID Temperature (prior to transient) (^{o}C)	EOL Peak Power (kW/m)	Peak Burnup (at %)	Clad OD (mm)	Pellet Density (% TD)	Pellet Diameter (mm)	Smear Density (% TD)	Fuel O/M	Pu Content (wt %)	Plenum to Fuel Ratio
WT028	630	35.0	2.5	6.985	90.4	6.166	88.0	1.95	22.5	1.12
WT118	650	34.7	9.3	5.842	93.4	4.996	90.3	1.96	33.0	1.18
WT107	640	42.4	7.7	6.985	92.9	6.149	90.0	1.97	22.5	1.12
WT022	600	31.8	6.0	6.985	90.3	6.093	85.9	1.95	30.0	1.12
WT033	600	33.1	5.9	6.985	90.4	6.165	88.0	1.95	30.0	1.12
WT180	635	37.6	6.9	6.985	94.6	6.162	89.7	1.97	22.5	1.12
WT179	650	39.0	7.1	6.985	94.6	6.162	89.7	1.97	22.5	1.12
WT011	610	34.6	6.4	6.985	90.3	6.093	85.9	1.95	22.5	1.12

Table-47: Initial and final conditions during the overpower transient

Test Element	Preconditionining (Peak Power (kW/m)	Preconditioning Peak Clad Temperature (^{o}C)	Transient Peak Power (kW/m)	Transient Peak Clad Temperature (^{o}C)
WT028	33.6	577	63.9	766
WT118	31.7	641	60.3	885
WT107	38.8	617	73.9	841
WT022	30.8	594	58.7	797
WT033	31.6	574	60.1	759
WT180	39.4	624	75.0	853
WT179	39.1	622	74.4	850
WT011	30.7	625	58.5	856

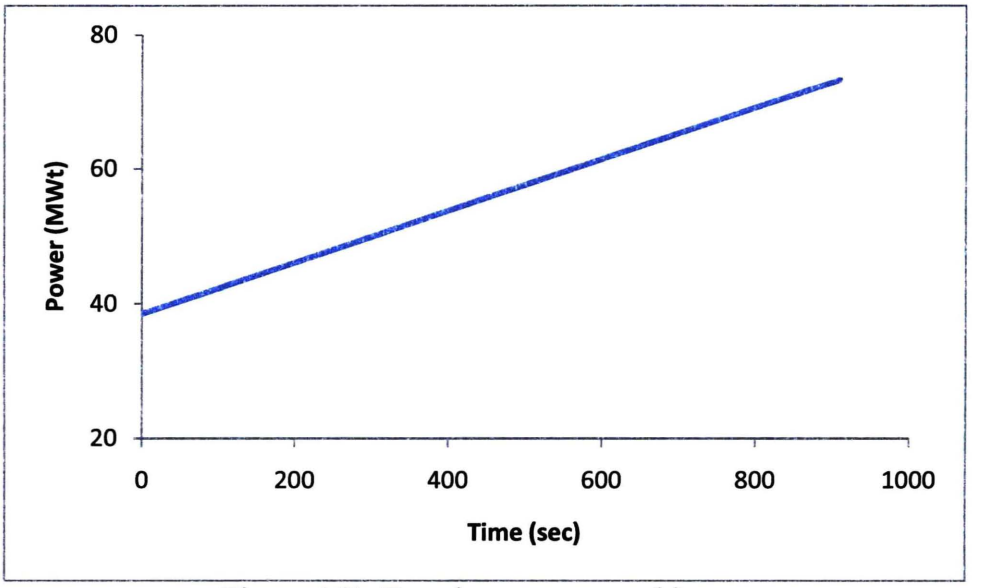


Figure-161: Transient overpower history

The temperature distribution, contact pressure and transient clad strain variation are depicted in Figure-162, 163 and 164 for the WT180 fuel element, as a representative example. Figure-162 shows that 37 % of the peak power fuel pellet (by area) is molten at the end of the transient. The Ref. [118] reports 32 % areal melt, which is consistent with FEAST-OXIDE predictions.

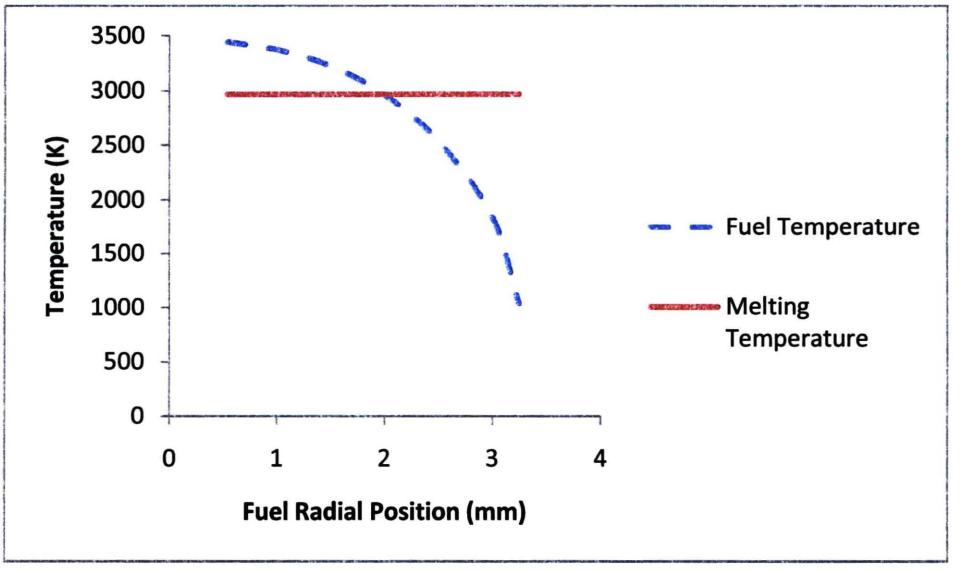


Figure-162: Peak fuel temperature for the WT180 fuel pin at 910 seconds (end of the transient)

Figure-163 shows the variation of the contact pressure and the plenum pressure during the transient at the top position of the fuel pin. The contact pressure first rises up to 400 seconds due mainly to the thermal expansion of the fuel. When the clad temperature is high enough for thermal creep straining (Figure-164), the contact pressure is relieved. Furthermore, there are some spikes appearing in Figure-163, which are due to the activation of the NEFIG intragranular gas model. If a fuel radial node exceeds 1800 ^{0}C, NEFIG model is activated to describe the rapid coarsening of the intragranular gas bubbles and the gas release. Hence, the spikes are due to rapid swelling of the intragranular gas bubbles.

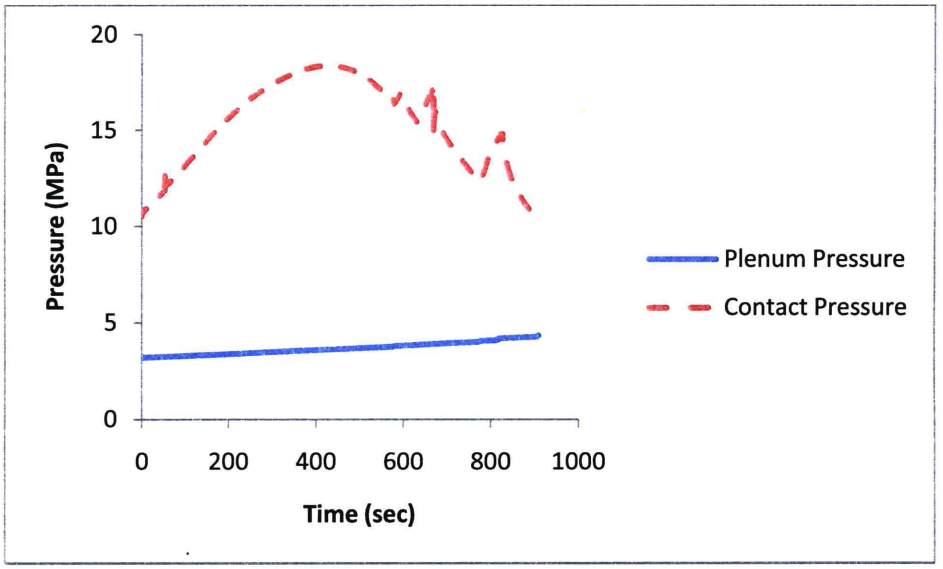


Figure-163: The variation of the contact pressure at the top node (WT180 fuel pin)

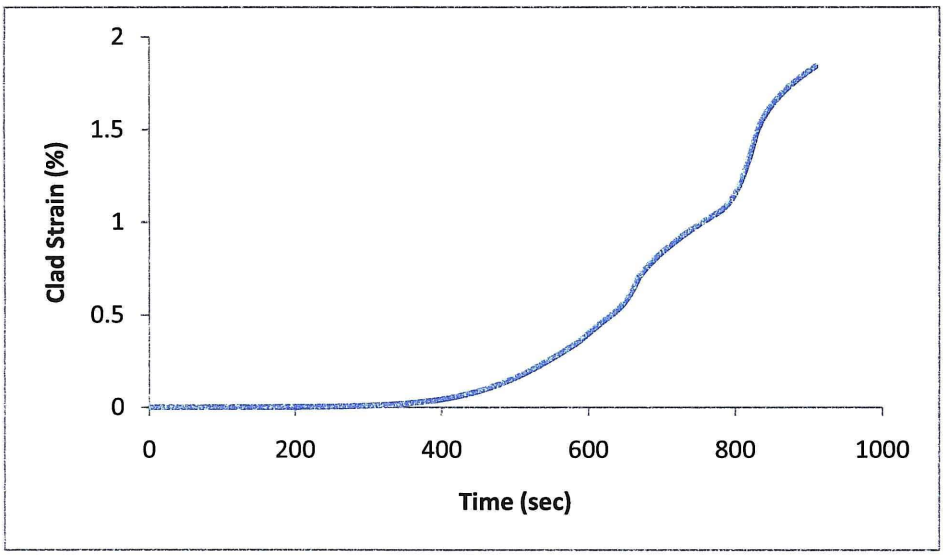


Figure-164: The increase in transient cladding strain (WT180 fuel pin)

Table-48 shows that no failure has been detected for this fuel pin, in spite of partial fuel melting. This is due to the accommodation of molten fuel in the central void, which prevents excessive FCMI. Similarly, FEAST-OXIDE predictions show no failure. Typically, the CDF remains below 0.3. Fuel pins tested with a transient peak power around 60 kW/m such as WT028, WT022, WT033 and WT011 show small cladding strain. The FEAST predictions are consistent with this behavior. The WT118 fuel pin also has a transient peak at 60 kW/m but a higher, transient clad strain occurs. Note that this fuel pin has a much higher burnup, its smear density is higher and the initial porosity (or central void diameter) is lower than the WT028, WT022, WT033 and WT011 cases. The experimental data shows that the magnitude of clad strain is somewhat higher. FEAST-OXIDE clad strain prediction is also higher and somewhat in the conservative side.

The WT107, WT179 and WT180 fuel pins were operated with a much higher peak transient overpower (75 kW/m) compared to the other fuel pins. The WT107 clad strain is much lower compared to WT179 and WT180, although the transient history is similar, because the initial porosity, or the central void diameter of WT107 is much larger; hence there is more space for accommodation of the expansion of the molten fuel. The WT179 and WT180 fuel pins have a low initial as-fabricated porosity and central void diameter. As a consequence, melting of the

fuel causes much higher straining of the clad in these cases. Note that the FEAST-OXIDE predictions are reasonably good and on the conservative side.

Table-48: Comparison of the results with FEAST-OXIDE

Test Element	Transient Clad Strain (Experimental Data) (%)	Transient Clad Strain (FEAST-OXIDE)	Axial Location (X/L)	Failure Time (Experimental Data)	Failure Time (FEAST-OXIDE)
WT028	0.15	0.0	0.8	No Failure	No Faillure
WT118	0.25	0.8	1.0		
WT107	0.10	0.36	1.0		
WT022	0.00	0.0	-		
WT033	0.06	0.07	0.9		
WT180	1.50	1.80	1.0		
WT179	0.70	1.40	1.0		
WT011	0.07	0.0	0.7		

Transient fission gas release experimental data show that low burnup fuel elements have 10-20 % fission gas release during the transient. The FEAST-OXIDE prediction for WT028 fuel element is 17 %, hence, it is consistent with the experimental data. The fission gas release for the high burnup fuel elements are reported as much smaller [106]. The FEAST-OXIDE predictions for the higher burnup fuel is of the order of 5 %; hence, it is also consistent with the experimental data.

7. SUMMARY, CONCLUSIONS AND FUTURE WORK

7.1. Summary

This work developed advanced codes for prediction of the thermo-mechanical behavior of metal and oxide fuels in Sodium Fast Reactor applications. The codes improve upon the existing models by adopting science based description of some of the phenomena. The codes are validated with the experimental database available in the literature. The codes capabilities cover both steady-state conditions and transient scenarios.

During irradiation the fast reactor fuel evolves drastically due to fission gas release and swelling, creep of the fuel and clad, irradiation-induced effects, thermal diffusion of the fuel constituents and fuel restructuring. Hence, a rigorous approach to modeling a fast reactor fuel pin should include thermal, mechanical, chemical, and fission gas behavior models in a coupled form, together with a complete material property data set. The Fuel Engineering And Structural analysis Tool (FEAST) code is composed of several modules inter-linked to simulate the fuel thermo-mechanical behavior. These modules are (1) Fission Gas Release and Swelling, (2) Fuel Chemistry and Restructuring, (3) Temperature Distribution, (4) Fuel Clad Chemical Interaction, (5) Fuel and Clad Mechanical Analysis and (6) Transient Creep-Fracture Model for the clad. Two separate code-components have been developed: one for metal fuel, the other for oxide fuel.

Metal Fuel:

Metal fuel typically consists of a binary alloy of uranium and zirconium or a ternary alloy of uranium, plutonium and zirconium. Addition of about 10 % by weight zirconium to a uranium-plutonium alloy raises the solidus temperature of the fuel and prevents fuel-cladding inter-diffusion at temperatures typical of steady operating conditions. The fuel/clad gap is filled with liquid sodium, which acts as a thermal bond.

Metal fuel experiences significantly higher gas and solid fission product swelling compared to oxide fuel. Designing the fuel with a low smear density (70-75 %) allows for accommodation of sufficient gas swelling and formation of interconnected open porosity. As a consequence, it becomes possible to operate metal fuel with a low fuel clad mechanical interaction while also

accommodating the solid fission product swelling up to high burnup. The distinguished advantage of the metal fuel is its softness, particularly at the upper (hotter) part of the fuel pin, which is mostly in the gamma phase. Therefore, it becomes easy to compress the porosity of the fuel, which mitigates fuel clad mechanical interaction; the main load on the clad is the plenum pressure; the thermal creep can be controlled. In the middle and lower parts of the fuel pin, the dominant mechanism for clad deformation is irradiation creep. The fuel is rather stiff in these regions and the porosity compression may require a relatively high fuel clad mechanical interaction stress; however, the clad temperature is also lower in this region; hence, the clad can bear the load to a greater extent. At high burnup, solid fission product swelling may counter the open porosity of the fuel and fuel clad mechanical interaction could cause a failure due to creep-fracture, even at steady state operation. In case of a transient scenario, the critical region becomes the upper part of the fuel pin due to the high clad temperature and low thermal creep resistance. Here, the advantage of metal fuel appears. Due to the high fuel compliance at the upper part, the load on the clad becomes close to the plenum pressure. On the other hand, with the formation of the U-Pu-Fe eutectic phase at the fuel clad interface, accelerated penetration of the clad may result. This behavior limits the steady state operating temperature as well as the transient performance of the metal fuel; however, it is a slow process compared to a typical transient time.

The FEAST-METAL code is composed of several modules in coupled form, to simulate the integrated metal fuel thermo-mechanical behavior.

The fission gas release and swelling module implements the GRSIS algorithm which was specifically developed for metal fuel. While the grain boundaries are the only significant locations for the oxide fuel gas swelling, metal fuel allows for significant gas swelling both at the grain and phase boundaries (inside the grains). As a result, gas swelling in metal fuel is a 3D problem. The GRSIS model allows for bubble nucleation in any location within the fuel. Hence, it reflects the metal fuel physics well. After nucleation the bubbles grow due to further diffusion of fission gas atoms from the fuel matrix and the coalescence with other gas bubbles. Above the threshold gas swelling (10 %), the interconnected open porosity starts to form. After that, the gas can escape from the fuel matrix by direct diffusion into the interconnected porosity or by

coalescence of gas bubbles with the interconnected porosity. Allowing about 30 % unconstrained fuel swelling, a significant amount of pores become interconnected, which makes the fuel "spongy" and compliant. Finally, solid fission product swelling has been modeled as 1.5 % per at % burnup; thus, its rate was assumed to be constant with burnup.

At power, different phases may form at different radial locations of the metal fuel. Because each phase has different chemical properties, zirconium and uranium atoms tend to migrate under the radial temperature gradient driving force. Upon constituent redistribution, the microstructure of irradiated metal fuel exhibits three distinct concentric zones, a zirconium-enriched central zone, a zirconium-depleted and uranium-enriched intermediate zone, and a zirconium-enriched zone on the outer periphery. A model developed at ANL has been adopted in this study to predict the migration behavior of the fuel constituents. This model is based on the thermo-transport theory, solves the diffusion equation, given the diffusion coefficients, heat of transport, enthalpy of solution of each phase and the phase diagram.

The temperature distribution module adopts a 1D radial approach; thus, heat conduction in the axial and azimuthal directions is neglected. It determines the radial temperature distribution by using the energy balance method. The model adopts a semi-implicit Crank-Nicholson numerical algorithm to simulate the time dependent behavior of the fuel pin temperature for transient scenarios. The key factors affecting the temperature distribution of metal fuel are known to be porosity, bond sodium infiltration into the porosity and thermal conductivity dependence on the fuel constituent redistribution. These parameters are incorporated into the fuel temperature calculation in FEAST-METAL. The coolant temperature distribution model adopts the single mass velocity model.

Fuel Clad Chemical Interaction (FCCI) and the resulting clad wastage are an important part of the fuel modeling codes. Lanthanides have a low solubility in metallic fuels. Migration of the lanthanides into the clad and migration of iron atoms into the fuel occur during normal and off-normal operations. Lanthanides form a brittle layer at the clad inner surface. Furthermore, the iron at the fuel surface forms $(U, Pu)_6Fe$ phase which has low eutectic melting temperature. Zirconium atoms within the fuel hinder this reaction significantly at typical steady state

operating condition. On the other hand, during a transient, liquefaction of the fuel surface may occur above the $(U, Pu)_6Fe$ eutectic temperature and the eutectic penetrates towards the cladding due to the enhanced iron diffusion. The FCCI model developed in this work is based on the precipitation kinetics approach. The model describes the time-dependent behavior of the clad wastage in a more mechanistic way compared to the empirical relations in the literature. Furthermore, the new model has a direct dependency on the concentration of the diffusing species; hence the burnup (or power) dependency of the FCCI has also been captured. In addition to wastage at its inner surface, the clad also experiences wastage at its outer surface due to sodium corrosion. Sodium corrosion was modeled with an Arrhenius type relation. However, it is typically only of the order of few microns.

The mechanical analysis model of FEAST-METAL adopts the LIFE algorithm. It is a 1D generalized plane strain approach. The model solves the mechanical continuity equation as well as the axial force balance equation, to calculate the principal stresses of the fuel and clad, fuel clad mechanical interaction and the axial friction force at each time step. Creep and plasticity, elastic, gas swelling, solid fission product swelling, compressibility of the interconnected open porosity, and thermal expansion strains are accounted for. The metal fuel slugs show anisotropic deformation during the early operation; as a consequence, the fuel touches the clad without significantly swelling in the axial direction. It is due to cracking and grain boundary tearing of the alpha phase region. This behavior has been modeled as a function of plutonium concentration and temperature gradient.

Transient creep fracture models are an essential part of the fuel modeling codes, to predict the failure time. Typically, fast reactor clad failure occurs due to intergranular creep-fracture. Two approaches were taken to model this behavior. First, the Cumulative Damage Fraction (CDF) model has been adopted. It predicts the time to rupture by properly averaging the constant stress and constant temperature creep-rupture database; this model is highly empirical. A more mechanistic model has also been developed in this work to predict the time to failure of the clad. The Constrained Diffusional Cavity Growth (CDCG) model predicts the nucleation and growth of the cavities at the grain boundaries, and thus produces an estimate of the crack radius of the cavities. When a critical value of the crack radius is reached, the model assumes that the cavities

coalesce and fracture occurs. It appears to be somewhat more conservative in contrast to the CDF model.

FEAST-METAL has been benchmarked against the available EBR-II database for steady state and furnace (transient) tests. Four steady state cases and six transients were simulated. The steady-state cases correspond burnup between 7 to 19 at %; whereas the transient analyses span between 2 to 11 at %. The peak clad temperature for the steady state simulations varies between 550 ^{0}C to 660 ^{0}C. It is between 650^{0}C to 820 ^{0}C for the transient simulations. The peak cladding dose was 100 dpa. The results show that metal fuel code is able to predict important phenomena such as cladding strain, fission gas release, clad wastage, clad failure time and axial fuel slug deformation, satisfactorily. Furthermore, parametric studies have been performed to examine the metal fuel behavior and show the numerical stability of the code for steady state and transient scenarios. The results are satisfactory. Finally, the capabilities of the code have been extended to annular metal fuel pins with simultaneous internal and external cooling. A preliminary parametric study and optimization are also reported.

Mixed Oxide Fuel:

Mixed oxide fuel is composed of UO_2 and PuO_2. It has a substantial database from research and practice in FFTF and French fast reactors. Mixed oxide fuel maturity and ease of fabrication make it a very attractive candidate for nuclear systems. Its main advantage is its good chemical stability, high melting point and compatibility with stainless steel. Hence, we can operate the reactor with a higher clad temperature compared to the metal fuels.

Oxide fuel gas and solid fission product swelling is much lower compared to metallic fuel. Similar to the metallic fuel, one needs to allow for the gas swelling and interlinkage and interconnected formation of porosity; otherwise, fuel clad mechanical interaction can become very significant. The grain boundary gas bubbles saturate at around 5-8 % swelling. After that, solid fission product swelling continues. Fuel restructuring takes place early in the irradiation. Fuel cracking, as-fabricated porosity migration, central void formation, irradiation-induced densification and grain growth occur. Typically, at 1-2 at % burnup, the fuel becomes constrained by the cladding. Later, the solid fission product swelling is compensated for by hot

pressing of the as-fabricated porosity as well as compression of the grain boundary bubbles and interconnected porosity under the fuel clad mechanical interaction load. If oxygen is available at the fuel surface and the temperature is above 600 ^{0}C, a significant diffusion of cesium and molybdenum atoms towards the surface and Joint Oxide Gain (JOG) formation occur. In these processes, internally generated stresses cause trans-granular fracture of the fuel grains at the cooler brittle part of the fuel (less than 1300 ^{0}C) which results in an enhancement of fission gas release. Furthermore, due to this compressive stresses, significant amount of shrinkage of the as-fabricated porosity may result. JOG has a high thermal conductivity and is very compliant. Hence, it reduces the fuel swelling and improves the gap conductance. At high burnup, the porosity within the fuel is reduced due to the accumulation of solid fission products. Also, a very significant solid fission product swelling may occur at the top part of the fuel pin due to axial migration of cesium atoms. The resulting FCMI stress may cause significant straining of the clad and breach may result due to thermal creep fracture.

Similar to the metal fuel code, the FEAST-OXIDE code is composed of several modules in coupled form.

The fission gas release and swelling module implements the OGRES algorithm developed at Harwell Laboratory in the UK. It is a mature model based on 20-year-long experimental and theoretical work. The model treats intragranular and intergranular gas behavior, separately. The intragranular model describes the gas release to the grain boundary and the behavior of the intragranular bubbles. It treats all the relevant processes assuming a single representative bubble size, which makes it computationally inexpensive, while retaining the correct representation of the physical phenomena. Furthermore, the behavior of intra-granular gas for transient heating scenarios was modeled with the NEFIG algorithm, also developed in Harwell, UK. The grain boundary model describes the swelling behavior of the grain boundary bubbles, interlinkage and release to the fuel pin free volume with a vacancy flow mechanism. The OGRES model does not allow for the enhanced fission gas release due to JOG formation. However, this effect is modeled in this study by modifying the fission enhanced part of the diffusion coefficient.

The fuel restructuring module includes fuel cracking, as-fabricated porosity migration and central void formation, irradiation-induced densification and the grain growth. Fuel cracking reduces the gap thickness and it may have a significant effect on the fuel temperature distribution. An empirical relation is adopted as a function of initial gap thickness and clad inner diameter. As-fabricated porosity migration and central void formation have been simulated with a temperature-dependent pore velocity and the continuity equation. Irradiation-induced densification has also been modeled with an empirical approach in which the fuel maximum porosity drops to 4 % in within 1 at % burnup. Finally, the growth of the fuel grains has been modeled by an empirical relation.

Fuel chemistry is another important part of the oxide fuel modeling. First, the evolution of the oxygen-to-metal ratio with burnup has been simulated by using the thermodynamic equilibrium relation between the fuel and fission products and the charge balance within the fuel. Second, the thermal diffusion model is applied to simulate radial redistribution of oxygen, plutonium and cesium atoms, as well as JOG formation. Finally, the axial migration of cesium and the resulting excessive swelling at the top of the fuel pin has been modeled by means of an evaporation/condensation mechanism.

The fuel temperature distribution adopts the 1D radial energy balance method, the same used in the metal fuel code. The gap conductance model includes conductance due to gas and JOG, and radiative heat transfer. Unlike metal fuel, the melting of the oxide fuel is included in the model.

A kinetics model for the fuel clad chemical interaction is adopted. The model is based on deposition of corrosive fission products into the gap and their absorption by the clad, including the kinetics behavior.

Similar to the metal fuel code, the FEAST-OXIDE mechanical analysis model adopts the 1D generalized plane strain approach. The effect of cracking and healing on the mechanical properties is included. Furthermore, the fuel is conservatively assumed to be axially locked with the clad if there is contact between the fuel and clad. A hot pressing model has been adopted to

simulate the compression of the as-fabricated porosity under the external stress. It is a creep-dependent process.

The steady state part of FEAST-OXIDE was benchmarked against available FFTF, EBR-II and JOYO database. Furthermore, the transient part was benchmarked against the EBR-II slow ramp overpower tests. Seven steady state cases and eight transients were simulated. The steady-state cases correspond burnup between 2 to 17 at %; whereas the transient analyses span between 2 to 9 at %. The peak clad temperature for the steady state simulations varies between 550 ^{0}C to 700 ^{0}C. It is between 760^{0}C to 860 ^{0}C for the transient simulations. The peak cladding dose was 125 dpa. The agreement was satisfactory.

7.2. Conclusions

FEAST-METAL has been written in FORTRAN-90 to simulate the steady and transient behavior of U-Zr and U-Pu-Zr metallic fuel alloys. Its mechanical analysis model is 1D generalized plane strain approach. Its attractive properties are: (1) a fission gas release and swelling model that was specifically developed for metallic fuels, (2) a fuel clad chemical interaction model that reflects the kinetics behavior for both steady state and transients, and (3) a physics-based approach for the transient creep-fracture. The code satisfactorily reproduces the EBR-II database for steady state and furnace (transient) tests including predictions for important phenomena such as cladding strain, fission gas release, clad wastage, clad failure time and axial fuel slug deformation. Parametric studies performed for the steady state and transient conditions reproduce the correct trends and give confidence in the code's numerical reliability. Finally, the code is capable of modeling also the behavior of annular metal fuel pins with simultaneous internal and external cooling.

Typically, transient scenarios for the Sodium Fast Reactors lie in the intergranular creep fracture regime. A physics based method describing intergranular creep-fracture has been developed in this study to improve the accuracy of predicting the time to rupture of the cladding element in transient simulations. The model tracks the nucleation and growth of the cavities at the grain boundaries. Above the critical crack radius, that the final joining of microcracks is triggered by the loss of mechanical strength; hence, the rupture results. Critical crack radius was calculated

and tabulated by using the experimental cladding rupture database at constant stress and temperature together the fuel thermal creep relations.

The FEAST-OXIDE code has the same mechanical analysis model of FEAST-METAL. The main attractive features of FEAST-OXIDE are (1) An advanced fission gas release and swelling model based on vacancy flow, (2) A detailed and physics-based fuel chemistry model and its effect on thermal and mechanical performance, (3) A kinetics model for the clad wastage prediction, (4) A physics-based approach for the transient creep-fracture is adopted. A comparison of the steady-state part of FEAST-OXIDE to EBR-II, FFTF and JOYO experimental data as well as to the LIFE-4 code predictions has been performed and the outcome of said comparison is good. Furthermore, the transient part has been benchmarked against slow ramp overpower tests performed at EBR-II, and the agreement is satisfactory.

The oxide fuel is rather stiff due to its high melting point; hence, Fuel Clad Mechanical Interaction is a significant issue during normal operation as well as in case of transient overpower accidents. The fuel porosity diminishes with burnup due to the formation of solid fission products and hot pressing. Furthermore, the cesium axial migration accelerates the depletion of the fuel porosity at the upper part of the fuel pin. Operation with an incompresible fuel may cause a very significant FCMI; hence one needs to adjust the as-fabricated fuel porosity and fuel smear density carefully so that the fuel will be rather compressible by the End of Life.

7.3. Future Work

- If more experimental data become available, the validity of the existing models for the key phenomena should be investigated further. If necessary, new and/or more advanced models should be pursued. Metallic fuel at power forms different phases in radial direction. It may be possible to develope a much more advanced fission gas release and swelling model unique for the each phase. Simulation of the growth and interlinkage of the bubbles with a vacancy flow mechanism could improve the reliability of the model. The oxide fuel chemistry today remains as an important and not fully understanding issue. Particularly, the effect of Joint Oxide Gain Formation and cesium axial migration should be investigated further.

- A more advanced numerical scheme can be applied to reduce the computational time, which is now of the order of an hour for FEAST-METAL and 5-10 hours for FEAST-OXIDE at a typical single CPU personal computer with 2.9 GHz processor speed.

- The material properties are the key to the success of the simulations; however, the literature database is limited. If more advanced data sets for the fuel thermal, mechanical and chemical properties of the fuel and cladding materials become available, the existing property set should be updated.

- Statistical analysis and an uncertainty estimate module can be added into FEAST to specify the safety margin in a more systematic manner. This would be an important improvement, if the code is to be used in design, optimization and, ultimately, licensing studies.

References

1- D. C. Crawford et al., "Fuels for Sodium-Cooled Fast Reactors: US Perspective," Journal of Nuclear Materials, Vol. 371, pp. 202-231, (2007).

2- D. R. Olander, "Fundamental Aspects of Nuclear Reactor Fuel Elements," U. S. DOE, (1976).

3- J. R. Matthews et al., "Twenty Five Years of Fuel Modeling in the UK," Nuclear Energy, Vol. 29, pp. 101-106, (1990).

4- V. Z. Jankus, "LIFE-II – A computer Analysis of Fast-Reactor Fuel-Element Behavior as a Function of Reactor Operating History," Nuclear Engineering and Design, Vol. 18, pp. 83-96, (1972).

5- R. Godesar, "COMETHE-II – A Computer Code for Predicting Mechanical and Thermal Behavior of the Fuel Pin," Nuclear Applications and Technology, Vol. 9, pp. 205-217, (1970).

6- D. Wilmore et al., "FRUMP – A Computer Programme for the calculation of Stresses in Reactor Fuel Pins," Atomic Energy Research Establishment, Harwell (England), 69p, (1973).

7- M. H. Wood et al., "A Simple Operational Gas Release and Swelling Model, I. Intragranular Gas," Journal of Nuclear Materials, Vol. 91, pp. 35-40, (1980).

8- M. H. Wood et al., "A Simple Operational Gas Release and Swelling Model, II. Grain Boundary Gas," Journal of Nuclear Materials, Vol. 91, pp. 241-256, (1980).

9- M. H. Wood et al., "A Model of Fission Gas Release at High Temperatures," Journal of Nuclear Materials, Vol. 102, pp. 223-225, (1981).

10- M. H. Wood et al., "Comparison of Experiment and NEFIG Model Calculations of Transient Fission Gas Release Behavior," Journal of Nuclear Materials, Vol. 87, pp. 167-174, (1979).

11- J. R. Matthews et al., "The Application of the TRAFIC Fuel Performance Code to Steady and Transient Conditions," Nuclear Fuel Performance, BNES, London, pp. 301-307, (1985).

12- J. Rest, "An Improved Model for Fission Product Behavior in Nuclear Fuel Under Normal and Accident Conditions," Journal of Nuclear Materials, Vol. 120, pp. 195-212, (1984).

13- A. Biancheria et al., "Steady-State and Transient Fuel Pin Performance Modeling: LIFE-4 Update," International Conference on Reliable Fuels for Liquid Metal Reactors, pp. 5-1 – 5.14, American Nuclear Society, Arizona, (1986).

14- J. C. Melis et al.,, "GERMINAL – A Computer Code for Predicting Fuel Pin Behavior," Journal of Nuclear Materials, Vol. 188, pp. 303-307, (1992).

15- J. C. Melis et al., "Fuel Modeling at High Burn-up: Recent Development of the GERMINAL Code," Journal of Nuclear Materials, Vol. 204, pp. 183-193, (1993).

16- K. Maeda et al., "Change of Fuel-to-Cladding Gap Width with the Burn-up in FBR MOX Fuel Irradiated to High Burnup," Journal of Nuclear Materials, Vol. 327, pp. 1-10, (2004).

17- M. Inoune et al., "Fuel-to-Cladding Gap Evolution and Its Impact on Thermal Performance of High Burnup Fast Reactor Type Uranium-Plutonium Oxide Fuel Pins," Journal of Nuclear Materials, Vol. 326, pp. 59-73, (2004).

18- M. C. Billone, et al., "Status of the Fuel Element Modeling Codes for Metallic Fuels," Proc. Int. Conf. Reliable Fuels for Liquid Metal Reactors, American Nuclear Society Tucson, Arizona (1986).

19- T. Ogata et al., "Development and Validation of ALFUS: An irradiation Behavior Analysis Code for Metallic Fast Reactor Fuels," Nuclear Technology, Vol. 128, pp. 113-123, (1999).

20- W. Hwang et al., "MACSIS: A Metallic Fuel Performance Analysis Code for Simulating In-Reactor Behavior under Steady-State Conditions," Nuclear Technology, Vol. 123, pp. 130-141, (1998).

21- G. L. Hoffman et al, "Metallic Fast Reactor Fuels," Progress in Nuclear Energy, Vol. 31, pp. 83-110, (1997).

22- P. Martin et al., "French and United Kingdom Experience of High Burnup Mixed Oxide Fuel in Sodium-Cooled Fast Breeder Reactors," Nuclear Technology, Vol. 161, pp. 35-44, (2008).

23- T. Kobayashi et al., "Development of the SESAME Metallic Fuel Performance Code," Nuclear Technology, Vol. 89, pp. 183-193, (1990).

24- T. Nakajima et al., "FEMAXI-III: A computer Code for the Analysis of Thermal and Mechanical Behavior of Fuel Rods," JAERI-1298, Japan Atomic Energy Research Institute, (1985).

25- Y. Tsuboi et al., "Mechanistic Model of Fission Gas Behavior in Metallic Fuel," Journal of Nuclear Materials, Vol. 188, pp. 312-318, (1992).

26- C. B. Lee et al., "Fission Gas Release and Swelling Model of Metallic Fast Reactor Fuel," Journal of Nuclear Materials, Vol. 288, pp.29-42, (2001).

27- N. E. Todreas et al., "Nuclear Systems-II, Elements of Thermalhydraulic Design," Taylor & Francis, (1990).

28- G. Strang, "Linear Algebra and its Applications," Brooks/Cole Pub. Co., (1988).

29- http://pagesperso-orange.fr/jean-pierre.moreau/Fortran/sysmat_f90.txt

30- W. Hwang et al., "Recent Improvements in Modeling Fission Gas Release and Rod Deformation on Metallic Fuel in LMR," Vol. 27, pp. 1057-1069, (2000).

31- W. G. Steele et al., "Steady-state Fission Gas Behavior in Uranium-Plutonium-Zirconium Metal Fuel Elements," Nuclear Engineering and Design, Vol. 113, pp. 289-295, (1989).

32- M. H. Wood et al., "Some Predictions from the OGRES Gas Release Code and Comparison with Experiment," Journal of Nuclear Materials, Vol. 92, pp. 354-356, (1980).

33- G. L. Hofman et al., "Swelling of U-Pu-Zr Fuel," Metallurgical Transactions A, Vol. 21A, pp. 517-528, (1990).

34- Y. S. Kim et al., "Modeling of Constituent Redistribution in U-Pu-Zr metallic Fuel," Journal of Nuclear Materials, Vol. 359, pp. 17-28, (2006).

35- T. Ogata et al., "Constituent Migration Model For U-Pu-Zr Metallic Fast Reactor Fuel," Vol. 104, pp. 37-51, (1993).

36- G. L. Hofman et al., "Temperature Gradient Driven Constituent Redistribution in U-Zr Alloys," Journal of Nuclear Materials, Vol. 227, pp. 277-286, (1995).

37- C. Nam et al., "Statistical Failure Analysis of Metallic Fuel U-10Zr/HT9 Fast Reactor Fuel Pin by Considering the Weibull Distribution and Cumulative Damage Fraction," Vol. 25, pp. 1441-1453, Annals of Nuclear Energy, (1998).

38- N. E. Todreas et al., "Nuclear Systems-I, Thermalhydraulic Fundamentals," Taylor & Francis, (1990).

39- F. Incropera et al., "Fundamentals of Heat and Mass Transfer," John Wiley & Sons, Fourth Edition, (1996).

40- T. H. Bauer et al., "In-pile Measurement of the Thermal Conductivity of Irradiated Metallic Fuel," Nuclear Technology, Vol. 110, (1995).

41- A. M. Yacout et al., "Average Irradiation Temperature for the Analysis of In-Pile Integral Measurements," Vol. 115, pp.61-72, Nuclear Technology, (1996).

42- L. Leibowitz et al. "Thermal Conductivity and Thermal Expansion of Stainless Steels D9 and HT9," Vol. 9, pp. 873-883, International Journal of Thermophysics, (1988).

43- H. Savage, "The Heat Content and Specific Heat of Some Metallic Fast-Reactor Fuels Containing Plutonium," Journal of Nuclear Materials, Vol. 25, pp. 249-259, (1968).

44- N. Yamanouchi et al., "Accumulation of Engineering Data for Practical Use of Reduced Activation Ferritic Steel: 8 % Cr-2%W-0.2%V-0.04%Ta-Fe," Journal of Nuclear Materials, Vol. 191, pp. 822-826, (1992).

45- R. G. Pahl et al., "Performance of HT9 Clad Metallic Fuel at High Temperature," Vol. 204, pp.141-147, Journal of Nuclear Materials, (1993).

46- K. Nakamura et al., "Reaction of U-Zr Alloy with Fe and Fe-Cr Alloy," Journal of Nuclear Materials, Vol. 275, pp. 246-254, (1999).

47- K. Nakamura et al., "Reaction of Uranium-Plutonium Alloys with Iron," Journal of Nuclear Science and Technology, Vol. 38, pp. 112-119, (2001).

48- A. B. Cohen et al., "Fuel/Cladding Compatibility in U-19Pu-10Zr/HT9-Clad Fuel at Elevated Temperatures," Journal of Nuclear Materials, Vol. 204, pp. 244-251, (1993).

49- T. H. Bauer et al., "Cladding Failure Margins for Metallic Fuel in the Integral Fast Reactor," Argonne National Laboratory, CONF-870812-22, (1987).

50- W. F. Hosford, "Physical Metallurgy," Taylor & Francis, (2005).

51- R. P. Anantatmula et al. "Sodium Compatibility of HT-9 and Fe-9Cr-1Mo Steels," HEDL-SA-2801FP, (1985).

52- E. E. Gruber et al., "Gas Bubble Growth Mechanisms in the Analysis of Metal Fuel Swelling," Proc. 13th Int. Symp. (Part-I) Radiation Induced Changes in Microstructure, ASTM-STP-955, p. 432, (1987).

53- R. G. Pahl et al., "Stedy-state Irradiation Testing of U-Pu-Zr Fuel > 18 at % Burnup," *Proceedings of the 1990 International Fast Reactor Safety Meeting*, pp. 129-137 vol.4, (1990).

54- D. C. Crawford et al., "Large-diameter, high-plutonium metallic fuel testing in EBR-II," Vol. 71, pp.178-179, Transaction of American Nuclear Society, (1994).

55- M. Li et al., "Fracture Mechanism Maps in Unirradiated and Irradiated Metals and Alloys," Journal of Nuclear Materials, Vol.361, pp. 192-205, (2007).

56- H. Reidel, "Continuous Nucleation of Grain Boundary Cavities in Creep Rupture," Zeitschrift fuer Metallkunde, vol.76, pp. 669-675, 1985.

57- G. Eggeler et al., "Microstructural Study of Creep Rupture in a 12 % Chromium Ferritic Steel," Acta metall., Vol. 37, pp. 49-60, 1989.

58- R. Wu et al., "Creep Cavity Nucleation and Growth in 12Cr-Mo-V Steel," Material Science and Technology, Vol. 11, page 579, 1995.

59- J. R. Rice, "Constraints on the Diffusive Cavitation of Isolated Grain Boundary Facets in Creeping Polycrystals," Acta Metallurgica, Vol. 29, pp. 675-681, (1980).

60- R. J. DiMelfi et al., "Strength and Rupture-Life Transitions Caused by Secondary Carbide Precipitation in HT-9 During High Temperature Low-Rate Mechanical Testing," First International Conference on Microstructures and Mechanical Properties of Aging Materials, pp. 187-196, (1993).

61- J. M. Kramer et al., "Modeling the behavior of metallic fast reactor fuels during extended transients," Journal of Nuclear Materials, Vol.204, pp. 203-211, (1993).

62- R. G. Pahl, "Irradiation Performance of Metallic Fast Reactor Fuels," Journal of Nuclear Materials, Vol. 188, pp. 3-9, (1992).

63-R. G. Pahl et al., "Irradiation experience with HT-9 Clad Metallic Fuel," ANL/CP-72040, (1992).

64- H. Ohta et al., "Irradiation Experiment on Fast Reactor Metal Fuels Containing Minor Actinides up to 7 at % Burnup," pp. 1346-1352, Global, (2007).

65- V. Murogov et al., "Prospects of Metallic Fuel Using in Fast Reactors," 63p, Report No: FEI-1913, (1988).

66- www.nea.fr/html/pt/docs/iem/lasvegas04/10_Session_IV/S4_01.pdf

67- J. Seran et al., "Behavior under Neutron Irradiation of the 15-15Ti and EM10 Steels Used as Standard Materials of the PHENIX Fuel Subassembly," ASTM STP 1125, pp. 1209-1233, (1992).

68- Y. Y. Liu, "Behavior of EBR-II MK-V-Type Fuel Element in Simulated Loss-of-Flow Tests," Journal of Nuclear Materials, Vol. 204, pp. 194-202, (1993).

69- A. E. Dubberley et al., "Transient Performance of S-PRISM," ICONE-9, (2001).

70- "Pre-application Safety Evaluation Report for the Power Reactor Innovative Small Module (PRISM) Liquid-Metal Reactor," NUREG-1368, (1994).

71- F. A. Garner et al., "Irradiation Creep and Swelling of the Fusion Heats of PCA, HT9 and 9Cr-1Mo Irradiated to High Neutron Fluence," Vol. 179, pp. 577-580, (1991).

72- M. B. Toloczko et al., "Variability of irradiation creep and swelling of HT9 Irradiated to High Neutron Fluence at 400 – 600 ^{0}C," Effect of Radiation on Materials 18th Symposium ASTM-1325, (1999).

73- A. L. Pitner et al., "Irradiation Performance of Fast Flux Test Facility Drivers Using D9 Alloy," WHC-SA-2261-FP, (1994).

74- T. Yamamoto et al., "Helium Effects on Microstructural Evolution in Tempered Martensitic Steels: In Situ Helium Implanter Studies in HFIR," Vol. 386, pp. 338-341, (2009).

75- G. R. Odette, "A Model for In-reactor Stress Rupture of Austenitic Stainless Steels", Vol. 122, pp. 435-441, (1984).

76- P. Hejzlar, M. S. Kazimi, "Annular Fuel for High Power Density PWRs: Motivation and Overview," Nuclear Technology, Vol. 160, pp. 2-15, (2007).

77- M. Memmott, J. Buongiorno, P. Hejzlar, "Subchannel Analysis of Sodium-Cooled Reactor Fuel Assemblies with Annular Fuel Pins," Paper 9033, Proceedings of ICAPP'09, Tokyo, Japan, May 10-14, (2009).

78- Y. de Carlan et al., "CEA Developments of New Ferritic ODS Alloys for Nuclear Applications," Journal of Nuclear Materials, Vol. 386, pp. 430-432, (2009).

79- E. Yoshida et al., "Sodium Compatibility of ODS Steels at Elevated Temperature," Journal of Nuclear Materials, Vol. 329, pp. 1393-1397, (2004).

80- T. Ishii et al., "An Investigation of the Pu Migration Phenomena during Irradiation in Fast Reactor," Journal of Nuclear Materials, Vol. 294, pp. 13-17, (2001).

81- A. H. Booth, "A method for Calculating Fission Gas Diffusion from U02 Fuel and Its Application to the X-2-f Loop Test," AECL-496, Atomic Energy of Canada Ltd., (1957).

82- R. F. Cameron et al., "Development and Application of the TRAFIC Code for the Analysis of Fast Reactor Safety Experiments," Nuclear Energy, Vol.29, pp. 141-147, (1990).

83- J. R. Matthews et al., "A Review of Fission Gas Modelling at Harwell," Eur. Appl. Res. Rept-Nucl. Sci. Technol., Vol. 5, pp. 1685-1729, (1984).

84- R. Brearley et al., "An improved Equation of State for Inert Gases at High Pressures," Journal of Nuclear Materials, Vol. 95, pp. 239-252, (1980).

85- K. Lassmann, "The OXIRED Model for Redistribution of Oxygen in Non-stoichiometric Uranium-Plutonium Oxides," Journal of Nuclear Materials, Vol. 150, pp. 10-16, (1987).

86- C. F. Clement et al., "Plutonium Redistribution in Mixed Oxide (U, Pu)O□ Nuclear Fuel Elements," Journal of Nuclear Materials, Vol. 75, pp. 193-200, (1978).

87- H. Furuya et al., "Axial Distribution of Cesium in Heterogeneous FBR Fuel Pins," Journal of Nuclear Materials, Vol. 201, pp. 46-53.

88- T. Ozawa et al., "Development and Verifications of Fast Reactor Fuel Design Code CEPTAR," Nuclear Technology, Vol. 156, pp. 39-55, (2006).

89- H. Kashihara et al., "Dimensional Stability of FBR Fuel Pins with Modified Type 316 Stainless Steel Cladding at High Burn-up," Fast Reactor Core and Fuel Structural Behavior, pp. 243-247, BNES, London, (1990).

90- M. G. Adamson et al., "Mechanistic Models for Cesium Thermo-migration and Cesium-Fuel Chemomechanical Interactions in Mixed-Oxide Fuel Pins," Transactions of American Nuclear Society, Vol. 38, pp. 289-291, (1981).

91- S. Vaidyanathan et al. "Model Predictions for Cesium Transport and Reaction Behavior in Irradiated Mixed-Oxide Fast Reactor Fuel Pins," Transactions of American Nuclear Society, Vol. 38, pp. 291-293 (1981).

92- R. A. Karnesky et al., "Cesium Migration in LMFBR Fuel Pins," International Conference on Fast Breeder Reactor Fuel Performance, Monterey, California, (1979).

93- W. J. Lackey et al., "Porosity and Actinide Redistribution During Irradiation of $(U,Pu)O_2$," Nuclear Technology, Vol. 16, pp. 120-141, (1972).

94- H. Többe, "IAMBUS: A Computer Code for the Design and Performance Prediction of Fast Breeder Fuel Rods," Technical Report, DE03FH121, (1990).

95- C. Sari, "Grain Growth Kinetics in Uranium-Plutonium Mixed Oxides," Journal of Nuclear Materials, Vol. 137, pp.100-106, (1986).

96- I. J. Hastings et al., "Grain Growth in UO□ In-reactor and Laboratory Testing," Journal of Nuclear Materials, Vol. 82, pp. 435-438, (1979).

97- J. E. Bainbridge et al., "The Grain Growth of Mixed Oxide Fuel During Irradiation," Journal of Nuclear Materials, Vol. 171, pp. 230-236, (1990).

98- M. Inoune et al., "Power-to-melts of Uranium-Plutonium Oxide Fuel Pins at a Beginning-of-Life Condition in the Experimental Fast Reactor JOYO," Journal of Nuclear Materials, Vol. 323, pp. 108-122, (2003).

99- M. F. Lyons et al., "UO_2 properties affecting performance," Nuclear Engineering and Design, Vol. 21, pp.167-199, 1972.

100- K. Konno et al., "Melting Temperature of Mixed Oxide Fuels for Fast Reactors," Journal of Nuclear Science and Technology, Vol. 39, pp. 771-777, (2002).

101- D. G. Martin, "A Re-appraisal of the Thermal Conductivity of UO_2 and Mixed (U,Pu) Oxide Fuels," Journal of Nuclear Materials, Vol. 110, pp. 73-94, (1982).

102- Y. Philipponneau, "Thermal Conductivity of $(U,Pu)O_{2-x}$ Mixed Oxide Fuel," Journal of Nuclear Materials, Vol. 188, pp. 194-197, (1992).

103- M. Inoue, "Thermal Conductivity of Uranium-Plutonium Oxide Fuel for Fast Reactors," Journal of Nuclear Materials, Vol. 282, pp. 186-195, (2000).

104- M. Inoune et al., "A Method for Determining an Effective Porosity Correction Factor for Thermal Conductivity in Fast Reactor Uranium-Plutonium Oxide Fuel Pellets," Journal of Nuclear Materials, Vol. 281, pp. 117-128, (2000).

105- C. M. Allison et al., "SCDAP/RELAP5/MOD3.1 Code Manual Volume IV: MATPRO – A Library of Materials Properties for Light-Water-Reactor Accident Analysis," NUREG/CR-6150, (1993).

106- D. C. Fee et al., "Fuel-Cladding Chemical Interaction in Uranium-Plutonium Oxide Fast Reactor Fuel Pins," Journal of Nuclear Materials, Vol. 96, pp. 80-104, (1980).

107- K. Konashi et al., "Model for Fuel/Cladding Chemical Interaction," Nuclear Technology, Vol. 72, pp. 328-337, (1985).

108- K. Konashi et al., "Model Analysis of Fuel Cladding Chemical Interaction," Nuclear Fuel Performance, pp. 43-46, BNES, London, (1985).

109- J. L. Routbort, "Compressive Creep of Mixed-Oxide Fuel Pellets," Journal of Nuclear Materials, Vol. 44, pp. 247-259, (1972).

110- P. Combette et al, "In-Pile Creep Study on Mixed Oxide $(U,Pu)O_2$," Journal of Nuclear Materials, Vol. 65, pp. 37-47, (1977).

111- A. E. Bridges et al., "Advanced Liquid Metal Reactor Fuel and Blanket Designs Using HT9," WHC-SA--1073, (1991).

112- R. B. Baker et al., "Performance of Fast Flux Test Facility Driver and Prototype Driver Fuels," WHC-SA—0974, (1990).

113- A. J. Lovell et al., "Demonstration of a High Burnup Heterogeneous Core Using Ferritic/Martensitic Materials," International Conference on Reliable Fuels for Liquid Metal Reactors, ANS, (1986).

114- J. W. Hales et al., "Evaluation of FFTF Reference Drive Fuel to 100 MWd/kg Burnup," International Conference on Reliable Fuels for Liquid Metal Reactors, ANS, (1986).

115- L. A. Lawrence et al., "Performance of Advanced Oxide Fuel Pins in EBR-II," International Conference on Reliable Fuels for Liquid Metal Reactors, ANS, (1986).

116- R. J. Puigh et al., "In-reactor Creep Rupture Behavior of the D9 Alloys," CONF-860605—44, (1986).

117- T. Shimada et al., "Operational Experience of Experimental Fast Reactor JOYO Driver Fuel," International Conference on Reliable Fuels for Liquid Metal Reactors, ANS, (1986).

118- H. Tsai et al., "Behavior of Mixed-Oxide Fuel Elements During an Overpower Transient," Journal of Nuclear Materials, Vol. 204, pp. 217-227, (1993).

119- M. B. Toloczko et al., "Variability of irradiation creep and swelling of HT9 Irradiated to High Neutron Fluence at 400 – 600 ^{0}C," Effect of Radiation on Materials 18th Symposium ASTM-1325, (1999).

120- H. J. Ryu et al., "Review of HT9 Cladding Creep Correlations for Advanced Liquid Metal Fast Reactors," Transactions of the American Nuclear Society, vol. 94, pp. 797-798, Transactions of the American Nuclear Society 2006 Annual Meeting and Embedded Topical Meeting - Nuclear Fuels and Structural Materials for the Next Generation Nuclear Reactors, (2006).

121- R. J. Amodeo et al., "Constitutive Design Equation for Thermal Creep Deformation of HT-9," Journal of Nuclear Materials, Vol. 122, pp. 91-95, (1984).

122- J. F. Bates, "Design Equations for Stress-Free Swelling of 20 % Cold Worked D9," Hanford Engineering Development Laboratory, (1979).

123- B. J. Makenas, "Swelling of 316 Stainless Steel and D9 Cladding in FFTF," CONF860605—45, (1986).

124- J. H. Kittel et al., "Plutonium and Plutonium Alloys as Nuclear Fuel Materials," Nuclear Engineering and Design, Vol. 15, pp. 373-440, (1971).

Appendix-A: Material Properties

A.1. HT9 Cladding Mechanical Properties

A.1.1. Young's Modulus, Shear Modulus and Poisson's Ratio

$E = 2.137\times10^{5} - 102.74T$ (MPa)

$G = 8.964\times10^{4} - 53.78T$ (MPa)

$$\nu = \frac{E}{2G} - 1$$

The unit of temperature is Celsius.

A.1.2. Thermal Expansion [42]

$$\alpha\Delta T = -0.2191 + 5.678\times10^{-4}T + 8.111\times10^{-7}T^{2} - 2.576\times10^{-10}T^{3}$$

T: Temperature (K)

$\alpha\Delta T$: Linear thermal expansion strain (%)

A.1.3. Irradiation Creep

$$\dot{\varepsilon}_{I} = \left[B_{o} + A\exp(-\frac{Q}{RT}) \right]\phi\bar{\sigma}^{1.3}$$

$\dot{\varepsilon}_{I}$ = Equivalent Strain rate (%/sec)

B_{o} = 1.83×10^{-4}

A = 2.59×10^{14}

Q = 73000 (Cal/g-mol)

R = 1.987 (Cal/g-mol-K)

T = Temperature (K)

ϕ = Neutron Flux (n/cm²/s)

$\bar{\sigma}$ = Equivalent Stress

Note that B_{o} , A and Q are fitting constant, calculated by using Ref. [119] data.

A.1.4. Thermal Creep

Thermal creep has three components. They are primary, steady-state (secondary) and tertiary creep [120].

$$\dot{\varepsilon}_T = \dot{\varepsilon}_{TP} + \dot{\varepsilon}_{TS} + \dot{\varepsilon}_{TT}$$

$$\dot{\varepsilon}_{TP} = \left[C_1 \exp\left(-\frac{Q_1}{RT}\right)\bar{\sigma} + C_2 \exp\left(-\frac{Q_2}{RT}\right)\bar{\sigma}^4 + C_3 \exp\left(-\frac{Q_3}{RT}\right)\bar{\sigma}^{0.5} \right] C_3 \exp\left(-\frac{Q_3}{RT}\right) C_4 \exp(-C_4 t)$$

$$\dot{\varepsilon}_{TS} = C_5 \exp\left(-\frac{Q_4}{RT}\right)\bar{\sigma}^2 + C_6 \exp\left(-\frac{Q_5}{RT}\right)\bar{\sigma}^5$$

$$\dot{\varepsilon}_{TT} = 4C_7 \exp\left(-\frac{Q_6}{RT}\right)\bar{\sigma}^{10} t^3$$

The values for the constants in these equations are as follows:

$C_1 = 13.4$
$C_2 = 8.43 \times 10^{-3}$
$C_3 = 4.08 \times 10^{18}$
$C_4 = 1.6 \times 10^{-6}$
$C_5 = 1.17 \times 10^{9}$
$C_6 = 8.33 \times 10^{9}$
$C_7 = 9.53 \times 10^{21}$
$Q_1 = 15027$
$Q_2 = 26451$
$Q_3 = 89167$
$Q_4 = 83142$
$Q_5 = 108276$
$Q_6 = 282700$
R = 1.987
T = Temperature, K
$\bar{\sigma}$ = Equivalent Stress (MPa)
$\dot{\varepsilon}_T$ = Effective Thermal Creep Strain (%/s)

Note that, fitting parameter were found by using the data in Refs. [37] and [121].

A.2. D9 Cladding Mechanical Properties

A.2.1. Thermal Expansion [42]

$$\alpha\Delta T = (-0.4247 + 1.282 \times 10^{-3}T + 7.362 \times 10^{2} - 2.069 \times 10^{-10}T^{3})$$

T: Temperature (K)

$\alpha\Delta T$: Linear thermal expansion strain (%)

A.2.2. Irradiation Creep [122]

$$B_{bar} = \left(1.0 \times 10^{-29} exp(4.8) + \frac{1.4 \times 10^{-12} exp\left(-\frac{Q_1}{RT}\right)}{1 + 1.8 \times 10^{32} exp\left(-\frac{Q_2}{RT}\right)} + 2 \times 10^{-12} exp\left(-\frac{Q_3}{RT}\right) \right)$$

$$\dot{\epsilon} = B_{bar}\sigma\varphi$$

R= 1.987

Q_1= 55000.0

Q_2= 125000.0

Q_3= 65000.0

σ: Equivalent Stress (MPa)

φ: Neutron/cm²/s

$\dot{\epsilon}$: Irradiation creep strain rate(%/s)

A.2.3. Swelling [123]

$$\varepsilon_s = \begin{cases} 0 & \text{fit} < 10 \\ \dfrac{\text{fit}}{10^7} & 13 > \text{fit} > 10 \\ 2.25\dfrac{\text{fit}}{10^7} & 15 > \text{fit} > 13 \\ 4\dfrac{\text{fit}}{10^7} & \text{fit} > 15 \end{cases}$$

ε_s : Volumetric swelling rate (1/s)

fit: Neutrons/cm²/10^{22}

A.2.4. Thermal Creep [122]

$$\dot{\epsilon} = 3 \times 10^{37} \left(\frac{\sigma}{y}\right)^7 exp\left(-\frac{Q_1}{RT}\right)$$
$$y = 2.235 \times 10^5 - 79.29T$$

$\dot{\epsilon}$: Thermal creep rate (%/h)

T: Temperature (K)

σ: Stress (MPa)

R = 1.987

Q_1= 82000.0

A.3. 20 % Cold Worked 316 Stainless Steel Mechanical Properties

A.3.1. Irradiation and Thermal Creep [122]

$$\dot{\epsilon} = \left(3a_1\varphi exp(-3\varphi t)\sigma + 26.36a_2\left(\frac{\varphi t}{\varphi}\right)^{-0.5}\sigma^{4.5} + a_4\varphi\sigma + \frac{a_5}{a_6}2.2\Omega tanh\left(\frac{\varphi t}{\Omega}\right)\sigma\right) \times 10^{-7}$$

Ω: 9

$$a_1 = 134exp\left(-\frac{188000}{RT}\right)$$

$$a_2 = exp\left(1.41 - \frac{24000}{T}\right)$$

$$a_3 = exp\left(77.84 - \frac{95000}{T}\right)$$

$$a_4 = 7.25 \times 10^{-4}$$

$$a_5 = exp\left(2.91 - \frac{16000}{RT}\right)$$

$$a_6 = 1 + exp\left(45 - \frac{80000}{RT}\right)$$

φ: Neutrons/cm²/s/10^{15}

φ: Neutrons/cm²/10^{22}

σ: Equivalent stress (MPa)

T: Temperature (K)

$\dot{\epsilon}$: Creep strain rate (%/s)

A.4 Fuel Mechanical Properties

According to Ref. [18] the fuel Poisson's Ratio is similar to that of the HT9 cladding.

A.4.1. Thermal Expansion Coefficient

The thermal expansion coefficient depends on the phases present in the fuel.

$$\alpha = 1.76\times10^{-5} \qquad T < T_3$$

$$\alpha = \frac{T-T_3}{T_6-T_3}1.76\times10^{-5} \qquad T_3 < T < T_6$$

$$\alpha = \frac{T-T_3}{T_6-T_3}(2.01\times10^{-5}-1.76\times10^{-5})+1.76\times10^{-5} \qquad T \geq T_6$$

T: Temperature (K)

α : Thermal expansion coefficient ($1/^0$C)

T_3: $\alpha+\delta \rightarrow \beta+\gamma$ phase transition temperature

T_6: $\beta+\gamma \rightarrow \gamma$ phase transition temperature

A.4.2. Modulus of Elasticity [23]

Similarly to the thermal expansion coefficient, the modulus of elasticity depends on the phases present.

$$E = 56-0.1158\times(T-T_3) \qquad T < T_3$$
$$E = 20-0.1273\times(T-T_3) \qquad T_3 \leq T < T_6$$
$$E = 31-0.08\times(T-T_6) \qquad T \geq T_6$$

E: Modulus of Elasticity (GPa)

T: Temperature (^oC)

T_3: $\alpha+\delta \rightarrow \beta+\gamma$ phase transition temperature

T_6: $\beta+\gamma \rightarrow \gamma$ phase transition temperature

A.4.3. Yield Strength

Using Ref. [26] and [124] the following relation has been derived for metallic fuel.

$$\sigma_y = \begin{Bmatrix} 0.04\times(T_6 - T)+10 & T \geq T_6 \\ 0.08\times(T_6 - T)+10 & T < T_6 \end{Bmatrix} \text{ MPa}$$

Appendix-B: Oxygen Potential

Gibbs free energy of formation oxygen is given as follows:

$$\Delta G_{O_2} = \Delta H_{O_2} - T\Delta S_{O_2}$$

Partial molar enthalpy and entropy of oxygen is defined as a function of plutonium valence. Table-49 and Table-50 shows the look-up table for ΔH_{O_2} and ΔS_{O_2}, respectively.

Table-49: Enthalpy [2]

Vpu (charge)	3	3.25	3.5	3.75	3.95	3.999	4.0	4.05	4.25
ΔH_{O_2} (kJ/mol)	-845	-822	-795	-762	-730	-670	-265	-260	-285

Table-50: Entropy [2]

Vpu (charge)	3	3.25	3.5	3.75	3.825	3.925	3.999	4.0	4.25
ΔS (J/mol/K)	-135.4	-137.9	-144.4	-151.9	-151.9	-146.3	-136.9	-7.5	-79.9

Appendix-C: FEAST Input Description

A line-by-line input description of the FEAST-METAL and FEAST-OXIDE codes is given. The input file mimics that of the popular oxide fuel performance code FRAPCON, to facilitate use of FEAST by FRAPCON users.

C.1. FEAST-METAL Input Description

FEAST-METAL Input file description is given in Table-51. Furthermore, a sample input file is given below. FEAST can be run with the executable file (.exe) together with the input text file (input.txt).

Table-51: FEAST-METAL input description

Line Number	Description	Symbol
1	Title	-
2	# of time nodes	im
3	# of axial nodes	Na
4	# of radial nodes within the fuel slug	nrf (six is recommended)
5	# of radial nodes within the clad	nrc (>2 is recommended)
6	Steady state time step	dt (30 seconds or less)
7	Plenum to fuel ratio	ptof
8	Fuel outer radius (m)	Rfo
9	Clad inner radius (m)	Rci
10	Clad outer radius (m)	Rco
11	Wire radius (m)	Rw
12	Fission gas release model (1 is the mechanistic model, 2 is the empirical model)	fgr (1 is recommended, 2 can be used for comparison purposes)
13	Plutonium weight fraction	xpu
14	Zirconium weight fraction	Xzr
15	Initial fill gas pressure (Pa)	fpgav
16	Bond sodium above the fuel level (m)	bonds
17	Fuel slug total length (m)	totl
18	Coolant pressure (Pa)	pco
19	Coolant inlet temperature (^{0}C)	tcin
20	Axial nodalization (1 specifies equal	

	nodalization, 2 specifies unequal nodalization)*	
21	Axial power distribution (normalized to one)	qf(i), i= 1,na
22	Burnup (at fraction)	burnup(i), i= 1,im
23	Average linear heat rate (kW/m)	qmpy(i), i=1,im
24	if 0, coolant mass flow rate will be specified; If 1, coolant outlet temperature will be specified next	bc
25	Coolant outlet temperature (^{o}C) or mass flow rate (kg/s)	mdot (i), i=1,im tco(i), i=1,im
26	0, if EBR-II neutronics condition is specified. It is assumed that flux and volumetric heat generation rate is proportional. The reference flux is 1.6E+15 The reference volumetric heat generation rate = 1.9E+9 W/m^3 1, if a different reference neutron flux and volumetric heat generation rate is specified; 2, if the fast flux as a function of burnup is specified next.	fl0
27	If fl0 = 1, the reference neutron flux and volumetric heat generation rate need to be specified. If fl0=2 1.0E+15 (n/cm^2/s)	Coef1, coef2 Flux(i) i=1,im
28	0, if this is only a steady state run, input is terminated 1, if transient analysis will be also be performed.	tr0
29	Transient clad wastage model specifier. 1.0 for precipitation kinetics model, 2.0 for the empirical model	flatr
30	# of transient time nodes	imt
31	Transient time step	Dttr (0.005 or lower time step is recommended)
32	Burnup at which transient begins (atom fraction)	buss
33	Transient time nodes	Imt
34	Transient linear heat rate (kW/m)	powt(i), i=1,imt
35	Coolant inlet temperature (^{0}C)	ciit(i), i=1,imt
36	Transient boundary condition specifier: If 0, coolant mass flow rate will be specified next. If 1, coolant outlet temperature will be specified;	bct
37	If bct = 0, coolant mass flow rate (kg/s) If bct = 1, coolant outlet temperature (^{0}C)	mdott(i), i=1,imt Coot(i), i=1,imt

* FEAST-METAL allows for for the subdivision of the top axial node to four equal pieces to model the thermal creep and rupture behavior of the clad for transient scenarios.

C.2. Metal Fuel Bencmhark Inputs

Steady State:

EBR-II X425 Input:

```
"FEAST: X425"
im= 50
na= 7
nrf= 6
nrc= 3
dt= 10.0
ptof= 1.0
rfo= 2.16e-03
rci= 2.539e-03
rco= 2.92e-03
rw= 0.71e-03
ct= 1
xpu= 0.19
xzr= 0.10
fgpav= 0.84E5
bonds= 6.35e-03
totl= 0.343
pco= 1.0e5
tcin= 370.0
axo= 0
qf= 0.952,1.062,1.116,1.115,1.056,0.939,0.760
burnup= 0.0,0.014,0.014,0.023,0.023,0.024,0.024,0.035,0.035,0.041,0.041,
0.052,0.052,0.052,0.052,0.061,0.061,0.065,0.065,0.067,0.067,0.067,0.067,
0.068,0.068,0.072,0.072,0.073,0.073,0.078,0.078,0.081,0.081,0.091,0.091,
0.092,0.092,0.092,0.092,0.095,0.095,0.095,0.095,0.104,0.104,0.104,0.104,
0.111,0.111,0.189
qmpy= 40.0,40.0,38.93,38.93,37.09,37.09,37.09,37.09,39.47,39.47,
35.23,35.23,28.34,28.34,31.26,31.26,31.52,31.52,27.81,27.81,32.58,32.58,32.58
32.58,31.26,31.26,30.47,30.47,29.67,29.67,29.67,29.67,29.67,29.67,28.08,28.08,28.34,28.34
28.87,28.87,29.1,29.1,28.87,28.87,28.08,28.08,28.08,28.08,28.61,28.61
bc= 1
 tcout= 559.0,559.0,559.0,553.0,553.0,547.0,547.0,541.0,541.0,557.0,557.0,
 534.0,534.0,509.0,509.0,522.0,522.0,522.0,522.0,505.0,505.0,527.0,527.0,
 526.0,526.0,518.0,518.0,516.0,516.0,514.0,514.0,514.0,514.0,516.0,516.0,
 510.0,510.0,514.0,514.0,514.0,514.0,511.0,511.0,510.0,510.0,510.0,510.0,
 510.0,510.0,510.0
```

fl= 0
tr= 0

EBR-II X430 Input:

"FEAST: X430"
im= 50
na= 7
nrf= 6
nrc= 3
dt= 20.0
ptof= 1.4
rfo= 2.858e-03
rci= 3.277e-03
rco= 3.683e-03
rw= 0.71e-03
ct= 1
xpu= 0.19
xzr= 0.10
fgpav= 0.84E5
bonds= 6.35e-03
totl= 0.343
pco= 1.0e5
tcin= 370.0
axo= 0
qf= 0.952,1.062,1.116,1.115,1.056,0.939,0.760
burnup= 0.0,0.014,0.014,0.023,0.023,0.024,0.024,0.035,0.035,0.041,0.041,
0.052,0.052,0.052,0.052,0.061,0.061,0.065,0.065,0.067,0.067,0.067,0.067,
0.068,0.068,0.072,0.072,0.073,0.073,0.078,0.078,0.081,0.081,0.091,0.091,
0.092,0.092,0.092,0.092,0.095,0.095,0.095,0.095,0.104,0.104,0.104,0.104,
0.111,0.111,0.116
qmpy= 49.54, 49.54,48.23,48.23,45.93,45.93,45.93,45.93,48.88,48.88,43.64,43.64,35.1,35.1
38.71,38.71,39.04,39.04,34.45,34.45,40.35,40.35,40.35,40.35,38.71,38.71,37.72,37.72,
36.75,36.75,36.75,36.75,36.75,36.75,34.78,34.78,35.76,35.76,36.09,36.09,35.76,35.76,
34.78,34.78,34.78,34.78,35.10,35.10,35.43,35.43
bc= 1
tcout= 559.0,559.0,553.0,553.0,547.0,547.0,541.0,541.0,557.0,557.0,534.0,
534.0,509.0,509.0,522.0,522.0,522.0,522.0,505.0,505.0,527.0,527.0,526.0,
526.0,518.0,518.0,516.0,516.0,514.0,514.0,514.0,514.0,516.0,516.0,510.0,
510.0,514.0,514.0,514.0,514.0,511.0,511.0,510.0,510.0,510.0,510.0,512.0,
512.0,512.0,512.0
fl= 0
tr= 0

EBR-II X447 Input:

"FEAST: X447"
im= 22
na= 10
nrf= 6
nrc= 3
dt= 10.0
ptof= 1.4
rfo= 2.1997e-03
rci= 2.54e-03
rco= 2.92e-03
rw= 0.71e-03
ct= 1
xpu= 0.0
xzr= 0.10
fgpav= 0.84E5
bonds= 6.35e-03
totl= 0.343
pco= 1.0e5
tcin= 370.85
axo= 1
qf= 0.952,1.062,1.116,1.115,1.056,0.939,0.8377,0.7903,0.7379,0.6724
burnup= 0.0,0.014,0.018,0.0224,0.027,0.0348,0.039,0.0477,0.0495,0.0515,0.054,
0.057,0.061,0.0653,0.066,0.067,0.069,0.0803,0.0853,0.0968,0.0988,0.100
qmpy= 33.0,33.0,31.2,31.2,30.7,30.7,29.5,29.5,29.2,29.2,30.2,30.2,
31.6,31.6,32.5,32.5,30.3,30.3,28.7,28.7,27.1,27.1
bc= 1
tcout= 635.0,635.0,620.5,620.5,616.5,616.5,606.9,606.9,604.5,604.5
612.5,612.5,623.8,623.8,631.0,631.0,613.3,613.3,600.4,600.4,587.6,587.6
fl= 0
tr= 0

Transients:

FM1 Furnace Test Input:

"FEAST: FM1"
im= 50
na= 10
nrf= 6
nrc= 3
dt= 10.0
ptof= 1.0
rfo= 2.1999e-03
rci= 2.539e-03
rco= 2.92e-03
rw= 0.71e-03
ct= 1
xpu= 0.0
xzr= 0.10
fgpav= 0.84E5
bonds= 6.35e-03
totl= 0.343
pco= 1.0e5
tcin= 370.0
ax= 1
qf= 0.952,1.062,1.116,1.115,1.056,0.939,0.8377,0.7903,0.7379,0.6724
burnup= 0.0,0.014,0.014,0.023,0.023,0.024,0.024,0.035,0.035,0.041,0.041,
0.052,0.052,0.052,0.052,0.061,0.061,0.065,0.065,0.067,0.067,0.067,0.067,
0.068,0.068,0.072,0.072,0.073,0.073,0.078,0.078,0.081,0.081,0.091,0.091,
0.092,0.092,0.092,0.092,0.095,0.095,0.095,0.095,0.104,0.104,0.104,0.104,
0.111,0.111,0.116
qmpy= 49.54, 49.54,48.23,48.23,45.93,45.93,45.93,45.93,48.88,48.88,43.64,43.64,35.1,35.1
38.71,38.71,39.04,39.04,34.45,34.45,40.35,40.35,40.35,40.35,38.71,38.71,37.72,37.72,
36.75,36.75,36.75,36.75,36.75,36.75,34.78,34.78,35.76,35.76,36.09,36.09,35.76,35.76,
34.78,34.78,34.78,34.78,35.10,35.10,35.43,35.43
bc= 1
tcout= 559.0,559.0,553.0,553.0,547.0,547.0,541.0,541.0,557.0,557.0,534.0,
534.0,509.0,509.0,522.0,522.0,522.0,522.0,505.0,505.0,527.0,527.0,526.0,
526.0,518.0,518.0,516.0,516.0,514.0,514.0,514.0,514.0,516.0,516.0,510.0,
510.0,514.0,514.0,514.0,514.0,511.0,511.0,510.0,510.0,510.0,510.0,512.0,
512.0,512.0,512.0
fl= 0
tr= 1
imt= 7
flagtr= 1.0
dttr= 0.005
buss= 0.03

trt= 0.0,100.0,600,650.0,800.0,900.0,15000.0
powt= 14.0,0.001,0.001,0.001,0.001,0.001,0.001
ciit= 370.0,370.0,370.0,670.0,720.0,720.0,720.0
bct= 1
coot= 541.0,500.0,500.0,801.7,841.7,821.7,821.7

FM2 Furnace Test Input:

"FEAST: FM2"
im= 50
na= 10
nrf= 6
nrc= 3
dt= 10.0
ptof= 1.0
rfo= 2.1999e-03
rci= 2.539e-03
rco= 2.92e-03
rw= 0.71e-03
ct= 1
xpu= 0.19
xzr= 0.10
fgpav= 0.84E5
bonds= 6.35e-03
totl= 0.343
pco= 1.0e5
tcin= 370.0
ax= 1
qf= 0.952,1.062,1.116,1.115,1.056,0.939,0.8377,0.7903,0.7379,0.6724
burnup= 0.0,0.014,0.014,0.023,0.023,0.024,0.024,0.035,0.035,0.041,0.041,
0.052,0.052,0.052,0.052,0.061,0.061,0.065,0.065,0.067,0.067,0.067,0.067,
0.068,0.068,0.072,0.072,0.073,0.073,0.078,0.078,0.081,0.081,0.091,0.091,
0.092,0.092,0.092,0.092,0.095,0.095,0.095,0.095,0.104,0.104,0.104,0.104,
0.111,0.111,0.116
qmpy= 49.54, 49.54,48.23,48.23,45.93,45.93,45.93,45.93,48.88,48.88,43.64,43.64,35.1,35.1
38.71,38.71,39.04,39.04,34.45,34.45,40.35,40.35,40.35,40.35,38.71,38.71,37.72,37.72,
36.75,36.75,36.75,36.75,36.75,36.75,34.78,34.78,35.76,35.76,36.09,36.09,35.76,35.76,
34.78,34.78,34.78,34.78,35.10,35.10,35.43,35.43
bc= 1
tcout= 559.0,559.0,553.0,553.0,547.0,547.0,541.0,541.0,557.0,557.0,534.0,
534.0,509.0,509.0,522.0,522.0,522.0,522.0,505.0,505.0,527.0,527.0,526.0,
526.0,518.0,518.0,516.0,516.0,514.0,514.0,514.0,514.0,516.0,516.0,510.0,
510.0,514.0,514.0,514.0,514.0,511.0,511.0,510.0,510.0,510.0,510.0,512.0,
512.0,512.0,512.0
fl= 0
tr= 1
imt= 7
flagtr= 1.0
dttr= 0.005
buss= 0.03
trt= 0.0,100.0,600,650.0,800.0,900.0,15000.0
powt= 14.0,0.001,0.001,0.001,0.001,0.001,0.001

ciit= 370.0,370.0,370.0,670.0,711.0,691.0,691.0
bct= 1
coot= 541.0,500.0,500.0,801.7,841.7,821.7,821.7

FM3 Furnace Test Input:

"FEAST: FM3"
im= 50
na= 10
nrf= 6
nrc= 3
dt= 10.0
ptof= 1.4
rfo= 2.1999e-03
rci= 2.539e-03
rco= 2.92e-03
rw= 0.71e-03
ct= 1
xpu= 0.26
xzr= 0.10
fgpav= 0.84E5
bonds= 6.35e-03
totl= 0.343
pco= 1.0e5
tcin= 370.0
ax= 1
qf= 0.952,1.062,1.116,1.115,1.056,0.939,0.8377,0.7903,0.7379,0.6724
burnup= 0.0,0.014,0.014,0.023,0.023,0.024,0.024,0.035,0.035,0.041,0.041,
0.052,0.052,0.052,0.052,0.061,0.061,0.065,0.065,0.067,0.067,0.067,0.067,
0.068,0.068,0.072,0.072,0.073,0.073,0.078,0.078,0.081,0.081,0.091,0.091,
0.092,0.092,0.092,0.092,0.095,0.095,0.095,0.095,0.104,0.104,0.104,0.104,
0.111,0.111,0.116
qmpy= 49.54, 49.54,48.23,48.23,45.93,45.93,45.93,45.93,48.88,48.88,43.64,43.64,35.1,35.1
38.71,38.71,39.04,39.04,34.45,34.45,40.35,40.35,40.35,40.35,38.71,38.71,37.72,37.72,
36.75,36.75,36.75,36.75,36.75,36.75,34.78,34.78,35.76,35.76,36.09,36.09,35.76,35.76,
34.78,34.78,34.78,34.78,35.10,35.10,35.43,35.43
bc= 1
tcout= 559.0,559.0,553.0,553.0,547.0,547.0,541.0,541.0,557.0,557.0,534.0,
534.0,509.0,509.0,522.0,522.0,522.0,522.0,505.0,505.0,527.0,527.0,526.0,
526.0,518.0,518.0,516.0,516.0,514.0,514.0,514.0,514.0,516.0,516.0,510.0,
510.0,514.0,514.0,514.0,514.0,511.0,511.0,510.0,510.0,510.0,510.0,512.0,
512.0,512.0,512.0
fl= 0
tr= 1
imt= 7
flagtr= 1.0
dttr= 0.005
buss= 0.022
trt= 0.0,100.0,600,650.0,800.0,900.0,15000.0
powt= 14.7,0.001,0.001,0.001,0.001,0.001,0.001

ciit= 370.0,370.0,370.0,670.0,711.0,691.0,691.0
bct= 1
coot= 541.0,500.0,500.0,801.7,841.7,821.7,821.7

FM4 Furnace Test Input:

"FEAST: FM4"
im= 50
na= 10
nrf= 6
nrc= 3
dt= 10.0
ptof= 1.5
rfo= 2.1999e-03
rci= 2.539e-03
rco= 2.92e-03
rw= 0.71e-03
ct= 1
xpu= 0.19
xzr= 0.10
fgpav= 0.84E5
bonds= 6.35e-03
totl= 0.343
pco= 1.0e5
tcin= 370.0
ax= 1
qf= 0.952,1.062,1.116,1.115,1.056,0.939,0.8377,0.7903,0.7379,0.6724
burnup= 0.0,0.014,0.014,0.023,0.023,0.024,0.024,0.035,0.035,0.041,0.041,
0.052,0.052,0.052,0.052,0.061,0.061,0.065,0.065,0.067,0.067,0.067,0.067,
0.068,0.068,0.072,0.072,0.073,0.073,0.078,0.078,0.081,0.081,0.091,0.091,
0.092,0.092,0.092,0.092,0.095,0.095,0.095,0.095,0.104,0.104,0.104,0.104,
0.111,0.111,0.116
qmpy= 49.54, 49.54,48.23,48.23,45.93,45.93,45.93,45.93,48.88,48.88,43.64,43.64,35.1,35.1
38.71,38.71,39.04,39.04,34.45,34.45,40.35,40.35,40.35,40.35,38.71,38.71,37.72,37.72,
36.75,36.75,36.75,36.75,36.75,36.75,34.78,34.78,35.76,35.76,36.09,36.09,35.76,35.76,
34.78,34.78,34.78,34.78,35.10,35.10,35.43,35.43
bc= 1
tcout= 559.0,559.0,553.0,553.0,547.0,547.0,541.0,541.0,557.0,557.0,534.0,
534.0,509.0,509.0,522.0,522.0,522.0,522.0,505.0,505.0,527.0,527.0,526.0,
526.0,518.0,518.0,516.0,516.0,514.0,514.0,514.0,514.0,516.0,516.0,510.0,
510.0,514.0,514.0,514.0,514.0,511.0,511.0,510.0,510.0,510.0,510.0,512.0,
512.0,512.0,512.0
fl= 0
tr= 1
imt= 6
flagtr= 1.0
dttr= 0.005
buss= 0.114
trt= 0.0,100.0,600.0,646.0,725.0,15000.0
powt= 10.8,0.1,0.1,0.1,0.1,0.1

ciit= 370.0,370.0,370.0,670.0,670.0,670.0
bct= 1
coot= 512.0,500.0,500.0,777.5,771.5,771.5

FM5 Furnace Test Input:

"FEAST: FM5"
im= 50
na= 10
nrf= 6
nrc= 3
dt= 10.0
ptof= 1.5
rfo= 2.1999e-03
rci= 2.539e-03
rco= 2.92e-03
rw= 0.71e-03
ct= 1
xpu= 0.19
xzr= 0.10
fgpav= 0.84E5
bonds= 6.35e-03
totl= 0.343
pco= 1.0e5
tcin= 370.0
ax= 1
qf= 0.952,1.062,1.116,1.115,1.056,0.939,0.8377,0.7903,0.7379,0.6724
burnup= 0.0,0.014,0.014,0.023,0.023,0.024,0.024,0.035,0.035,0.041,0.041,
0.052,0.052,0.052,0.052,0.061,0.061,0.065,0.065,0.067,0.067,0.067,0.067,
0.068,0.068,0.072,0.072,0.073,0.073,0.078,0.078,0.081,0.081,0.091,0.091,
0.092,0.092,0.092,0.092,0.095,0.095,0.095,0.095,0.104,0.104,0.104,0.104,
0.111,0.111,0.116
qmpy= 49.54, 49.54,48.23,48.23,45.93,45.93,45.93,45.93,48.88,48.88,43.64,43.64,35.1,35.1
38.71,38.71,39.04,39.04,34.45,34.45,40.35,40.35,40.35,40.35,38.71,38.71,37.72,37.72,
36.75,36.75,36.75,36.75,36.75,36.75,34.78,34.78,35.76,35.76,36.09,36.09,35.76,35.76,
34.78,34.78,34.78,34.78,35.10,35.10,35.43,35.43
bc= 1
tcout= 559.0,559.0,553.0,553.0,547.0,547.0,541.0,541.0,557.0,557.0,534.0,
534.0,509.0,509.0,522.0,522.0,522.0,522.0,505.0,505.0,527.0,527.0,526.0,
526.0,518.0,518.0,516.0,516.0,514.0,514.0,514.0,514.0,516.0,516.0,510.0,
510.0,514.0,514.0,514.0,514.0,511.0,511.0,510.0,510.0,510.0,510.0,512.0,
512.0,512.0,512.0
fl= 0
tr= 1
imt= 4
flagtr= 1.0
dttr= 0.005
buss= 0.114
trt= 0.0,45.0,80.0,180.0
powt= 10.8,2.16,1.08,0.54

ciit= 370.0,370.0,370.0,370.0
bct= 1
coot= 512.0,780.0,550.0,417.0

FM6 Furnace Test Input:

"FEAST: FM6"
im= 50
na= 10
nrf= 6
nrc= 3
dt= 10.0
ptof= 1.0
rfo= 2.1999e-03
rci= 2.539e-03
rco= 2.92e-03
rw= 0.71e-03
ct= 1
xpu= 0.19
xzr= 0.10
fgpav= 0.84E5
bonds= 6.35e-03
totl= 0.343
pco= 1.0e5
tcin= 370.0
ax= 1
qf= 0.952,1.062,1.116,1.115,1.056,0.939,0.8377,0.7903,0.7379,0.6724
burnup= 0.0,0.014,0.014,0.023,0.023,0.024,0.024,0.035,0.035,0.041,0.041,
0.052,0.052,0.052,0.052,0.061,0.061,0.065,0.065,0.067,0.067,0.067,0.067,
0.068,0.068,0.072,0.072,0.073,0.073,0.078,0.078,0.081,0.081,0.091,0.091,
0.092,0.092,0.092,0.092,0.095,0.095,0.095,0.095,0.104,0.104,0.104,0.104,
0.111,0.111,0.116
qmpy= 49.54, 49.54,48.23,48.23,45.93,45.93,45.93,45.93,48.88,48.88,43.64,43.64,35.1,35.1
38.71,38.71,39.04,39.04,34.45,34.45,40.35,40.35,40.35,40.35,38.71,38.71,37.72,37.72,
36.75,36.75,36.75,36.75,36.75,36.75,34.78,34.78,35.76,35.76,36.09,36.09,35.76,35.76,
34.78,34.78,34.78,34.78,35.10,35.10,35.43,35.43
bc= 1
tcout= 559.0,559.0,553.0,553.0,547.0,547.0,541.0,541.0,557.0,557.0,534.0,
534.0,509.0,509.0,522.0,522.0,522.0,522.0,505.0,505.0,527.0,527.0,526.0,
526.0,518.0,518.0,516.0,516.0,514.0,514.0,514.0,514.0,516.0,516.0,510.0,
510.0,514.0,514.0,514.0,514.0,511.0,511.0,510.0,510.0,510.0,510.0,512.0,
512.0,512.0,512.0
fl= 0
tr= 1
imt= 5
flagtr= 1.0
dttr= 0.02
buss= 0.113
trt= 0.0,100.0,600.0,625.0,150000.0
powt= 10.8,0.001,0.001,0.001,0.001

ciit= 370.0,370.0,370.0,521.0,521.0
bct= 1
coot= 512.0,500.0,500.0,651.0,651.0

C.3. FEAST-OXIDE Input Description

FEAST-OXIDE input file description is given in Table-52. Furthermore, a sample input file is given below. FEAST can be run with the executable file (.exe) together with the input text file (input.txt).

Table-52: FEAST-OXIDE input description

Line Number	Description	Symbol
1	Title	-
2	# of time nodes	im
3	# of axial nodes	Na
4	# of radial nodes within the fuel pellet	nrf (six is recommended)
5	# of radial nodes within the clad	nrc (>2 is recommended)
6	Steady state time step	dt (5 seconds or less)
7	Plenum to fuel ratio	ptof
8	Fuel pellet inner radius	Rfi
9	Fuel pellet outer radius (m)	Rfo
10	Clad inner radius (m)	Rci
11	Clad outer radius (m)	Rco
12	Wire radius (m)	Rw
13	Initial Oxygen to metal ratio	Om
14	PuO_2 weight fraction	Xpu
15	Initial as-fabricated porosity fraction	Xpor
16	Initial fill gas pressure (Pa)	fpgav
17	As –fabricated grain size (μm) (default is 8)	Gra
18	Fuel active height (m)	Totl
19	Coolant pressure (Pa)	Pco
20	Coolant inlet temperature (^{0}C)	Tcin
21	Axial Power distribution (normalized to one)*	qf(i), i= 1,na
22	Burnup (atom fraction)	burnup(i), i= 1,im
23	Average Linear Heat Rate (kW/m)	qmpy(i), i=1,im
24	if 0, coolant mass flow rate will be specified; If 1, coolant outlet temperature will be specified next	bc

25	Coolant outlet temperature ^{0}C or mass flow rate (kg/s)	mdot (i), i=1,im tco(i), i=1,im
26	0, if EBR-II neutronics condition is specified. It is assumed that flux and volumetric heat generation rate is proportional. The reference flux is 1.6E+15 The reference volumetric heat generation rate = 1.9E+9 W/m^3 1, if a different reference neutron flux and volumetric heat generation rate is specified; 2, if the fast flux as a function of burnup is specified next.	fl0
27	If fl0 = 1, the reference neutron flux and volumetric heat generation rate need to be specified. If fl0=2 1.0E+15 (n/cm^2/s)	Coef Flux(i) i=1,im
28	0, if this is only a steady state run, input is terminated 1, if transient analysis will be also be performed.	tr0
29	0, if this is not an overpower accident 1, if it is an overpower accident	ttype
30	# of transient time nodes	imt
31	Transient time step	Dttr (0.0001 is recommended)
32	Burnup at which transient begins	Buss1
33	Transient time nodes	Imt
34	Transient linear heat rate (kW/m)	powt(i), i=1,imt
35	Coolant inlet temperature (^{0}C)	ciit(i), i=1,imt
36	Transient boundary condition specifier: If 0, coolant mass flow rate will be specified next. If 1, coolant outlet temperature will be specified;	bct
37	If bct = 0, coolant mass flow rate (kg/s) If bct = 1, coolant outlet temperature (^{0}C)	mdott(i), i=1,imt Coot(i), i=1,imt

* The top axial node is 5 cm. It is modeled in such a way to simulate the cesium axial migration behavior as well as thermal creep and rupture behavior of the cladding in an accurate manner.

C.4. Oxide Fuel Benhmark Inputs

Steady State:

FFTF ACO-1 Input:

```
"FEAST: ACO-1"
 im= 8
 na= 8
 nrf= 6
 nrc= 3
 dt= 4.0
 ptof= 1.0
 rfi= 0.7365e-03
 rfo= 2.7750e-03
 rci= 2.8700e-03
 rco= 3.430e-03
 rw= 0.7e-03
 om= 1.95
 xpu= 0.225
 xpor= 0.085
 fgpav= 3.0E5
 gra= 8.0
 totl= 0.9144
 pco= 1.0e5
 tcin= 360.0
 qf= 0.889,1.041,1.152,1.173,1.129,0.971,0.782,0.672
 burnup= 0.0,0.019,0.038,0.057,0.076,0.095,0.114,0.125
 qmpy= 42.0,38.46,35.67,33.31,30.87,29.28,27.84,26.42
 bc= 1
 tcout= 685.0,657.6,636.0,617.8,603.9,586.6,575.4,564.5
 fl= 1
 coef= 4.72E+15,1.9E+9
 tr= 0
```

FFTF ACO-3 Input:

"FEAST: ACO-3"
im= 10
na= 8
nrf= 6
nrc= 3
dt= 4.0
ptof= 1.0
rfi= 0.7365e-03
rfo= 2.7750e-03
rci= 2.8700e-03
rco= 3.430e-03
rw= 0.7e-03
om= 1.95
xpu= 0.225
xpor= 0.085
fgpav= 3.0E5
gra= 8.0
totl= 0.9144
pco= 1.0e5
tcin= 360.0
qf= 0.889,1.041,1.152,1.173,1.129,0.971,0.782,0.672
burnup= 0.0,0.019,0.038,0.057,0.076,0.095,0.114,0.133,0.152,0.163
qmpy= 42.6,39.01,36.18,33.79,31.97,29.7,28.24,26.8,25.85,25.37
bc= 1
tcout= 654.0,629.2,609.7,593.2,580.6,565.0,554.9,545.0,538.4,535.1
fl= 1
coef= 3.68E+15,1.9E+9
tr= 0

FFTF CDE Input:

"FEAST: CDE"
im= 10
na= 8
nrf= 6
nrc= 3
dt= 4.0
ptof= 1.0
rfi= 0.7365e-03
rfo= 2.7750e-03
rci= 2.8700e-03
rco= 3.430e-03
rw= 0.7e-03
om= 1.95
xpu= 0.225
xpor= 0.085
fgpav= 3.0E5
gra= 8.0
totl= 0.9144
pco= 1.0e5
tcin= 360.0
qf= 0.889,1.041,1.152,1.173,1.129,0.971,0.782,0.672
burnup= 0.0,0.019,0.038,0.057,0.076,0.095,0.114,0.133,0.152,0.171
qmpy= 44.5,40.75,37.80,35.30,33.40,31.0,29.5,28.0,27.0,26.5
bc= 1
tcout= 588.0,569.4,556.2,544.8,537.0,530.5,522.9,515.5,511.0,507.3
fl= 1
coef= 4.72E+15,1.9E+9
tr= 0

EBR-II P42R-1:

"FEAST: P42R-1"
im= 2
na= 7
nrf= 6
nrc= 3
dt= 4.0
ptof= 1.0
rfi= 0.100e-04
rfo= 3.132e-03
rci= 3.150e-03
rco= 3.430e-03
rw= 0.7e-03
om= 1.945
xpu= 0.225
xpor= 0.066
fgpav= 3.0E5
gra= 8.0
totl= 0.343
pco= 1.0e5
tcin= 370.0
qf= 0.930,1.047,1.108,1.113,1.063,0.957,0.786
burnup= 0.0,0.05
qmpy= 40.4,40.4
bc= 1
tcout= 550.0,550.0
fl= 1
coef= 2.4E+15,1.9E+9
tr= 0

EBR-II P42R-2:

"FEAST: P42R-2"
im= 2
na= 7
nrf= 6
nrc= 3
dt= 4.0
ptof= 1.0
rfi= 0.100e-04
rfo= 3.132e-03
rci= 3.150e-03
rco= 3.430e-03
rw= 0.7e-03
om= 1.916
xpu= 0.225
xpor= 0.066
fgpav= 3.0E5
gra= 8.0
totl= 0.343
pco= 1.0e5
tcin= 370.0
qf= 0.930,1.047,1.108,1.113,1.063,0.957,0.786
burnup= 0.0,0.05
qmpy= 47.3,47.3
bc= 1
tcout= 536.0,536.0
fl= 1
coef= 2.4E+15,1.9E+9
tr= 0

EBR-II P42R-3:

"FEAST: P42R-3"
im= 2
na= 7
nrf= 6
nrc= 3
dt= 4.0
ptof= 1.0
rfi= 0.100e-04
rfo= 3.132e-03
rci= 3.150e-03
rco= 3.430e-03
rw= 0.7e-03
om= 1.916
xpu= 0.225
xpor= 0.066
fgpav= 3.0E5
gra= 8.0
totl= 0.343
pco= 1.0e5
tcin= 370.0
qf= 0.930,1.047,1.108,1.113,1.063,0.957,0.786
burnup= 0.0,0.05
qmpy= 45.6,45.6
bc= 1
tcout= 600.0,600.0
fl= 1
coef= 2.4E+15,1.9E+9
tr= 0

JOYO MK-I input:

"FEAST: JOYO MK1"
im= 4
na= 8
nrf= 6
nrc= 3
dt= 4.0
ptof= 1.0
rfi= 0.100e-04
rfo= 2.700e-03
rci= 2.800e-03
rco= 3.150e-03
rw= 0.6e-03
om= 1.98
xpu= 0.25
xpor= 0.065
fgpav= 3.0E5
gra= 8.0
totl= 0.6
pco= 1.0e5
tcin= 370.0
qf= 0.889,1.041,1.152,1.173,1.129,0.971,0.782,0.672
burnup= 0.0,0.019,0.038,0.057
qmpy= 32.0,29.3,27.1,25.4
bc= 1
tcout= 554.0,538.0,526.0,516.0
fl= 1
coef= 4.16E+15,1.9E+9
tr= 0

JOYO MK-II Input:

```
"FEAST: JOYO MK2"
  im= 4
  na= 8
  nrf= 6
  nrc= 3
  dt= 4.0
  ptof= 1.0
  rfi= 0.1000e-04
  rfo= 2.3150e-03
  rci= 2.4000e-03
  rco= 2.750e-03
  rw= 0.5e-03
  om= 1.98
  xpu= 0.25
  xpor= 0.07
  fgpav= 3.0E5
  gra= 8.0
  totl= 0.55
  pco= 1.0e5
  tcin= 370.0
  qf= 0.889,1.041,1.152,1.173,1.129,0.971,0.782,0.672
  burnup= 0.0,0.019,0.038,0.057
  qmpy= 40.0,36.6,33.9,31.73
  bc= 1
  tcout= 600.0,580.0,565.0,552.0
  fl= 1
  coef= 4.16E+15,1.9E+9
  tr= 0
```

Transients:

EBR-II WT028 Input:

```
"FEAST: WT028"
 im= 3
 na= 7
 nrf= 6
 nrc= 3
 dt= 4.0
 ptof= 1.12
 rfi= 0.1000e-04
 rfo= 3.0830e-03
 rci= 3.1240e-03
 rco= 3.4925e-03
 rw= 0.7e-03
 om= 1.95
 xpu= 0.225
 xpor= 0.096
 fgpav= 3.0E5
 gra= 8.0
 totl= 0.343
 pco= 1.0e5
 tcin= 370.0
 qf= 0.93,1.047,1.108,1.113,1.063,0.957,0.786
 burnup= 0.0,0.023,0.025
 qmpy= 35.0,35.0,33.6
 bc= 1
 tcout= 597.0,597.0,547.0
 fl= 1
 coef= 2.72E+15,1.9E+9
 tr= 1
 imt= 2
 dttr= 0.0001
 buss= 0.025
 tr= 0.0,910.0
 powt= 33.6,63.9
 ciit= 370.0,370.0
 coot= 547.0,726.0
```

EBR-II WT118 Input:

"FEAST: metal fuel code"
im= 3
na= 7
nrf= 6
nrc= 3
dt= 4.0
ptof= 1.18
rfi= 0.1000e-04
rfo= 2.498e-03
rci= 2.541e-03
rco= 2.921e-03
rw= 0.7e-03
om= 1.96
xpu= 0.33
xpor= 0.066
fgpav= 3.0E5
gra= 8.0
totl= 0.343
pco= 1.0e5
tcin= 370.0
qf= 0.93,1.047,1.108,1.113,1.063,0.957,0.786
burnup= 0.0,0.091,0.093
qmpy= 34.7,34.7,31.7
bc= 1
tcout= 617.0,617.0,608.0
fl= 1
coef= 2.72E+15,1.9E+9
tr= 1
imt= 2
dttr= 0.0001
buss= 0.093
tr= 0.0,910.0
powt= 31.7,60.3
ciit= 370.0,370.0
coot= 608.0,840.0

EBR-II WT107 Input:

"FEAST: WT107"
im= 3
na= 7
nrf= 6
nrc= 3
dt= 4.0
ptof= 1.12
rfi= 0.1000e-04
rfo= 3.0745e-03
rci= 3.124e-03
rco= 3.4925e-03
rw= 0.7e-03
om= 1.97
xpu= 0.225
xpor= 0.071
fgpav= 3.0E5
gra= 8.0
totl= 0.343
pco= 1.0e5
tcin= 370.0
qf= 0.93,1.047,1.108,1.113,1.063,0.957,0.786
burnup= 0.0,0.075,0.077
qmpy= 42.4,42.4,38.8
bc= 1
tcout= 607.0,607.0,584.0
fl= 1
coef= 2.72E+15,1.9E+9
tr= 1
imt= 2
dttr= 0.0001
buss= 0.077
tr= 0.0,910.0
powt= 38.8,73.9
ciit= 370.0,370.0
coot= 584.0,796.0

EBR-II WT022 Input:

"FEAST: WT022"
im= 3
na= 7
nrf= 6
nrc= 3
dt= 4.0
ptof= 1.12
rfi= 0.1000e-04
rfo= 3.0465e-03
rci= 3.124e-03
rco= 3.4925e-03
rw= 0.7e-03
om= 1.95
xpu= 0.3
xpor= 0.097
fgpav= 3.0E5
gra= 8.0
totl= 0.343
pco= 1.0e5
tcin= 370.0
qf= 0.93,1.047,1.108,1.113,1.063,0.957,0.786
burnup= 0.0,0.058,0.06
qmpy= 31.8,31.8,30.8
bc= 1
tcout= 568.0,568.0,562.0
fl= 1
coef= 2.72E+15,1.9E+9
tr= 1
imt= 2
dttr= 0.0001
buss= 0.060
tr= 0.0,910.0
powt= 30.8,58.7
ciit= 370.0,370.0
coot= 562.0,757.0

EBR-II WT033 Input:

"FEAST: WT033"
im= 3
na= 7
nrf= 6
nrc= 3
dt= 4.0
ptof= 1.12
rfi= 0.1000e-04
rfo= 3.083e-03
rci= 3.124e-03
rco= 3.4925e-03
rw= 0.7e-03
om= 1.95
xpu= 0.3
xpor= 0.096
fgpav= 3.0E5
gra= 8.0
totl= 0.343
pco= 1.0e5
tcin= 370.0
qf= 0.93,1.047,1.108,1.113,1.063,0.957,0.786
burnup= 0.0,0.057,0.059
qmpy= 33.1,33.1,31.6
bc= 1
tcout= 568.0,568.0,542.0
fl= 1
coef= 2.72E+15,1.9E+9
tr= 1
imt= 2
dttr= 0.0001
buss= 0.059
tr= 0.0,910.0
powt= 31.6,60.1
ciit= 370.0,370.0
coot= 542.0,719.0

EBR-II WT180 Input:

"FEAST: WT180"
im= 3
na= 7
nrf= 6
nrc= 3
dt= 4.0
ptof= 1.12
rfi= 0.1000e-04
rfo= 3.081e-03
rci= 3.164e-03
rco= 3.4925e-03
rw= 0.7e-03
om= 1.97
xpu= 0.225
xpor= 0.054
fgpav= 3.0E5
gra= 8.0
totl= 0.343
pco= 1.0e5
tcin= 370.0
qf= 0.93,1.047,1.108,1.113,1.063,0.957,0.786
burnup= 0.0,0.062,0.064
qmpy= 37.6,37.6,39.4
bc= 1
tcout= 603.0,603.0,592.0
fl= 1
coef= 2.72E+15,1.9E+9
tr= 1
imt= 2
dttr= 0.0001
buss= 0.069
tr= 0.0,910.0
powt= 39.4,75.0
ciit= 370.0,370.0
coot= 592.0,808.0

EBR-II WT179 Input:

"FEAST: WT179"
im= 3
na= 7
nrf= 6
nrc= 3
dt= 4.0
ptof= 1.12
rfi= 0.1000e-04
rfo= 3.081e-03
rci= 3.164e-03
rco= 3.4925e-03
rw= 0.7e-03
om= 1.97
xpu= 0.225
xpor= 0.054
fgpav= 3.0E5
gra= 8.0
totl= 0.343
pco= 1.0e5
tcin= 370.0
qf= 0.93,1.047,1.108,1.113,1.063,0.957,0.786
burnup= 0.0,0.062,0.064
qmpy= 39.0,39.0,39.1
bc= 1
tcout= 618.0,618.0,590.0
fl= 1
coef= 2.72E+15,1.9E+9
tr= 1
imt= 2
dttr= 0.0001
buss= 0.071
tr= 0.0,910.0
powt= 39.4,74.4
ciit= 370.0,370.0
coot= 590.0,805.0

EBR-II WT011 Input:

"FEAST: WT011"
im= 3
na= 7
nrf= 6
nrc= 3
dt= 4.0
ptof= 1.12
rfi= 0.1000e-04
rfo= 3.0465e-03
rci= 3.124e-03
rco= 3.4925e-03
rw= 0.7e-03
om= 1.95
xpu= 0.225
xpor= 0.097
fgpav= 3.0E5
gra= 8.0
totl= 0.343
pco= 1.0e5
tcin= 370.0
qf= 0.93,1.047,1.108,1.113,1.063,0.957,0.786
burnup= 0.0,0.062,0.064
qmpy= 34.6,34.6,30.7
bc= 1
tcout= 577.0,577.0,592.0
fl= 1
coef= 2.72E+15,1.9E+9
tr= 1
imt= 2
dttr= 0.0001
buss= 0.064
tr= 0.0,910.0
powt= 31.7,58.5
ciit= 370.0,370.0
coot= 592.0,811.0